UNIVERSITY OF CALIFORNIA

Los Angeles

The coordination and role of activity in developing neural circuits

A dissertation submitted in partial satisfaction of the

requirements for the degree Doctor of Philosophy

in Neuroscience

by

Bryce Thomas Bajar

2021

ABSTRACT OF THE DISSERTATION

The coordination and role of activity in developing neural circuits

by

Bryce Thomas Bajar

Doctor of Philosophy in Neuroscience

University of California, Los Angeles, 2021

Professor Stephen Lawrence Zipursky, Co-Chair

Professor Orkun Akin, Co-Chair

The stereotyped synaptic connections that define neural circuit function are established during development. Neuronal activity independent of environmental stimulus contributes to neural circuit assembly in vertebrates, but its precise role remains an open question, particularly at the level of defined cell types. By contrast, invertebrate neurodevelopment was thought to proceed in the absence of such developmental activity. Here I show that developmental activity accompanies synaptogenesis in the *Drosophila* brain. Using *Drosophila* genetics, epifluorescence microscopy, two-photon microscopy, immunohistochemistry, and visual behavior, I characterize this developmental activity, determine its role in synapse formation, and identify regulatory mechanisms at the cellular and molecular level. This patterned-stimulus independent neural activity occurs in a brain-wide fashion, and is characterized by stereotyped oscillations and cellular dynamics that reflect synaptic connectivity. Activity patterns instruct

synapse development in a cell-type-specific manner. A transient and genetically specified population of neurons propagates this activity throughout the brain. Glia participate with complementary cycles of activity in a cell-type-specific fashion, and astrocytes are necessary for activity to occur. These data indicate that developmental activity is an evolutionarily conserved and fundamental component of neural circuit assembly that is coordinated by multiple molecular and cellular mechanisms.

Supplemental Materials (attached separately)

Supplemental movie 1: Imaging of optic lobe expressing GCaMP6s pan-neuronally. Clips from three time periods (pre-PSINA at 45 hAPF, periodic stage at 58 hAPF, and turbulent stage at 70 hAPF) are shown. Images were sampled at 0.4 Hz and playback is 60 frames per second (fps). Scale bar is 40 μm.

Supplemental movie 2: Imaging of whole-brain activity in intact pupae under a wide-field epifluorescence microscope. Three animals expressing GCaMP6s pan-neuronally were imaged in parallel. Images were sampled at 0.67 Hz for the movie; playback is 60 fps.

Supplemental movie 3: Imaging of L1 expressing iGluSnFR (blue) and jRCaMP1b (orange). Sweeps within a single active phase at 62 hAPF are shown. Images were sampled at 1.76 Hz and playback is 60 fps. Scale bar is 40 μm.

Supplemental movie 4: Imaging of L1 expressing ArcLight (blue) and jRCaMP1b (orange). Three cycles (starting at 55.3818, 55.6194, and 55.9373 hAPF, or 5, 11, and 19 s into playback) at 55 hAPF are shown. Note that, by contrast to the GECI signal, ArcLight fluorescence intensity decreases during each active phase in response to increases in membrane voltage. Images were sampled at 0.4 Hz and playback is 60 fps. Scale bar is 40 μm.

Supplemental movie 5: Composite time series of L3 and L1. Three cycles at 61 hAPF for L3 and 63 hAPF for L1 are shown. Images were sampled at 0.4 Hz and playback is 60 fps. Scale bar is 40 μm.

Supplemental movie 6: Composite time series of the cell types analyzed in Figures 2.3E-F. Three cycles at approximately 60 hAPF are shown for each. Images were sampled at 0.4 Hz and playback is 60 fps. Scale bar is 40 μm.

Supplemental movie 7: Two-color time series of Tm3 (blue) and T4-5 (orange). Note that observing the relative differences in correlation between the Tm3-T4 and Tm3-T5 pairs may require slower playback. Three cycles at 60 hAPF are shown. Images were sampled at 0.4 Hz and playback is 60 fps. Scale bar is 40 μm.

Supplemental movie 8: Wide-field imaging of whole-brain activity and traces in control (top) or *trpγ* null (bottom) pupae expressing GCaMP6s pan-neuronally. Images were sampled at 1 Hz and playback is 60 frames per second (fps). Scale bar is 200 μm. Activity scale is 0.1 $\Delta F/F_0$.

Supplemental movie 9: Composite time series of the cell types analyzed in Figure 3.2. Three cycles at approximately 60 hAPF are shown for each. Images were sampled at 0.4 Hz and playback is 60 fps. Scale bar is 40 μm.

Supplemental movie 10: 2-photon imaging of $Trp\gamma^{G4}$ expressing GCaMP6s in control (top) or *trpγ* null (bottom) pupae. Three cycles at approximately 60 hAPF are shown for each. Images were sampled at 0.4 Hz and playback is 60 fps. Scale bar is 40 μm.

Supplemental movie 11: Wide-field imaging of whole-brain activity and traces in control (empty-GAL4, top), panN-GAL4>Kir2.1 (middle), and $Trp\gamma^{G4}$>Kir2.1 (bottom) pupae expressing GCaMP6s pan-neuronally. Images were sampled at 1 Hz and playback is 60 fps. Scale bar is 200 μm. Activity scale is 0.1 $\Delta F/F_0$.

The dissertation of Bryce Thomas Bajar is approved.

Mark A. Frye

Baljit S. Khakh

Alapakkam P. Sampath

Orkun Akin, Committee Co-Chair

S. Lawrence Zipursky, Committee Co-Chair

University of California, Los Angeles

2021

TABLE OF CONTENTS

LIST OF FIGURES

LIST OF TABLES

LIST OF ABBREVIATIONS

2P: two-photon

2PM: two-photon microscopy

AIP: average intensity projection

ATP: adenosine triphosphate

ANOVA: analysis of variance

Ca^{2+}: calcium ions

CB: central brain

CG: cortex glia

CNS: central nervous system

CPG: central pattern generator

Df: deficiency

EG: ensheathing glia

EM: electron microscopy

GABA: Gamma aminobutyric acid

GECI: genetically encoded calcium indicator

GFP: green fluorescent protein

hAPF: hours after pupal formation

LGN: lateral geniculate nucleus

MARCM: mosaic analysis with a repressible cell marker

MIP: maximum intensity projection

Myr: myristoylated

OL: optic lobe

PBS: phosphate buffered saline

PFA: paraformaldehyde

PI: pars intercerebralis

PSINA: patterned, stimulus-independent neural activity

RGC: retinal ganglion cell

RNA: ribonucleic acid

RNAi: RNA interference

RT: room temperature

SAC: starburst amacrine cell

SC: superior colliculus

SD: standard deviation

SM: Schneider medium

SPARC: sparse predictive activity through recombinase competition

STaR: synaptic tagging with recombination

STDP: spike timing dependent plasticity

STTC: spike time tiling coefficient

TARGET: temporal and regional gene expression targeting

tdTom: tandem Tomato

TRI: tritocerebrum

TRP: Transient receptor potential

TNT: tetanus toxin

TTX: tetrodotoxin

UAS: upstream activator sequence

ACKNOWLEDGMENTS

My graduate school experience has been fantastic, and none of it would have been possible without the dear colleagues and mentors who have been with me throughout this journey. First, I thank my advisors Dr. Larry Zipursky and Dr. Orkun Akin. Larry gave me a chance to try an unprecedented experiment when I rotated in the lab that developed into an unprecedented project when I joined the lab. He has been exceptionally supportive and generous along the way, and, among many other important lessons, has taught me to ask questions and to collaborate early and often. Speaking of which: Orkun has been the best collaborator possible. We have worked together every day since our accidental discovery of PSINA during my 2016 rotation, and I have enjoyed every minute of our voyage together. The work described here is a reflection of his mentorship and diligence.

I am fortunate to be a part of so many wonderful communities within the scientific world at UCLA. I thank the members of the Zipursky and Akin labs, past and present, for engaging discussions, technical training, and countless fond memories ranging from bagels to birding. I thank my committee members, Dr. Mark Frye, Dr. Baljit Khakh, and Dr. Alapakkam Sampath, for valuable feedback and guidance. From the MSTP, I thank Dr. Carlos Portera-Cailliau for his mentorship throughout my time in the program, as well as Susie Esquivel and Josephine Alviar for their support. I also thank the leadership and administration of the NSIDP and Biological Chemistry, particularly Dr. Felix Schweizer and Jenny Lee, for their help navigating graduate school. From before my time at UCLA, I thank my undergraduate research mentors, Dr. Markus Covert and Dr. Michael Lin, who gave me the opportunity to fall in love with science.

Chapter 2 is modified from published work: Akin O.*, Bajar B.T.*, Keles M.F., Frye M.A., Zipursky S.L. Cell-type-specific patterned stimulus-independent neural activity in the

developing Drosophila visual system during synapse formation. *Neuron*. 2019 Mar 6;101(5):894-904. PMID: 30711355 (*co-first authors). Dr. Larry Zipursky and I conceived the initial approach of studying developmental activity with live calcium imaging. Dr. Larry Zipursky, Dr. Orkun Akin and I developed the project. Dr. Orkun Akin and I designed the imaging and analysis protocols, collected, and analyzed developmental imaging data. Dr. Mehmet Keles and I collected and analyzed adult imaging and behavior data. Dr. Larry Zipursky and Dr. Mark Frye supervised the project.

Chapter 3 is modified from work currently in revision: Bajar B.T., Phi N.T., Isaacman-Beck J., Reichl J., Randhawa H., Akin O. Synaptic development depends on brain-wide activity coordinated by a discrete neuronal population. *Nature*, In Revision. Dr. Orkun Akin and I conceived and developed the project. Nguyen Phi performed confocal imaging and developed the MARCM experiment. Dr. Jesse Isaacman-Beck developed SPARC-Out-Gal80 constructs. Jun Reichl assisted with temperature-shift experiments. Harpreet Randhawa assisted with dissections and image analysis.

Chapter 4 is modified from a submitted manuscript: Bajar B.T., Phi N.T., Akin O. Developmental neuronal activity requires neuron-astrocyte interactions. Dr. Orkun Akin and I conceived and developed the project. I performed and analyzed epifluorescence and two-photon imaging experiments. Nguyen Phi and Dr. Orkun Akin performed and analyzed confocal imaging experiments.

All of these experiments were made possible by the generosity of collaborators and colleagues who have gifted reagents. The collegiality of the fly community at large has been a highlight of graduate school. I direct the reader to the acknowledgments section of each of the above publications for a comprehensive list.

My graduate training was supported by the UCLA Medical-Scientist Training Program (T32-GM008042), the UCLA Neurobehavioral Genetics Training Program (T32-MH73526), and the National Eye Institute NRSA F30 Training Fellowship (F30-EY029952). This work was also supported by the Howard Hughes Medical Institute, at which Dr. Zipursky is an investigator.

Of course, the work described here would not have been worthwhile or feasible without the love and support of my family and friends. I thank the friends I have made throughout the years at Mitty, Stanford, and UCLA for their companionship and our many adventures. I am grateful for my family on both the Bajar and Kwok sides who have been so kind and generous throughout my training, particularly my sister and my grandmother. I thank my partner Leah Kim who has been superlatively caring and inspiring. I could not ask for a better companion through this journey. Finally, I cannot begin to articulate my gratitude to my parents Sophia and Pompeyo Bajar: their guidance and unwavering support mean everything to me.

VITA

Education

2010 – 2014 B.S. in Bioengineering, Stanford University, Stanford, CA

Selected Publications

1. **Bajar B.T.**, Phi N.T., Akin O. Developmental neuronal activity requires neuron-astrocyte interactions. *Submitted*.
2. **Bajar B.T.**, Phi N.T., Isaacman-Beck J., Reichl J., Randhawa H., Akin O. Synaptic development depends on brain-wide activity coordinated by a discrete neuronal population. *Nature*. *In Revision*.
3. **Bajar B.T.**, Lam A., Lin M.Z., Yasuda R., Laviv T., Chu J. FRET imaging of Rho GTPase activity with red fluorescent protein-based FRET pairs. *Methods in Molecular Biology*. 2021. *In Press*.
4. **Bajar B.T.**, Lin M.Z. Simultaneous detection of four cell cycle phases with live fluorescence imaging. *Methods in Molecular Biology*. 2021. *In Press*.
5. Chung H.K., Zou X., **Bajar B.T.**, Brand V.R., Huo Y., Alcudia J.F., Ferrell J.E., Lin M.Z. A compact synthetic pathway rewires cancer signaling to therapeutic effector release. *Science*. 2019 May 3;364(6439). PMID: 31048459
6. Akin O.*, **Bajar B.T.***, Keles M.F., Frye M.A., Zipursky S.L. Cell-type-specific patterned stimulus-independent neural activity in the developing Drosophila visual system during synapse formation. *Neuron*. 2019 Mar 6;101(5):894-904. PMID: 30711355
   * These authors contributed equally.
7. **Bajar B.T.***, Lam A.J.*, Badiee R.K., Oh Y.H., Chu J., Zhou X.X., Kim N., Chung M., Yablonovitch A.L., Cruz B.F., Kulalert K., Tao J.J., Meyer T., Su X.D., Lin M.Z.

Fluorescent indicators for simultaneous reporting of all four cell cycle phases. *Nature Methods*. 2016 Dec;13(12):993-996. PMID: 27798610. * These authors contributed equally.

8. **Bajar B.T.**, Wang E.S., Zhang S., Lin M.Z., Chu J. A guide to fluorescent protein FRET pairs. *Sensors (Basel)*. 2016. 16(9), 1488. pii: E1488. PMID: 27649177
9. **Bajar B.T.**, Wang E.S., Lam A.J., Kim B.B., Jacobs C.L., Howe E.S., Davidson M.W., Lin M.Z., Chu J. Improving brightness and photostability of green and red fluorescent proteins for live cell imaging and FRET reporting. *Scientific Reports*. 2016. 6:20889. doi:10.1038/srep20889. PMID: 26879144
10. Regot S., Hughey J.J., **Bajar B.T.**, Carrasco S., Covert M.W.: High-sensitivity measurements of multiple kinase activities in live single cells. *Cell*. 2014. 157(7):1724-34. PMID: 24949979.

Selected Honors and Awards

2021 29th Samuel Eiduson Student Lectureship

2018 NIH Individual Predoctoral NRSA for MD/PhD Fellowship (NIH F30EY029952)

2018 NIH Predoctoral Training Grant in Neurobehavioral Genetics at UCLA (NIH T32MH073526)

2015 NIH Medical Scientist Training Program Fellowship (NIH T32GM008042)

2014 Stanford Award of Excellence

2012 NASA California Space Grant Consortium Scholarship

2010 Comcast Leaders and Achievers Scholar

Chapter 1

Introduction

1.1. DEVELOPMENTAL ACTIVITY DURING NEURAL CIRCUIT ASSEMBLY

The human brain is a complex organ in which billions of neurons form trillions of synapses. The connectivity of these synapses within neural circuits underlies sensory processing, behavior, and cognition. Understanding how these neural circuits are established during development is a central challenge in neurobiology. Circuit assembly requires the precise selection of synaptic partners, subcellular localization of synaptic proteins, and tuning of both the number and strength of pre- and post-synaptic structures. Neural activity plays a role in these processes that lead to the maturation of neural circuits, but its precise role in establishing synapses during development remains an open question.

Much of circuit development proceeds without electrical activity. Neurons are born, differentiate, and undergo axon guidance prior to the emergence of chemical synapses. These processes are largely mediated by signaling molecules and hardwired morphogenetic programs that determine cell fate, guide axons to terminal positions, and elaborate dendrites (Yogev and Shen, 2014). Although gap junctions may play a role during these early stages (Hasegawa and Turnbull, 2014), electrical communication between neurons is unlikely to occur prior to the onset of synaptogenesis. For example, in the *Drosophila* visual system, the expression of the various ion channels and receptors needed for neurons to be electrically competent only occurs after the completion of axon guidance (Kurmangaliyev et al., 2020).

During development, neural activity can occur dependently and independently of environmental stimulus. As sensory systems become functional later in development, environmental stimuli induce activity in sensory and downstream circuits. The role of this *stimulus-dependent* activity in sculpting and refining circuitry with respect to synaptic plasticity, learning and memory, largely during postnatal life, has been a key line of inquiry in

neurobiology with decades of literature (Citri and Malenka, 2008). By contrast, the role of *stimulus-independent* activity in neural development has not been explored to a comparable extent.

Rhythmic activity has been observed throughout the developing vertebrate brain in time periods that coincide with phases of synaptogenesis. This activity is characterized by periodic cycles of stereotyped frequency, oscillating between bouts of activity within a network of neurons followed by periods of quiescence. Activity emerges after neural circuits complete axon guidance and begin synaptogenesis. In sensory systems, this activity typically ends as sensory receptive cells become functional. Thus, this activity is largely stimulus-independent, although recent reports have shown that light influences the activity patterns in the retina (Tiriac et al., 2018).

Different groups have referred broadly to this patterned activity during development as 'spontaneous network activity' (Blankenship and Feller, 2010), 'emergent neural activity' (Burbridge et al., 2014), or simply 'spontaneous activity'. Here I will use 'developmental activity' to 1) distinguish patterned activity during development from spontaneous patterns of activity in adult circuitry and, 2) indicate that such activity can be driven by discrete populations of cells that generate rhythmicity (Tritsch et al., 2007) rather than being an emergent, spontaneous property of a neuronal network.

Developmental activity has been observed in the cochlea, hippocampus, cerebellum, neocortex, brainstem, and spinal cord (Blankenship and Feller, 2010), across a variety of vertebrate species (Pratt et al., 2016). The best-characterized regime of activity is in the visual system, where so-called retinal waves initiate in the eye and propagate to the superior colliculus,

lateral geniculate nucleus, and visual cortex (Galli and Maffei, 1988; Meister et al., 1991; Ackman et al., 2012).

Retinal waves were first observed decades ago in the rat (Galli and Maffei, 1988), ferret, and cat (Meister et al., 1991). Retinal waves are divided into 3 stages. Stage I retinal waves begin embryonically and are mediated by gap junctions. Stage II retinal waves depend on cholinergic release from starburst amacrine cells and last from postnatal day 1 to 10. Stage III retinal waves depend on glutamate spillover from bipolar cells and continue until eye opening at around postnatal day 14 (Blankenship and Feller, 2010).

Retinal waves have been shown to mediate refinement of retinotopy and eye-specific segregation in the lateral geniculate nucleus (Bansal et al., 2000; Xu et al., 2011; Burbridge et al., 2014; McLaughlin et al., 2003). These data largely come from either pharmacological inhibition of activity (Shatz and Stryker, 1988), or the use of mice mutant for the ß2 nicotinic subunit: in this genetic background, retinal waves are strongly attenuated (Bansal et al., 2000; McLaughlin et al., 2003). The cell type diversity in both the retina (Sanes and Masland, 2015) and the visual cortex (Sarah Cheng & Larry Zipursky, unpublished data) is rich; how retinal waves contribute to circuit development at the level of individual cell types is unknown. Additionally, the complexity vertebrate circuits has made it difficult to assess how retinal waves influence synaptogenesis at the resolution of individual cells or synapses.

1.2. DEVELOPMENTAL ACTIVITY IN *DROSOPHILA* NEURAL CIRCUIT FORMATION

By contrast to vertebrates, the presence and role of stimulus-independent activity in the development of invertebrate neural circuits has not been characterized historically. This is exemplified in *Drosophila melanogaster*, a classic and commonly used model system in developmental neurobiology.

In *Drosophila*, existing evidence prior to this work suggested that the adult nervous system formed its circuitry without input from sensory experience. Work in the fly visual system showed that in mutants deficient for phototransduction, there were no defects in photoreceptor neuron axonal pathfinding or synaptogenesis (Hiesinger et al., 2006). Additionally, dark rearing flies or ablating photoreceptors had no significant effect on the elaboration of dendrites in higher order visual system neurons (Scott et al., 2003). Outside of the visual system, blocking olfactory stimuli did not have a significant effect on the development of the adult olfactory system with respect to elaboration of processes and establishment of the glomerular map (Jefferis et al., 2004; Berdnik et al., 2006). Due to these results, the prevailing notion was that activity did not play a role in the development of the adult brain (Sugie et al., 2018).

A key distinction with the aforementioned experiments is that the vast majority focused on the role of stimulus-dependent activity on development. Hiesinger et al. showed that tetrodotoxin injection did not affect axon guidance in photoreceptors, although synapse formation was not assessed in this context (Hiesinger et al., 2006). Outside of this experiment, neither the presence of stimulus-independent activity nor its potential role of synapse formation had been a topic of focus in the development of the adult brain.

Existing evidence suggests a role for activity in the development of the larval nervous system. During embryogenesis, peristaltic waves of neuromuscular activity occur during the last hours before the larva hatches (Baines and Bate, 1998). Additionally, existing data suggest that the development of the larval neuromuscular junction is activity-dependent. During this period of embryogenesis that neural activity occurs, Sema2a-dependent chemorepulsion is activated via a calcium-dependent pathway (Vonhoff and Keshishian, 2017). Further, manipulation of this activity during embryogenesis results in deficits to motoneuron electrophysiology (Giachello and Baines, 2015), suggesting that the pattern of this peristaltic activity instructs the sculpting of circuits. Finally, alteration of activity output in the chordotonal motoneuron during embryogenesis affects circuit formation with downstream partners at the level of synapse count and synaptic strength, resulting in deficits in motor behavior throughout larval life (Valdes-Aleman et al., 2021). Whether embryonic neural activity occurs within the central nervous system and affects synaptogenesis outside of the neuromuscular junction has yet to be described.

1.3. ORGANIZATION OF THE *DROSOPHILA* VISUAL SYSTEM

The *Drosophila* visual system is a favorable and common model system for the study of neural development. The fly visual system shares remarkable homology with the vertebrate visual system, with direct parallels in organization, circuit logic, and function among component cell types (Sanes and Zipursky, 2010).

The fly compound eye consists of ~750 stereotyped and repeating visual units, or ommatidia. The repeated nature of this structure persists throughout the optic lobe as columns that reflect retinotopy. Information from the retina passes into the fly optic lobe, which is populated by ~60,000 neurons (Del Valle Rodríguez et al., 2020). In the optic lobe, cell bodies exist in the outer cortical layer, and processes extend into densely packed structures called neuropils. The four neuropils of the optic lobe, the lamina, medulla, lobula, and lobula plate, are organized into discrete layers where cells of a type elaborate processes and form synapses in a stereotyped manner (**Figure 1.1**).

The cell types of the optic lobe, especially those of the lamina and medulla, have been well-characterized. The morphology of many visual processing cells were described by Cajal, and the majority of cell types in the optic lobe were identified using Golgi staining by Fischbach and Dittrich (Fischbach and Dittrich, 1989). The size of the optic lobe, the discrete repetition of the optic lobe columns, and the characterization of visual system neurons by morphology made the visual system a prime candidate for analysis via transmission electron microscopy or scanning electron microscopy. Using serial electron microscopy approaches, the connectome of the entire optic lobe (Takemura et al., 2013; Takemura et al., 2017), and more recently, the whole *Drosophila* brain (Scheffer et al., 2020), has been mapped at the level of individual cells and synapses, offering a powerful toolkit to investigate the wiring and function of neural circuits.

Additionally, recent single-cell RNA sequencing work has established the transcriptome of individual cell types throughout development (Kurmangaliyev et al., 2020; Özel et al., 2021). Together with the powerful genetic toolkit available in the fly, the connectomics and transcriptomics resources offer an opportunity to investigate the wiring and function of neural circuits at resolution of individual cells, synapses, and molecules.

Among the ~100 cell types that populate the medulla are classes of cells organized by either function or morphology. For example, R cells are photoreceptor cells: R1-6 are the primary photoreceptor cells of the visual system whereas R7 and R8 distinguish color. There are five types of lamina cells (L cells), which elaborate processes in the lamina and/or medulla, and play roles in circuits for either motion detection or color vision (Tuthill et al., 2013). Additional cell types are named by morphology: for example, distal medulla (Dm) or proximal medulla (Pm) neurons extend along distinct layers in medulla layers M1-6 or M7-10, respectively; medulla intrinsic (Mi) neurons are columnar neurons restricted to the medulla; transmedullary neurons (Tm) neurons extend from the medulla to form outputs in other neuropils. These cell classes include both spiking and nonspiking neurons (Mu et al., 2012).

Visual processing circuits have been identified by analysis of the optic lobe connectome and subsequent physiological and behavioral studies (Takemura et al., 2013; Joesch et al., 2010; Strother et al., 2017). Remarkably, the circuit logic of the fly visual system closely mirrors that of the vertebrate visual system (**Figure 1.2**). Perhaps the best-characterized visual processing pathway is the ON motion pathway, which detects transitions from dark-to-light edges. The most elementary components of the ON motion pathway consists of the glutamatergic neuron L1, which receives input from photoreceptors and is presynaptic to cholinergic cells Mi1 and Tm3, which in turn excite the first direction-selective cell of the pathway, T4 (**Figure 1.3**). T4 receives

inhibitory input from GABAergic Mi4 and glutamatergic Mi9. The numbers of synapses between each of these elements (Takemura et al., 2013), the physiological strength of synaptic inputs and outputs (Strother et al., 2017), the expression of neurotransmitter synthesis enzymes and ion channels (Kurmangaliyev et al., 2020), and the role of each of these components in behavior (Joesch et al., 2010; Tuthill et al., 2013), have been experimentally determined.

Figure 1.1.

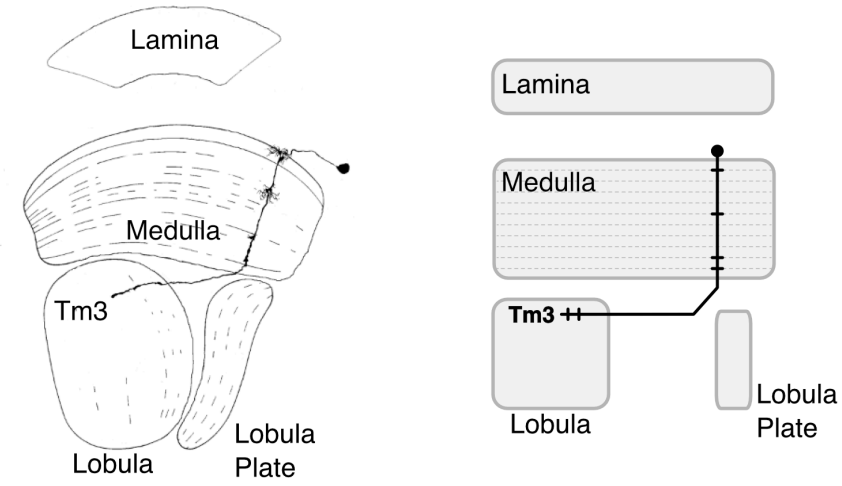

Figure 1.1. Organization of the *Drosophila* visual system

Left: Schematic of the neuropils of the optic lobe and a representative cell, transmedullary neuron Tm3, which elaborates processes in the medulla and lobula. Adapted from Fischbach & Dittrich, 1989.

Right: Stylized "subway map" view of the visual system used in Chapters 1-3. The same neuron Tm3 is shown in this representation.

Figure 1.2.

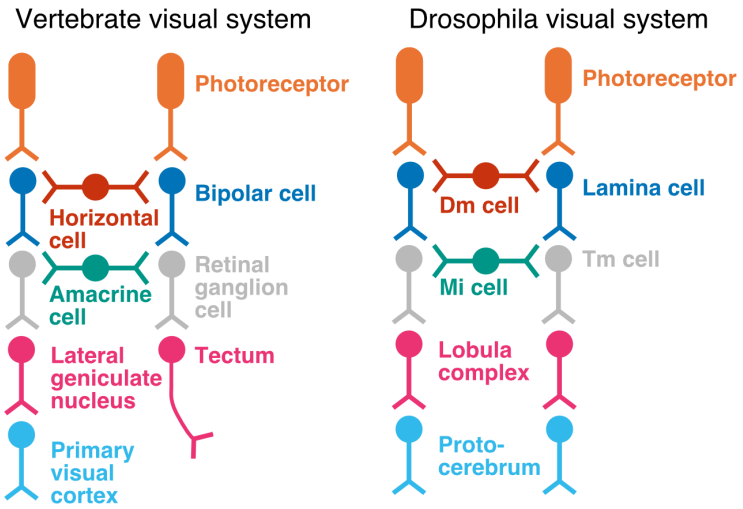

Figure 1.2. Comparison of vertebrate and *Drosophila* visual system

Vertebrate (left) and *Drosophila* (right) visual systems have comparable wiring logic through early stages of visual processing. Adapted from Sanes & Zipursky 2010.

Figure 1.3.

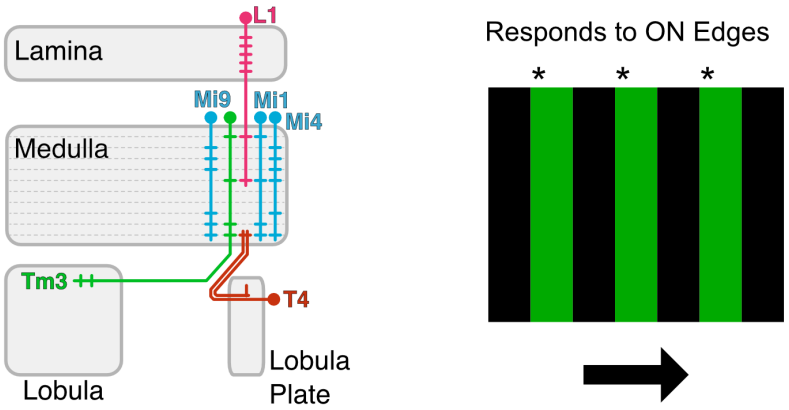

Figure 1.3. Elements of the ON motion pathway of the *Drosophila* visual system.

Left, Neuronal components of the ON motion pathway. Glutamatergic L1 synapses onto cholinergic Mi1 and Tm3, which in turn excite T4. Glutamatergic Mi9 and GABAergic Mi4 inhibit T4. T4 is the first directionally-selective cell in the pathway. Right, schematic showing representative visual stimuli that activate the ON motion pathway.

1.4. DEVELOPMENT OF THE *DROSOPHILA* VISUAL SYSTEM

As a holometabolous organism, *Drosophila* undergoes separate periods of development to produce distinct nervous systems between larval and adult stages. The adult nervous system develops during metamorphosis, or pupal development. The period of metamorphosis begins with puparium formation, when the larval locomotion stops completely and a pupal case begins to form, and ends with eclosion after 100 hours after pupal formation (hAPF), when the adult fly emerges from the pupal case. During this period, the larval nervous system degenerates and is replaced by the adult nervous system, although there is considerable conservation or reformation of existing tissue (Truman, 2019).

By the first third of metamorphosis, neurogenesis and differentiation is largely complete (Nériec and Desplan, 2016). Much of the first half of metamorphosis is dedicated to axon guidance, where contact and avoidance between neural processes is determined by cell-type-specific expression of cell surface molecules (Sanes and Zipursky, 2020).

Synaptogenesis primarily occurs in the second half of pupal development (Chen et al., 2014). In the visual system, cell types show a monotonic increase in synapses through the second half of pupal development, and reach their adult synaptic complement by ~84 hAPF (Chen et al., 2014). During this period, expression of ion channels and neurotransmitter synthesis enzymes suggest that neurons gain the capability to be electrically active (Kurmangaliyev et al., 2020). Simultaneously, cell-surface molecules that are thought to play a role in synaptic specificity are expressed (Tan et al., 2015).

Prior to the investigation described here, there was no direct report of activity occurring during this period in development. However, published work hinted at the presence of synaptic communication during the latter half of metamorphosis. First, work by Muthukumar and

colleagues indicated that silencing the synaptic output of GABA neurons between ~40 hAPF and eclosion has significant effects on the expression of neurotransmitter receptors in astrocyte-like glia (Muthukumar et al., 2014), suggesting that, at some point in development after 40 hAPF, there is synaptic release in GABA neurons. Second, imaging experiments by Constance et al. in developing pupal motoneurons showed the presence of bouts of activity interspersed by silent periods (Constance et al., 2018). This activity developed over time, with increases in frequency at later developmental timepoints. Whether comparable activity occurred in the central nervous system was not assessed.

Figure 1.4.

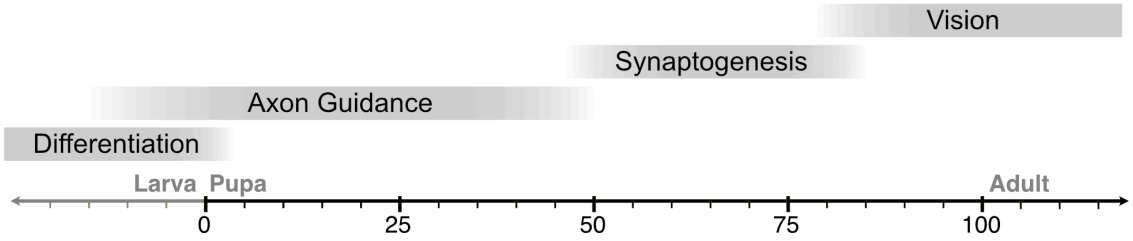

Figure 1.4. Development of the *Drosophila* visual system.

Pupal development or metamorphosis occurs over 100 hours after pupal formation (hAPF). Axon guidance primarily occurs during the first half of pupal development. Synaptogenesis primarily occus during the second half of pupal development. Photoreceptors become active after 80 hAPF (Hardie et al., 1993).

1.5. SUMMARY

The precise role of developmental activity in neural circuit assembly remains an open question. This is especially true in invertebrate neurodevelopment, where previous experiments suggested that developmental activity either did not exist or did not play a role in the development of the adult brain.

Here I show that developmental activity accompanies synaptogenesis in the *Drosophila* central nervous system. This activity is coordinated in a brain-wide manner, and, like developmental activity in vertebrate systems, oscillates regularly between periods of active and silent phases. This activity influences synapse formation in a cell-type-specific manner. A discrete population of neurons, defined by expression of a cation channel, coordinates developmental activity throughout the brain. Finally, neuron-astrocyte interactions are necessary for this activity to occur.

These results indicate that developmental activity is a fundamental feature of brain development. The discovery of developmental activity in *Drosophila* will facilitate further understanding of how activity contributes to the formation of functional neural circuits.

1.6. REFERENCES

Ackman, J. B., Burbridge, T. J., and Crair, M. C. (2012). Retinal waves coordinate patterned activity throughout the developing visual system. Nature *490*, 219-225.

Baines, R. A., and Bate, M. (1998). Electrophysiological development of central neurons in the Drosophila embryo. J Neurosci *18*, 4673-4683.

Bansal, A., Singer, J. H., Hwang, B. J., Xu, W., Beaudet, A., and Feller, M. B. (2000). Mice lacking specific nicotinic acetylcholine receptor subunits exhibit dramatically altered spontaneous activity patterns and reveal a limited role for retinal waves in forming ON and OFF circuits in the inner retina. J Neurosci *20*, 7672-7681.

Berdnik, D., Chihara, T., Couto, A., and Luo, L. (2006). Wiring stability of the adult Drosophila olfactory circuit after lesion. J Neurosci *26*, 3367-3376.

Blankenship, A. G., and Feller, M. B. (2010). Mechanisms underlying spontaneous patterned activity in developing neural circuits. Nat Rev Neurosci *11*, 18-29.

Burbridge, T. J., Xu, H. P., Ackman, J. B., Ge, X., Zhang, Y., Ye, M. J., Zhou, Z. J., Xu, J., Contractor, A., and Crair, M. C. (2014). Visual circuit development requires patterned activity mediated by retinal acetylcholine receptors. Neuron *84*, 1049-1064.

Chen, Y., Akin, O., Nern, A., Tsui, C. Y., Pecot, M. Y., and Zipursky, S. L. (2014). Cell-type-specific labeling of synapses in vivo through synaptic tagging with recombination. Neuron *81*, 280-293.

Citri, A., and Malenka, R. C. (2008). Synaptic plasticity: multiple forms, functions, and mechanisms. Neuropsychopharmacology *33*, 18-41.

Constance, W. D., Mukherjee, A., Fisher, Y. E., Pop, S., Blanc, E., Toyama, Y., and Williams, D. W. (2018). Neurexin and Neuroligin-based adhesion complexes drive axonal arborisation growth independent of synaptic activity. Elife *7*,

Del Valle Rodríguez, A., Cera, M., and Portillo, J. R. (2020). A network approach to analyze neuronal lineage and layer innervation in the Drosophila optic lobes. PLoS One *15*, e0227897.

Fischbach, K. F., and Dittrich, A. P. M. (1989). The optic lobe of Drosophila melanogaster. 1. A Golgi analysis of wild-type structure. Cell and Tissue Research *258*, 441-475.

Galli, L., and Maffei, L. (1988). Spontaneous impulse activity of rat retinal ganglion cells in prenatal life. Science *242*, 90-91.

Giachello, C. N., and Baines, R. A. (2015). Inappropriate Neural Activity during a Sensitive Period in Embryogenesis Results in Persistent Seizure-like Behavior. Curr Biol *25*, 2964-2968.

Hardie, R. C., Peretz, A., Pollock, J. A., and Minke, B. (1993). Ca2+ limits the development of the light response in Drosophila photoreceptors. Proc Biol Sci *252*, 223-229.

Hasegawa, D. K., and Turnbull, M. W. (2014). Recent findings in evolution and function of insect innexins. FEBS Lett *588*, 1403-1410.

Hiesinger, P. R., Zhai, R. G., Zhou, Y., Koh, T. W., Mehta, S. Q., Schulze, K. L., Cao, Y., Verstreken, P., Clandinin, T. R., Fischbach, K. F., Meinertzhagen, I. A., and Bellen, H. J. (2006). Activity-independent prespecification of synaptic partners in the visual map of Drosophila. Curr Biol *16*, 1835-1843.

Jefferis, G. S., Vyas, R. M., Berdnik, D., Ramaekers, A., Stocker, R. F., Tanaka, N. K., Ito, K., and Luo, L. (2004). Developmental origin of wiring specificity in the olfactory system of Drosophila. Development *131*, 117-130.

Joesch, M., Schnell, B., Raghu, S. V., Reiff, D. F., and Borst, A. (2010). ON and OFF pathways in Drosophila motion vision. Nature *468*, 300-304.

Kurmangaliyev, Y. Z., Yoo, J., Valdes-Aleman, J., Sanfilippo, P., and Zipursky, S. L. (2020). Transcriptional Programs of Circuit Assembly in the Drosophila Visual System. Neuron *108*, 1045-1057.e6.

McLaughlin, T., Torborg, C. L., Feller, M. B., and O'Leary, D. D. (2003). Retinotopic map refinement requires spontaneous retinal waves during a brief critical period of development. Neuron *40*, 1147-1160.

Meister, M., Wong, R. O., Baylor, D. A., and Shatz, C. J. (1991). Synchronous bursts of action potentials in ganglion cells of the developing mammalian retina. Science *252*, 939-943.

Mu, L., Ito, K., Bacon, J. P., and Strausfeld, N. J. (2012). Optic glomeruli and their inputs in Drosophila share an organizational ground pattern with the antennal lobes. J Neurosci *32*, 6061-6071.

Muthukumar, A. K., Stork, T., and Freeman, M. R. (2014). Activity-dependent regulation of astrocyte GAT levels during synaptogenesis. Nat Neurosci *17*, 1340-1350.

Nériec, N., and Desplan, C. (2016). From the Eye to the Brain: Development of the Drosophila Visual System. Curr Top Dev Biol *116*, 247-271.

Özel, M. N., Simon, F., Jafari, S., Holguera, I., Chen, Y. C., Benhra, N., El-Danaf, R. N., Kapuralin, K., Malin, J. A., Konstantinides, N., and Desplan, C. (2021). Neuronal diversity and convergence in a visual system developmental atlas. Nature *589*, 88-95.

Pratt, K. G., Hiramoto, M., and Cline, H. T. (2016). An Evolutionarily Conserved Mechanism for Activity-Dependent Visual Circuit Development. Front Neural Circuits *10*, 79.

Sanes, J. R., and Masland, R. H. (2015). The types of retinal ganglion cells: current status and implications for neuronal classification. Annu Rev Neurosci *38*, 221-246.

Sanes, J. R., and Zipursky, S. L. (2010). Design principles of insect and vertebrate visual systems. Neuron *66*, 15-36.

Sanes, J. R., and Zipursky, S. L. (2020). Synaptic Specificity, Recognition Molecules, and Assembly of Neural Circuits. Cell *181*, 536-556.

Scheffer, L. K., Xu, C. S., Januszewski, M., Lu, Z., Takemura, S. Y., Hayworth, K. J., Huang, G. B., Shinomiya, K., Maitlin-Shepard, J., Berg, S., Clements, J., Hubbard, P. M., Katz, W. T., Umayam, L., Zhao, T., Ackerman, D., Blakely, T., Bogovic, J., Dolafi, T., Kainmueller, D., Kawase, T., Khairy, K. A., Leavitt, L., Li, P. H., Lindsey, L., Neubarth, N., Olbris, D. J., Otsuna, H., Trautman, E. T., Ito, M., Bates, A. S., Goldammer, J., Wolff, T., Svirskas, R., Schlegel, P., Neace, E., Knecht, C. J., Alvarado, C. X., Bailey, D. A., Ballinger, S., Borycz, J. A., Canino, B. S., Cheatham, N., Cook, M., Dreher, M., Duclos, O., Eubanks, B., Fairbanks, K., Finley, S., Forknall, N., Francis, A., Hopkins, G. P., Joyce, E. M., Kim, S., Kirk, N. A., Kovalyak, J., Lauchie, S. A., Lohff, A., Maldonado, C., Manley, E. A., McLin, S., Mooney, C., Ndama, M., Ogundeyi, O., Okeoma, N., Ordish, C., Padilla, N., Patrick, C. M., Paterson, T., Phillips, E. E., Phillips, E. M., Rampally, N., Ribeiro, C., Robertson, M. K., Rymer, J. T., Ryan, S. M., Sammons, M., Scott, A. K., Scott, A. L., Shinomiya, A., Smith, C., Smith, K., Smith, N. L., Sobeski, M. A., Suleiman, A., Swift, J., Takemura, S., Talebi, I., Tarnogorska, D., Tenshaw, E., Tokhi, T., Walsh, J. J., Yang, T., Horne, J. A., Li, F., Parekh, R., Rivlin, P. K., Jayaraman, V., Costa, M., Jefferis, G. S., Ito, K., Saalfeld, S., George, R., Meinertzhagen, I. A., Rubin, G. M., Hess, H. F., Jain, V., and Plaza, S. M. (2020). A connectome and analysis of the adult. Elife *9*,

Scott, E. K., Reuter, J. E., and Luo, L. (2003). Dendritic development of Drosophila high order visual system neurons is independent of sensory experience. BMC Neurosci *4*, 14.

Shatz, C. J., and Stryker, M. P. (1988). Prenatal tetrodotoxin infusion blocks segregation of retinogeniculate afferents. Science *242*, 87-89.

Strother, J. A., Wu, S. T., Wong, A. M., Nern, A., Rogers, E. M., Le, J. Q., Rubin, G. M., and Reiser, M. B. (2017). The Emergence of Directional Selectivity in the Visual Motion Pathway of Drosophila. Neuron *94*, 168-182.e10.

Sugie, A., Marchetti, G., and Tavosanis, G. (2018). Structural aspects of plasticity in the nervous system of Drosophila. Neural Dev *13*, 14.

Takemura, S. Y., Bharioke, A., Lu, Z., Nern, A., Vitaladevuni, S., Rivlin, P. K., Katz, W. T., Olbris, D. J., Plaza, S. M., Winston, P., Zhao, T., Horne, J. A., Fetter, R. D., Takemura, S., Blazek, K., Chang, L. A., Ogundeyi, O., Saunders, M. A., Shapiro, V., Sigmund, C., Rubin, G. M., Scheffer, L. K., Meinertzhagen, I. A., and Chklovskii, D. B. (2013). A visual motion detection circuit suggested by Drosophila connectomics. Nature *500*, 175-181.

Takemura, S. Y., Nern, A., Chklovskii, D. B., Scheffer, L. K., Rubin, G. M., and Meinertzhagen, I. A. (2017). The comprehensive connectome of a neural substrate for 'ON' motion detection in. Elife *6*,

Tan, L., Zhang, K. X., Pecot, M. Y., Nagarkar-Jaiswal, S., Lee, P. T., Takemura, S. Y., McEwen, J. M., Nern, A., Xu, S., Tadros, W., Chen, Z., Zinn, K., Bellen, H. J., Morey, M., and Zipursky, S. L. (2015). Ig Superfamily Ligand and Receptor Pairs Expressed in Synaptic Partners in Drosophila. Cell *163*, 1756-1769.

Tiriac, A., Smith, B. E., and Feller, M. B. (2018). Light Prior to Eye Opening Promotes Retinal Waves and Eye-Specific Segregation. Neuron *100*, 1059-1065.e4.

Tritsch, N. X., Yi, E., Gale, J. E., Glowatzki, E., and Bergles, D. E. (2007). The origin of spontaneous activity in the developing auditory system. Nature *450*, 50-55.

Truman, J. W. (2019). The Evolution of Insect Metamorphosis. Curr Biol *29*, R1252-R1268.

Tuthill, J. C., Nern, A., Holtz, S. L., Rubin, G. M., and Reiser, M. B. (2013). Contributions of the 12 neuron classes in the fly lamina to motion vision. Neuron *79*, 128-140.

Valdes-Aleman, J., Fetter, R. D., Sales, E. C., Heckman, E. L., Venkatasubramanian, L., Doe, C. Q., Landgraf, M., Cardona, A., and Zlatic, M. (2021). Comparative Connectomics Reveals How Partner Identity, Location, and Activity Specify Synaptic Connectivity in Drosophila. Neuron *109*, 105-122.e7.

Vonhoff, F., and Keshishian, H. (2017). Cyclic nucleotide signaling is required during synaptic refinement at the Drosophila neuromuscular junction. Dev Neurobiol *77*, 39-60.

Xu, H. P., Furman, M., Mineur, Y. S., Chen, H., King, S. L., Zenisek, D., Zhou, Z. J., Butts, D. A., Tian, N., Picciotto, M. R., and Crair, M. C. (2011). An instructive role for patterned spontaneous retinal activity in mouse visual map development. Neuron *70*, 1115-1127.

Yogev, S., and Shen, K. (2014). Cellular and molecular mechanisms of synaptic specificity. Annu Rev Cell Dev Biol *30*, 417-437.

Chapter 2

Cell-type specific patterned stimulus-independent neuronal activity in the *Drosophila* visual system during synapse formation

ABSTRACT

Stereotyped synaptic connections define the neural circuits of the brain. In vertebrates, stimulus-independent activity contributes to neural circuit formation. It is unknown whether this type of activity is a general feature of nervous system development. Here, we report patterned, stimulus-independent neural activity in the Drosophila visual system during synaptogenesis. Using in vivo calcium, voltage, and glutamate imaging, we found that all neurons participate in this spontaneous activity, which is characterized by brain-wide periodic active and silent phases. Glia are active in a complementary pattern. Each of the 15 examined of the over 100 specific neuron types in the fly visual system exhibited a unique activity signature. The activity of neurons that are synaptic partners in the adult was highly correlated during development. We propose that this cell type-specific activity coordinates the development of the functional circuitry of the adult brain.

2.1. INTRODUCTION

Synaptic connections between neurons determine how neural circuits process information. Understanding how the specificity of these connections is established is a central challenge in neurobiology. In vertebrates, cell autonomous genetic programs and neural activity—both evoked and spontaneous—contribute to the development of synapses. Spontaneous activity has been observed throughout the developing central nervous system (CNS)—in the hippocampus (Ben-Ari et al., 1989), spinal cord (Landmesser and O'Donovan, 1984), cerebellum (Watt et al., 2009), auditory system (Tritsch et al., 2007), and visual system (Galli and Maffei, 1988; Meister et al., 1991). Retinal waves were discovered over 20 years ago (Galli and Maffei, 1988; Meister et al., 1991) and are the best characterized examples of spontaneous activity (reviewed in Ackman and Crair, 2014; Blankenship and Feller, 2009; Kirkby et al., 2013; Sernagor and Hennig, 2013). In mice and other mammalian models, retinal waves begin soon after the completion of axon guidance and persist through eye opening. During this period, bursts of activity propagate from the retina to higher visual centers, including the lateral geniculate nucleus (LGN), the superior colliculus (SC), and the visual cortex (Ackman et al., 2012). In each of these areas, large populations of neighboring cells exhibit correlated firing patterns. Significant progress has been made toward characterizing and identifying the organizing principles of spontaneous activity in the developing vertebrate brain, and the precise developmental role of this activity is an area of active interest.

By contrast to vertebrates, brain development in invertebrates is thought to be driven by hardwired morphogenetic programs driven by cell recognition molecules, with little role for spontaneous or experience-dependent neural activity. Previous work has shown that, in the *Drosophila* visual system, photoreceptor neurons can develop the wild-type complement of

synapses in a stimulus-independent manner (Hiesinger et al., 2006). However, the existence and significance of spontaneous activity during invertebrate brain development remains an open question.

Some of the most detailed understanding of brain development in the fly comes from the visual system. Visual information from the compound eye is relayed in a topographic fashion to the optic neuropils—the lamina, medulla, and the lobula complex. These neuropils are organized into columns and layers. In general, columns process information from different points in visual space, and layers process different types of visual information. Over 100 different neuronal cell types form precise synaptic connections, typically with several different cell types. The three dimensional EM re-constructions of the optic neuropils that reveal this wiring complexity (Rivera-Alba et al., 2011; Takemura et al., 2013, 2017) also underscore the challenge of understanding the mechanisms of synaptic specificity: Most neurons make synapses with only a subset of their contact neighbors, and the area of contact has little bearing on this decision.

Visual system development in the fly takes place during the last stage of larval development and the ensuing 100 hours of metamorphosis, or pupal development. Synapse formation, as well as axon guidance and morphogenesis, are predicated on cell-cell contacts. As such, much of the focus in the study of neural development has been on the roles of cell surface and recognition molecules. This body of work, carried out at the level of individual cell types, paints the picture of a dynamic self-assembly process in which local interactions shape the developmental trajectory of each neuron (Hadjieconomou et al., 2011; Huang et al., 1998; Pecot et al., 2014). By 50 hours after pupa formation (hAPF), these specific and genetically hardwired molecular push-pulls bring most of the cell types of the visual system to where they belong in the adult brain, ready for synaptogenesis. Over the remaining 50 hours of pupal development,

synapse assembly proceeds in parallel with notable changes in gene expression, including the upregulation of genes involved in neural activity and new sets of cell recognition molecules (Chen et al., 2014; Tan et al., 2015; Zhang et al., 2016). It is during this time that vast networks are assembled, comprising distant cells which must be linked through specific synaptic connections and compatible gene expression profiles (e.g. matching neurotransmitter systems and receptors). Little is known about the molecules and mechanisms that coordinate this period of brain development.

Here we report the discovery of stimulus-independent neural activity in the developing *Drosophila* CNS and its initial characterization in the visual system. We find that the visual system as a whole, all 15 of the individual neuronal cell types examined, as well as astrocytic glia, participate in patterned, stimulus-independent neural activity (PSINA), during the late stages of circuit assembly. We speculate on the function of this globally organized, cell type-specific activity in regulating the development of the connectome.

2.2. PATTERNED NEURONAL AND GLIAL ACTIVITY IN THE DEVELOPING FLY BRAIN

To assess whether neural activity contributes to visual system development in *Drosophila*, we used an *in vivo* 2-photon live imaging protocol that enables continuous observation over several days (i.e. from ~16 hrs after puparium formation (hAPF) to eclosion) (Akin and Zipursky, 2016; Langen et al., 2015). We expressed the genetically-encoded calcium indicator (GECI) GCaMP6s (Chen et al., 2013) throughout the central nervous system using a pan-neuronal GAL4 driver. Between 40 and 50 hAPF, the optic lobe is largely inactive, aside from sporadic activity in isolated cells or groups of cells with no discernable spatial or temporal coordination (**Supplementary movie 1**). Starting shortly before 50 hAPF, a subset of neuronal processes begins to exhibit periodic pulse trains of increased fluorescence. By 55 hAPF, neuronal processes in all optic neuropils, as well as fibers originating from the central brain, participate in regular 12-15 minute long cycles comprising active and silent phases (**Figures 2.1A-1B, Supplementary movie 1**).

The active phase of each cycle comprises several distinct bouts of activity, each of which may have one or a set of closely spaced peaks (**Figure 2.1B**). We term these bouts *sweeps*. Between 55 and 65 hAPF, the cycle period remains roughly constant while the number of sweeps per cycle and the duration of the active phase increase at the expense of a shrinking silent phase (**Figure 2.1C**). Fourier analysis captures the simple periodicity of the activity pattern with a single dominant band for the cycle frequency (~0.001-0.002 Hz) over what we call the *periodic stage* (**Figure 2.1C**)**.** There were no significant differences between periodicity, sweeps per cycle, active and silent phase durations between different animals, consistent with the notion that

the developmental mechanisms underlying these metrics are stereotyped (**Supplementary Figure 2.1A**).

To further characterize the time evolution of the neuronal activity, we moved our expression system to the *cn,bw* genetic background (Thimann and Beadle, 1937), which eliminated pigmentation in the retina and allowed us to image through eclosion. We found no significant differences in periodic stage activity metrics between *cn,bw* flies and control flies (**Supplementary Figure 2.1A**). Imaging beyond this stage revealed that by 70 hAPF, the earlier, simple temporal pattern is replaced with multiple frequencies reflecting cycles with variable periods (**Figure 2.1D, Supplementary movie 1**). Compared to the periodic stage, during this later, *turbulent stage*, individual cycles exhibit higher sweeps per cycle, and, on average, longer active and shorter silent phases (**Figure 2.1D**). The turbulent stage persists until the final hour of pupal development, after which the number and amplitude of peaks drop before eclosion (**Supplementary Figure 2.1B**). Thus, activity during development is divided into an early periodic stage and a later turbulent stage, and continues until an hour before the adult fly emerges (**Figure 2.1E**).

We next asked whether activity was present beyond the visual system. Recently, a detailed study of motoneuron development showed that the neurons of the peripheral nervous system exhibit periodic bouts of activity, starting at 48 hAPF, which grow stronger as development proceeds (Constance et al., 2018). In pupae, the pan-neuronally driven GCaMP6s was sufficiently bright to detect using a wide field-of-view epifluorescence microscope, making it possible to image the whole CNS of multiple animals simultaneously. We used this alternative preparation to follow the GECI signal between 58 and 60 hAPF, and observed cycles of activity that matched our observations from the 2-photon setup in both the optic lobes and the central

brain (**Figure 2.2A, Supplementary movie 2**). We also established that the pattern of activity is the same in males and females (**Supplementary Figure 2.2A**).

Given the broad domain of the activity, we assessed whether the glial complement of the CNS also participate in this process. Using orthogonal expression systems, we expressed GCaMP6s in astrocytic glia and RCaMP1b in all neurons (**Figure 2.2B, Supplementary Figure 2.2B-2.2C**). Prior to 55 hAPF, there is no significant correlation between the glial GECI signal and neuronal activity (**Supplementary Figure 2.2B**). This changes markedly further into the periodic stage when the glial signal begins periodic oscillations alongside neurons (**Figures 2.2B and Supplementary Figure 2.2C**). While, by contrast to the rapid neuronal responses, the changes to the glial GECI signal are tonic, these cells also exhibit cycles of high and low intensity with comparable periodicity to neurons, albeit with a notable phase shift: when neurons are active, astrocytes exhibit a progressive loss in GECI signal which is rebuilt during the neuronal silent phase (**Figure 2.2B**). Indeed, both glial and neuronal signals exhibit shared frequencies as reported by frequency analysis and correlation of both signals (**Supplementary Figures 2.2D-2.2E**), although cross-correlation of glial and neuronal population activity reflects a consistent phase shift across each cycle (**Supplementary Figure 2.2E**).

As flies leave the field of view of the microscope upon eclosion (i.e. they leave the pupal case and walk away), it was not possible to establish whether the oscillatory activity observed in intact pupae ceases altogether in the adult. To address this question, we used a head-fixed cranial window preparation of adult flies expressing GCaMP6s pan-neuronally (Aptekar et al., 2015; Seelig et al., 2010). We observed stimulus-independent activity in newly eclosed (1 hr old) flies as well as 1- and 5-day old adults, all of which also had intact, robust responses to visual stimuli (**Supplementary Figure 2.3A**). By contrast to what we observed during development,

spontaneous activity in the adult did not engage the entire optic lobe, exhibited fewer sweeps in a given cycle and oscillated at a higher frequency (**Supplementary Figure 2.3B**). Further, with increasing age, less activity was observed, suggesting that the mechanisms driving this regime of activity decreased over a period of days. These differences suggest the involvement of different molecules and mechanisms in generating the pupal and adult stimulus-independent activities.

Figure 2.1.

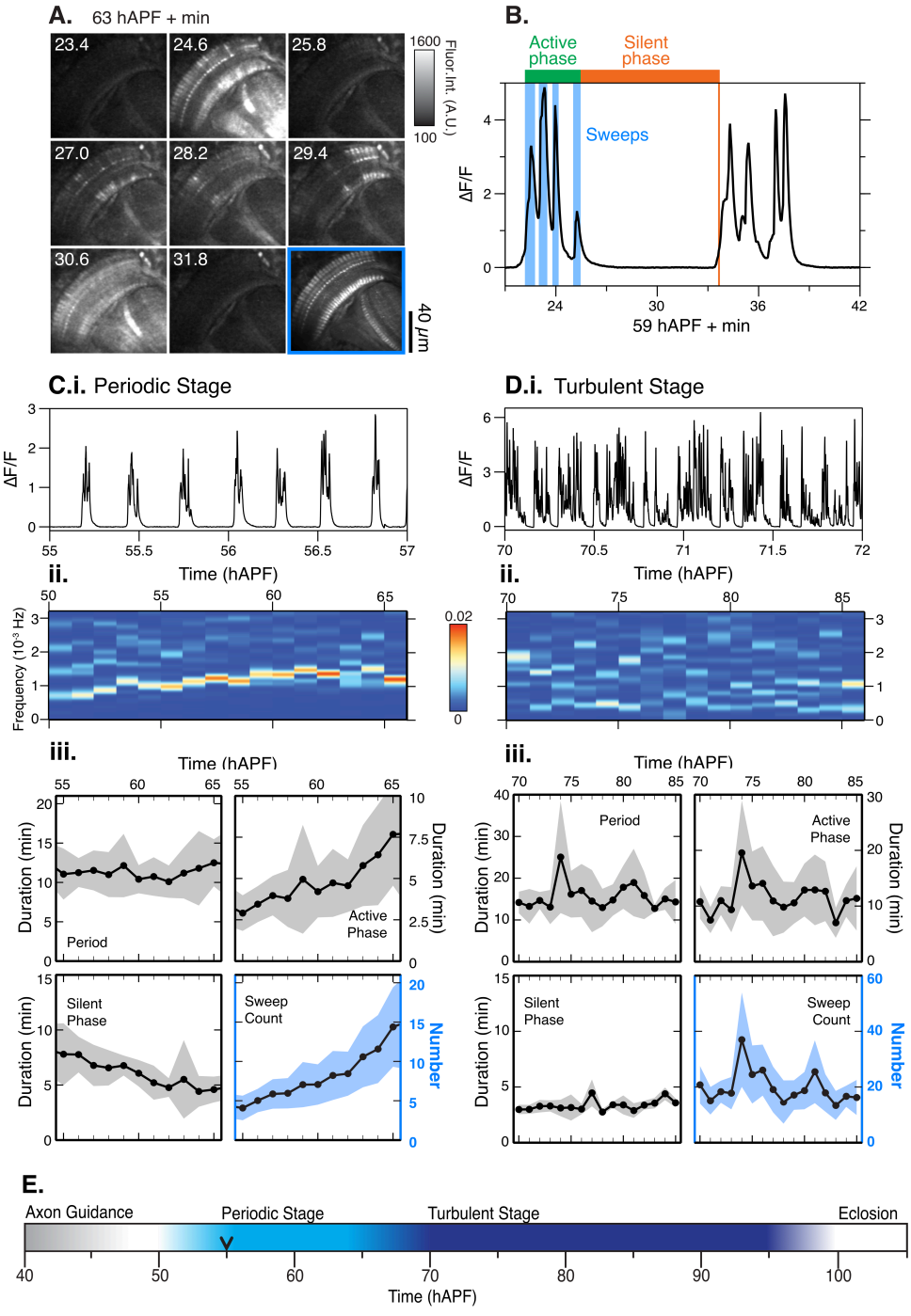
A.
63 hAPF + min
23.4
24.6
25.8
27.0
28.2
29.4
30.6
31.8
1600
100
Fluor.Int. (A.U.)
40 μm
B.
Active phase
Silent phase
Sweeps
ΔF/F
59 hAPF + min
C.i. Periodic Stage
D.i. Turbulent Stage
ii.
Time (hAPF)
Frequency (10⁻³ Hz)
0.02
iii.
Duration (min)
Period
Active Phase
Silent Phase
Sweep Count
Number
E.
Axon Guidance
Periodic Stage
Turbulent Stage
Eclosion
Time (hAPF)

Figure 2.1. Patterned stimulus independent neural activity (PSINA) in the developing visual system

A. Micrograph montage showing a single cycle at 63 hAPF; framed panel (lower right) is the average intensity projection through the active phase. **B.** Representative cycle showing four sweeps (duration indicated in blue) during a shared active phase (green), and a shared silent phase (orange). **C.i.** Representative trace of a 2 hr interval during the periodic stage (50-65 hAPF). **C.ii.** Frequency analysis (Fourier transform) between 50-65 hAPF; **C.iii.** Average traces of cycle metrics in the periodic stage (n = 54 columns from 6 flies). Shaded areas represent standard deviation. **D.i.** Representative trace during the turbulent stage (70 hAPF to eclosion); **D.ii.** Frequency analysis (Fourier transform) between 70-85 hAPF; **D.iii.** Average traces of cycle metrics in the turbulent stage (n = 46 columns from 4 flies), shaded areas represent standard deviation; **E.** Summary of spontaneous activity stages during pupal development. Black arrowhead marks the time point after which 100% of columns participate in each cycle. See Table 1 for genotypes used in this figure.

2.3. ACTIVITY CORRELATES WITH CHANGES IN MEMBRANE VOLTAGE AND NEUROTRANSMITTER RELEASE AND IS INDEPENDENT OF VISUAL STIMULUS

The clear separation between stimulus-dependent and spontaneous GECI signals in the adult, and the interpretation of the former as evoked neuronal activity, raised two questions about the activity observed during metamorphosis. First, are the signals we observe during development reporting the electrical excitation across neurons, or rather are they indicative of membrane activity-independent modulation of intracellular calcium levels? And second, if the GECI signals in the visual system do indeed reflect neuronal activity, do they depend on visual stimuli and phototransduction?

To address whether the pupal activity reflects neuronal activity, we first asked if the GECI signal is accompanied by temporally matched neurotransmitter (e.g. glutamate) release and changes in membrane voltage by co-expressing the red-shifted GECI, RCaMP1b (Dana et al., 2016), with either the genetically encoded glutamate sensor iGluSnFR (Marvin et al., 2013) or the genetically encoded voltage indicator ArcLight (Cao et al., 2013; Jin et al., 2012). Pan-neuronal co-expression of both indicator pairings revealed glutamate release and membrane voltage dynamics that were closely correlated with the GECI signal cycles (**Supplementary Figure 2.4A-B**). As discussed below, all neuronal cell types we studied individually also display the same GECI reported activity pattern we describe for pan-neuronal expression. As such, we constrained the source of the co-expressed indicators to a single cell type, the L1 lamina monopolar neuron, a glutamatergic first-order interneuron (Gao et al., 2008; Takemura et al., 2011). With L1, we observed strong correlation between the GECI signal and both the iGluSnFR-reported glutamate release (**Figure 2.2C, Supplementary movie 3**) and ArcLight-reported drops in membrane voltage (**Figures 2.2D, Supplementary movie 4**) at the level of

individual sweeps. Indeed, cross-correlograms between GECI signals and iGluSnFR or ArcLight showed a sharp peak at a lag time of 0 s, and both cross-correlograms and auto-correlograms showed subsequent peaks at lag times of ± ~15 mins, reflecting the shared active and silent phases between indicators (**Supplementary Figure 2.4C**).

To further examine the nature of the pupal activity, we used the head-fixed cranial window preparation in late stage pupae (90-95 hAPF) to enable pharmacological manipulations. We found that on-going calcium activity at this stage is severely attenuated with the administration of tetrodotoxin, a voltage-gated sodium channel blocker that inhibits action potentials (**Figure 2.2E and Supplementary Figure 2.4D**). Together, these results indicate that the GECI signal observed during pupal development reflects neuronal electrical activity.

Next, we assessed the contribution of visual stimulus to developmental neuronal activity by following the GECI signal in three classic vision mutants: *hdc* (histidine carboxylase, required for the synthesis of the photoreceptor neurotransmitter histamine (Burg et al., 1993; Hardie, 1987)), *ort* (histamine receptor expressed by the post-synaptic partners of photoreceptors (Gengs et al., 2002)), and *norpA* (phospholipase C essential to phototransduction (Bloomquist et al., 1988)). Returning to our calcium imaging preparation, we found that for all mutants the activity was still present during pupal development (**Figure 2.2F,** $norpA^{null}$ ***shown***), with cycles of active and silent phases similar to wildtype (**Supplementary Figure 2.5A**). In *hdc* and *ort* null animals, the frequency of these cycles was comparable to wildtype **(Supplementary Figure 2.5B)**, suggesting that histamine signaling in visual processing, or more broadly in the CNS, is not required to drive the activity or establish its rhythm. By contrast, with *NorpA* we found a dose dependent-decrease in the frequency of the cycles **(Supplementary Figure 2.4A-B)**. The null allele used in this work, $norpA^{36}$ (Pearn et al., 1996), removes both the retina-specific isoform of

the gene, as well as the more broadly expressed second isoform (Kim et al., 1995). We confirmed that retinal function was indeed abolished by testing *norpA*^{36} animals for optomotor response to widefield stimulus and closed-loop bar fixation (**Supplementary Figure 2.5C-E**). Given our results with *Hdc* and *Ort*, we suspect that the dose-dependent changes to the period of the activity we observed with *NorpA* reflects its function as a non-specialized phospholipase C acting broadly in the developing CNS, or in a subset of cells, to regulate some aspect of intracellular signaling or Ca^{2+} homeostasis. These results are consistent with the reported timing for the onset of photoreceptor light response at 82 hAPF, which is some 27 hours after the neuronal activity begins (Hardie et al., 1993). We conclude that the pupal neuronal activity is independent of a visual stimulus.

In the remainder of the text we refer to this phenomenon observed in the development of the *Drosophila* CNS as patterned, stimulus-independent neuronal activity, or PSINA (pronounced 'see-na'). Taken together, our observations indicate that PSINA is a globally coordinated process that involves the entire developing CNS.

Figure 2.2.

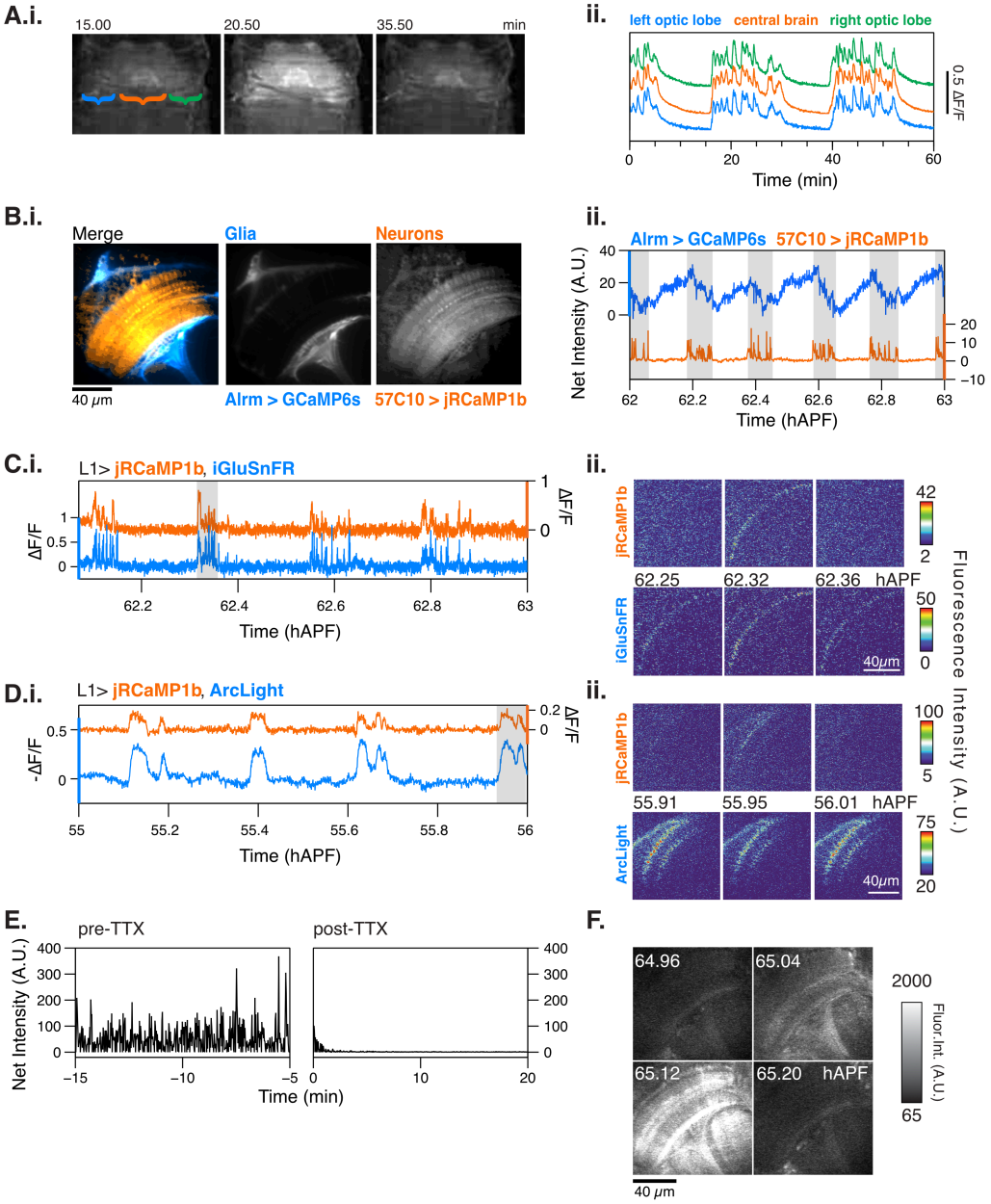
A.i.
15.00
20.50
35.50
min
ii.
left optic lobe
central brain
right optic lobe
0.5 ΔF/F
0
20
40
60
Time (min)
B.i.
Merge
Glia
Neurons
40 μm
AIrm > GCaMP6s
57C10 > jRCaMP1b
ii.
AIrm > GCaMP6s
57C10 > jRCaMP1b
Net Intensity (A.U.)
40
20
0
20
10
0
−10
62
62.2
62.4
62.6
62.8
63
Time (hAPF)
C.i.
L1> jRCaMP1b, iGluSnFR
ΔF/F
1
0.5
0
62.2
62.4
62.6
62.8
63
Time (hAPF)
ii.
jRCaMP1b
iGluSnFR
42
2
50
0
62.25
62.32
62.36
hAPF
40μm
Fluorescence Intensity (A.U.)
D.i.
L1> jRCaMP1b, ArcLight
-ΔF/F
0.5
0
0.2
0
55
55.2
55.4
55.6
55.8
56
Time (hAPF)
ii.
jRCaMP1b
ArcLight
100
5
75
20
55.91
55.95
56.01
hAPF
40μm
E.
pre-TTX
post-TTX
Net Intensity (A.U.)
400
300
200
100
0
−15
−10
−5
0
10
20
Time (min)
F.
64.96
65.04
65.12
65.20
hAPF
2000
Fluor.Int. (A.U.)
65
40 μm

Figure 2.2. Characterization of PSINA

A.i. Representative epifluorescence images of a single cycle in an intact pupa expressing pan-neuronal GCaMP6s. Brackets mark left optic lobe (blue), central brain (orange), and right optic lobe (green). **A.ii.** Average traces from ROIs encircling the left optic lobe (blue), central brain (orange), and right optic lobe (green) between 58-60 hAPF. **B.i**. Representative micrograph showing astrocytic glia expressing GCaMP6s (blue) and pan-neuronal expression of jRCaMP1b (orange). Scale bar, 40 μm. **B.ii.** Representative trace comparing glial (blue) and neuronal activity from (orange) between 62-63 hAPF. Active phases of the neuronal cycles are shaded in gray. **C.** Representative traces (**i.**) and micrographs (**ii.**) from L1 neurons expressing jRCaMP1b (orange, top) and iGluSnFr (blue, bottom). Note that iGluSnFr reports more sweeps than jRCaMP1b; we suspect that this is due to the L1-expressed glutamate sensor's response to neurotransmitter released by L1 itself, neighboring cells or both. **D.** Representative traces (**i.**) and micrographs (**ii.**) from L1 neurons expressing jRCaMP1b (orange, top) and ArcLight (blue, bottom). **E.** Representative traces of activity as reported by pan-neuronal GCaMP6s before (left) and after (right) addition of 1μM tetrodotoxin. **F.** Micrographs of *norpA*^{null} mutant flies expressing pan-neuronal GCaMP6s shows that visual stimuli are not required for activity to occur. See Table 1 for genotypes used in this figure.

2.4. CELL TYPE-SPECIFIC DYNAMICS OF PSINA

We returned to 2-photon imaging of the developing visual system to assess PSINA in specific neuronal types. Using GCaMP6s, we followed calcium activity in 15 cell types, representing some of the major visual system classes (i.e. photoreceptors (R7, R8), lamina monopolar neurons (L1, L3, L5), medulla intrinsic neurons (Mi1, Mi4), distal medulla neurons (Dm3, Dm4, Dm9), transmedullary neurons (Tm3, Tm4, Tm9), and T neurons (T4, T5)) **(Figure 2.3A)**. Between 50 and 65 hAPF, the temporal pattern of PSINA in all neurons closely followed the pan-neuronal archetype of the periodic stage; as a group, cells of a type cycled through active and silent phases lasting 12-15 minutes, starting around 50-55 hAPF and gradually increasing the duration and the sweep complement of the active phase over time **(Figure 2.3B)**.

Whereas the broad temporal characteristics of PSINA are shared between all neuronal types, how the activity propagates across the repeated columnar array of a given cell type varies significantly. For example, nearly all L3 neurons participate in every sweep of an active phase while in L1s fractional participation can change notably between sweeps **(Figures 2.3C-3D, Supplementary movie 5)**. Further, during a sweep, L3s reach peak intensity within narrower time window compared to L1s **(Figures 2.3C-3D)**. In order to compare PSINA dynamics between repeated observations of the same cell type and across different cell types, we defined two scalar metrics, *coordination* and *coherence*, to represent the distributions of fractional participation and peak time spread values, respectively. Coordination is the average of the fraction of columns that participate in each sweep. Coherence is the largest fraction of columns that peak within the same time point, averaged over all sweeps. Accordingly, distinct observations of PSINA in L3s all yield comparably high coordination and coherence values in contrast to L1, which scores consistently lower for both metrics **(Figure 2.3E)**. We extended this

analysis to 13 other cell types and found that coordination and coherence values from separate observations cluster around means characteristic to each cell type, independent of the specific drivers used for GECI expression or transgenic constitution of the animals **(Figure 2.3F and Supplementary Figure 2.6A, Supplementary movie 6)**. For most cell types, coordination and coherence are roughly constant during the periodic stage, between 55-65 hAPF **(Supplementary Figure 2.6B)**. In the few that do show changes, we observe loss of coordination that is attributable to loss of image quality as developing retinal pigmentation degrades the observed GECI signal, particularly with weaker cell type-specific drivers. A notable exception is L1; here, despite the loss of net signal, both metrics increase over time **(Supplementary Figure 2.6B)**, indicating that the observed trends reflect evolving PSINA dynamics. Visual inspection of the L1 activity pattern over time confirms this conclusion **(Supplementary Figures 2.6C-6D)**.

As a complement to coordination and coherence, we also analyzed cell type specific PSINA dynamics using the spike time tiling coefficient (STTC, Cutts and Eglen, 2014) method **(Supplementary Figure 2.7)**. STTC was developed as a generalized approach to measure correlated activity and has been used to study the distance-dependent correlation of propagating activity, such as the retinal waves (e.g. Xu et al., 2016). With this approach, we again found that different cell types cluster around characteristic values, both for STTC at the shortest distance value (4.5 μm) and for a measure of STTC decay at a fixed distance (36 μm) **(Supplementary Figure 2.7C-7D)**. While differences in both sampling rate and the physical scales involved confound direct quantitative comparisons to STTC analyses of retinal waves (Cutts and Eglen, 2014), this analysis points to a diversity of wave-like propagation patterns, some of which are qualitatively similar to the dynamics seen in the developing vertebrate retina. We note that while there are some similarities in how coordination-coherence and STTC rank each cell type, such as

the highly synchronous set of Tm9, L3, and Dm4, these approaches are not directly comparable since the former analyzes individual sweeps and the latter full active phases of each cycle.

In summary, we find that the fine spatio-temporal structure of PSINA is cell type-specific, stereotyped and can be dynamic over the course of development.

The two approaches used to analyze cell type specific PSINA patterns rely on ensemble metrics that do not preserve cell or column specific phase or timing information, and, as such cannot inform on correlated activity between two different cell types. To measure this directly, we imaged pairs of neurons expressing red and green GECIs **(Figure 2.4)**. For example, we compared the activity in Tm3 transmedullary neurons, with processes in both the medulla and the lobula neuropils, to the medulla-resident dendrites of the T4 class and the lobula-resident dendrites of T5s **(Figures 2.4A-D, Supplementary movie 2.7)**. Between 55-65 hAPF, the Tm3-T4 activity was highly correlated (0.8±0.06, n=3) while the Tm3-T5 correlation was significantly lower (0.55±0.1, n=2) **(Figures 2.4D-2.4E, Supplementary Figure 2.8A-2.8B)**. The results were the same when these measurements were repeated with the opposite cell type and color pairing **(Supplementary Figure 2.8C)**. Notably, in the adult, Tm3 and T4 are synaptic partners in the ON-motion circuit (Takemura et al., 2013) while T5, which is part of the OFF-motion circuit, is not a synaptic partner with Tm3 (Shinomiya et al., 2014).

Downstream of photoreceptors, L1 is considered to provide the principal input to the ON-motion circuit (Joesch et al., 2010), with Tm3 and Mi1 as its major post-synaptic partners, which then synapse with T4 (Behnia et al., 2014; Takemura et al., 2013), the first direction selective neuron in the pathway (Maisak et al., 2014) **(Figure 2.3A)**. We found that the activities of the Mi1-Tm3 and Mi1-T4 pairs are also well correlated while L1-Tm3 has lower correlation **(Figure 2.4E)**. As discussed above, the dynamics of PSINA in L1 evolve through pupal development,

and may eventually converge with a presumptive ON-motion PSINA channel during the ensuing turbulent stage. Alternatively, if PSINA is propagated through some form of synaptic coupling, the low L1-Tm3 correlation may be reporting on the sign of the interaction; that is, L1 could be an inhibitory synaptic partner at this stage of development.

Returning to T5, we found that its activity is highly correlated with Tm4, an OFF-motion circuit input into T5 in the adult (Serbe et al., 2016; Shinomiya et al., 2014) **(Figure 2.4E)**. Finally, we observed highly correlated activity between a pair of high coordination-coherence cells, L3 and Dm4 **(Figure 2.4E)**, which are also synaptic partners in the adult. Together, these results confirm the presence of multiple distinct channels of PSINA activity.

Correlated activity patterns between many adult synaptic partners some 45 hours before the end of pupal development hinted at the existence of an early form of synaptic pairing. To explore whether the observed correlations depend on synaptic release, we expressed tetanus toxin (TNT) in one cell type of a pair and measured the correlation of the PSINA activities as before. Driving TNT expression in Tm3s reduced the correlation of the Tm3-T4 pair significantly while the Tm3-T5 value was unaffected **(Figure 2.4F)**. By contrast, T4 expression of TNT had no effect on the Tm3-T4 correlation **(Figure 2.4F)**. These results indicate that the coordinated PSINA activity in Tm3 and T4 is dependent on synaptic release from Tm3, consistent with the notion that PSINA propagation is achieved through some form of synaptic coupling.

Figure 2.3.

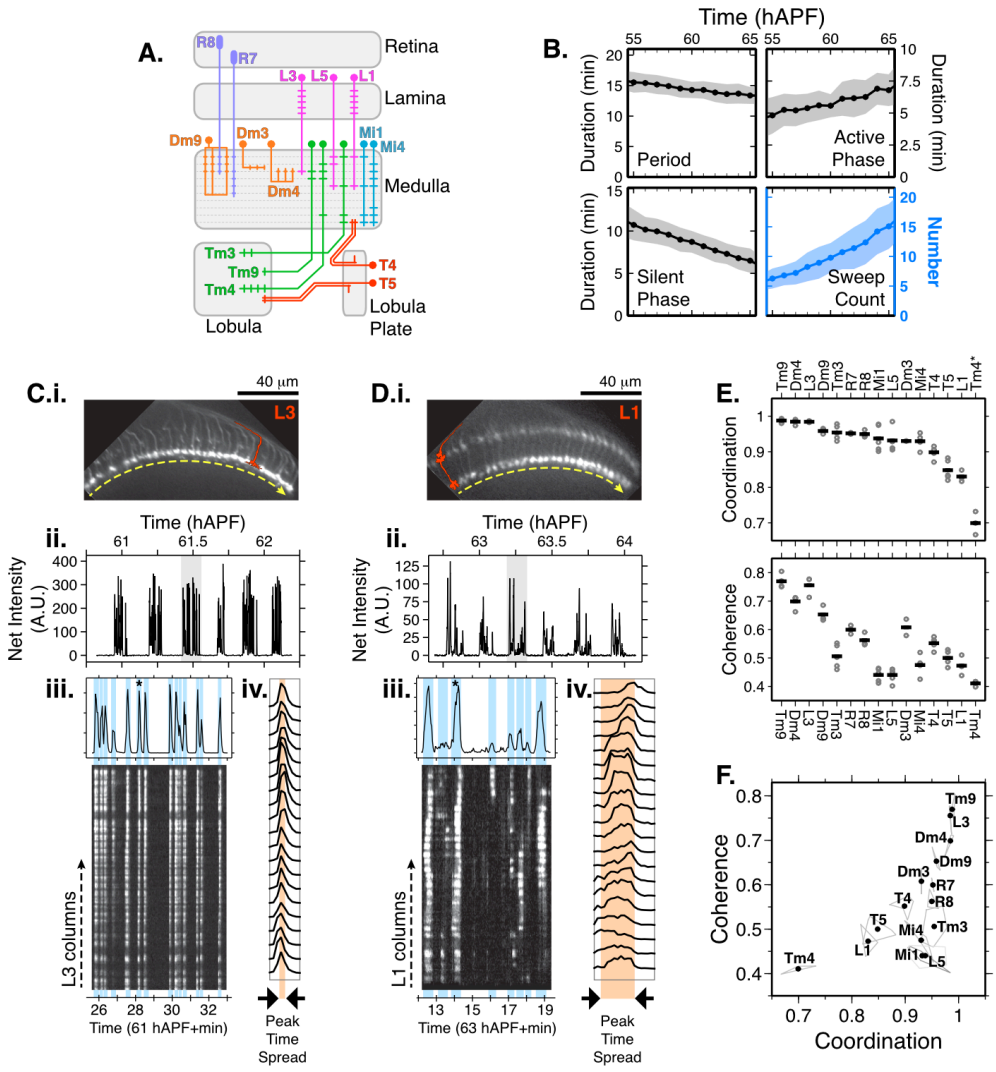
A.
R8
R7
L3
L5
L1
Retina
Lamina
Dm9
Dm3
Mi1
Mi4
Dm4
Medulla
Tm3
Tm9
Tm4
T4
T5
Lobula
Lobula Plate
B.
Time (hAPF)
Duration (min)
Period
Active Phase
Silent Phase
Sweep Count
Number
C.i.
40 μm
L3
ii.
Time (hAPF)
Net Intensity (A.U.)
iii.
iv.
L3 columns
Time (61 hAPF+min)
Peak Time Spread
D.i.
L1
L1 columns
Time (63 hAPF+min)
E.
Coordination
Coherence
F.
Coherence
Coordination

Figure 2.3. Cell type specific PSINA dynamics

A. Schematic of visual system cell types described in Figures 3 and 4; adapted from (Strother et al., 2017) **B.** Cycle metrics in the periodic stage, averaged over 15 cell types and 55 time series. Shaded areas, standard deviation. **C.** PSINA dynamics in L3 cells. **C.i.** Average intensity projection of GCaMP6s expressing L3 processes in the M3 layer of the medulla neuropil. Single L3 schematically shown in red. Dashed yellow arrow sits below the thin profile through M3 used to generate the kymograph in (iii); direction matches the layout of the columns in the kymograph. **C.ii.** Average net fluorescence intensity along the profile described in (i). Active phase with gray background shown in greater detail in (iii). **C.iii.** Plot shows expanded view of an active phase with sweeps highlighted in light blue. Star marks the sweep expanded into individual column traces in (iv). Kymograph of net fluorescence derived from the profile described in (i). **C.iv.** Plot of fluorescence change in individual medulla columns in the star marked sweep in (iii). **D.** Same as (C) for an L1 time series. Kymograph generated from a thin profile through the L1 processes in M5 (i.e. layer just above the yellow line). **E.** Coordination (top) and coherence (bottom) values calculated for different cell types. Round gray markers are individual time series, black bars are the average for each cell type. Between two and six time series shown for each cell type. Metrics for each time series calculated over 55-65 hAPF, using an average of 41±9 cycles and 10-20 columns per cycle. *The outlier coordination value of Tm4 is due to sparse labeling of this cell type with the driver used. **F.** Scatter plot of coordination v. coherence. Vertices of light gray polygons, individual time series; black dots, average for each cell type. See Table 1 for genotypes used in this figure.

Figure 2.4

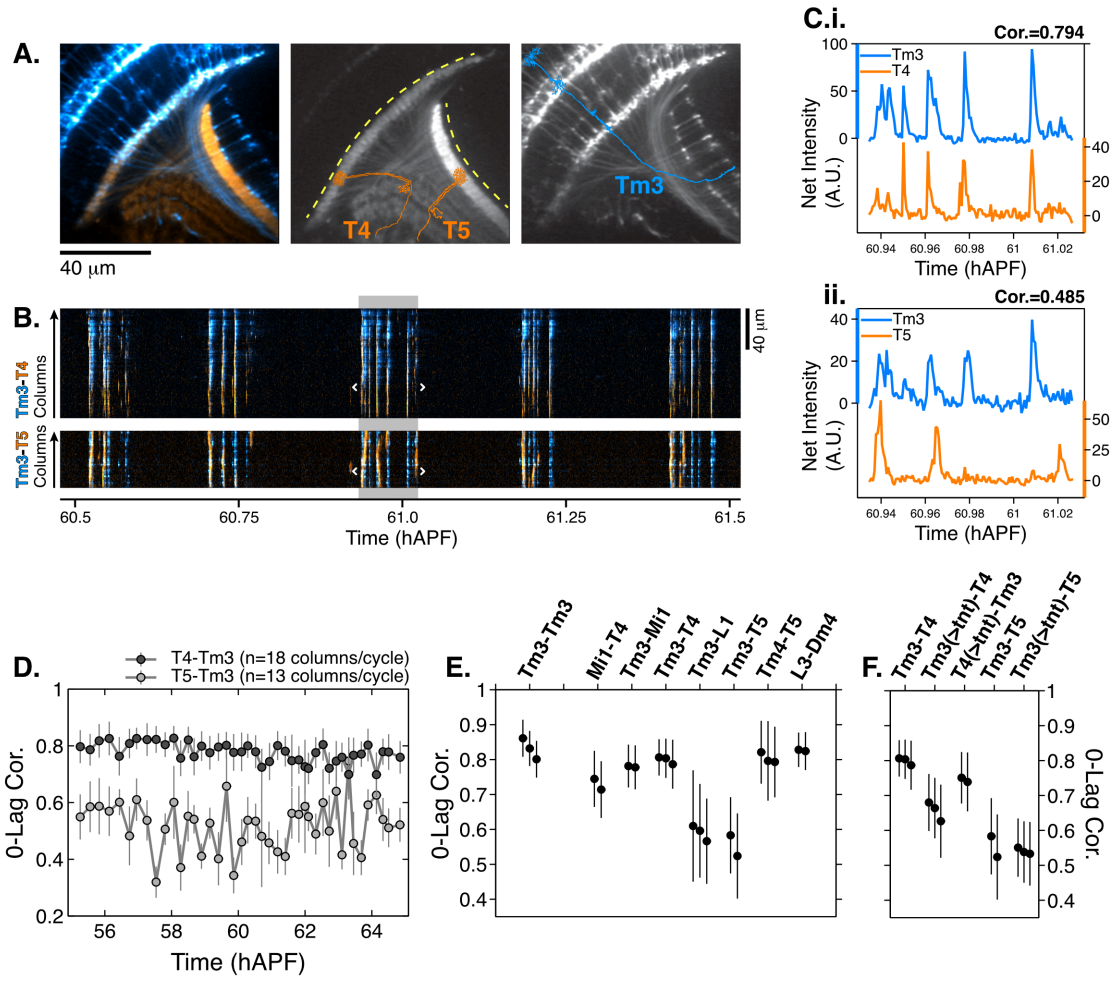
A.
T4
T5
Tm3
40 μm
B.
Tm3-T4 Columns
Tm3-T5 Columns
40 μm
60.5
60.75
61.0
61.25
61.5
Time (hAPF)
C.i.
Cor.=0.794
Tm3
T4
Net Intensity (A.U.)
Time (hAPF)
ii.
Cor.=0.485
Tm3
T5
Net Intensity (A.U.)
Time (hAPF)
D.
T4-Tm3 (n=18 columns/cycle)
T5-Tm3 (n=13 columns/cycle)
0-Lag Cor.
Time (hAPF)
E.
Tm3-Tm3
Mi1-T4
Tm3-Mi1
Tm3-T4
Tm3-L1
Tm3-T5
Tm4-T5
L3-Dm4
0-Lag Cor.
F.
Tm3-T4
Tm3(>tnt)-T4
T4(>tnt)-Tm3
Tm3-T5
Tm3(>tnt)-T5
0-Lag Cor.

Figure 2.4. Synaptic release is required for correlated PSINA activity.

A. Average intensity projection images of GCaMP6s expressing Tm3 (blue) and RCaMP1b expressing T4-5 (orange) cells. Single Tm3, T4, and T5 projections are schematically shown in blue and orange. Dashed yellow arcs in center panel abut the thin profiles through M9-10 and the lobula used to generate the kymographs in (B). **B.** Tm3-T4 (top) and Tm3-T5 (bottom) kymographs of net fluorescence derived from the profiles described in (A). Columns between the white brackets in active phase with gray background were used to generate the plots in (C). **C.** Tm3-T4 (**i**) and Tm3-T5 (**ii**) net fluorescence intensity along the columns marked in (B). **D.** 0-Lag cross correlation values between 55-65 hAPF for Tm3-T4 (dark gray) and Tm3-T5 (light gray) for the time series used in (A-C). Markers are the average correlation value for 10-20 columns per cycle, gray vertical lines are standard deviation. **E.** 0-lag correlation values for pairs of cell types, averaged over 55-65 hAPF. Black markers and vertical lines are the average and standard deviation for each time series. 2-3 time series shown per pair. 43±10 cycles with 15±3 columns per cycle used for each time series. The Tm3-Tm3 pair represents the highest correlation we expect to observe for a perfect match given the signal-to-noise statistics of the data (see **Figures S6A-S6B**). **F.** TNT expression in Tm3 reduces Tm3-T4 correlation but has no effect on Tm3-T5 correlation. Data statistics as in (E). Unperturbed pairs reproduced from (E) for ease of comparison. See Table 1 for genotypes used in this figure.

2.5. DISCUSSION

In summary, here we report the discovery and initial characterization of PSINA in the developing fly visual system. We observe three distinct stages of PSINA: a periodic stage between 55 and 65 hAPF, a turbulent stage lasting from 70 hAPF to the final hour of pupal development, and an adult stage that persists alongside mature stimulus responses through at least the first four days following eclosion. During the periodic stage, which coincides with the onset of synaptogenesis in the fly CNS (Chen et al., 2014; Muthukumar et al., 2014), each neuronal cell type of the 15 analyzed exhibited stereotyped and distinct activity patterns. Many adult synaptic partners had correlated activity, which depended on synaptic release.

Distinct periodic calcium dynamics were also seen in astrocytes. Astrocytes in the developing adult brain elaborate processes which infiltrate the neuropil during synapse formation (Muthukumar et al., 2014). Ablating astrocytes leads to a significant reduction in the total synapse count (32-47%, depending on the region) in the brain, supporting a role for these cells in regulating synaptogenesis (Muthukumar et al., 2014). Astrocytes of the optic neuropils also elaborate their processes over the same time period (Richier et al., 2017). Here we report that astrocytes exhibit cycles of GECI signal that are matched, though offset, to the periodic PSINA. These findings raise the possibility that astrocytes, spontaneous activity in them, and PSINA contribute to the formation, specificity, or maturation of synapses within the visual system.

What is the contribution of PSINA to building a brain? The best characterized system are retinal waves, which drive the activity of retinal ganglion cells (RGCs), the exclusive conduit of information from the eyes to the brain. Here, RGC projections from both eyes target the LGN and the SC, where they create retinotopic maps of the visual field and segregate based on the eye of origin. In the mouse, retinal waves are described in three stages: The gap-junction mediated

stage I from embryonic day 17 (E17) to post-natal day 1 (P1), the 'cholinergic' stage II between P1-P10, and the 'glutamatergic' stage III from P10 to eye opening at P14 (Blankenship and Feller, 2009; Sernagor and Hennig, 2013). Retinotopy and eye-specific segregation in the LGN and SC are refined over the same period as the second stage of retinal waves. This cholinergic stage is driven by starburst amacrine cells (SACs) (Zheng et al., 2006, 2004). Early work in the field established that pharmacological manipulation of spontaneous activity in the cat retina disrupts the organization of RGC projections in the LGN (Shatz and Stryker, 1988; Sretavan et al., 1988). Later studies, using progressively more refined methods, have shown that disrupting the cholinergic circuit of SACs and RGCs largely eliminates retinal waves and leads to defects in the refinement of retinotopy and eye-specific segregation of RGC projections (Bansal et al., 2000; Burbridge et al., 2014; McLaughlin et al., 2003; and others). In brief, retinal waves are necessary for the correct patterning of RGC projections in the brain.

Five classes of neurons comprise the retina: Photoreceptors, bipolar cells, amacrine cells, horizontal cells, and retinal ganglion cells (RGCs). The diversity of cell types within these classes—as many as 30 for RGCs (Sanes and Masland, 2015)—is comparable to the fly visual system. Whether there is cell type-specific texture to the retinal waves similar to PSINA described here is not known, although broad classes of RGCs and cone bipolar cells have been shown to exhibit temporally offset firing patterns (Akrouh and Kerschensteiner, 2013; Kerschensteiner and Wong, 2008) With improving genetic handles for distinct retinal cell types and ongoing efforts at describing the high resolution connectome, it will be possible to explore cell type-specific patterns and the contribution of retinal waves to retinal circuitry (Seung and Sümbül, 2014).

In *Drosophila*, peristaltic contractions of body wall muscles have recently been appreciated as part of broad neuronal activity during embryonic development (Baines and Bate, 1998; Vonhoff and Keshishian, 2016). This activity is similar to PSINA observed during pupal development with respect to periodicity and timing relative to synapse formation and refinement. Preventing motor neurons from participating in this neuronal activity, or disrupting calcium-dependent intracellular signaling results in ectopic synapses (Carrillo et al., 2010; Jarecki and Keshishian, 1995; Vonhoff and Keshishian, 2016). In the wildtype, the calcium transients in motor neurons are thought to enable synaptic pruning in response to the muscle-derived chemorepellent Sema2a (Vonhoff and Keshishian, 2016). A similar link between spontaneous activity and axon guidance has also been demonstrated in the developing mammalian visual system. Here, oscillatory Ca^{2+} activity in RGCs were shown to be required for the ephrin-A5 dependent re-positioning of RGC projections in the SC in *ex vivo* cultures (Nicol et al., 2007). These observations from the fly and the mouse suggest that axon guidance and, more broadly, neuronal morphogenesis may be common effectors of spontaneous activity during brain development.

Based on the studies we reference here, previous studies in the fly visual system, and of the role of spontaneous activity in other systems, we propose a general conceptual framework for the role of PSINA in regulating the assembly of the adult connectome. Here, we provide evidence to suggest that some adult synaptic pairings are already established by 55 hAPF, soon after the first pre-synapses can be detected and co-incident with the onset of periodic PSINA. The global coordination of PSINA indicates that an early connectome, one that must be built without activity, is present at this time. This early connectome, comprising the processes of over 100 different neuronal cell types, would be built through local, largely contact-dependent

biochemical interactions. While the level of organization achieved through such mechanisms is astonishing, the early connectome may still be a rough approximation of what is required in the adult.

PSINA, by orchestrating cellular communication at temporal and spatial scales inaccessible to other signaling mechanisms, may be acting to refine this draft connectome to complete the self-assembly of the brain. In the vertebrate visual system, retinal waves are required for the correct topographic organization of RGC projections in higher brain centers. In the fly, retinotopy, as reflected in the cartridges of the lamina and the columnar organization of the medulla and lobula complex, is established early, during the last larval and early pupal stages, and is driven largely by the differentiation and patterning of photoreceptors in the eye disc. However, little is known about how these columnar relays are integrated for visual computation. Coordination of multiple pre-synaptic inputs from neighboring columns is a feature of the motion detection circuit (Takemura et al., 2017) as well as of the visual projection neurons of the lobula, which are thought to relay computed visual features from the optic lobes to the central brain (Otsuna and Ito, 2006; Wu et al., 2016). The diversity of spatio-temporal patterns in PSINA presents many opportunities to establish circuit-specific topographic integration. Sweeps of activity repeatedly coursing through the brain through different ‘channels’ could link distinct sets of neurons to direct coordinated morphological changes and sculpt cell-cell contacts, strengthen synapses with correct targets while weakening and pruning incorrect pairings, and control transcription programs that direct circuit refinement (Lee et al., 2017; Nakashima et al., 2013; Serizawa et al., 2006; Tyssowski et al., 2018). PSINA may act as a ‘dress rehearsal’ for neural networks, preparing for ‘opening night’ at the completion of development. Individual cells know their own lines, with whom they interact, and their respective positions on the stage;

however, repeated practice of each scene is necessary to refine interactions and ensure that each of the cast can perform as part of a whole ensemble.

We find it remarkable that as a process that appears to engage most, if not all, of the CNS, PSINA is the collective output of the genetically hardwired developmental programs of individual neurons. Thus, despite its complexity, the organizing principles, the driving forces, and the functional significance of PSINA at the level of circuits, cells, and molecules should be discoverable through genetic analysis. Undertaking this effort in the fly visual system, where structures analogous to the vertebrate retinal plexiforms, the LGN, and the SC (Sanes and Zipursky, 2010) are compactly organized in a single microscopic field of view and for which the EM-derived connectome is available, may yield valuable insights into whether and how PSINA affects synaptic specificity and circuit maturation. We expect that the ever-expanding genetic toolkit of *Drosophila*, complemented with improvements in genomic/transcriptomic analysis and imaging technology, will offer a robust experimental track toward understanding PSINA's contribution to brain development and function.

2.6. METHODS

2P Imaging of the Developing Visual System

Pupae were prepared for imaging as previously described (Akin and Zipursky, 2016). Briefly, the cuticle around the heads were removed with fine forceps and the animals were attached eye-down on a coverslip coated with a thin layer of embryo glue. A water reservoir on the objective side of the coverglass provided sufficient immersion medium to last through the hours-long imaging sessions; another reservoir below the pupae kept the animals from dehydrating.

Time-lapse imaging of the visual system was carried out on a custom-built 2P microscope (Akin and Zipursky, 2016) equipped with a 20x water immersion objective (Zeiss, W Plan-Apochromat 10x/1.0 DIC) and 2 GaAsP detectors (Hamamatsu). Over the 2-24 hr imaging sessions, the pupae were kept at 25°C using an objective heater system (Bioptechs). A tunable Ti:Sapphire pulsed laser (Chameleon Ultra II, Coherent) was used as the light source. Green fluors were excited at 940 or 970 nm with ~30 mW under-the-objective power; 1020 nm at ~60 mW was used for red fluors and two-color imaging. Animals imaged under these conditions developed normally and eclosed on schedule. To observe a thicker cross-section of the visual system than possible with a single optical slice, we used the maximum intensity projection of three successive images taken 2 μm apart in the z-axis as the frame for an individual time point. Thus, the effective sampling rate of these time series was 0.4 Hz (2.5s per frame).

Wide-field Imaging

Pupae were staged for head eversion and reared at 25ºC. At 58-60 hAPF, pupae were affixed to a Sylgard 184 Silicone Elastomer plate (Dow Corning) with double-stick adhesive tape (3M). Images were acquired with a SteREO Discovery.V8 stereomicroscope (Zeiss) with illumination

provided by an X-Cite Series 120PC light source (Excelitas) and captured on a Vixia HF R20 1/4.85 inch CMOS camera (Canon). Images were acquired at 30 Hz. Time series were processed with Fiji (ImageJ) (Schindelin et al., 2012) and analyzed using MATLAB (Mathworks, Natick, MA, USA).

Adult Functional Imaging

Calcium imaging was performed as previously described (Keleş and Frye, 2017). Briefly, a single fly was anesthetized at 4°C and placed into a chemically etched metal shim attached to a custom 3D-printed holder. Holder design was based on (Weir et al., 2016); details can be found at http://ptweir.github.io/flyHolder/. The head capsule and thorax were glued to the metal shim using a UV-curable glue (www.esslinger.com). Legs and the antennae were immobilized using beeswax applied with a heated metal probe (Waxelectric-1, Renfert). The head capsule was bathed in saline (103mM NaCl, 3mM KCl, 1.5mM CaCl2, 4mM MgCl2, 26mM NaHCO3, 1mM NaH2PO4, 10mM trehalose, 10mM glucose, 5mM TES, 2mM sucrose) and a small window was opened using fine forceps (Dumont, #5SF). Muscles and fat covering the optic lobe were cleared before placing the fly under a 2P microscope (3i, Denver, CO). Neurons expressing GCaMP6s were imaged at 920 nm using a Ti:Sapphire pulse laser (Chameleon Vision, Coherent). Images were acquired at 10 Hz.

An arena of 48 8x8 LED matrices (470 nm, Adafruit) was used to deliver the visual stimulus. Three layers of blue filter (Rosco no. 59 Indigo) were placed between the screen and the fly to eliminate leakage of the LED light into the PMTs. The screen extended ±108° along the azimuth and ± 72° in elevation. Each LED pixel corresponded to a coverage of 2.2° on the retina equator. However, the projection of each pixel on the retina was variable due to the difference between the curvature of the eye and that of the screen. Visual stimulus consisted of a

wide-field grating with a spatial frequency of 35° and presented at a temporal frequency of 0.62 Hz in both directions (ipsi-to-contra and contra-to-ipsi) along the horizontal axis. The presentation order of the visual stimuli was randomized to prevent sensory adaptation. Each experimental condition was tested three to four times per animal.

Tetrodotoxin Treatment

Pupal development was staged for white pre-pupa formation and reared at 25ºC. Between 90-95 hAPF, the pupal case was removed with fine forceps. These late pupae were prepared for imaging following the protocol described above for adult functional imaging. Viability was verified by leg or trachea movement. Neurons expressing GCaMP6s were imaged at 920 nm using a Ti:Sapphire pulsed laser (Chameleon Vision, Coherent). Images were acquired at 10 Hz.

Tetrodotoxin at 1μM final concentration was mixed into the saline solution after 40 minutes of imaging and the fly was observed for another 20 minutes after the application of the drug. Viability was confirmed before and after tetrodotoxin administration, and the data were excluded from analysis if the animal did not survive the experiment.

Visual Flight Simulator

Flies were cold anesthetized at 4°C, tethered to tungsten pins using UV activated glue, and allowed to recover for 1-2 hours in a small, humidified acrylic container with a red desk lamp providing heat. This recovery regime improves flight performance consistency. The majority of the experiments were performed in the afternoon when flies are most active.

A visual flight simulator composed of 32x96 cylindrical green (570 nm) LEDs was used to deliver visual stimuli (Reiser and Dickinson, 2008). The arena covered ± 180° along the azimuth and ± 60° in elevation. Single flies were positioned in the center of the arena and illuminated from above with an 880 nm infrared LED. The shadow cast by the wings was

detected with an optical sensor. Signal form this sensor was analyzed by an instrument called the wingbeat analyzer (JFI Electronics Laboratory, University of. Chicago, Chicago, IL, USA) that calculates left and right wing beat amplitudes (WBA). The difference in the left and right WBA is proportional to the fly's steering effort in the yaw axis.

For bar fixation closed-loop experiments, a dark bar that is 120° in height and 30° in width was presented to the flies. Positional displacement of the bar in the yaw axis was coupled to the steering effort of the fly, allowing the animal to have the active control of the bar position. Each fly was tested for closed-loop fixation behavior for four minutes. To test open-loop optomotor responses, flies were presented with wide-field gratings with a spatial frequency of 30° and a temporal frequency of 3 Hz for four seconds.

Quantification and Statistical Analysis

Analysis of Pupal Imaging Data

Pre-processing: Processing and analysis of image data were carried out with custom scripts written in MATLAB (Mathworks, Natick, MA, USA). Fiji (ImageJ) was used for some user-assisted tasks and figure preparation. Time series were processed in blocks corresponding to ~6 hours of observation (~9000 frames). In the pre-processing step of reducing lateral motion, the general approach of maximizing the cross correlation of individual frames to a reference image was modified to meet the specific challenges of developmental imaging. First, a series of reference images were generated as averages of pools of high signal frames distributed across each block. After ~55 hAPF, the optic lobes begin to twitch with a period similar to that of PSINA. These fast movements can introduce significant blur into the pool-averaged reference images. To reduce this blur, 300 random subsets of each pool were tested to find the sharpest average reference image. Sequential registration of this series of reference images to each other

produced a stabilized representation of the visual system which continues to move and grow over the course of observation (Akin and Zipursky, 2016; Langen et al., 2015). In a second step, the registration of the reference series was refined to minimize the movement of a user defined region of interest (ROI). These internally registered reference images then served as local registration targets for nearby frames of the full block. Finally, the block was corrected for any rotational motion of the ROI.

Signal and Feature Extraction: Per frame pixel averages of masked regions were used to define raw signal (F) traces from the image time series. Time-dependent fluorescence baseline (F_o) was estimated using a moving window approach and used to calculate the net signal ($F-F_o$, Figures 2.2, 2.3 and 2.4) and change-in-signal ($(F-F_o)/ F_o$, Figures 2.1 and 2.2) traces. User-defined, static masks were used for pan-neuronal and glial expression experiments. For cell type-specific experiments, *dynamic masks*, corresponding to the active columns in each cycle, were defined automatically from the kymograph representation of the time series. Briefly, kymographs were generated as concatenated line profiles from user-defined, segmented arcs of 7-9 pixel (3-4 μm) thickness, drawn across a single layer of the medulla or lobula neuropil. Baseline subtracted, net signal kymographs were used in all subsequent analysis. Projecting along the spatial dimension of the kymographs yielded one dimensional net signal traces, which were used to identify the limits of PSINA cycles. Within each active phase, sweeps were defined by ordering intensity peaks with respect to their amplitudes, and, from the largest peak on down, marking the continuous time spans with net signal intensity greater than 75% of peak value; lesser peaks present in the sweep of a larger one were removed from the ordered peak list used in sweep identification. Dynamic masks were based on peaks in the *activity profiles* of PSINA cycles, produced for each active phase by projecting along the temporal dimension of the kymographs.

The width of each mask was determined by testing the spatial neighborhood of each peak for correlated net intensity changes in the time domain. The maximum number of dynamic masks identified in each cycle was set to 20.

Frequency Analysis: Analysis was implemented in MATLAB, following the guidelines of Uhlen (Uhlén, 2004). Change-in-signal (ΔF/F) traces were processed using a 2-hour sliding window which traversed the time series in 1-hour steps. After filtering with a Hanning window to reduce spectral leakage, each 2-hour block was transformed with the FFT algorithm to obtain non-parametric power spectrum density estimates. The fidelity of the power spectrum density estimate was confirmed by applying the inverse transform on the highest-power peak and comparing the resultant signal to the raw data. One-sided power spectrum density estimates were plotted for each 2-hour block in Figure 2.1 and Supplementary Figure 2.2.

PSINA Dynamics: For each cycle, unit signal-to-noise (S2N) value was defined as twice the standard deviation of the net signal trace in the silent phase. A dynamically masked column was considered to participate in a given sweep if it had a net intensity peak greater than or equal to 1.0 S2N within the sweep limits. This scoring scheme was the basis of the definition of the coordination metric. For coherence, the largest fraction of columns that reach peak intensity at the same time point within each sweep was calculated. To ensure consistent comparisons across different cell types, only high participation (≥90%) sweeps were considered for the coherence metric.

STTC analysis was carried out according to Cutts and Eglen (Cutts and Eglen, 2014), with a key script sourced from a Github submission by Leonardo D. Garma (Leo-GG, 2017). For each time series, the active phase of each cycle was treated as a separate recording. The net intensity traces from dynamically masked columns were converted to spike trains using a hard threshold of four

times the standard deviation of the net trace in the preceding silent phase. STTC values were calculated for a range of Δts; the value of 5 s marked a decrease in the slope of STTC v. Δt and yielded the greatest dynamic range across different cell types and therefore was chosen for the analysis shown in Supplementary **Figures 2.8B-2.8D**. Distances between columns were binned in increments of 4.5 μm, the average column width in the optic neuropils during development. As a measure of how STTC decays over distance for a cell type, we report the ratio of the STTC value at 36 μm to that at 4.5 μm; the 36 μm mark was chosen to ensure that all cell types could be compared using this metric, including ones with processes in the lobula plate (e.g. T5), which is only partially visible in our setup.

Correlation Analysis: For the analysis of two-color neuronal imaging experiments, two separate kymographs were generated using the same segmented arc. Dynamic masks were derived from the average activity profile of these two kymographs to ensure that the masks captured columns active in both channels. Cycle limits were determined using the brighter channel. For each cycle, masks with a maximum S2N value of at least 1.0 in both channels were used to calculate pairwise 0-lag cross-correlation. Cycles with fewer than 10 masks above the signal quality threshold were excluded in the calculation of time series ensemble statistics (i.e. mean and standard deviation.)

For correlation analysis of GECI combined with voltage or glutamate imaging, one ROI was generated using a segmented arc over the first layer of the medulla. Mean population traces were generated for both indicators; single column analysis was not possible due to low S2N. MATLAB functions for normalized cross-correlation and auto-correlation were used to compare lags between traces. The same approach was used for two-color calcium imaging of neurons and glia; however, separate ROIs were used for neuronal signals (medulla) and glia (inner optic

chiasm).

Analysis of Adult Calcium Imaging Data

Images were pre-processed to correct for lateral motion using the registration algorithm described above. To find active pixels in the lobula, we defined a mask excluding other neuropils (medulla and lobula plate). For every pixel in this mask, the mean value and standard deviation were calculated for the full time series; the test value for each pixel was defined as the product of these metrics. Pixels with test values greater than or equal to twice the mean value of all pixels in the mask were used in analysis. In our experience, this thresholding approach enriches for active pixels over background and shot noise in the selected mask. The frame average of active pixels were used to produce the signal trace for the time series. Repeated observations were averaged for each fly and a single average trace per experiment was generated.

Analysis of Visual Fixation Behavior

Behavioral data from the visual display and the wing beat analyzer was collected with a Digidata 1440A digitizer (Molecular Devices, San Jose, CA, USA) sampled at 1 kHz. Data were processed using custom written scripts in MATLAB (Mathworks, Natick, MA, USA). Briefly, the first 100 milliseconds of the trials were removed and the first data point of the remaining signal was subtracted from the entire trial to set the initial WBA to zero. ΔWBA was calculated by subtracting left from right WBA. Flies which stopped flying during the experiments were excluded from further analysis. Trials for the same experimental conditions were averaged and calculated for all animals. No statistical tests were conducted to pre-determine the sample size. To analyze closed-loop fixation data, the bar position was binned into 96 positions around the visual azimuth and bar histograms for each fly was calculated. Data were then averaged across the animals for the time bar spent at each position.

2.7. SUPPLEMENTARY FIGURES

Supplementary Figure 2.1.

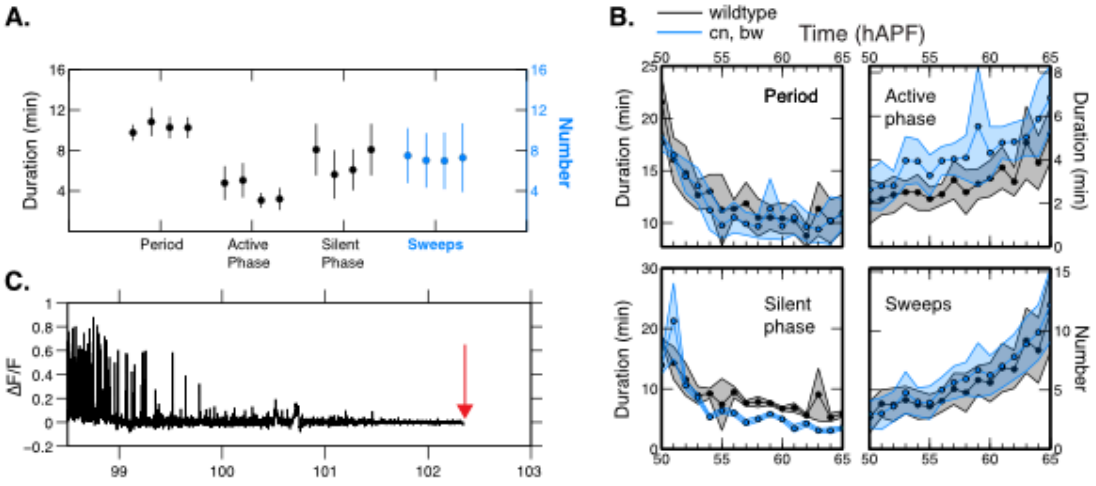

Supplementary Figure 2.1. Related to Figure 2.1.

A. Comparison of mean period, active phase duration, silent phase duration, and sweeps per cycle among wildtype flies (n=21 columns from 3 animals) averaged between 55-65 hAPF. Error bars, standard deviation. **B.** Comparison of mean period, active phase duration, silent phase duration, and sweeps per cycle between *cn,bw* flies (n = 28 columns from 2 animals) and wildtype flies (n = 21 columns from 3 animals) from 50-65 hAPF. Error bars, standard deviation. **C.** Representative trace during the last hour before eclosion (one shown of n = 3 flies). Arrow marks time of eclosion. See Table 1 for genotypes used in this figure.

Supplementary Figure 2.2

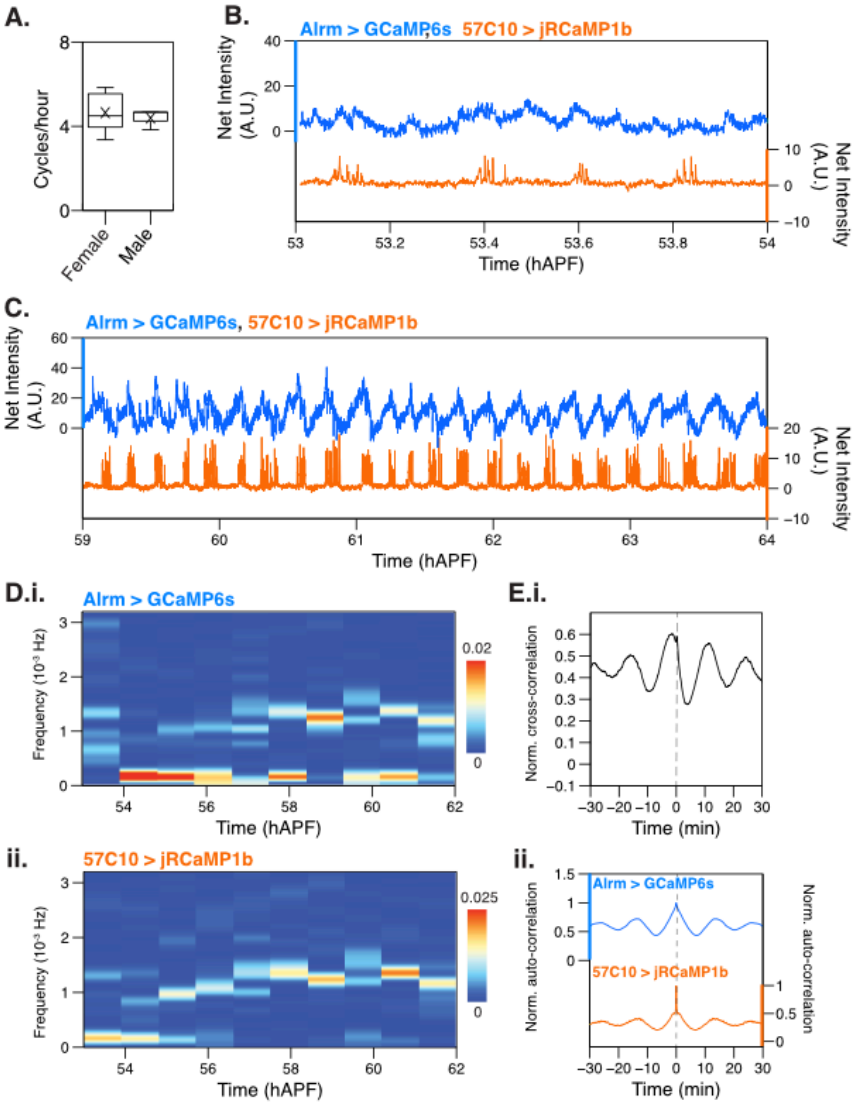

Supplementary Figure 2.2. Related to Figure 2.2.

A. Cycles per hour for female (n=6) and male (n=3) pupae. Error bars, standard deviation. X, mean. Horizontal bar, median. **B.** Representative trace comparing glial and neuronal activity from 53-54 hAPF, when glial and neuronal activity are not in phase. **C.** Representative trace comparing glial and neuronal activity from 59-64 hAPF, when glial and neuronal activity are in phase. **D.** Frequency analysis (Fourier transform) between 53-62 hAPF of glial GECI signal (**i**) and neuronal GECI signal (**ii**). **E.** Normalized cross-correlation (i) and auto-correlations (ii) of glial and neuronal population traces from 59-64 hAPF (n = 24 cycles). See Table 1 for genotypes used in this figure.

Supplementary Figure 2.3.

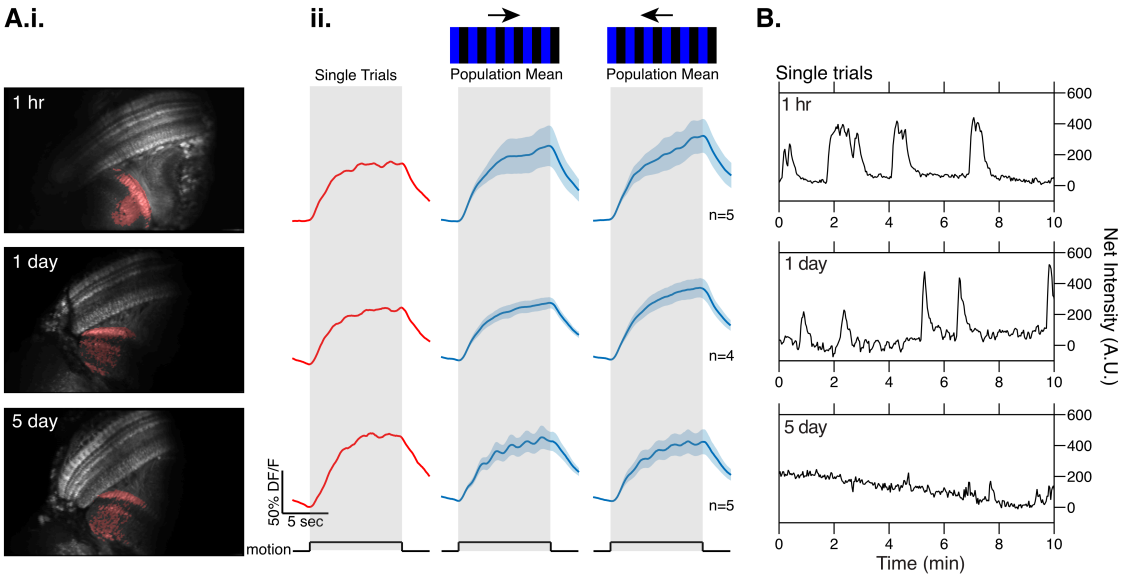

Supplementary Figure 2.3. Related to Figure 2.2.

A.i. Representative images of optic lobes from 1 hr, 1 day, and 5 day old flies expressing pan-neuronal GCaMP6s. Red areas are regions of interest used for the analyses shown in (A.ii) and (B). **A.ii.** *Left Panel*: Single trial responses to a contra-to-ipsilaterally moving visual stimulus. *Middle Panel*: A wide-field grating with a spatial frequency of 35° is presented contra-to-ipsilaterally at a temporal frequency of 0.62 Hz. Population mean is shown in blue and shaded regions indicate S.E.M. *Right Panel*: Same as middle panel with stimulus moving ipsi-to-contralaterally. **B.** Spontaneous activity in newly eclosed (i.e. 1 hr old), 1 day, and 5 day old flies. Single representative traces shown of n = 2, 3, and 5 flies from 1 hr, 1 day, and 5 day old flies, respectively. See Table 1 for genotypes used in this figure.

Supplementary Figure 2.4.

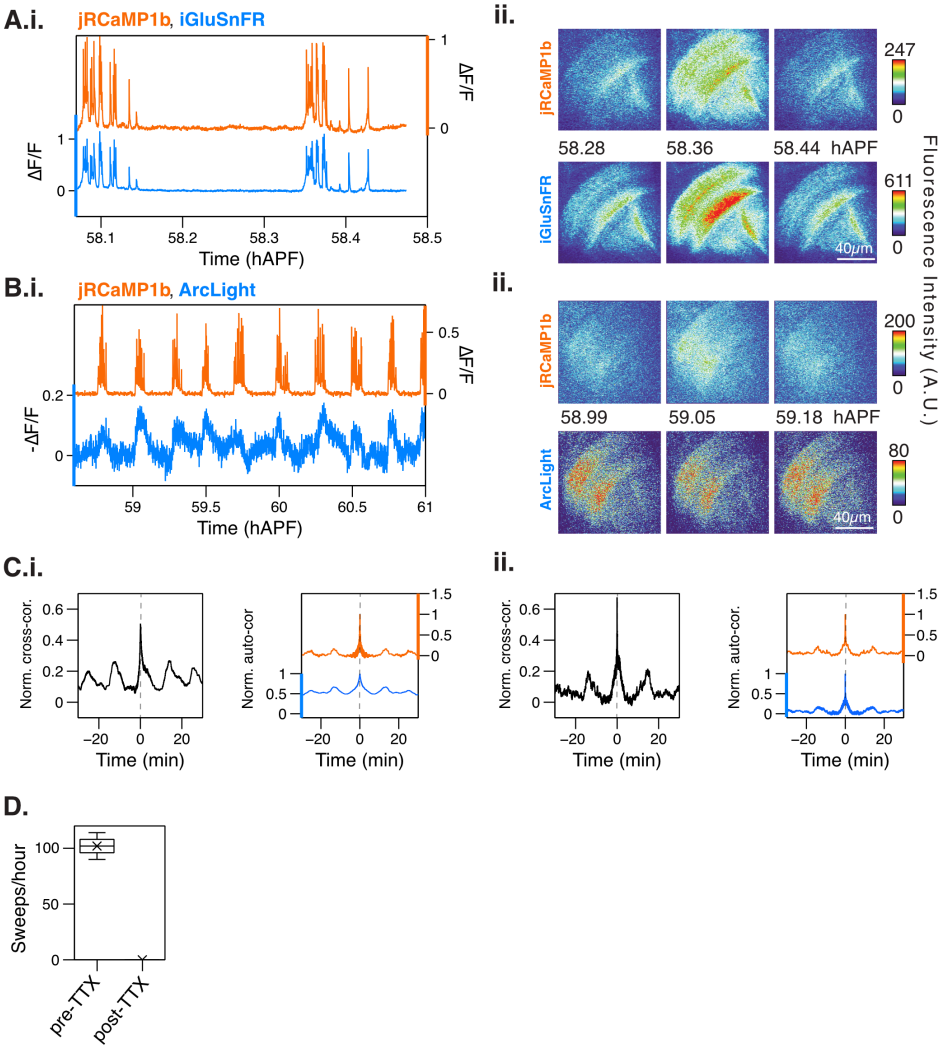

Supplementary Figure 2.4. Related to Figure 2.2.

A. Representative traces (**i.**) and micrographs (**ii.**) from optic lobes of flies with pan-neuronal expression of jRCaMP1b (orange, top) and iGluSnFr (blue, bottom), left. Scale bar, 40μm. **B.** Representative traces (**i.**) and micrographs (**ii.**) from optic lobes of flies with pan-neuronal expression of jRCaMP1b (orange, top), and ArcLight (blue, bottom). Scale bar, 40μm. **C.** Normalized cross-correlation (left) and auto-correlations (right) between population traces of L1 cells expressing jRCaMP1b and either iGluSnFR (**i**) or ArcLight (**ii**). n=10 and 23 cycles, respectively. **D.** Average sweep count per hour before (20-0 mins) and after (5-20 mins) addition of 1μM TTX. Experiments performed with the head-fixed cranial window preparation in late stage pupae (90-95 hAPF). Error bars, standard deviation (n=3 flies). X, mean. Horizontal bar, median. See Table 1 for genotypes used in this figure.

Supplementary Figure 2.5.

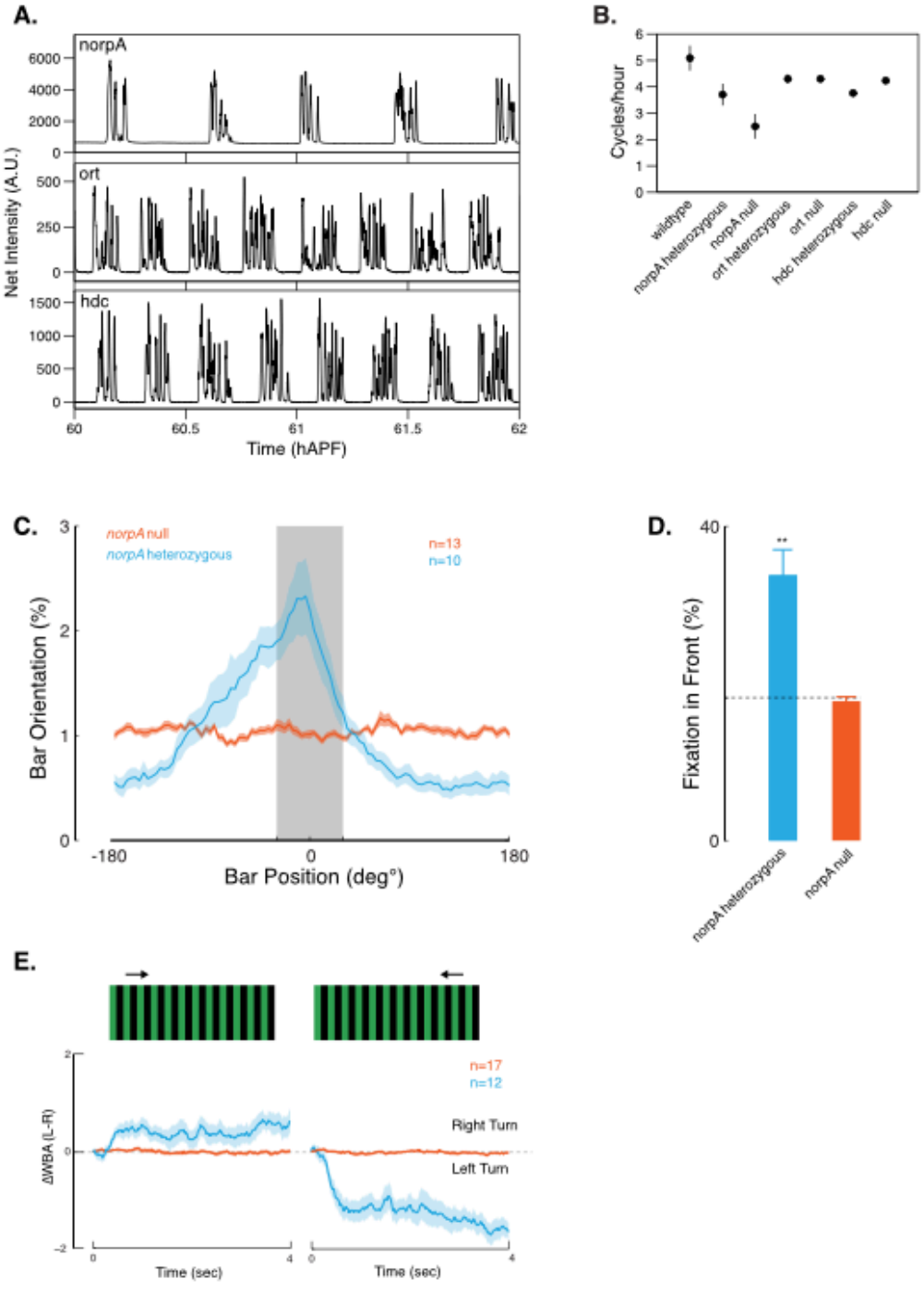

Supplementary Figure 2.5. Related to Figure 2.2.

A. Representative traces from *norpA* (top), *ort* (middle), and *hdc* (bottom) null mutant flies expressing pan-neuronal GCaMP6s. For each genotype, periodic activity persists, indicating that sensory input from photoreceptors is not driving this activity. However, the *norpA* period is altered. *norpA* is expressed broadly in the developing CNS, suggesting that this Ca^{2+}-sensitive phospholipase may be contributing to PSINA regulation beyond its later role in phototransduction in the adult. See Table 1 for genotypes used in this figure. **B.** Comparison of mean cycles per hour for wildtype flies (n=8) compared to *norpA* heterozygous (n=6), *norpA* homozygous (n=4), *ort* heterozygous (n=3), *ort* homozygous (n=3), *hdc* heterozygous (n=3), and *hdc* homozygous (n=3) mutant flies. Error bars, standard deviation. Markers for mean values may obscure small error bars. **C.** Comparison of closed-loop fixation behavior between *norpA* null (orange, n = 13) and *norpA* heterozygous (blue, n = 10) flies. Fixation in front is the percentage of time the bar was between -30 and +30 degrees. Shaded error bar, S.E.M. **D.** Quantification of closed-loop fixation behavior between *norpA* hemizygous (orange) and heterozygous (blue) flies. Wilcoxon signed-rank text p = 0.0039 when heterozygous flies tested against chance. p = 0.4548 when hemizygous flies tested against chance. Dashed line = chance. Error bars, S.E.M. **E.** Grating experiment testing widefield optomotor response between *norpA* hemizygous (orange) and heterozygous (blue) flies. Temporal frequency = 3 Hz. Delta WBA = right wingbeat amplitude subtracted from left wingbeat amplitude.

Supplementary Figure 2.6.

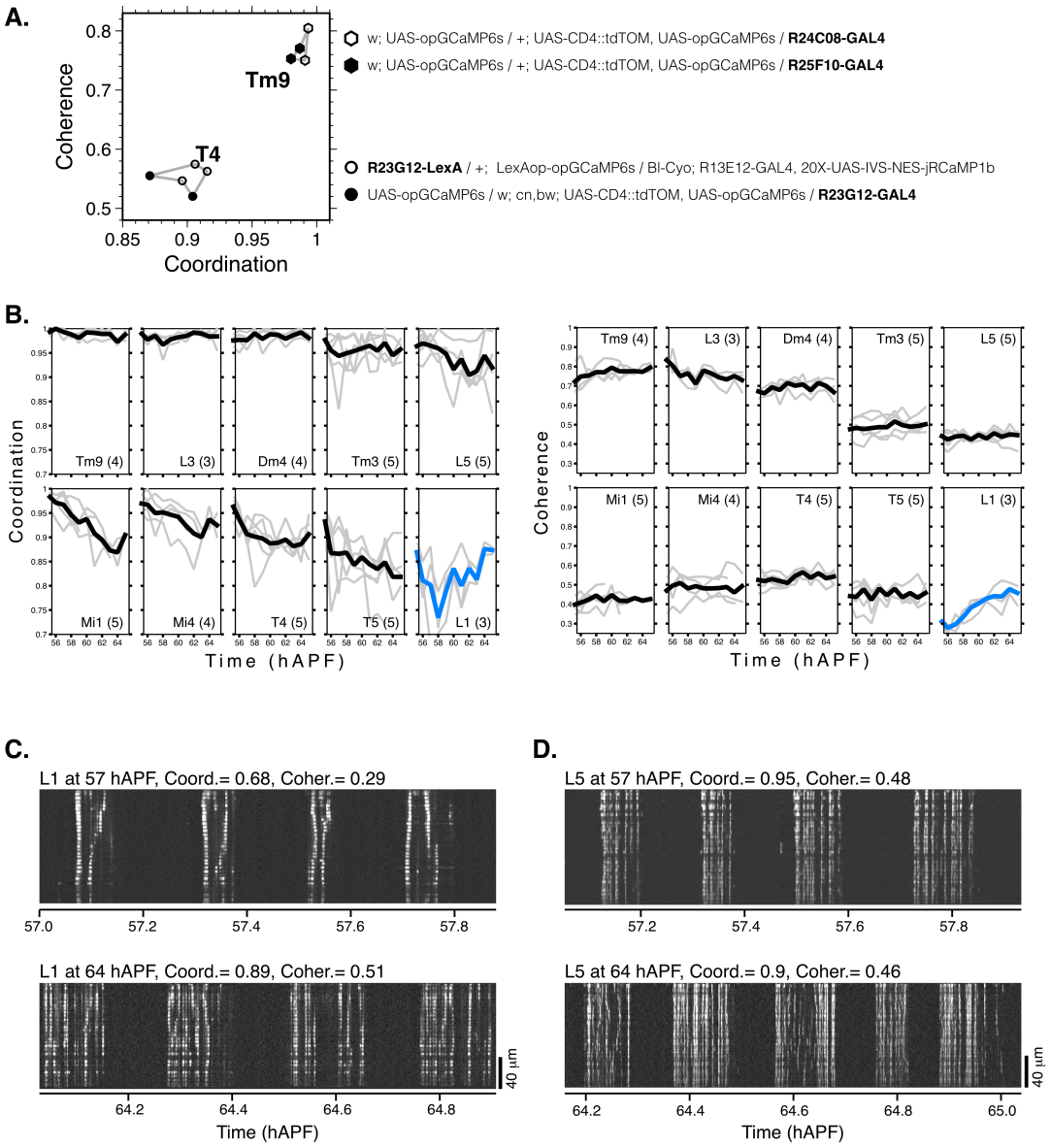

Supplementary Figure 2.6. Related to Figure 2.3.

A. Coordination and coherence values are not sensitive to the specific drivers used for GECI expression or transgenic constitution of the animals. Genotypes used for the Tm9 and T4 data shown in Figures 3E-3F are shown next to the measured values in the coordination v. coherence scatter plot. The Tm9 set is drawn from two different enhancer elements (24C08 and 25F10) while the T4 set uses GAL4 and LexA drivers of the same enhancer element (23G12) in otherwise different transgenic backgrounds. **B.** Coordination (left) and coherence (right) time courses of 10 cell types. Parenthetical values are the number of individual time series (plotted in light gray) used to calculate the cell type-specific average trends plotted in black. Time course of L1, the only cell type in the set for which both coordination and coherence increases over development, is plotted in blue. **C.** Kymographs from an L1 time series show PSINA cycles at 57 (top) and 64 (bottom) hAPF alongside the calculated coordination and coherence values. While the increase in the number of sweeps is the clearest difference between the two images, both the fraction of sweeps which engage more columns and how rapidly many of the sweeps run through the L1 array also increase between 57 and 64 hAPF. These changes, which account for the qualitative difference in the look of the images is quantitatively captured by the coordination and coherence metrics. **D.** Kymographs from an L5 time series show PSINA cycles at 57 (top) and 64 (bottom) hAPF alongside the calculated coordination and coherence values. The increase in the number of sweeps per cycle is not as pronounced in L5 as it is in L1. Additionally, the 'texture' of the active phases look very similar in L5 between 57 and 64 hAPF; this similarity is reflected in the measured coordination and coherence metrics. See Table 1 for genotypes used in this figure.

Supplementary Figure 2.7.

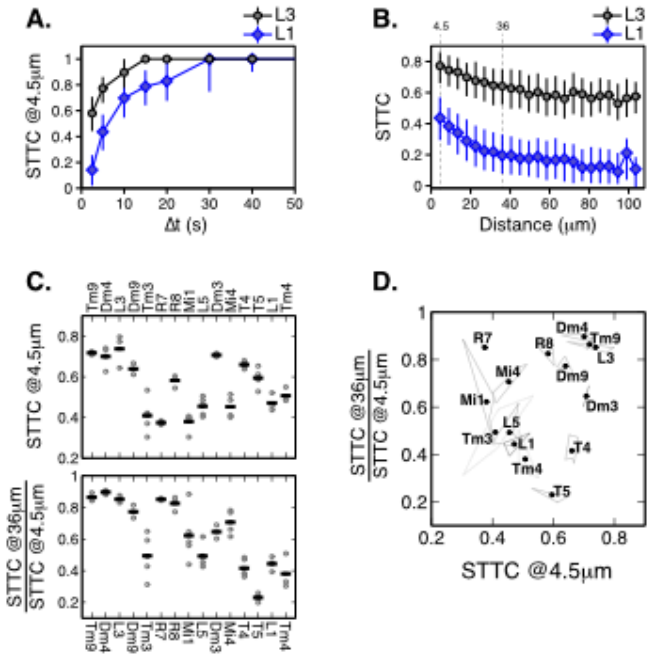

Supplementary Figure 2.7. Related to Figure 2.3.

A. Spike time tiling coefficient (STTC) v. deltaT, measured for adjacent columns (i.e. smallest distance bin of 4.5 μm) for L3 and L1. Median values and interquartile range for 824 (L3) and 782 (L1) column pairs measured from 47 (L3) and 46 (L1) cycles between 55-65 hAPF are plotted. **B.** STTC, calculated for deltaT=5s, v. distance for L3 and L1. Median values and interquartile range of an average of 370 column pairs measured from 47 (L3) and 46 (L1) cycles between 55-65 hAPF are plotted. The distance bins (4.5 and 36 μm) used in the data compilations of (C) and (D) are marked. **C.** Adjacent column STTC (top, 'STTC @4.5μm') and normalized STTC at 36 μm (bottom, 'STTC @36μm / STTC @4.5μm') was calculated for different cell types for deltaT=5s. The 36 μm mark was chosen to ensure that all cell types could be compared using this metric, including ones with processes in the lobula plate (e.g. T5), which is only partially visible in our setup. Round gray markers are medians for individual time series, black bars are the average of medians for each cell type. Between two and six time series shown for each cell type. Metrics for each time series calculated over 55-65 hAPF, using an average of 41±9 cycles and 10-20 columns per cycle. **D.** Scatter plot of STTC @4.5μm v. STTC @36μm / STTC @4.5μm for deltaT=5s. Vertices of light gray polygons, medians of individual time series; black dots, average of medians for each cell type. See Table 1 for genotypes used in this figure.

Supplementary Figure 2.8.

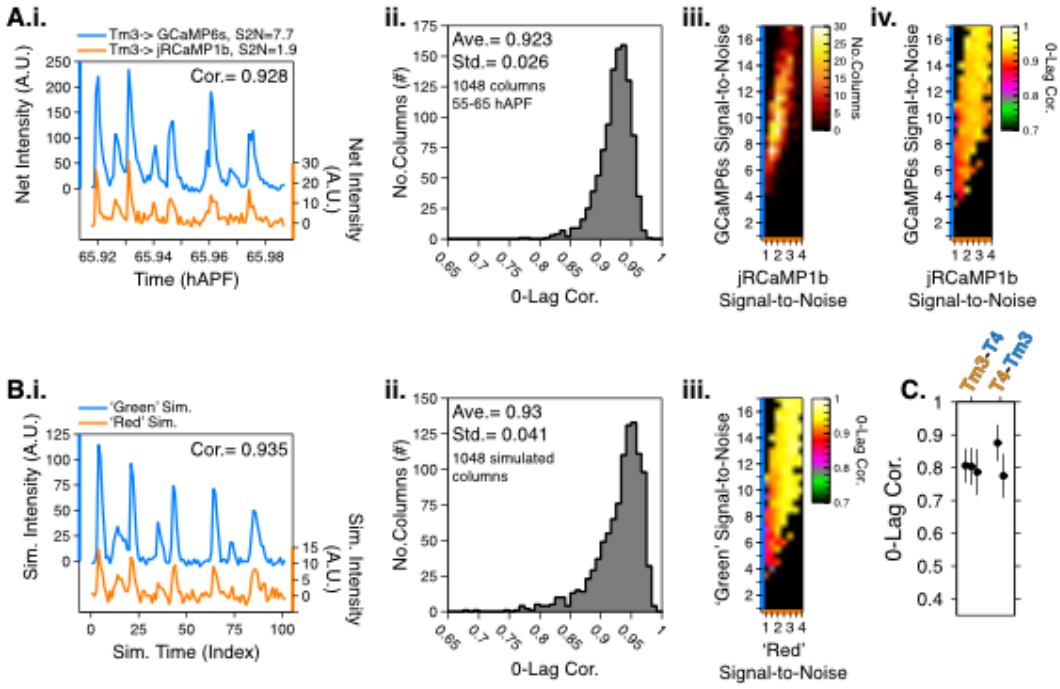

Supplementary Figure 2.8. Related to Figure 2.4.

A. Measured correlation in neuronal activity reported by GCaMP6s and jRCaMP1b is affected by the signal strength of both probes. **A.i.** Representative GCaMP6s (blue) and jRCaMP1b (orange) single column traces taken from a Tm3-Tm3 two-color time-series. The signal-to-noise (S2N) ratio of each trace is defined as the ratio of maximum signal to twice the standard deviation of baseline fluctuations. The measured 0-lag correlation value is 0.928. **A.ii.** Histogram of 0-lag correlation values for 1048 paired Tm3-Tm3 columns measured for 53 cycles over 55-65 hAPF (~19.8 columns/cycle). **A.iii.** 2D histogram of column counts in paired bins of GCaMP6s (blue, vertical axis) and jRCaMP1b (orange, horizontal axis) S2N values; colorbar is shown on the right. **A.iv.** 2D histogram of the 0-lag correlation values in (ii) in paired bins of GCaMP6s (blue, vertical axis) and jRCaMP1b (orange, horizontal axis) S2N values; colorbar is shown on the right. Measured correlation increases with increasing S2N in both channels. **B.** Noise degrades perfect correlation. **B.i**. Simulated traces matched to data shown in (A.i.) using measured sweep amplitudes, positions, and S2N statistics. **B.ii.** Histogram of 0-lag correlation values for 1048 column pairs simulated based on the source data for (A.ii.). **B.iii.** 2D histogram of the 0-lag correlation values in (ii) in paired bins of 'Green' (blue, vertical axis) and 'Red' (orange, horizontal axis) S2N values; colorbar is shown on the right. As with the data in (A.iv), correlation between simulated traces increases with increasing S2N in both channels. **C.** Correlation is not sensitive to cell type and GECI configuration. 0-lag correlation values for Tm3->jRCaMP1b, T4->GCaMP6s (n=3) and T4->jRCaMP1b, Tm3->GCaMP6s (n=2) pairs averaged over 55-65 hAPF. Black markers and vertical lines are the average and standard deviation for each time series. See Table 1 for genotypes used in this figure.

Table 1. List of genotypes used in this work

Used in Figure	Cells Imaged / Label	Cells Silenced / Effector	Fly Genotype	Notes
2.1A-C	PanNeuronal / GCaMP6s	None	*w;* *R57C10-lexA (attp40), 13XLexAop2-IVS-Syn21-OpGCaMP6s-p10 (su(Hw)attP5);* +	
2.1A-C, 2.2A, 2.2E, S2.1A, S2.1B, S2.1C, S2.2A, S2.3A, S2.3B, S2.4D, MovieS1, MovieS2	PanNeuronal / GCaMP6s	None	*w;* *20XUAS-IVS-Syn21-opGCaMP6s-p10 (su(Hw)attP5) / Sp-Cyo;* *UAS-CD4-tdTOM (VK00033), 20XUAS-IVS-Syn21-opGCaMP6s-p10 (su(Hw)attP1) /* *R57C10-Gal4 (attP2)*	
2.1D, S2.1B, S2.1C, MovieS1	PanNeuronal / GCaMP6s	None	*20XUAS-IVS-Syn21-OpGCaMP6s-p10 (su(Hw)attP8) / w;* *cn [1], bw [1];* *20XUAS-IVS-Syn21-OpGCaMP6s-p10 (su(Hw)attP1), 20XUAS-myr::tdTomato (VK00033)/R57C10-Gal4 (attP2)*	tdTOM not used for analysis
2.2B, S2.2B, S2.2C, S2.2D, S2.2E	Astrocytic Glia / GCaMP6s; PanNeuronal / RCaMP1b	None	*20XUAS-IVS-Syn21-OpGCaMP6s-p10 (su(Hw)attP8)/w;* *R57C10-lexA (attP40), 13XLexAop2-IVS-NES-jRCaMP1b (VK00005) / alrm-Gal4.D.3;* *20XUAS-IVS-Syn21-OpGCaMP6s-p10 (su(Hw)attP1) / alrm-Gal4.D.2*	
2.2C, S2.4C, MovieS3	L1 / iGluSnFR.A184V; L1 / RCaMP1b	None	*w;* *27G05-FLP (su(Hw)attP5), tubP-(FRT.GAL80) (attP40) / +;* *svp-GAL4 (87B5), 20X-UAS-IVS-NES-jRCaMP1b-p10 (VK00005) / 20XUAS-iGluSnFR.A184V (attP2)*	Expression domain constrained to L1 by removing GAL80 inhibition in lamina neurons
2.2D, S2.4C, MovieS4	L1 / ArcLight; L1 / RCaMP1b	None	*w;* *27G05-FLP (su(Hw)attP5), tubP-(FRT.GAL80) (attP40) / +;* *svp-GAL4 (87B5), 20X-UAS-IVS-NES-jRCaMP1b-p10 (VK00005) / UAS-ArcLight (attP2)*	Expression domain constrained to L1 by removing GAL80 inhibition in lamina neurons
2.2F, S2.5A, S2.5B	PanNeuronal / GCaMP6s	None	*norpA [36];* *cn[1], bw[1];* *UAS-CD4-tdTOM (VK00033), 20XUAS-IVS-Syn21-opGCaMP6s-p10 (su(Hw)attP1) /* *R57C10-Gal4 (attp2), 20XUAS-IVS-Syn21-opGCaMP6s-p10 (su(Hw)attP1)*	
2.3B, 2.3C, 2.3E, 2.3F, S2.6B, S2.7A, S2.7B, S2.7C, S2.7D,	L3 / GCaMP6s	None	*w;* *20XUAS-IVS-Syn21-opGCaMP6s-p10 (su(Hw)attP5) / tubP-(FRT.GAL80) (attP40), 27G05-FLP (su(Hw)attP5,51E);* *UAS-CD4-tdTOM (VK00033), 20XUAS-IVS-Syn21-opGCaMP6s-p10 (su(Hw)attP1) /* *R29F12-GAL4 (attP2) , 20XUAS-IVS-Syn21-opGCaMP6s-p10 (su(Hw)attP1)*	tdTOM not used for analysis

Used in Figure	Cells Imaged / Label	Cells Silenced / Effector	Fly Genotype	Notes
MovieS5, MovieS6				
2.3B-F, S2.6B, S2.6C, S2.7A-D, MovieS5, MovieS6	L1 / GCaMP6s	None	*w;* *20XUAS-IVS-Syn21-opGCaMP6s-p10 (su(Hw)attP5) / tubP-(FRT.GAL80) (attP40), 27G05-FLP (su(Hw)attP5,51E);* *UAS-CD4-tdTOM (VK00033), 20XUAS-IVS-Syn21-opGCaMP6s-p10 (su(Hw)attP1) / 20X-UAS-IVS-NES-jRCaMP1b-p10 (VK00005), svp-GAL4 (87B5)*	tdTOM or jRCaMP1b not used for analysis.
2.3B, 2.3E, 2.3F, S2.7C, S2.7D	Dm9 / GCaMP6s	None	*w;* *20XUAS-IVS-Syn21-opGCaMP6s-p10 (su(Hw)attP5) / Sp-Cyo;* *UAS-CD4-tdTOM (VK00033), 20XUAS-IVS-Syn21-opGCaMP6s-p10 (su(Hw)attP1) / VT025981.GAL4 (attP2)*	tdTOM not used for analysis
2.3B, 2.3E, 2.3F, 2.4A-F, S2.6B, S2.7C, S2.7D, S2.8C, MovieS7	Tm3 / GCaMP6s; T4,T5 / RCaMP1b	None	*w;* *R13E12-LexA (attP40), 13XLexAop2-IVS-Syn21-OpGCaMP6s-p10 (su(Hw)attP5);* *R23G12-GAL4 (attP2), 20X-UAS-IVS-NES-jRCaMP1b-p10 (VK00005)*	
2.3B, 2.3E, 2.3F, 2.4E, 2.4F, S2.6B, S2.7C, S2.7D, S2.8C	T4,T5 / GCaMP6s; Tm3 / RCaMP1b	None	*R23G12-LexA (su(Hw)attP8)/+;* *13XLexAop2-IVS-Syn21-OpGCaMP6s-p10 (su(Hw)attP5) / Bl-Cyo;* *R13E12-GAL4 (attP2), 20X-UAS-IVS-NES-jRCaMP1b-p10 (VK00005)*	
2.3B, 2.3E, 2.3F, 2.4E, S2.6B, S2.7C, S2.7D	Mi1 / GCaMP6s; T4 / RCaMP1b	None	*w;* *R89C04-LexA (attP40), 13XLexAop2-IVS-Syn21-OpGCaMP6s-p10 (su(Hw)attP5);* *R23G12-GAL4 (attP2), 20X-UAS-IVS-NES-jRCaMP1b-p10 (VK00005)*	
2.3B, 2.3E, 2.3F, 2.4E, S2.6B, S2.7C, S2.7D	Dm4 / GCaMP6s; L3 / RCaMP1b	None	w; R75F06-LexA (attp40), 13XLexAop2-IVS-Syn21-OpGCaMP6s-p10 (su(Hw)attP5) / 13XLexAop2-IVS-Syn21-OpGCaMP6s-p10 (su(Hw)attP5); R29F12-GAL4 (attP2), 20X-UAS-IVS-NES-jRCaMP1b-p10 (VK00005)	
2.3B, 2.3E, 2.3F, 2.4E, S2.6B, S2.7C, S2.7D, MovieS6	Mi1 / GCaMP6s; Tm3 / RCaMP1b	None	*w;* *R89C04-LexA (attP40), 13XLexAop2-IVS-Syn21-OpGCaMP6s-p10 (su(Hw)attP5);* *R13E12-GAL4 (attP2), 20X-UAS-IVS-NES-jRCaMP1b-p10 (VK00005)*	
2.3B, 2.3E, 2.3F, 2.4E, S2.6B, S2.7C-D, S2.8A, MovieS6	Tm3 / GCaMP6s; Tm3 / RCaMP1b	None	*w;* *R13E12-LexA (attP40), 13XLexAop2-IVS-Syn21-OpGCaMP6s-p10 (su(Hw)attP5);* *R13E12-GAL4 (attP2), 20X-UAS-IVS-NES-jRCaMP1b-p10 (VK00005)*	
2.3B, 2.3E, 2.3F, S2.7C-D, MovieS6	Dm9 / GCaMP6s	None	*w;* *20XUAS-IVS-Syn21-opGCaMP6s-p10 (su(Hw)attP5) / Sp-Cyo;* *UAS-CD4-tdTOM (VK00033), 20XUAS-IVS-Syn21-opGCaMP6s-p10 (su(Hw)attP1) /*	tdTOM not used for analysis

Used in Figure	Cells Imaged / Label	Cells Silenced / Effector	Fly Genotype	Notes
			R56G04-GAL4 (attP2)	
2.3B, 2.3E, 2.3F, S2.7C-D, MovieS6	Dm3 / GCaMP6s	None	*w;* *20XUAS-IVS-Syn21-opGCaMP6s-p10 (su(Hw)attP5) / Sp-Cyo;* *UAS-CD4-tdTOM (VK00033), 20XUAS-IVS-Syn21-opGCaMP6s-p10 (su(Hw)attP1) / R25F07-GAL4 (attP2)*	
2.3B, 2.3E, 2.3F, S2.7C-D, MovieS6	R7 / GCaMP6s	None	*w;* *20XUAS-IVS-Syn21-opGCaMP6s-p10 (su(Hw)attP5) / sevEP-GAL4.B ;* *UAS-CD4-tdTOM (VK00033), 20XUAS-IVS-Syn21-opGCaMP6s-p10 (su(Hw)attP1) / +*	
2.3B, 2.3E, 2.3F, S2.7C-D, MovieS6	R8 / GCaMP6s; (Dm9 / RCaMP1b)	None	*sens-R.pest (su(Hw)attP8) / 13xLexAop2-IVS-Syn21-opGCaMP6s-p10 (su(Hw)attP8);* *brp(RSRT.Stop)V5-2A-LexA-VP16 (VK00003b), 13XLexAop2-IVS-Syn21-OpGCaMP6s-p10 (su(Hw)attP5) / 13XLexAop2-IVS-Syn21-OpGCaMP6s-p10 (su(Hw)attP5);* *VT025981.GAL4 (attP2), 20X-UAS-IVS-NES-jRCaMP1b-p10 (VK00005) / 20X-UAS-IVS-NES-jRCaMP1b-p10 (VK00005)*	Dm9->RCaMP1b signal low; channel not analyzed.
2.3B, 2.3E, 2.3F, S2.7C-D, MovieS6	Tm9 / GCaMP6s	None	*w;* *20XUAS-IVS-Syn21-opGCaMP6s-p10 (su(Hw)attP5) / Bl-Cyo;* *UAS-CD4-tdTOM (VK00033), 20XUAS-IVS-Syn21-opGCaMP6s-p10 (su(Hw)attP1) / R25F10-GAL4 (attP2)*	cell type-specific expression in the lobula
2.3B, 2.3E, 2.3F, S2.6A-B, S2.7C-D, MovieS6	T4,T5 / GCaMP6s	None	*20XUAS-IVS-Syn21-opGCaMP6s-p10 (su(Hw)attP8) / w;* *cn[1], bw[1];* *UAS-CD4-tdTOM (VK00033), 20XUAS-IVS-Syn21-opGCaMP6s-p10 (su(Hw)attP1) / R23G12-GAL4 (attP2)*	tdTOM not used for analysis
2.3B, 2.3E, 2.3F, S2.7C-D, MovieS6	Mi1 / GCaMP6s	None	*w;* *20XUAS-IVS-Syn21-opGCaMP6s-p10 (su(Hw)attP5) / R55C05-p65ADZp (attP40);* *UAS-CD4-tdTOM (VK00033), 20XUAS-IVS-Syn21-opGCaMP6s-p10 (su(Hw)attP1) / R71D01-ZpGdbd (attP2)*	tdTOM not used for analysis
2.3B, 2.3E, 2.3F, S2.7C-D, MovieS6	Mi4 / GCaMP6s	None	*w;* *20XUAS-IVS-Syn21-opGCaMP6s-p10 (su(Hw)attP5) / +;* *UAS-CD4-tdTOM (VK00033), 20XUAS-IVS-Syn21-opGCaMP6s-p10 (su(Hw)attP1) / R49B06-GAL4 (attP2)*	tdTOM not used for analysis
2.3B, 2.3E, 2.3F, S2.7C-D, MovieS6	Mi4 / GCaMP6s	None	*w;* *R49B06-LexA (attP40), 13XLexAop2-IVS-Syn21-OpGCaMP6s-p10 (su(Hw)attP5);* *R23G12-GAL4 (attP2), 20X-UAS-IVS-NES-jRCaMP1b-p10 (VK00005)*	RCaMP1b not used in Mi4 analysis
2.3B, 2.3E, 2.3F, S2.7C-D, MovieS6	Tm3 / GCaMP6s	None	*w;* *20XUAS-IVS-Syn21-opGCaMP6s-p10 (su(Hw)attP5) / Bl-Cyo;* *UAS-CD4-tdTOM (VK00033), 20XUAS-IVS-Syn21-opGCaMP6s-p10 (su(Hw)attP1) / R13E12-GAL4 (attP2)*	
2.3B, 2.3E, 2.3F, S2.7C-D, MovieS6	L3 / GCaMP6s	None	*27G05-FLP1 (attP18) / w;* *20XUAS-IVS-Syn21-opGCaMP6s-p10 (su(Hw)attP5) / tubP-(FRT.GAL80) (attP40);* *20XUAS-IVS-Syn21-opGCaMP6s-p10 (su(Hw)attP1) / UAS-CD4-tdTOM (VK00033), R9D03-GAL4 (attP2)*	Expression domain constrained to L3 by removing GAL80 inhibition in

Used in Figure	Cells Imaged / Label	Cells Silenced / Effector	Fly Genotype	Notes
				lamina neurons; tdTOM not used for analysis.
2.3B, 2.3E, 2.3F, S2.7C-D, MovieS6	Dm4 / GCaMP6s	None	*w;* *20XUAS-IVS-Syn21-opGCaMP6s-p10 (su(Hw)attP5) / Sp-Cyo;* *UAS-CD4-tdTOM (VK00033), 20XUAS-IVS-Syn21-opGCaMP6s-p10 (su(Hw)attP1) / R75F06-GAL4 (attP2)*	
2.3B, 2.3E, 2.3F, S2.6B-C, S2.7C-D, MovieS6	L5 / GCaMP6s	None	*w;* *20XUAS-IVS-Syn21-opGCaMP6s-p10 (su(Hw)attP5) / tubP-(FRT.GAL80) (attP40), 27G05-FLP (su(Hw)attP5);* *UAS-CD4-tdTOM (VK00033), 20XUAS-IVS-Syn21-opGCaMP6s-p10 (su(Hw)attP1) / 6-60-GAL4*	Expression domain constrained to L5 by removing GAL80 inhibition in lamina neurons; tdTOM not used for analysis.
2.3B, 2.3E, 2.3F, S2.6A, S2.7C-D, MovieS6	Tm9 / GCaMP6s	None	*w;* *20XUAS-IVS-Syn21-opGCaMP6s-p10 (su(Hw)attP5) / +;* *UAS-CD4-tdTOM (VK00033), 20XUAS-IVS-Syn21-opGCaMP6s-p10 (su(Hw)attP1) / R24C08-GAL4 (attP2)*	
2.3B, 2.3E, 2.3F, S2.7C-D, MovieS6	Tm4 / GCaMP6s; T5 / RCaMP1b	None	*13XLexAop2-IVS-Syn21-OpGCaMP6sp10 (su(Hw)attP8);* *R35H01-LexA (attP40);* *R23G12-GAL4 (attP2), 20XUAS-IVS-NES-jRCaMP1b-p10 (VK00005)*	
2.4E	Tm3 / GCaMP6s; L1 / RCaMP1b	None	13XLexAop2-IVS-Syn21-OpGCaMP6sp10 (su(Hw)attP8) / w; tubP-(FRT.GAL80) (attP40), 27G05-FLP (su(Hw)attP5) / R13E12-LexA (attP40), 13XLexAop2-IVS-Syn21-OpGCaMP6s-p10 (su(Hw)attP5); 20X-UAS-IVS-NES-jRCaMP1b-p10 (VK00005), svp-GAL4 (87B5) / 20X-UAS-IVS-NES-jRCaMP1b-p10 (VK00005)	
2.4F	T4,T5 / GCaMP6s; Tm3 / RCaMP1b	Tm3 (Gal4) / tnt	*R23G12-LexA (su(Hw)attP8)/+;* *13XLexAop2-IVS-Syn21-OpGCaMP6s-p10 (su(Hw)attP5) / UAS-TeTxLC.tnt;* *R13E12-GAL4 (attP2), 20X-UAS-IVS-NES-jRCaMP1b-p10 (VK00005)*	
2.4F	Tm3 / GCaMP6s; T4,T5 / RCaMP1b	T4,T5 (Gal4) / tnt	*UAS-TeTxLC.tnt, w;* *R13E12-LexA (attP40), 13XLexAop2-IVS-Syn21-OpGCaMP6s-p10 (su(Hw)attP5);* *R23G12-GAL4 (attP2), 20X-UAS-IVS-NES-jRCaMP1b-p10 (VK00005)*	
S2.4A	PanNeuronal / iGluSnFR.A184V; PanNeuronal / RCaMP1b	None	*w;* *+;* *svp-GAL4 (87B5), 20X-UAS-IVS-NES-jRCaMP1b-p10 (VK00005) / 20XUAS-iGluSnFR.A184V (attp2)*	
S2.4B	PanNeuronal / ArcLight; PanNeuronal / RCaMP1b	None	*w;* *+;* *R57C10-Gal4 (attP2), 20X-UAS-IVS-NES-jRCaMP1b-p10 (VK00005) / UAS-ArcLight (attP2)*	

Used in Figure	Cells Imaged / Label	Cells Silenced / Effector	Fly Genotype	Notes
S2.5B, S2.5C, S2.5D, S2.5E	PanNeuronal / GCaMP6s	None	*w, norpA[36]/Y;* *20XUAS-IVS-Syn21-opGCaMP6s-p10 (su(Hw)attP5) / +;* *UAS-CD4-tdTOM (VK00033), 20XUAS-IVS-Syn21-opGCaMP6s-p10 (su(Hw)attP1) / R57C10-Gal4 (attp2)*	hemizygous for norpA[36]
S2.5B, S2.5C, S2.5D, S2.5E	PanNeuronal / GCaMP6s	None	*w, norpA[36]/w;* *20XUAS-IVS-Syn21-opGCaMP6s-p10 (su(Hw)attP5) / +;* *UAS-CD4-tdTOM (VK00033), 20XUAS-IVS-Syn21-opGCaMP6s-p10 (su(Hw)attP1) / R57C10-Gal4 (attp2)*	heterozygous for norpA[36]
S2.5A, S2.5B	PanNeuronal / GCaMP6s	None	*w;* *R57C10-lexA (attp40), 13XLexAop2-IVS-Syn21-OpGCaMP6s-p10 (su(Hw)attP5) / 13XLexAop2-IVS-Syn21-OpGCaMP6s-p10 (su(Hw)attP5);* *ort[1]*	homozygous for ort[1]
S2.5B	PanNeuronal / GCaMP6s	None	*w;* *R57C10-lexA (attp40), 13XLexAop2-IVS-Syn21-OpGCaMP6s-p10 (su(Hw)attP5) / 13XLexAop2-IVS-Syn21-OpGCaMP6s-p10 (su(Hw)attP5);* *ort[1] / +*	heterozygous for ort[1]
S2.5A, S2.5B	PanNeuronal / GCaMP6s	None	*w;* *Hdc[JK910] / Hdc[MB07212] ;* *R57C10-Gal4 (attp2), 20XUAS-IVS-Syn21-opGCaMP6s-p10 (su(Hw)attP1) / 20XUAS-IVS-Syn21-opGCaMP6s-p10 (su(Hw)attP1)*	heteroallelic null for Hdc
S2.5B	PanNeuronal / GCaMP6s	None	*w;* *+ / Hdc[MB07212] ;* *R57C10-Gal4 (attp2), 20XUAS-IVS-Syn21-opGCaMP6s-p10 (su(Hw)attP1) / 20XUAS-IVS-Syn21-opGCaMP6s-p10 (su(Hw)attP1)*	heterozygous for Hdc[MB07212]

2.8. REFERENCES

Ackman, J.B., and Crair, M.C. (2014). Role of emergent neural activity in visual map development. Curr. Opin. Neurobiol. 24, 166–175.

Ackman, J.B., Burbridge, T.J., and Crair, M.C. (2012). Retinal waves coordinate patterned activity throughout the developing visual system. Nature 490, 219–225.

Akin, O., and Zipursky, S.L. (2016). Frazzled promotes growth cone attachment at the source of a Netrin gradient in the Drosophila visual system. eLife 5.

Akrouh, A., and Kerschensteiner, D. (2013). Intersecting circuits generate precisely patterned retinal waves. Neuron 79, 322–334.

Aptekar, J.W., Keles, M.F., Mongeau, J.-M., Lu, P.M., Frye, M.A., and Shoemaker, P.A. (2014). Method and software for using m-sequences to characterize parallel components of higher-order visual tracking behavior in Drosophila. Front. Neural Circuits 8, 130.

Baines, R.A., and Bate, M. (1998). Electrophysiological Development of Central Neurons in the Drosophila Embryo. J. Neurosci. 18, 4673–4683.

Bansal, A., Singer, J.H., Hwang, B.J., Xu, W., Beaudet, A., and Feller, M.B. (2000). Mice lacking specific nicotinic acetylcholine receptor subunits exhibit dramatically altered spontaneous activity patterns and reveal a limited role for retinal waves in forming ON and OFF circuits in the inner retina. J. Neurosci. Off. J. Soc. Neurosci. 20, 7672–7681.

Behnia, R., Clark, D.A., Carter, A.G., Clandinin, T.R., and Desplan, C. (2014). Processing properties of ON and OFF pathways for Drosophila motion detection. Nature 512, 427–430.

Ben-Ari, Y., Cherubini, E., Corradetti, R., and Gaiarsa, J.L. (1989). Giant synaptic potentials in immature rat CA3 hippocampal neurones. J. Physiol. 416, 303–325.

Blankenship, A.G., and Feller, M.B. (2009). Mechanisms underlyingspontaneous patterned activityin developing neural circuits. Nat. Rev. Neurosci. 11, 18–29.

Bloomquist, B.T., Shortridge, R.D., Schneuwly, S., Perdew, M., Montell, C., Steller, H., Rubin, G., and Pak, W.L. (1988). Isolation of a putative phospholipase C gene of Drosophila, norpA, and its role in phototransduction. Cell 54, 723–733.

Brand, A.H., and Perrimon, N. (1993). Targeted gene expression as a means of altering cell fates and generating dominant phenotypes. Development 118, 401–415.

Burbridge, T.J., Xu, H.-P., Ackman, J.B., Ge, X., Zhang, Y., Ye, M.-J., Zhou, Z.J., Xu, J., Contractor, A., and Crair, M.C. (2014). Visual Circuit Development Requires Patterned Activity Mediated by Retinal Acetylcholine Receptors. Neuron 84, 1049–1064.

Burg, M.G., Sarthy, P.V., Koliantz, G., and Pak, W.L. (1993). Genetic and molecular identification of a Drosophila histidine decarboxylase gene required in photoreceptor transmitter synthesis. EMBO J. 12, 911–919.

Cao, G., Platisa, J., Pieribone, V.A., Raccuglia, D., Kunst, M., and Nitabach, M.N. (2013). Genetically targeted optical electrophysiology in intact neural circuits. Cell 154, 904–913.

Carrillo, R.A., Olsen, D.P., Yoon, K.S., and Keshishian, H. (2010). Presynaptic Activity and CaMKII Modulate Retrograde Semaphorin Signaling and Synaptic Refinement. Neuron 68, 32–44.

Chen, T.-W., Wardill, T.J., Sun, Y., Pulver, S.R., Renninger, S.L., Baohan, A., Schreiter, E.R., Kerr, R.A., Orger, M.B., Jayaraman, V., et al. (2013). Ultrasensitive fluorescent proteins for imaging neuronal activity. Nature 499, 295–300.

Chen, Y., Akin, O., Nern, A., Tsui, C.Y.K., Pecot, M.Y., and Zipursky, S.L. (2014). NeuroResource. Neuron 81, 280–293.

Constance, W.D., Mukherjee, A., Fisher, Y.E., Pop, S., Blanc, E., Toyama, Y., and Williams, D.W. (2018). Neurexin and Neuroligin-based adhesion complexes drive axonal arborisation growth independent of synaptic activity. eLife 7.

Cutts, C.S., and Eglen, S.J. (2014). Detecting pairwise correlations in spike trains: an objective comparison of methods and application to the study of retinal waves. J. Neurosci. Off. J. Soc. Neurosci. 34, 14288–14303.

Dana, H., Mohar, B., Sun, Y., Narayan, S., Gordus, A., Hasseman, J.P., Tsegaye, G., Holt, G.T., Hu, A., Walpita, D., et al. (2016). Sensitive red protein calcium indicators for imaging neural activity. eLife 5.

Galli, L., and Maffei, L. (1988). Spontaneous impulse activity of rat retinal ganglion cells in prenatal life. Science 242, 90–91.

Gao, S., Takemura, S., Ting, C.-Y., Huang, S., Lu, Z., Luan, H., Rister, J., Thum, A.S., Yang, M., Hong, S.-T., et al. (2008). The Neural Substrate of Spectral Preference in Drosophila. Neuron 60, 328–342.

Gengs, C., Leung, H.-T., Skingsley, D.R., Iovchev, M.I., Yin, Z., Semenov, E.P., Burg, M.G., Hardie, R.C., and Pak, W.L. (2002). The target of Drosophila photoreceptor synaptic transmission is a histamine-gated chloride channel encoded by ort (hclA). J. Biol. Chem. 277, 42113–42120.

Hadjieconomou, D., Timofeev, K., and Salecker, I. (2011). A step-by-step guide to visual circuit assembly in Drosophila. Curr. Opin. Neurobiol. 21, 76–84.

Hardie, R.C. (1987). Is histamine a neurotransmitter in insect photoreceptors? J. Comp. Physiol. [A] 161, 201–213.

Hardie, R.C., Peretz, A., Pollock, J.A., and Minke, B. (1993). Ca2+ limits the development of the light response in Drosophila photoreceptors. Proc. Biol. Sci. 252, 223–229.

Hiesinger, P.R., Zhai, R.G., Zhou, Y., Koh, T.-W., Mehta, S.Q., Schulze, K.L., Cao, Y., Verstreken, P., Clandinin, T.R., Fischbach, K.-F., et al. (2006). Activity-Independent Prespecification of Synaptic Partners in the Visual Map of Drosophila. Curr. Biol. 16, 1835–1843.

Huang, Z., Shilo, B.Z., and Kunes, S. (1998). A retinal axon fascicle uses spitz, an EGF receptor ligand, to construct a synaptic cartridge in the brain of Drosophila. Cell 95, 693–703.

Jarecki, J., and Keshishian, H. (1995). Role of neural activity during synaptogenesis in Drosophila. J. Neurosci. Off. J. Soc. Neurosci. 15, 8177–8190.

Jin, L., Han, Z., Platisa, J., Wooltorton, J.R.A., Cohen, L.B., and Pieribone, V.A. (2012). Single action potentials and subthreshold electrical events imaged in neurons with a fluorescent protein voltage probe. Neuron 75, 779–785.

Joesch, M., Schnell, B., Raghu, S.V., Reiff, D.F., and Borst, A. (2010). ON and OFF pathways in Drosophila motion vision. Nature 468, 300–304.

Keleş, M.F., and Frye, M.A. (2017). Object-Detecting Neurons in Drosophila. Curr. Biol. 27, 680–687.

Kerschensteiner, D., and Wong, R.O.L. (2008). A precisely timed asynchronous pattern of ON and OFF retinal ganglion cell activity during propagation of retinal waves. Neuron 58, 851–858.

Kim, S., McKay, R.R., Miller, K., and Shortridge, R.D. (1995). Multiple Subtypes of Phospholipase C Are Encoded by the norpA Gene of Drosophila melanogaster. J. Biol. Chem. 270, 14376–14382.

Kirkby, L.A., Sack, G.S., Firl, A., and Feller, M.B. (2013). A Role for Correlated Spontaneous Activity in the Assembly of Neural Circuits. Neuron 80, 1129–1144.

Lai, S.-L., and Lee, T. (2006). Genetic mosaic with dual binary transcriptional systems in Drosophila. Nat. Neurosci. 9, 703–709.

Landmesser, L.T., and O'Donovan, M.J. (1984). Activation patterns of embryonic chick hind limb muscles recorded in ovo and in an isolated spinal cord preparation. J. Physiol. 347, 189–204.

Langen, M., Agi, E., Altschuler, D.J., Wu, L.F., Altschuler, S.J., and Hiesinger, P.R. (2015). The Developmental Rulesof Neural Superposition in Drosophila. Cell 162, 120–133.

Lee, P.R., Cohen, J.E., Iacobas, D.A., Iacobas, S., and Fields, R.D. (2017). Gene networks activated by specific patterns of action potentials in dorsal root ganglia neurons. Sci. Rep. 7, 43765.

Leo-GG (2017). Neuronal Cultures Characterization Tool for MEA recordings: Leo-GG/NeuroFun.

Maisak, M.S., Haag, J., Ammer, G., Serbe, E., Meier, M., Leonhardt, A., Schilling, T., Bahl, A., Rubin, G.M., Nern, A., et al. (2014). A directional tuning map of Drosophila elementary motion detectors. Nature 500, 212–216.

Marvin, J.S., Borghuis, B.G., Tian, L., Cichon, J., Harnett, M.T., Akerboom, J., Gordus, A., Renninger, S.L., Chen, T.-W., Bargmann, C.I., et al. (2013). An optimized fluorescent probe for visualizing glutamate neurotransmission. Nat. Methods 10, 162–170.

McLaughlin, T., Torborg, C.L., Feller, M.B., and O'Leary, D.D.M. (2003). Retinotopic map refinement requires spontaneous retinal waves during a brief critical period of development. Neuron 40, 1147–1160.

Meister, M., Wong, R.O., Baylor, D.A., and Shatz, C.J. (1991). Synchronous bursts of action potentials in ganglion cells of the developing mammalian retina. Science 252, 939–943.

Muthukumar, A.K., Stork, T., and Freeman, M.R. (2014). Activity-dependent regulation of astrocyte GAT levels during synaptogenesis. Nat. Publ. Group 17, 1340–1350.

Nakashima, A., Takeuchi, H., Imai, T., Saito, H., Kiyonari, H., Abe, T., Chen, M., Weinstein, L.S., Yu, C.R., Storm, D.R., et al. (2013). Agonist-independent GPCR activity regulates anterior-posterior targeting of olfactory sensory neurons. Cell 154, 1314–1325.

Nicol, X., Voyatzis, S., Muzerelle, A., Narboux-Nême, N., Südhof, T.C., Miles, R., and Gaspar, P. (2007). cAMP oscillations and retinal activity are permissive for ephrin signaling during the establishment of the retinotopic map. Nat. Neurosci. 10, 340–347.

Otsuna, H., and Ito, K. (2006). Systematic analysis of the visual projection neurons of Drosophila melanogaster. I. Lobula-specific pathways. J. Comp. Neurol. 497, 928–958.

Pearn, M.T., Randall, L.L., Shortridge, R.D., Burg, M.G., and Pak, W.L. (1996). Molecular, Biochemical, and Electrophysiological Characterization of Drosophila norpA Mutants. J. Biol. Chem. 271, 4937–4945.

Pecot, M.Y., Chen, Y., Akin, O., Chen, Z., Tsui, C.Y.K., and Zipursky, S.L. (2014). Sequential Axon-Derived Signals Couple Target Survival and Layer Specificityin the Drosophila Visual System. Neuron 82, 320–333.

Reiser, M.B., and Dickinson, M.H. (2008). A modular display system for insect behavioral neuroscience. J. Neurosci. Methods 167, 127–139.

Richier, B., de Miguel Vijandi, C., Mackensen, S., and Salecker, I. (2017). Lapsyn controls branch extension and positioning of astrocyte-like glia in the Drosophila optic lobe. Nat. Commun. 1–17.

Rivera-Alba, M., Vitaladevuni, S.N., Mishchenko, Y., Lu, Z., Takemura, S., Scheffer, L., Meinertzhagen, I.A., Chklovskii, D.B., and de Polavieja, G.G. (2011). Wiring Economy and Volume Exclusion Determine Neuronal Placementin the Drosophila Brain. Curr. Biol. 21, 2000–2005.

Sanes, J.R., and Masland, R.H. (2015). The Types of Retinal Ganglion Cells: Current Status and Implications for Neuronal Classification. Annu. Rev. Neurosci. 38, 221–246.

Sanes, J.R., and Zipursky, S.L. (2010). Design Principles of Insect and Vertebrate Visual Systems. Neuron 66, 15–36.

Schindelin, J., Arganda-Carreras, I., Frise, E., Kaynig, V., Longair, M., Pietzsch, T., Preibisch, S., Rueden, C., Saalfeld, S., Schmid, B., et al. (2012). Fiji: an open-source platform for biological-image analysis. Nat. Methods 9, 676–682.

Seelig, J.D., Chiappe, M.E., Lott, G.K., Dutta, A., Osborne, J.E., Reiser, M.B., and Jayaraman, V. (2010). Two-photon calcium imaging from head-fixed Drosophila during optomotor walking behavior. Nat. Methods 7, 535–540.

Serbe, E., Meier, M., Leonhardt, A., and Borst, A. (2016). Comprehensive Characterization of the Major Presynaptic Elements to the Drosophila OFF Motion Detector. Neuron 89, 829–841.

Serizawa, S., Miyamichi, K., Takeuchi, H., Yamagishi, Y., Suzuki, M., and Sakano, H. (2006). A neuronal identity code for the odorant receptor-specific and activity-dependent axon sorting. Cell 127, 1057–1069.

Sernagor, E., and Hennig, M.H. (2013). Retinal Waves: underlying cellular mechanisms and theoretical considerations. In Comprehensive Developmental Neuroscience: Cellular Migration and Formation of Neuronal Connections, ed Rubenstein JLR & Rakic P, pp. 909–920, Academic Press, Amsterdam.

Seung, H.S., and Sümbül, U. (2014). Neuronal cell types and connectivity: lessons from the retina. Neuron 83, 1262–1272.

Shatz, C.J., and Stryker, M.P. (1988). Prenatal tetrodotoxin infusion blocks segregation of retinogeniculate afferents. Science 242, 87–89.

Shinomiya, K., Karuppudurai, T., Lin, T.-Y., Lu, Z., Lee, C.-H., and Meinertzhagen, I.A. (2014). Candidate Neural Substrates for Off-Edge Motion Detection in Drosophila. Curr. Biol. 24, 1062–1070.

Sretavan, D.W., Shatz, C.J., and Stryker, M.P. (1988). Modification of retinal ganglion cell axon morphology by prenatal infusion of tetrodotoxin. Nature 336, 468–471.

Strother, J.A., Wu, S.-T., Wong, A.M., Nern, A., Rogers, E.M., Le, J.Q., Rubin, G.M., and Reiser, M.B. (2017). The Emergence of Directional Selectivity in the Visual Motion Pathway of Drosophila. Neuron 94, 168–182.e10.

Takemura, S., Karuppudurai, T., Ting, C.-Y., Lu, Z., Lee, C.-H., and Meinertzhagen, I.A. (2011). Cholinergic circuits integrate neighboring visual signals in a Drosophila motion detection pathway. Curr. Biol. CB 21, 2077–2084.

Takemura, S., Bharioke, A., Lu, Z., Nern, A., Vitaladevuni, S., Rivlin, P.K., Katz, W.T., Olbris, D.J., Plaza, S.M., Winston, P., et al. (2013). A visual motion detection circuit suggested by Drosophila connectomics. Nature 500, 175–181.

Takemura, S., Nern, A., Chklovskii, D.B., Scheffer, L.K., Rubin, G.M., and Meinertzhagen, I.A. (2017). The comprehensive connectome of a neural substrate for "ON" motion detection in Drosophila. eLife 6.

Tan, L., Zhang, K.X., Pecot, M.Y., Nagarkar-Jaiswal, S., Lee, P.-T., Takemura, S.-Y., McEwen, J.M., Nern, A., Xu, S., Tadros, W., et al. (2015). Ig Superfamily Ligand and Receptor Pairs Expressed in Synaptic Partners in Drosophila. Cell 163, 1756–1769.

Thimann, K.V., and Beadle, G.W. (1937). Development of the Eye Colors in Drosophila: Extraction of the Diffusible Substances Concerned. Proc. Natl. Acad. Sci. U. S. A. 23, 143–146.

Tritsch, N.X., Yi, E., Gale, J.E., Glowatzki, E., and Bergles, D.E. (2007). The origin of spontaneous activity in the developing auditory system. Nature 450, 50–55.

Tyssowski, K.M., DeStefino, N.R., Cho, J.-H., Dunn, C.J., Poston, R.G., Carty, C.E., Jones, R.D., Chang, S.M., Romeo, P., Wurzelmann, M.K., et al. (2018). Different Neuronal Activity Patterns Induce Different Gene Expression Programs. Neuron 98, 530–546.e11.

Uhlén, P. (2004). Spectral analysis of calcium oscillations. Sci. STKE 2004, pl15.

Vonhoff, F., and Keshishian, H. (2016). Cyclic nucleotide signaling is required during synaptic refinement at the Drosophilaneuromuscular junction. Dev. Neurobiol. 77, 39–60.

Watt, A.J., Cuntz, H., Mori, M., Nusser, Z., Sjöström, P.J., and Häusser, M. (2009). Traveling waves in developing cerebellar cortex mediated by asymmetrical Purkinje cell connectivity. Nat. Neurosci. 12, 463–473.

Weir, P.T., Henze, M.J., Bleul, C., Baumann-Klausener, F., Labhart, T., and Dickinson, M.H. (2016). Anatomical Reconstruction and Functional Imaging Reveal an Ordered Array of Skylight Polarization Detectors in Drosophila. J. Neurosci. 36, 5397–5404.

Wu, M., Nern, A., Williamson, W.R., Morimoto, M.M., Reiser, M.B., Card, G.M., and Rubin, G.M. (2016). Visual projection neurons in the Drosophila lobula link feature detection to distinct behavioral programs. eLife 5.

Xu, H.P., Burbridge, T.J., Ye, M., Chen, M., Ge, X., Zhou, Z.J., and Crair, M.C. (2016). Retinal Wave Patterns Are Governed by Mutual Excitation among Starburst Amacrine Cells and Drive the Refinement and Maintenance of Visual Circuits. J. Neurosci. 36, 3871–3886.

Zhang, K.X., Tan, L., Pellegrini, M., Zipursky, S.L., and McEwen, J.M. (2016). Rapid Changes in the Translatome during the Conversion of Growth Cones to Synaptic Terminals. Cell Reports 14, 1258–1271.

Zheng, J., Lee, S., and Zhou, Z.J. (2006). A transient network of intrinsically bursting starburst cells underlies the generation of retinal waves. Nat. Neurosci. 9, 363–371.

Zheng, J.-J., Lee, S., and Zhou, Z.J. (2004). A developmental switch in the excitability and function of the starburst network in the mammalian retina. Neuron 44, 851–864.

Chapter 3

Synaptic development depends on brain-wide activity coordinated by a discrete neuronal subpopulation

ABSTRACT

Developmental activity accompanies neural circuit assembly. How broadly this activity is coordinated across disparate brain regions is unknown. Similarly, the contribution of patterned activity to synaptic development at the level of defined cell types remains an open question. Here we show that neurons expressing the cation channel Trpγ relay and pattern developmental activity throughout the *Drosophila* brain. In *trpγ* mutants, activity is attenuated globally, and both patterns of activity and synapse structure are altered in a cell-type-specific fashion. Less than 2% of the neurons in the brain express Trpγ. These neurons arborize throughout the brain, and silencing or activating them leads to loss or gain of brain-wide activity. We propose that, in *Drosophila,* developmental activity is driven by a genetically-specified network to instruct circuit assembly.

3.1. INTRODUCTION

Understanding how specific synaptic connections are established during development is a fundamental challenge in neurobiology. During circuit formation, stimulus-independent neural activity is known to contribute to synapse development. Such developmental activity has been observed throughout the developing central nervous system (CNS) (Blankenship and Feller, 2010; Ackman and Crair, 2014). For example, retinal waves initiate in the eye, propagate to higher-order visual centers(Galli and Maffei, 1988; Meister et al., 1991; Ackman et al., 2012), and contribute to eye-specific segregation and refinement of retinotopy (Bansal et al., 2000; Burbridge et al., 2014; McLaughlin et al., 2003).

The integration of different visual centers with activity raises the possibility of broader coordination of circuit assembly across other interconnected regions of the brain through developmental activity. The size and complexity of vertebrate models pose challenges to exploring this question of scale. Notably, the same challenges have also checked progress at the cellular level, where our understanding of the role of activity on cell-type-specific synaptic development remains limited.

We recently showed that activity accompanies the development of the adult nervous system in *Drosophila melanogaster* (Akin et al., 2019), challenging the long-held view that neural circuit assembly in invertebrates occurs independently of activity (Sugie et al., 2018; Hiesinger et al., 2006). The adult CNS of the fly is built during the 100 hours of pupal development; synapse formation takes place in the latter half of this period,(Chen et al., 2014; Muthukumar et al., 2014). Patterned, stimulus-independent neuronal activity (PSINA, '*see-nah*') coincides with synaptogenesis, starting at ~50 hours after puparium formation (hAPF) (Akin et al., 2019). The entire CNS participates in PSINA, which is characterized by periodic active and

silent phases coordinated throughout the brain (**Figure 3.1A**). Each active phase consists of multiple bouts of neural activity, termed *sweeps*. PSINA evolves from a *periodic stage* with regular active phases to a more irregular *turbulent stage* at ~70 hAPF. The brain-wide coordination of PSINA suggests a global mechanism that contrasts with existing models of local activity initiation (Blankenship and Feller, 2010).

We have previously characterized PSINA in the visual system (Akin et al., 2019), which contains three neuropils: the lamina, medulla, and lobula complex. Each of the optic neuropils is organized by columns, which are repetitive, retinotopic relays that map the input from the compound eye, and by distinct layers where different visual circuits make connections. The synaptic connectivity of the >100 cell types populating these neuropils has been mapped by dense electron microscopic (EM) reconstruction (Takemura et al., 2013). Visual system neurons participate in PSINA with individualized activity patterns that reflect adult connectivity, suggesting that PSINA may play a role in synapse formation in a cell-type-specific manner.

Here we report that a population of neurons that express the cation channel transient receptor potential gamma (Trpγ) is necessary for the patterning and propagation of PSINA throughout the brain. Disruption of PSINA through the *trpγ* mutation leads to altered synapse count in visual processing neurons, indicating that activity contributes to synaptogenesis in a cell-type-specific manner. These results provide insight into the regulation of developmental activity and establish a role for stimulus-independent activity in synapse development.

3.2. *TRPγ* IS NECESSARY AND SUFFICIENT FOR WILDTYPE PSINA

Through a targeted screen, we found that PSINA is attenuated in mutants of *trpγ*. In mutant pupae expressing GCaMP6s (Chen et al., 2013) in pan-neuronal fashion (**Figure 3.1B,C, Supplementary Figure 3.1A**), PSINA amplitude is reduced during the periodic stage (55-65 hAPF, 45±12% at 60 hAPF) and the turbulent stage (70 hAPF through eclosion, 73±20% at 75 hAPF) relative to heterozygous controls (**Figure 3.1B-E, Supplementary Figure 3.1A,B, Supplementary movie 8**). By contrast, the number of sweeps per active phase increases by up to two-fold (**Figure 3.1E, Supplementary Figure 3.1A,B**). The duration or frequency of cycles does not change significantly (**Supplementary Figure 3.1C**). Genetic complementation analysis carried out with a Trpγ enhancer trap ($Trp\gamma^{G4}$) (Akitake et al., 2015), a Drop-In allele ($Trp\gamma^{DropIn\text{-}TG4}$) (Kanca et al., 2019), and two deficiencies confirmed that the described PSINA phenotype is monogenic (**Supplementary Figure 3.1D,E**). Trpγ has been reported to interact with Trp and TrpL (Xu et al., 2000). *Trp* and *trpL* mutants did not have altered PSINA, and *trp+trpγ* or *trpL+trpγ* double mutants did not further attenuate PSINA (**Supplementary Figure 3.2**). These results indicate that *Trpγ* is necessary for wild-type PSINA.

The *Trpγ* gene produces three isoforms: -A, -B (Xu et al., 2000), and -D (Batut and Gingeras, 2013) (**Supplementary Figure 3.3A**). When expressed under $Trp\gamma^{G4}$, the common coding sequence of Trpγ-A/B rescues behavioral defects of *trpγ* mutant animals in the adult (Akitake et al., 2015). *Trpγ*-D was identified more recently in a high-throughput study of development-specific promoter use (Batut and Gingeras, 2013). Compared to -A/B, Trpγ-D has an extra 60 aa N-terminal leader sequence and has not been previously studied. $Trp\gamma^{G4}$-driven expression of Trpγ-D results in complete rescue of PSINA in a dose-dependent manner (**Figure 3.1D, Supplementary Figure 3.3B,C**). Driving Trpγ-D with the independently generated

Trpγ$^{DropIn\text{-}TG4}$ allele produces similar results (**Supplementary Figure 3.3B,C**), confirming the efficacy of these transgenic reagents in capturing the *Trpγ* expression domain (i.e. Trpγ+ cells). By contrast to Trpγ-D, Trpγ-A/B does not rescue sweep dynamics, and combined expression of Trpγ-A/B and -D results in a neomorphic phenotype (**Supplementary Figure 3.3B,C**). These results indicate that the Trpγ-D isoform, expressed in Trpγ+ cells, is sufficient for wild-type PSINA.

To establish when Trpγ-D is required, we used the TARGET system (McGuire et al., 2003) to control the timing of Trpγ-D expression (**Figure 3.1F, Supplementary Figure 3.3**). Expression of Trpγ-D throughout development up to the onset of PSINA does not rescue the mutant phenotype (**Figure 3.1G,H**). By contrast, the reciprocal expression control scheme leads to rescue that is comparable to constitutive Trpγ-D expression (**Figure 3.1I,J**).

We conclude that Trpγ-D expression in Trpγ+ cells during the second half of pupal development is necessary and sufficient for wild-type PSINA.

Figure 3.1.

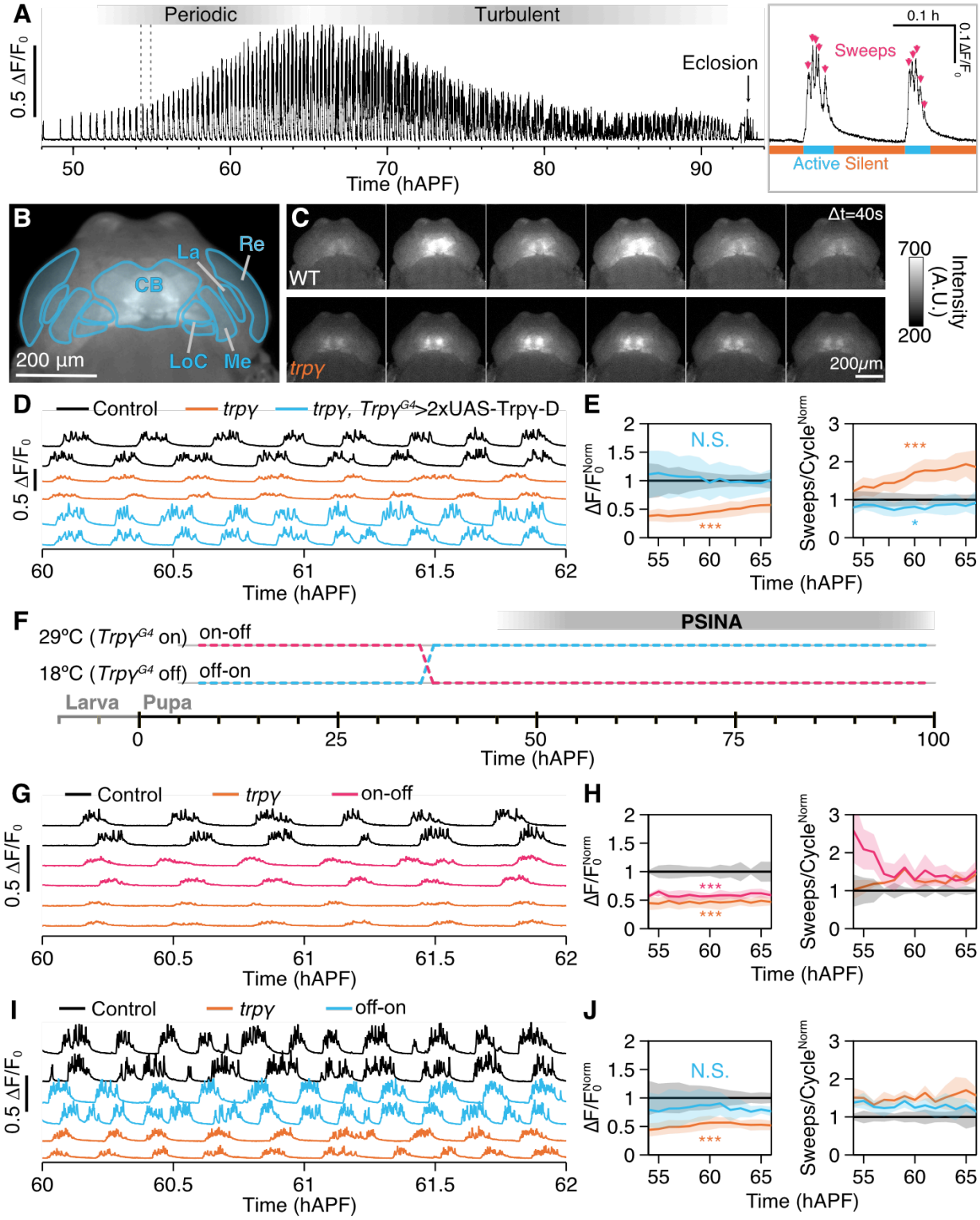
A
Periodic
Turbulent
Eclosion
0.5 ΔF/F0
50
60
70
80
90
Time (hAPF)
0.1 h
0.1ΔF/F0
Sweeps
Active Silent
B
La
Re
CB
LoC
Me
200 µm
C
Δt=40s
WT
trpγ
200µm
700
Intensity (A.U.)
200
D
Control
trpγ
trpγ, TrpγG4>2xUAS-Trpγ-D
0.5 ΔF/F0
60
60.5
61
61.5
62
Time (hAPF)
E
N.S.
***
*
ΔF/F0Norm
Sweeps/CycleNorm
55
60
65
Time (hAPF)
F
PSINA
29°C (TrpγG4 on)
on-off
18°C (TrpγG4 off)
off-on
Larva
Pupa
0
25
50
75
100
Time (hAPF)
G
Control
trpγ
on-off
0.5 ΔF/F0
60
60.5
61
61.5
62
Time (hAPF)
H
***
***
ΔF/F0Norm
Sweeps/CycleNorm
55
60
65
Time (hAPF)
I
Control
trpγ
off-on
0.5 ΔF/F0
60
60.5
61
61.5
62
Time (hAPF)
J
N.S.
***
ΔF/F0Norm
Sweeps/CycleNorm
55
60
65
Time (hAPF)

Figure 3.1. *Trpγ* is necessary for control PSINA.

A. Representative trace of PSINA, recorded with wide-field fluorescence imaging from pupa expressing pan-neuronal GCaMP6s. This animal eclosed at ~93 hAPF. Dotted lines mark limits of inset trace with two cycles (right). Arrows (magenta) mark individual sweeps; bars mark active (cyan) and silent (orange) phases. **B.** Average intensity projection (AIP) from wide-field fluorescence series of a pupa expressing pan-neuronal GCaMP6s. CB, central brain. La, lamina. Re, retina. LoC, lobula complex. Me, medulla. Scale bar, 200μm. **C.** Panels span one active phase at 60 hAPF in control (top), and *trpγ* mutant pupae (bottom). Frames ~40 seconds apart. Scale bar, 200μm. **D.** PSINA traces in control (black, n=19), *trpγ* (orange, n=31), and *trpγ, $Trp\gamma^{G4}$>* 2xUAS-Trpγ-D (cyan, n=4) animals. **E.** Active phase average amplitude (left) and sweeps/cycle (right) binned by hour and normalized to control. Shaded areas, standard deviation (SD). Genotypes color-matched to D. **F.** Expression control of UAS-Trpγ-D with TARGET (i.e. GAL80ts); temperature shift at 36 hAPF. **G.** PSINA traces in control (black, n=8), *trpγ* (orange, n=8), and 'on-off' pupae (magenta, n=5). **H.** Same as E. Genotypes color-matched to G. **I.** PSINA traces in control (black, n=3), *trpγ* (orange, n=3), and 'off-on' pupae (cyan, n=3). **J.** Same as E. Genotypes color-matched to I. Throughout figure, *, $p<0.05$; **, $p<0.01$; ***, $p<0.001$ by Welch's t-test following Shapiro-Wilk test, tested against control at 60 hAPF.

3.3. VISUAL PROCESSING NEURON ACTIVITY PATTERNS ARE *TRPγ*-DEPENDENT.

To characterize the *trpγ* phenotype at the level of cell types, we followed PSINA in the visual system of developing pupae using two-photon microscopy (2PM) (Akin and Zipursky, 2016). We focused on 10 cell types (**Figure 3.2A**), representing major classes of visual processing neurons, including lamina monopolar neurons (L1, L3, L5), medulla intrinsic neurons (Mi1, Mi4), transmedullary neurons (Tm3, Tm4, Tm9), and T4/5 neurons. At the population level, cells of a type begin the periodic stage of PSINA (55-65 hAPF) with fewer cycles per hour in the mutant; the cycle frequency gradually becomes comparable to wild-type (**Figure 3.2B**). While active phase duration of these cycles are similar across wild-type and mutant flies, the sweep count per cycle is higher in the *trpγ* background (**Figure 3.2B**), consistent with pan-neuronal trends (**Supplementary Figure 3.1A**).

At the cellular level, visual system neurons display cell-type-specific PSINA dynamics ranging from synchronous bursts of activity to wave-like patterns (Akin et al., 2019). To compare activity across cell types and genotypes, we previously developed two scalar metrics: *Coordination* is the average of the fraction of cells that participate in each sweep. *Coherence* is the largest fraction of cells that peak within the same time point, averaged over all sweeps (Akin et al., 2019). In the *trpγ* background, all cell types have higher coordination and nearly all cell types have lower coherence (**Figure 3.2C-H, Supplementary movie 9**). Lower coordination indicates that fewer cells of a type participate in each sweep, suggesting that the pan-neuronal loss of PSINA amplitude in mutant animals is due to reduced overall neuronal participation (**Figure 3.1D, E**). The opposite trend in coherence reports a shift away from wave-like activity propagation in favor of more synchronous populations. L5 is the lone exception to this trend in

coherence. Taken together, these results indicate that *Trpγ* is necessary for wild-type, cell-type-specific PSINA dynamics in visual processing neurons.

Figure 3.2.

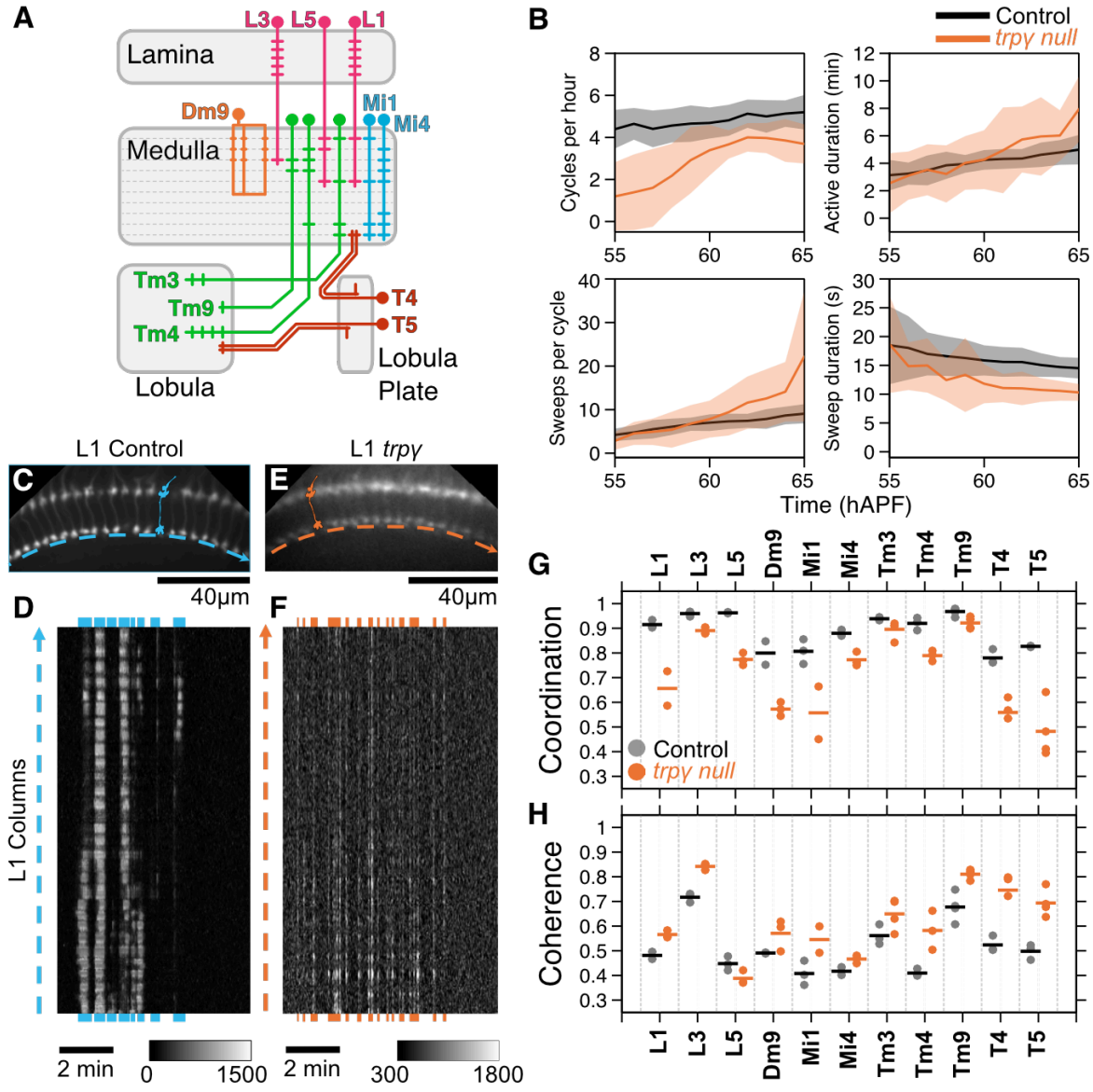
A
L3
L5
L1
Lamina
Dm9
Mi1
Mi4
Medulla
Tm3
Tm9
Tm4
T4
T5
Lobula
Lobula Plate
B
Control
trpy null
Cycles per hour
Active duration (min)
Sweeps per cycle
Sweep duration (s)
Time (hAPF)
L1 Control
L1 trpy
C
E
40μm
40μm
D
F
L1 Columns
2 min
0
1500
2 min
300
1800
G
Coordination
Control
trpy null
H
Coherence
L1
L3
L5
Dm9
Mi1
Mi4
Tm3
Tm4
Tm9
T4
T5

Figure 3.2. Activity patterns in visual processing neurons are altered in *trpγ* mutants.

A. Schematic of visual system cell types studied. **B.** Average metrics pooled from 2PM imaging of all cell types in control (black, n=31) and *trpγ* (orange, n=33) pupae. Shaded areas, SD. **C, E.** AIP of L1 medulla projections in control (C) and *trpγ* pupae (E). Cartoons illustrate single L1s in each array. Dashed arrows sit below thin profiles used to generate the kymographs in (D) and (F); arrow direction matches layout of kymographs (D,F). **D, F.** Kymographs of net fluorescence from profiles in C, E, showing one active phase (~60 hAPF) with sweeps highlighted in blue (D) or orange (F). **G, H.** Coordination (G) and coherence (H) values over 55-65 hAPF calculated for different cell types in control (black) or *trpγ* (orange) pupae. Round markers are values from individual time series, bars are averages for each cell type. n=2-3 time series for each cell type.

3.4. SYNAPTOGENESIS DEPENDS ON DEVELOPMENTAL ACTIVITY

To assess whether loss of *Trpγ* affects synapse formation, we used the synaptic tagging with recombination (STaR) technique, which enables cell-specific labeling of the active zone structural protein bruchpilot (Brp) (Chen et al., 2014). As the labeled Brp is expressed at physiological levels with STaR, wild-type synapse counts track closely with those reported in EM reconstructions, particularly for cells with sparser active zones such as R8 and L4 (Takemura et al., 2008; Takemura et al., 2013) (**Supplementary Figure 3.5A**). There are other neurons, such as Mi1, where STaR under-reports the actual synapse count due to resolution constraints. While we refer to STaR-derived data as synapse count, reported changes may reflect any combination of altered synapse count, structure, or density.

All 10 visual processing neurons we studied have significantly altered synapse counts in *trpγ* mutants (**Figure 3.3**). Notably, these changes are cell-type and domain specific. For example, the synaptic output domains of Mi1—in medulla layers M1, M5, and M9-10—are differentially affected, with the largest decrease in synapse counts occurring in M9-10 (**Figure 3.3A-C**). By contrast, in L1 and L5, the relative synapse count drops are comparable in each layer. (**Supplementary Figure 3.5B, D**). In one cell type, Tm9, synapse counts increase in the mutant (**Figure 3.3D, Supplementary Figure 3.5G**). We conclude that *Trpγ* is necessary for establishing the stereotyped, cell-type-specific synaptic structure of the *Drosophila* visual system.

For two cell types, Dm9 and Tm9, we combined STaR analysis with $Trp\gamma^{G4}$-driven Trpγ-D and found that expression of a single copy of this transgene in Trpγ+ cells significantly rescues the synaptic phenotypes (**Figure 3.3D, Supplementary Figure 3.5H**). As our genetic scheme

specifically inhibited expression of Trpγ-D in Dm9 and Tm9, these results are also consistent with a non-cell-autonomous requirement for *Trpγ*.

To follow up on cell autonomy, we performed mosaic analysis with a repressible cell marker (MARCM) (Lee and Luo, 1999) in combination with STaR to label pre-synaptic sites of *trpγ* mutant clones in a wild-type background. We focused on L5, which expresses *Trpγ* during development (Kurmangaliyev et al., 2020). There is no significant difference in synapse counts between mutant and wild-type clones (**Supplementary Figure 3.5I**), indicating that the L5 *trpγ* synaptic phenotype is not due to a cell autonomous requirement for this gene.

If the *trpγ* synaptic phenotypes are due to the attenuation of PSINA, then a more severe perturbation of developmental activity should also affect synapse formation. To this end, we expressed tetanus-toxin (TNT) pan-neuronally during the second half of pupal development and assessed synaptic structure with STaR in Dm9 and Tm9 cells. Global TNT expression effectively suppresses PSINA (**Supplementary Figure 3.17, 3.18**), and, remarkably, the resulting changes in synapse counts are indistinguishable from the *trpγ* phenotypes (**Figure 3.3D**). These results indicate that the synaptic defects are caused by the attenuation of PSINA in *trpγ* mutants. Additionally, the alteration of cell-type-specific PSINA dynamics is as severe a perturbation to synaptic development as the loss of nearly all developmental activity.

The specificity of the Tm9 driver made it possible to compare the time-course of synaptic development with and without PSINA. Synapse counts under these two conditions are comparable at 60 hAPF, begin diverging at 72 hAPF, and reach their respective adult complements at 84 hAPF (**Supplementary Figure 3.5G, J**). The wild-type trend is consistent with previous studies (Chen et al., 2014; Muthukumar et al., 2014), and the similarly monotonic

increase in the absence of PSINA suggests that developmental activity acts to influence a default synaptogenesis program.

Figure 3.3.

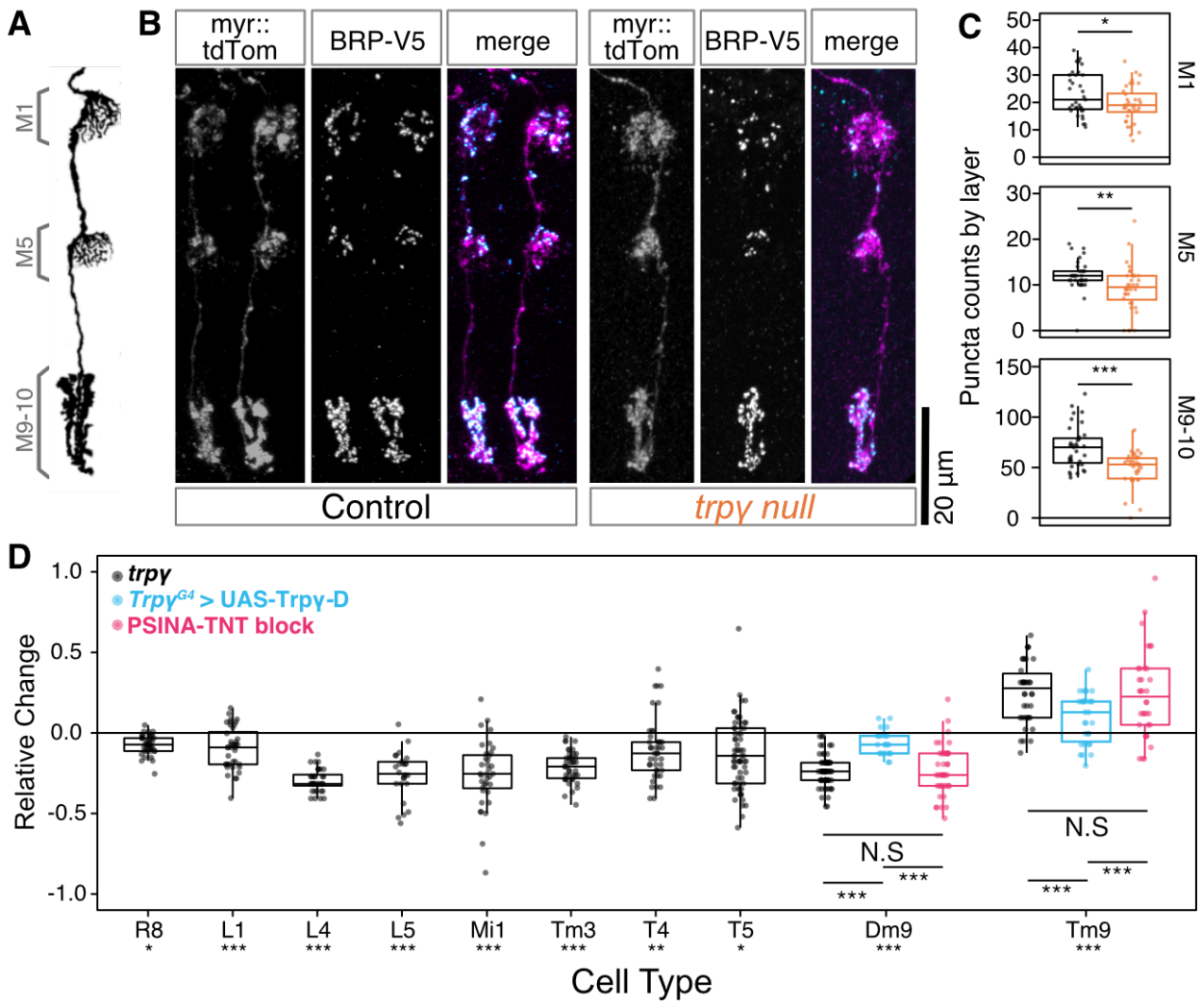
A
M1
M5
M9-10
B
myr::
tdTom
BRP-V5
merge
myr::
tdTom
BRP-V5
merge
Control
trpγ null
20 µm
C
Puncta counts by layer
M1
M5
M9-10
D
trpγ
Trpγ^G4 > UAS-Trpγ-D
PSINA-TNT block
Relative Change
Cell Type
R8
L1
L4
L5
Mi1
Tm3
T4
T5
Dm9
Tm9
N.S

Figure 3.3. Synapse formation in the visual system depends on PSINA.

A. Schematic of Mi1, with processes in medulla layers M1, M5, and M9-10 (adapted from Ref. *38*). **B**. Micrographs of Mi1 neurons in control (left set) and *trpγ* (right set) animals with cell membranes (myr::tdTOM, magenta in merged) and presynaptic sites (BRP-V5, cyan in merged) labeled. Scale bar 20μm. **C.** Mi1 Brp puncta counts by layer in heterozygous control (black, n=35) and *trpγ* (orange, n=36) animals. Box-and-whiskers mark 5^{th}, 25^{th}, 50^{th}, 75^{th}, and 95^{th} percentiles. *, $p<0.05$; **, $p<0.01$; ***, $p<0.001$ by Welch's t-test following Shapiro-Wilk test. **D.** Cell-type-specific Brp puncta counts in *trpγ* mutants (black, n=26-65 per cell type), in the *trpγ, Trpγ^{G4}>* 2xUAS-Trpγ-D rescue condition (cyan, n=24 for Dm9, n=30 for Tm9), and in animals expressing TNT pan-neuronally (magenta, n=43 for Dm9, n=35 for Tm9), normalized to respective control averages (n=18-61 per cell type). Data display as in C. Asterisks below cell type names report tests of *trpγ* mutants against control. *, $p<0.05$; **, $p<0.01$; ***, $p<0.001$ by Welch's t-test following Shapiro-Wilk test or Tukey's post-hoc test following ANOVA for multiple groups.

3.5. ACTIVITY IN *TRPγ*+ NEURONS IS THE TEMPLATE FOR PAN-NEURONAL PSINA

The correspondence of synaptic defects seen with pan-neuronal inhibition and the *trpγ* mutation as well as the non-autonomous origin of the mutant phenotypes shifted our attention from the gene to the expression domain. From 24 to 72 hAPF, $Trp\gamma^{G4}$ labels an increasing number of cells in the brain (**Figure 3.4A, Supplementary Figure 3.6**). The half-brain count peaks at 1095±105 at 72 hAPF; by eclosion this figure is reduced by 40%. Throughout pupal development, the majority of Trpγ+ cells are found in the central brain with optic lobes accounting for at most 25% of all and 8% of the strongly labeled Trpγ+ cells (**Figure 3.4A, Supplementary Figure 3.6**).

We characterized the Trpγ expression domain at 72 hAPF with immunofluorescence. A comparison of the neuronal anti-elav and glial anti-repo co-stainings revealed that Trpγ+ cells are neurons (**Supplementary Figure 3.7**). Consistent with this, we found that RNAi-mediated Trpγ knock-down in neurons produces to a PSINA phenotype comparable to the whole animal mutant while the knock down in glia has no effect (**Supplementary Figure 3.8**). Trpγ+ neurons are a diverse group that includes cholinergic, glutamatergic, GABAergic, serotonergic, and dopaminergic cells (**Supplementary Figure 3.9A-E**). The expression domain also contains DH31, DH44, Pdf, and SIFamide producing neuro-peptide cells (**Supplementary Figure 3.9F-I**).

Trpγ+ neuronal processes cover all regions of the developing brain in apparent space-filling fashion (**Figure 3.4B**). We aimed to visualize individual neuronal morphologies. FLP recombinase-mediated approaches resulted in high density labeling independent of recombinase activity. Thus, we generated a new series of reagents, SPARC3-Out-GAL80, based on the recent

Sparse Predictive Activity through Recombinase Competition (SPARC) approach to sparse labeling (Isaacman-Beck et al., 2020)(Supp. Discussion). Using SPARC3-Out-GAL80 in series with UAS-SPARC2-LexA to control $Trp\gamma^{G4}$ output, we reduced the labeling density from ~2,000 to ~5 neurons per brain, making it possible to discern morphologies of individual Trpγ+ cells (**Supplementary Figure 3.10**). This effort revealed a number of visual processing neurons, including ones (e.g. L5, L2) that have been reported to express *Trpγ* during development (**Supplementary Figure 3.11**). We also observed a number of less familiar neurons that innervate the visual system from the central brain (**Figure 3.4C**), suggesting possible structural origins to the non-autonomous *trpγ* phenotypes.

The fly brain comprises some 150,000 neurons (Chiang et al., 2011); Trpγ is expressed in <2% of this complement. To compare pan-neuronal PSINA to the activity in Trpγ+ neurons, we performed two-color calcium imaging (**Figure 3.4D**) (Dana et al., 2016). In both wild-type and *trpγ* mutants, PSINA is highly correlated between these two sets of neurons (**Figure 3.4E**). Additionally, the mutation causes the same loss of amplitude in Trpγ+ neurons as it does for all neurons (**Figure 3.4F**, compare **Figure 3.1E**). With the greater sensitivity of 2PM, we found that the *trpγ* mutation also leads to an increased sweep count in Trpγ+ neurons (**Figure 3.4G-H, Supplementary movie 10**). Notably, Trpγ+ morphologies visible by 2PM were dominated by wide-field processes reminiscent of innervating neurons observed with sparse labeling (**Figure 3.4G**). Taken together, these results suggest that the ~2,000 Trpγ+ neurons provide the immediate template for pan-neuronal PSINA.

Figure 3.4.

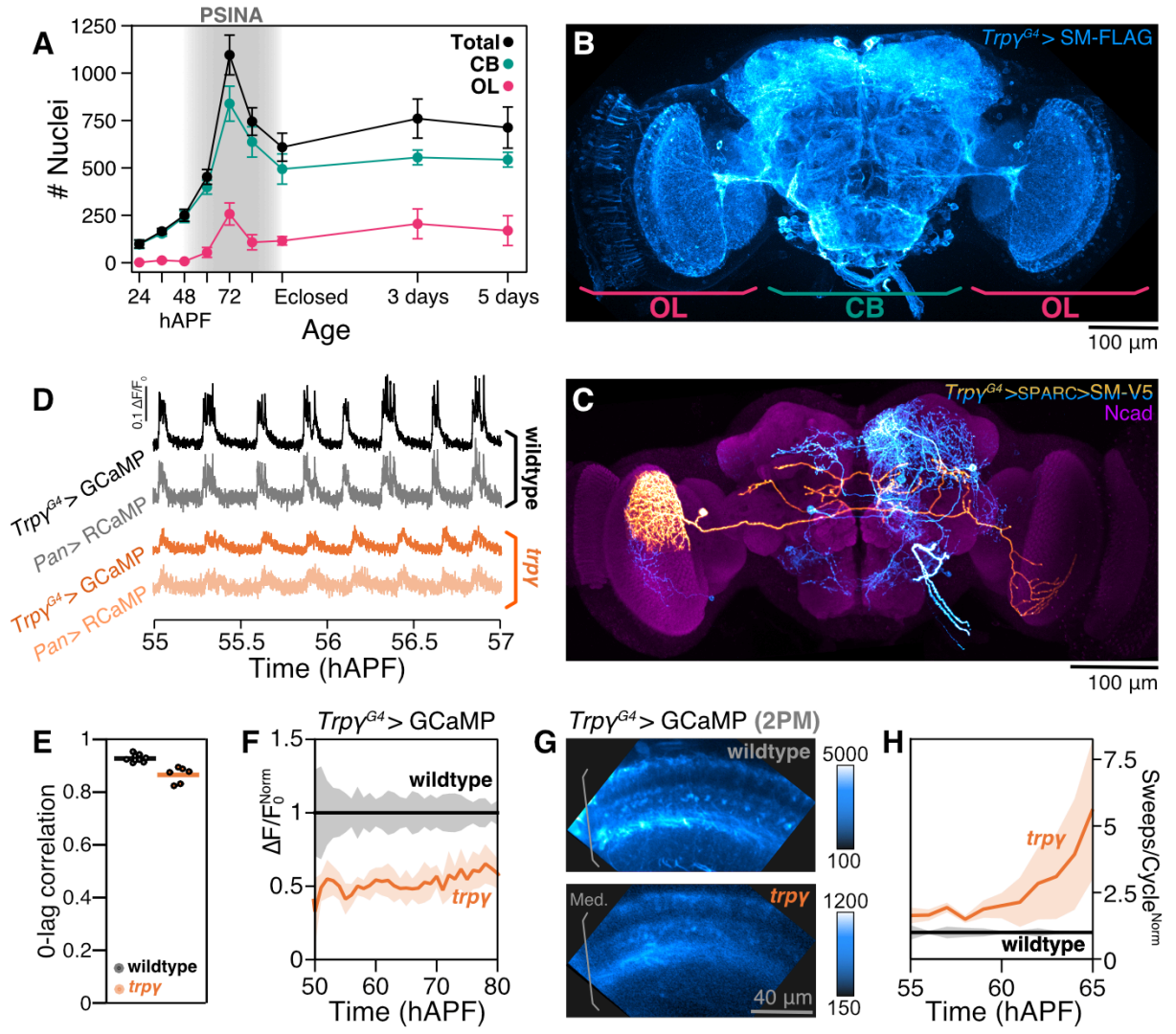
A
PSINA
Nuclei
Total
CB
OL
24 48 72 Eclosed 3 days 5 days
hAPF
Age
B
TrpγG4 > SM-FLAG
OL
CB
OL
100 µm
C
TrpγG4 >SPARC>SM-V5
Ncad
100 µm
D
0.1 ΔF/F0
TrpγG4 > GCaMP
Pan> RCaMP
TrpγG4 > GCaMP
Pan> RCaMP
wildtype
trpγ
Time (hAPF)
E
0-lag correlation
wildtype
trpγ
F
TrpγG4 > GCaMP
ΔF/F0Norm
wildtype
trpγ
Time (hAPF)
G
TrpγG4 > GCaMP (2PM)
wildtype
Med.
trpγ
40 µm
H
trpγ
wildtype
Sweeps/CycleNorm
Time (hAPF)

Figure 3.4. Trpγ+ neurons are the template for brain-wide PSINA.

A. Half-brain Trpγ+ nuclei counts over time. CB, central brain. OL, optic lobe. Error bars, SD. n=3-8 per time point. **B.** Coverage of the 72 hAPF brain by *Trpγ*+ neurons expressing myr::SM-FLAG. Most *Trpγ*+ neurons are labeled; some sparseness was introduced using FLP-Out to improve staining. Image maximum intensity projection (MIP) of confocal stack. Scale bar, 100μm. **C.** Single *Trpγ*+ neuron (orange, manually segmented) in the context of others (cyan) labeled using SPARC. Neurons expressing myr::SM-V5. Reference marker (magenta), Ncad. Image MIP of three stitched confocal stacks of 72 hAPF brain. Scale bar, 100μm. **D.** PSINA traces in control (top two, grayscale) and *trpγ* (bottom two, orange) pupae, recorded from co-expressed GCaMP6s in Trpγ+ neurons (darker hues) and pan-neuronal RCaMP1b (lighter hues). Acquired with wide-field imaging. **E.** 0-lag correlation of PSINA in Trpγ+ and pan-neuronal expression domains. Round markers, single time series. Bars, genotype average. n=9, control. n=6, *trpγ*. **F.** Active phase average amplitude recorded in Trpγ+ neurons binned by hour and normalized to control. Shaded areas, SD. n=9, control. n=6, *trpγ*. **G.** 2PM AIP of GCaMP6s expressing Trpγ+ processes in the visual system of control (top) and *trpγ* (bottom) pupae at ~62 hAPF. Med., Medulla. Scale bar, 40μm. **H.** Sweeps/cycle measured in 2PM time series binned by hour and normalized to control. Shaded areas, SD. (n=3 for both genotypes).

3.6. DEVELOPMENTAL ACTIVITY DEPENDS ON *TRPγ* + NEURON ACTIVITY

To directly test the contribution of activity in Trpγ+ cells to PSINA, we expressed the inward-rectifying potassium channel and neuronal inhibitor Kir2.1 (Baines et al. 2001) from 40-100 hAPF, while performing pan-neuronal calcium imaging (**Figure 3.5A-B, Supplementary Figure 3.12**).

Silencing Trpγ+ neurons severely attenuates PSINA at a level comparable to pan-neuronal expression of Kir2.1 (**Figure 3.5C-D, Supplementary movie 11**). The extent of attenuation cannot be explained by simply a loss of Trpγ+ neuron activity, which contributes ~15% of the total PSINA signal amplitude (**Supplementary Figure 3.13**). Wide-field imaging reveals residual cycles with fewer sweeps, shorter active phases, and perturbed periodicity (**Figure 3.5D, Supplementary Figure 3.12**). This residual activity remains coordinated throughout the brain (**Supplementary Figure 3.14**). With 2PM in the visual system, the reduced cycles are evident with both Trpγ+ and pan-neuronal silencing, and, in both cases, only distinct layers in the distal medulla become active (**Supplementary Figure 3.12B-C**). The profound impact of driving Kir2.1 with $Trp\gamma^{G4}$ indicates that the neurons that shape the spatiotemporal structure of PSINA reside in the *Trpγ* expression domain.

Specifically silencing Trpγ+ neurons in the central brain, but not in the optic lobes, attenuates PSINA across the brain (**Supplementary Figure 3.15**). Notably, the converse experiment has no significant effect, even in the optic lobes where Trpγ+ neurons are made to express Kir2.1 (**Supplementary Figure 3.15**). These results are consistent with the non cell-autonomous origin of the visual system *trpγ* synaptic phenotypes, and, together with the Trpγ+ neurons that bridge the central brain and the optic lobes, suggest that Trpγ+ neurons carry, or relay, PSINA into the visual system.

Additional perturbations of the Trpγ+ domain also lead to PSINA attenuation. Ablating Trpγ+ neurons during PSINA results in loss of PSINA comparable to Kir2.1 silencing (**Supplementary Figure 3.16**). TNT expression in Trpγ+ neurons also attenuates PSINA (**Supplementary Figure 3.17**). While the least potent of the three perturbations, TNT is still much more effective at inhibiting PSINA when expressed in the ~2,000 Trpγ+ neurons than in other neuronal populations: expressing tetanus toxin in aminergic, glutamatergic, or GABAergic neurons has no significant effect on PSINA (**Supplementary Figure 3.18**). We conclude that the Trpγ+ silencing results are specific to this set of neurons.

For a complementary gain-of-function approach, we used the thermogenetic neuronal activator TrpA1 (Pulver et al., 2009). Activating TrpA1 pan-neuronally leads to sustained high frequency, low amplitude events that sit on an elevated plateau of GCaMP fluorescence, consistent with constitutive contributions from spiking and non-spiking neurons (**Figure 3.5E-G, Supplementary Figure 3.19**). By contrast, TrpA1-mediated activation of Trpγ+ neurons produces an uninterrupted burst of sweeps that are comparable in amplitude to controls, but lack the periodic structure of wild-type PSINA (**Figure 3.5E-G, Supplementary Figure 3.19**). Notably, while pan-neuronal activation stimulated brain-wide responses as early as 36 hAPF, Trpγ+ neurons became effective drivers of stimulated activity starting at 48 hAPF, co-incident with the onset of PSINA (**Figure 3.5F**). These results are consistent with the notion that Trpγ+ neurons are sufficient to trigger brain-wide spiking activity during PSINA.

Figure 3.5.

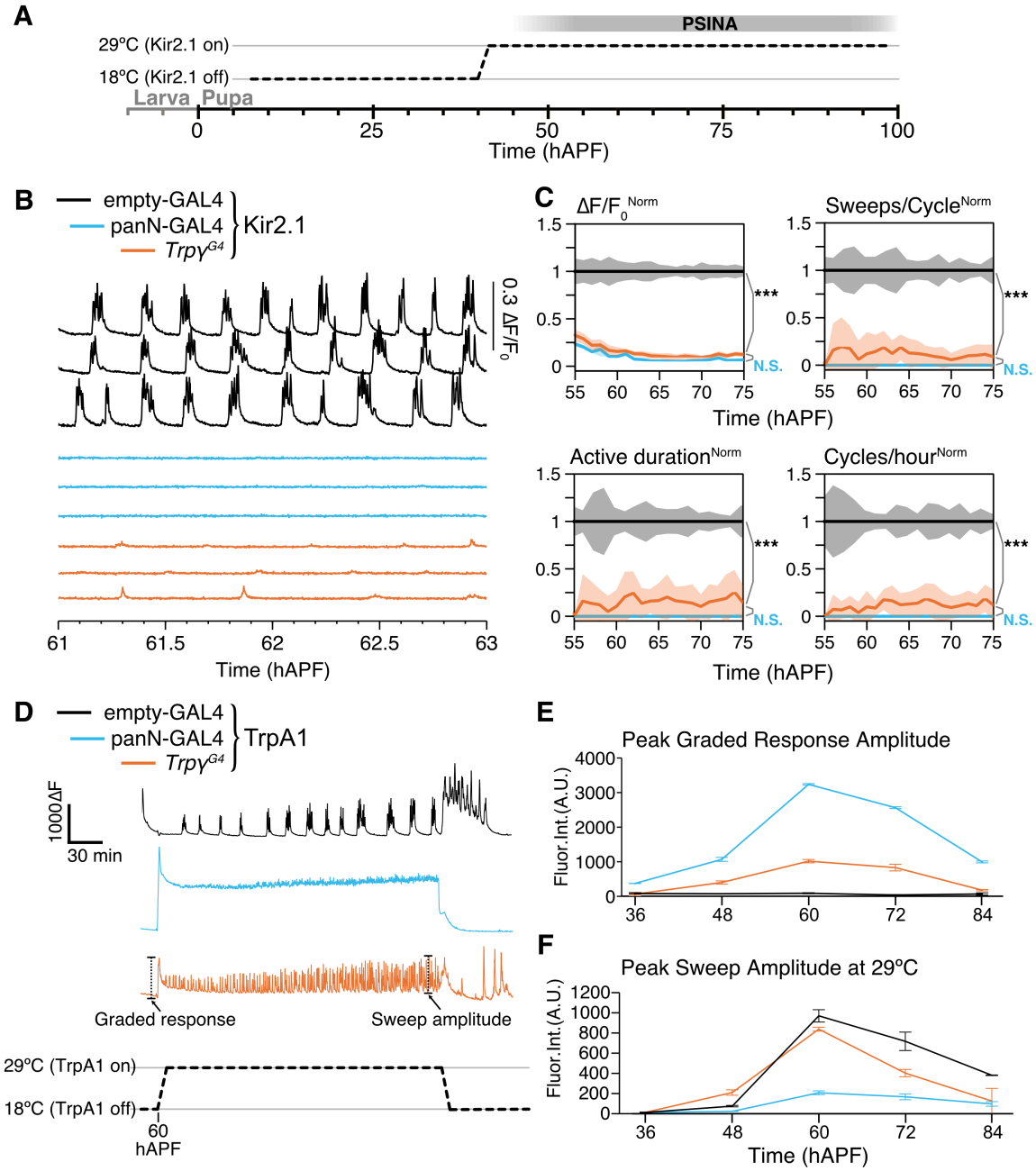
A
PSINA
29°C (Kir2.1 on)
18°C (Kir2.1 off)
Larva Pupa
0
25
50
75
100
Time (hAPF)
B
empty-GAL4
panN-GAL4
Trpγ^G4
Kir2.1
0.3 ΔF/F0
61
61.5
62
62.5
63
Time (hAPF)
C
ΔF/F0 Norm
Sweeps/Cycle Norm
Active duration Norm
Cycles/hour Norm
1.5
1
0.5
0
***
N.S.
55
60
65
70
75
Time (hAPF)
D
empty-GAL4
panN-GAL4
Trpγ^G4
TrpA1
1000ΔF
30 min
Graded response
Sweep amplitude
29°C (TrpA1 on)
18°C (TrpA1 off)
60
hAPF
E
Peak Graded Response Amplitude
Fluor.Int.(A.U.)
4000
3000
2000
1000
0
36
48
60
72
84
F
Peak Sweep Amplitude at 29°C
Fluor.Int.(A.U.)
1200
1000
800
600
400
200
0
36
48
60
72
84
Time (hAPF)

Figure 3.5. PSINA requires Trpγ+ neuron activity.

A. Expression control of UAS-Kir2.1 with TARGET; animals shifted from 18ºC to 29ºC at 40 hAPF. **B**. PSINA traces from pan-neuronal GCaMP6s in control (empty-GAL4, black, n=7), panN-GAL4>Kir2.1 (blue, n=7), and $Trp\gamma^{G4}$>Kir2.1 (orange, n=9) pupae. **C.** Active phase average amplitude (top-left), sweeps/cycle (top-right), active phase duration (bottom-left), and cycles per hour (bottom-right), binned by hour and normalized to control. Shaded areas, SD. Genotypes color-matched to B. ***, $p<0.001$ by Welch's t-test following Shapiro-Wilk test, compared to $Trp\gamma^{G4}$>Kir2.1 activity at 60 hAPF. **D.** Activity from pan-neuronal GCaMP6s in control (empty-GAL4, black), panN-GAL4>TrpA1 (blue), and $Trp\gamma^{G4}$>TrpA1 (orange) pupae at 60 hAPF. Pupae reared at 18ºC and shifted to 29ºC. Initial graded response to temperature shift and maximum sweep amplitude are marked. **E,F.** Peak graded response to temperature shift (E) and peak sweep amplitude at 29ºC (F). Error bars, SD. n=2-4 per timepoint and condition. Genotypes color-matched to D.

3.7. DISCUSSION

We report that perturbing PSINA leads to cell-type-specific changes to synaptic structure in the fly visual system (**Figure 3.3E**). We see the same changes with both the near-complete block of PSINA with pan-neuronal tetanus toxin and the distinctive attenuation due loss of *Trpγ*, suggesting that wild-type synaptic development requires the stereotyped activity patterns of PSINA. This, together with the observations that synapses still form without activity (**Figure 3.3D**) and that activity across the brain is templated by a discrete population of neurons (**Figure 3.4D-F**), support an instructive role for PSINA.

The synaptic changes due to altered PSINA are comparable to recent findings that used EM reconstructions to compare the effects of cell-type-specific perturbations to wiring in the developing larval nervous system (Valdes-Aleman et al., 2021). This study found that silencing a mechanosensory neuron during development reduced the number of pre-synaptic sites and changed the relative strength of connections to post-synaptic partners. These changes produced altered behavioral responses, indicating that quantitatively modest perturbations of synaptic structure can significantly alter circuit function and output.

Trpγ is a non-selective cation channel in the classical TRP (TRPC) sub-family of TRP channel super-family (Xu et al., 2000). It can interact with the other two fly TRPCs (Xu et al., 2000), TrpL and the eponymous Trp, and its expression in both the neurons and glia of proprioceptive organs is required for regulating fine motor control (Akitake et al., 2015). Here, we show that expression of *Trpγ* in ~2,000 neurons in the developing brain is necessary and sufficient for wild-type PSINA (**Figure 3.5B-C**).

The significance of the *Trpγ* expression domain to PSINA is underscored by two results: (1) Silencing Trpγ+ neurons results in activity inhibition comparable to pan-neuronal silencing

(**Figure 3.5B-C**); and (2) pan-neuronal activity phenocopies the cell-autonomous *trpγ* phenotype; that is, loss of *trpγ* has the same effect on activity across the whole brain as it does in Trpγ+ neurons (**Figure 3.4D-F**). Together, these indicate that Trpγ+ neurons both relay PSINA across the brain and form an *activity scaffold* that templates the spatiotemporal patterns of PSINA.

Notably, residual rhythmic activity persists with both pan-neuronal and Trpγ+ silencing (**Figure 3.5B, Supplementary Figure 3.12**), revealing the presence of a PSINA central pattern generator (CPG) that is outside the reach of these manipulations. That PSINA arises independent of sensory input (Akin et al., 2019) and its temporal patterns are temperature sensitive (**Supplementary Figure 3.19**) provide further support (Mulloney and Smarandache, 2010) for describing the rhythm generating circuit of PSINA as a CPG. While some Trpγ+ neurons may contribute to the modulation of the PSINA CPG, the overall picture that emerges for PSINA is that of a hierarchical cascade with a CPG triggering a small set of relay neurons which subsequently activate the rest of the brain in specific spatiotemporal patterns (**Figure 3.6A-B**).

The dynamic expression domain of *Trpγ*, peaking at a cell count of ~2,000 at 72 hAPF and contracting thereafter, suggests that the PSINA relay may be a functionally or structurally transient feature. Transient populations have been documented in mammalian models of developmental activity, including the Kölliker's organ in the cochlea and sub-plate and Cajal-Retzius neurons in the neocortex (Tritsch et al., 2007; Wang et al., 2015; Luhmann et al., 2016). The existence of temporally dedicated neurons supports the notion that developmental activity is a hardwired phase of nervous system development. Evidence for transient neuronal populations in the developing fly brain (Özel et al., 2021), including PDF-TRI cells (Helfrich-Förster, 1997)

which are Trpγ+ neurons (**Supplementary Figure 3.9G**), raises the possibility of a population of neurons that exist only during pupal development to coordinate PSINA.

Consistent with their role as a relay system, the processes of Trpγ+ neurons occupy every region of the fly brain (**Figure 3.4B**). In the optic lobes, the Trpγ+ domain is represented by both resident visual processing neurons, such as L5, and by expansive processes originating from the central brain (**Figure 3.4C**). The *trpγ* synapse and activity phenotypes are due to loss of function outside the visual system (**Figure 3.3D**), suggesting that only the subset of Trpγ+ neurons with long range projections are responsible for relaying PSINA across the brain.

In many mammalian models of developmental activity, such as the retina, hippocampus, cerebellum, and spinal cord, neurons intrinsic to the local circuitry are known to initiate activity (Blankenship and Feller, 2010). While initiation and patterning of activity may be local, the high degree of inter-connectivity in the adult brain does suggest the feasibility of a larger scale of coordination. Indeed, activity waves that originate in the retina are relayed out to higher visual centers by retinal ganglion cells (Ackman et al., 2012). Here, the more approachable scale of the fly nervous system reveals that it is possible to coordinate developmental activity across the whole brain. Studies of brain-wide, low frequency activity in the adult (Leong et al., 2016) suggest that the neuronal infrastructure for such long-range coordination exists in mammals; it remains to be seen if similar infrastructure is used during development.

In summary, here we identify a brain-wide relay system to produce PSINA, which in turn modulates synaptogenesis. The structure and connectivity of this relay circuit will be critical for understanding how brain-wide developmental activity is generated. A mechanistic description of developmental activity will be necessary to address how and to what extent such activity represents a fundamental ingredient in the recipe for building a brain.

Figure 3.6.

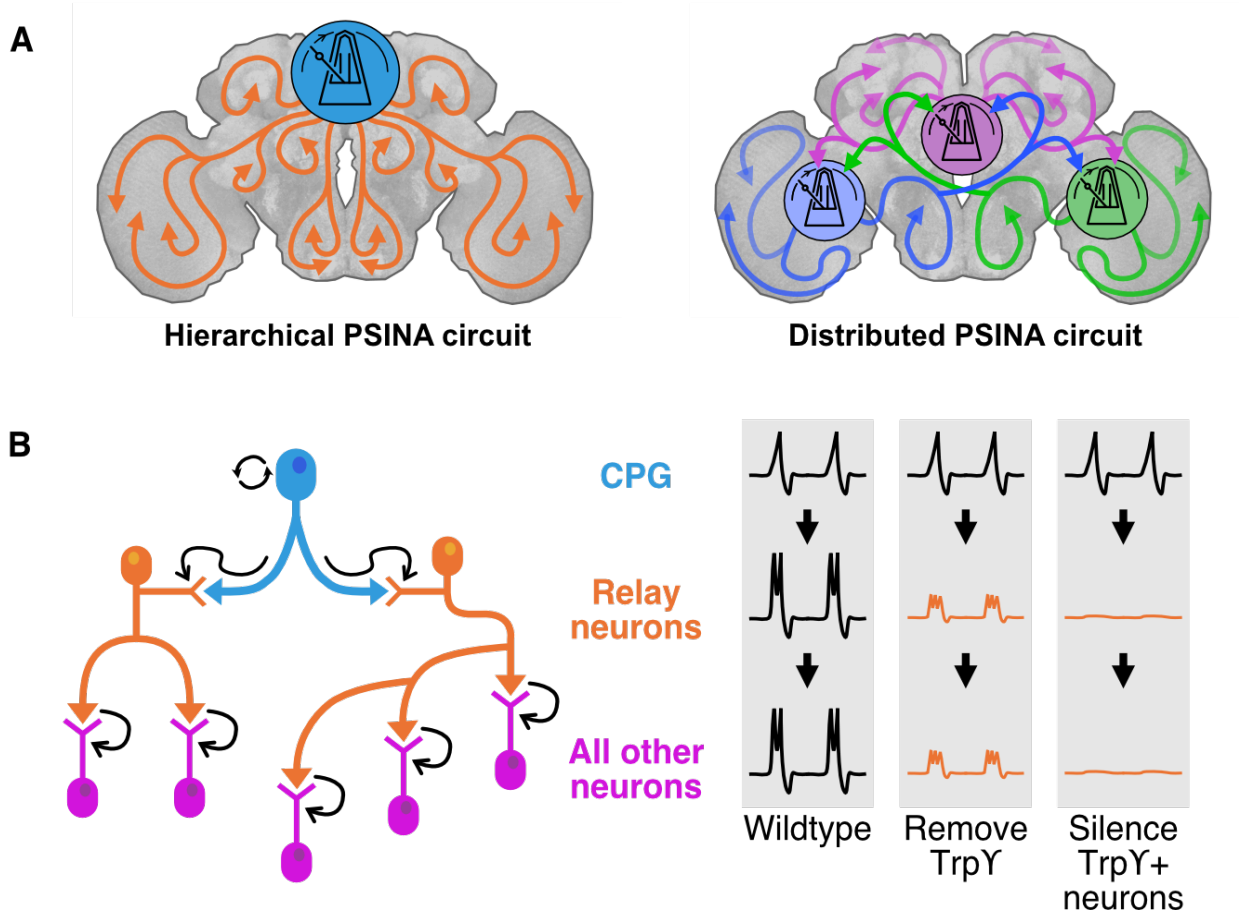
A
Hierarchical PSINA circuit
Distributed PSINA circuit
B
CPG
Relay neurons
All other neurons
Wildtype
Remove TrpY
Silence TrpY+ neurons

Figure 3.6. Model for PSINA relay system.

A. Conceptual circuit organizations for coordinating and propagating PSINA. Metronomes indicate CPGs. Colored arrows indicate Trpγ+ and other relay neurons. **B**. Intrinsically active CPG neurons (cyan) activate Trpγ+ relay neurons (orange), which, in turn, activate all other neurons (magenta) in specific spatio-temporal patterns. When relay activity is attenuated or silenced, all downstream neurons are similarly affected.

3.8. METHODS

Experimental Model and Subject Details

Flies were reared at 18°C, 25°C, or 29°C on standard cornmeal/molasses medium; developmental time was matched to the 25°C standard (1x) using relative rates of 0.5x and 1.25x for 18°C and 29°C, respectively (Bainbridge and Bownes, 1981). Pupal development was staged with respect to white pre-pupa formation (w.p.p., 0 hAPF) or head eversion (h.e., 12 hAPF). GAL4/UAS and LexA/LexAop expression systems (Brand and Perrimon, 1993; Lai and Lee, 2006) were used to drive cell-type-specific transgene expression. Complete genotypes used in each experiment can be found in Table 2.

Generation of UAS-Trpγ-A/B and UAS-Trpγ-D transgenic lines.

We PCR amplified the Trpγ coding sequence from pcDNA3-Trpγ (Akitake et al., 2015) using the following primers:

Isoform	Sequence (5'-3')
A/B	ATTCTTATCCTTTACTTCAGGCGGCCGCATGATGGAGGAGGAGAACACG
A/B	AGGTTCCTTCACAAAGATCCTCTAGATCAACCAATAGCTCCCGTGG
D	ATTCTTATCCTTTACTTCAGGCGGCCGCATGCACTTTGTGAGTCCCG
D	AGGTTCCTTCACAAAGATCCTCTAGATCAACCAATAGCTCCCGTGG

We subcloned these fragments between the NotI and the XbaI sites of pJFRC165. Note that in our Trpγ-D ORF, the non-canonical start codon CTG is converted to ATG to ensure robust GAL4-driven expression. After sequence-verifying the new plasmids, we introduced UAS-Trpγ-A/B or -D DNA into y[1] w[*]; P(y[+t7.7]=CaryIP)su(Hw)attP1embryos via phiC31 integrase-mediated germline transformation (BestGene Inc., Chino Hills, CA).

Generation SPARC3-Out-GAL80 flies

All plasmids were generated through synthesis and molecular cloning by Genscript (Piscataway, NJ, USA); see below for more details. Listed plasmids are available upon request.

Plasmid Name	Function
pHD-Su(Hw)attP5-αTub84B-SPARC3-D-Out-GAL80	Swap out effector and terminator to generate αTub84B-SPARC3-D-Out CRISPR-donor vector for genomic insertion near the Su(Hw)attP5 locus
pHD-Su(Hw)attP5-αTub84B-SPARC3-I-Out-GAL80	Swap out effector and terminator to generate αTub84B-SPARC3-I-Out CRISPR-donor vector for genomic insertion near the Su(Hw)attP5 locus
pHD-Su(Hw)attP5-αTub84B-SPARC3-S-Out-GAL80	Swap out effector and terminator to generate αTub84B-SPARC3-S-Out CRISPR-donor vector for genomic insertion near the Su(Hw)attP5 locus.
pCFD5-U6-3-t-Su(Hw)attP5	Guide RNA plasmid to co-inject with pHD-3XP3-dsRed-DattP-CRISPR-donor-Su(Hw)attP5 SPARC variants for CRISPR-HDR

gRNA-targeting vector:

pCFD5-U6-3-t-Su(Hw)attP5 was designed as described (Isaacman-Beck et al., 2020) with the following gRNA sequences:

gRNA Target	Genomic Location	Sequence	Strand
Su(Hw)attP5_1	2R:14305046..14305068	CCGCCGGACAATAGACCGAATTT	Minus

Su(Hw)attP5_2	2R:14305111..14305133	CATTCCAAGCTTCCCTTTGAAGG	Plus
Synthetic gRNA	Not applicable	CCATCCGTAAGATGCTTTTCTGT	Minus

αTub84B-SPARC3 CRISPR donor synthesis:

To generate CRISPR donor plasmids targeting sequences near Su(Hw)attP5 and VK00005, we defined homology arms directly adjacent to the gRNA targets defined above. For the region near Su(Hw)attP5, we defined a 1044bp left homology arm (2R: 14304046..14305089) and a 1044bp right homology arm (2R:14305090..14306133). We designed these homology arms to fully recapitulate genomic DNA after CRISPR-HDR by overlapping the gRNA target sites and mutating the Proximal Adjacent Motifs (PAMs) of gRNA targets. Genscript synthesized these homology arms and cloned them into pHD-3xP3-dsRed-DattP using AarI for left homology arms and Sap-I for right homology arms to generate pHD-3XP3-dsRed-DattP-CRISPR-donor-Su(Hw)attP5.

Next, the SPARC3-OUT-D-GAL80 module was synthesized by Genscript (Piscataway, NJ, USA) and cloned into the unique Kpn-I site of either pHD-3XP3-dsRed-DattP-CRISPR-donor-Su(Hw)attP5 to generate pHD-SPARC3-OUT-D-GAL80-Su(Hw)attP5. Then Genscript PCR amplified the αTub84B promoter (Lee and Luo, 1999) from pJFRC-αTub84B-IVS-PhiC31 (Isaacman-Beck et al., 2020) and cloned it into pHD-SPARC3-OUT-D-GAL80-Su(Hw)attP5 to generate pHD-αTub84B-SPARC3-OUT-D-GAL80-Su(Hw)attP5. Genscript next synthesized attP38 and attP34 fragments (Isaacman-Beck et al., 2020) and cloned them into pHD-αTub84B-SPARC3-OUT-D-GAL80-Su(Hw)attP5 via Stu-I and Asc-I sites to generate pHD-αTub84B-SPARC3-OUT-I-GAL80-Su(Hw)attP5 and pHD-αTub84B-SPARC3-OUT-S-GAL80-

Su(Hw)attP5 respectively:

For detailed construct maps of αTub84B-SPARC3-OUT, see **Supplementary Figure 3.10**.

Generation of transgenic flies:

αTub84B-SPARC3-OUT-GAL80 transgenic flies were generated by Bestgene (Chino Hills, CA, USA) via standard construct injections and CRISPR-HDR. Transformants were identified by the marker 3xP3-DsRed. The three fly lines (i.e. D, I, and S variants) are available upon request.

Wide-field imaging

Pupae were staged for w.p.p formation or h.e. and reared at 25ºC unless otherwise noted. The cuticle around the heads were removed with fine forceps and the animals were affixed to a metal plate (McMaster-Carr, CA, USA) with double-stick adhesive tape (3M, MN, USA). The metal plate was placed in a custom environmental chamber to maintain humidity and temperature. This chamber comprised: a PTC1 temperature-controlled breadboard (Thorlabs, NJ, USA) to maintain sample temperature at 18ºC, 25ºC, or 29ºC; a set of four 35mm dishes filled with deionized water to maintain humidity; and a 150mm petri-dish lid to provide enclosure. To improve imaging quality, a large format coverslip was fitted into a rectangular opening made in the lid. This coverslip sat in the optical path, between the pupae and the objective lens, and was treated with Barbasol shaving cream (Perio, OH, USA) to prevent condensation during temperature shifts.

Images were captured using an Axio Zoom.V16 epifluorescence microscope (Zeiss, Germany) equipped with a Retiga R1 CCD Camera (QImaging, Canada) and X-Cite TURBO LED 6-Channel Light Source (Excelitas Technologies, MA, USA). Images were acquired at 0.4 Hz with a PlanNeoFluar Z 1X objective (Zeiss, Germany) with 100ms exposure time for green fluorophores and 500ms exposure time for red fluorophores. Acquisition was controlled by

Slidebook 6 software (Intelligent Imaging, CO, USA). Time series were processed with Fiji (Schindelin et al., 2012) and analyzed using MATLAB (Mathworks, MA, USA).

Two-photon imaging of the developing visual system

Pupae were prepared for imaging as previously described (Akin and Zipursky, 2016). Briefly, the cuticle around the heads were removed with fine forceps and the animals were attached eye-down on a coverslip coated with a thin layer of embryo glue. A water reservoir on the objective side of the coverglass provided sufficient immersion medium to last through the hours-long imaging sessions; another reservoir below the pupae kept the animals from dehydrating.

Time-lapse imaging of the visual system was performed on a custom-built two-photon microscope (Akin and Zipursky, 2016) with a 20x water immersion objective (Zeiss, W Plan-Apochromat 10x/1.0 DIC) and 2 GaAsP detectors (Hamamatsu, Japan). The pupae were kept at 25°C using an objective heater system (Bioptechs, PA, USA). A tunable Ti:Sapphire pulsed laser (Chameleon Ultra II, Coherent) was used as the light source. GCaMP6s was excited at 940 nm with ~30 mW under-the-objective power. Animals imaged under these conditions developed normally and eclosed on schedule. To observe a thicker cross-section of the visual system than possible with a single optical slice, we used the maximum intensity projection of three successive images taken 2μm apart in the z-axis as the frame for an individual time point. The effective sampling rate of these time series was 0.38 Hz (2.6s per frame).

Immunofluorescence and confocal microscopy

Brains were dissected in cold Schneider Medium (SM, Gibco #21720–024) and fixed with 3% v/v glyoxal solution (Electron Microscopy Sciences #16525) for 30 minutes at room temperature (RT) or with 4% v/v PFA (Electron Microscopy Sciences #15710) in SM for 20 minutes at RT.

Brains were then washed out of fixative into PBS (Quality Biological), solubilized in PBST (0.5% Triton-X100 (Sigma #T9284) in PBS) for 1 h, and blocked in PBTN (5% Normal Donkey Serum (Jackson ImmunoResearch #017-000-121) in PBST) for 1-2 h, all at RT. Brains were sequentially incubated in primary and secondary antibodies diluted in PBTN for 24-48h at 4ºC, with at least 3 washes through PBST over 2 h at RT in between and afterwards. Brains were post-fixed with 3% v/v glyoxal for 30 minutes at RT or with 4% v/v PFA in SM for 20 minutes at RT, followed by multiple washes into PBST over 10 minutes. Brains were finally transferred to Everbrite mounting medium (Biotium #23001) and mounted on to slides for imaging.

Primary antibodies and dilutions used in this study were as follows: Mouse monoclonal anti-V5 (Novus Biologicals #NBP2-52703-0.2mg, 1:150), rat monoclonal anti-FLAG (DYKDDDDK) (Novus Biologicals #NBP1-06712, 1:100), mouse monoclonal anti-c-MYC (Developmental Studies Hybridoma Bank (DSHB) #9E10-concentrate, 1:100), rabbit polyclonal anti-dsRed (Clontech #632496, 1:125), chicken anti-GFP (Abcam #ab13970, 1:1000), rabbit monoclonal anti-HA (Cell Signaling Technology #3724, 1:300), rat monoclonal anti-Ncad (DSHB #DN-Ex #8-c, 1:100), mouse monoclonal anti-Elav (DHSB #Elav-9F8A9, 1:100), mouse monoclonal anti-Repo (DHSB #8D12 anti-Repo, 1:100), mouse monoclonal anti-Chat (DHSB #ChAT4B1, 1:20), mouse monoclonal anti-Pdf (DHSB #PDF C7, 1:1000), rabbit polyclonal anti-DVGLUT ((Daniels et al., 2004), 1:1000), rabbit polyclonal anti-DVGAT ((Fei et al., 2010), 1:200), mouse monoclonal anti-TH (Immunostar #22941, 1:200), rabbit polyclonal anti-5-HT (Immunostar #20080, 1:1000), rabbit polyclonal anti-DH31 ((Park et al., 2008), 1:1000), rabbit polyclonal anti-DH44 ((Cabrero et al., 2002), 1:1000), rabbit polyclonal anti-SIFamide ((Terhzaz et al., 2007), 1:1000).

Secondary antibodies and dilutions used in this study were as follows: Alexa 488 donkey polyclonal anti-chicken (Jackson ImmunoResearch # 703-545-155, 1:400), Alexa 488 donkey polyclonal anti-mouse (Jackson ImmunoResearch #715-545-151, 1:400), Alexa 568 donkey polyclonal anti-rabbit (Invitrogen #A10042, 1:400), Alexa 647 donkey polyclonal anti-rat (Jackson ImmunoResearch #712-605-153, 1:400).

Immunofluorescence images were acquired using Zeiss LSM 780 confocal microscope with 20x/0.8 air, 40x/1.4 oil immersion, or 40x/1.2 glycerol immersion objectives (Zeiss).

Analysis of pupal two-photon imaging data

Analysis of two-photon imaging data was carried out as described (Akin et al., 2019).

Analysis of pupal wide-field imaging data

Preparation of time lapse imaging data was performed in Fiji (ImageJ). Per frame pixel averages of user-defined ROIs were used to define raw signal (F) traces from the image time series. The raw signal was baseline subtracted and the resulting net signal (ΔF) was used in subsequent analysis, performed in MATLAB. $\Delta F/F_0$ is defined as the baseline-subtracted net signal divided by the raw baseline signal.

For each time series, sweeps were defined by growing the 'domain' of each signal local maximum (i.e. peak) through preceding and succeeding time-points until another peak at least 75% as large as the original was reached in both directions. Ordered signal peaks were processed iteratively in this fashion, starting from the largest on down, and lesser peaks which were

subsumed in the sweep domain of a larger one were removed from separate evaluation. Clusters of sweeps were used to define active phases; silent phases were defined by the span between active phases; cycles were defined as the sum of an active phase and the subsequent silent phase.

Processing and quantification of confocal images.

To create high resolution, full-brain composite images, confocal stacks were digitally joined together using the Fiji (ImageJ) Pairwise Stitching (Preibisch et al., 2009) plug-in.

Quantification of presynaptic sites: Preparation of confocal images for analysis was performed in Fiji (ImageJ), in which individual color channels were merged into a single TIFF file. Analysis was performed on vaa3d (Peng et al., 2010) by an analyzer blinded to genotype. Puncta associated with labeled cell processes were manually counted and sorted by cell morphological location (e.g. medulla layer). Manual counts for different cell types were cross-referenced with an automated feature detection algorithm to confirm count fidelity.

Counting Trpγ+ nuclei: Three-dimensional binary masks of the half-brain and one optic lobe were manually generated for each confocal stack using Fiji (ImageJ). Labeled nuclei were segmented from confocal stacks using custom scripts written in MATLAB and were assigned to different regions of the brain using the masks; a function critical to this task was sourced from the MathWorks File Exchange repository (Jerman Enhancement Filter (2021), GitHub). The same segmentation approach was used to analyze the co-localization of glia and Trpγ+ nuclei (**Supplementary Figure 3.8**).

Statistical analysis.

Statistical analysis was performed using RStudio. We used either un-paired, two-tailed Welch's t-test following the Shapiro-Wilk test for normality, or Tukey's post-hoc test following ANOVA to assess statistical significance of differences between groups. Bonferroni corrections were applied to multiple comparisons where appropriate. Population averages are given as mean ± standard deviation (SD).

3.9. SUPPLEMENTARY DISCUSSION

Instructive role for PSINA

What is PSINA's role in the development of the connectome? While the significance of PSINA to synaptic specificity and circuit function remain unknown, *trpγ* activity phenotypes (**Figure 3.2**) are consistent with Hebbian mechanisms: given the global participation in PSINA, cell- and circuit-specific patterns of activity may be critical for temporally isolating and matching synaptic partners to fire together. In *trpγ* mutants, the general trends are for cells of a type to decrease their participation in PSINA and to become active more synchronously (**Figure 3.2**). These shifts would decrease the co-incidence of synaptic partner activity and—with many cell types losing their distinctive activity waves—reduce the temporal corralling of elements of emerging neural circuits from surrounding activity. If so, we would expect to find more off-circuit connections, altered synaptic weights, and a more variable connectome to result from perturbing PSINA. As the activity patterns are derived from the Trpγ+ relay, tracing the origins of these patterns for elements of a defined circuit to a small number of Trpγ+ neurons would provide the tools to test this temporal corralling model.

Role for developmental activity in invertebrates

Previous data indicate that circuit formation in the fly visual and olfactory systems can broadly develop normally in the absence of sensory input. In the absence of phototransduction, photoreceptors form their expected complement of synapses (Hiesinger et al., 2006), and visual projection neurons elaborate processes normally (Scott et al., 2003). Further, blocking odor-evoked activity does not significantly affect the formation of the glomerular map in the antennal

lobe (Berdnik et al., 2006). Based on these data, a commonly held notion was that activity in general was dispensable for the development of the adult nervous system (Sugie et al., 2018).

Since the presence of stimulus-independent activity in fly development has been observed only recently (Akin et al., 2019), previous studies have not focused on the role of stimulus-independent activity in synapse formation. However, photoreceptor morphology has been studied in the absence of both stimulus-independent and evoked activity, via tetrodotoxin injection or *paralytic* mutants (Hiesinger et al., 2006). In these conditions, the photoreceptor cell R7 elaborates processes similar to wildtype animals, although synapse formation was not assessed in the context of these interventions. Here we show that photoreceptor synapse counts, like those of other visual processing cells, are indeed altered by activity.

The fly visual system is suitable for understanding cell-type-specific roles of developmental activity in circuit formation. Many of the ~100 cell types in the medulla have been characterized with respect to connectivity at the EM level in the adult (Takemura et al., 2013) and transcription through developmental timepoints (Kurmangaliyev et al., 2020). Further, thanks to the presence of GAL4 drivers specific for many visual processing cell types, the PSINA dynamics for many of these cells have been characterized (Akin et al., 2019). Here we leveraged these resources to show that stimulus-independent activity modulates synaptogenesis in the visual system in a cell-type-specific manner. In the vertebrate visual system, activity after eye opening has been shown to affect synaptogenesis in a cell-type-specific manner (Soto et al., 2012). However, it is unknown whether these observations extend to stimulus-independent activity, where differential dynamics in retinal waves has been observed between classes of retinal ganglion cells (Akrouh and Kerschensteiner, 2013). The mammalian retina contains diversity in cell types comparable to the fly visual system (Sanes and Masland, 2015). Specific

genetic handles for these cell types will make it possible to ask whether retinal waves are differentially interpreted by individual cell types and/or represent a signal that modulates generalized and universal developmental programs.

Mammalian orthologs of *Trpγ*

The two mammalian orthologs of *Trpγ*, TRPC4 and TRPC5, offer important insights into the functional contribution of this channel to PSINA. In thalamic interneurons, TRPC4 is reported to act as a Ca^{2+} influx amplifier downstream of activated serotonin receptors to facilitate the release of dendritic GABA (Munsch et al., 2003). TRPC5 is required cell-autonomously in the dopamine neurons of the hypothalamic arcuate nucleus to maintain their stereotyped infra-slow bursting oscillations; loss of TRPC5 alters their dynamics (Blum et al., 2019). TRPC5 is also necessary for prolactin-evoked tonic excitation of these cells. We found that $Trp\gamma^{G4}$-driven expression of TRPC4 or TRPC5 does not rescue the *trpγ* PSINA phenotype. However, the common theme of acting downstream of non-ionotropic receptors to facilitate excitation may inform efforts to identify the PSINA CPG.

SPARC3-Out-GAL80 produces sparse labeling of neurons

To visualize individual neuronal morphologies, we first turned to established methods of sparse labeling (Nern et al., 2015) which rely on titrating the expression level of FLP recombinase to turn on cell markers in a small number of cells. Due to constitutive FLP-mediated labeling of some Trpγ+ neurons with expansive projections, these methods did not produce the desired results. SPARC3-Out-GAL80, used in series with another SPARC element, enabled consistent visualization of 5-10 members of the 2000+ neuron strong *Trpγ* expression

domain. SPARC moves the control of labeling density from recombinase activity level to the engineered recombination efficiency of the recognition sequences. In the absence of phiC31 recombinase, the SPARC3-Out-GAL80 transgenes drive ubiquitous expression of the GAL4 inhibitor GAL80. With the recombinase, the GAL80 open reading frame is 'SPARC'ed' out at a high, intermediate, or low probability, depending on the flanking recognition sequences. Loss of the GAL80 in a cell disinhibits GAL4, which allows for all UAS effectors in that cell to be expressed. We expect that SPARC3-Out-GAL80 will be a useful addition to the set of available SPARC tools.

3.10. SUPPLEMENTARY FIGURES

Supplementary Figure 3.1.

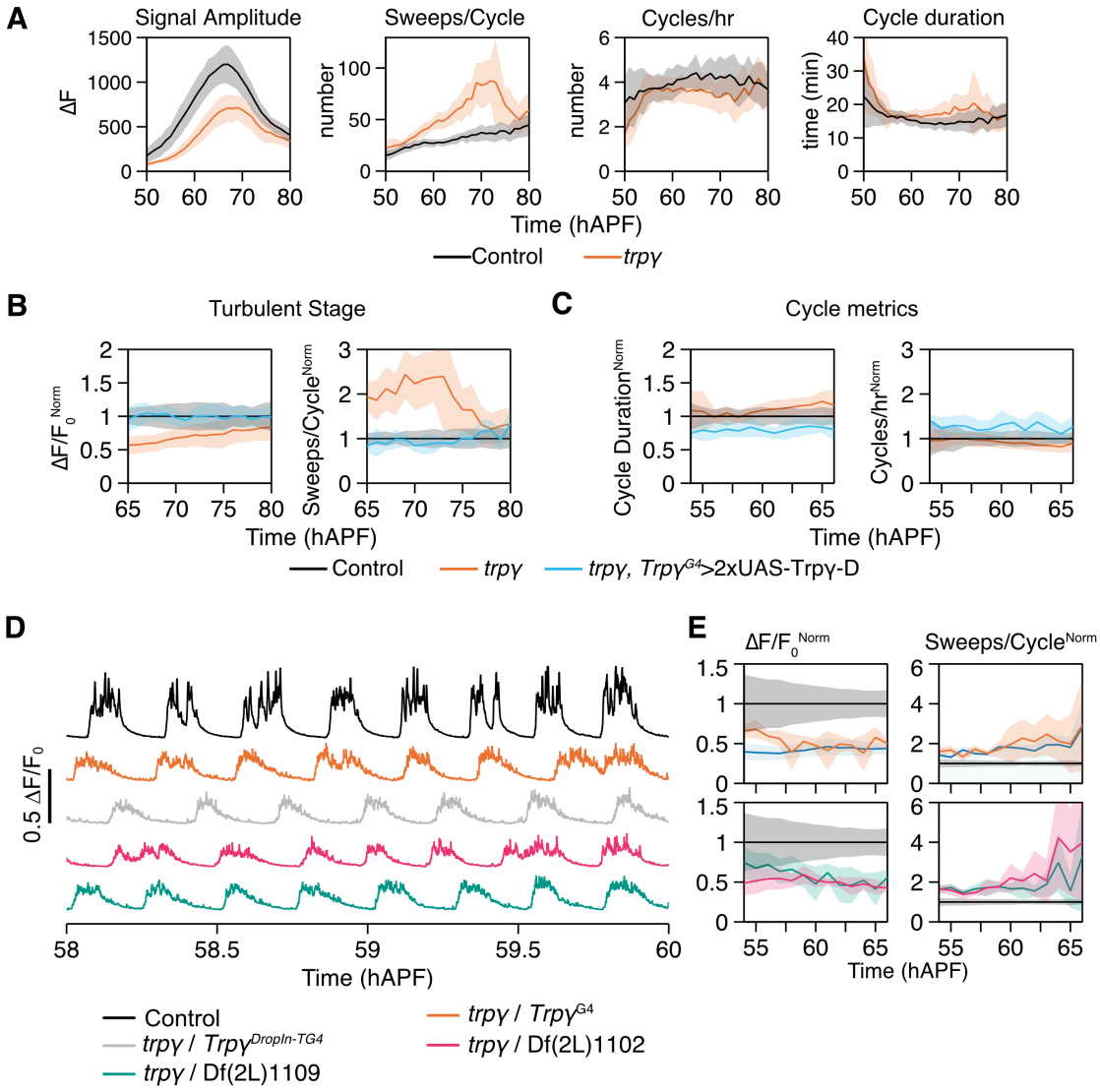

Supplementary Figure 3.1. *Trpγ* is necessary for wildtype PSINA.

A. Raw values binned by hour for active phase signal amplitude, sweeps/cycle, cycles/hour, and cycle duration for control (black, n=19) and *trpγ* null (orange, n=31) pupae. Shaded areas, SD.

B. Active phase average amplitude (left) and sweeps/cycle (right) binned by hour and normalized to control activity during the turbulent stage, between 65 and 80 hAPF, for control (black, n=19), *trpγ* null (orange, n=31), and *trpγ* null with Trpγ-D expressed in Trpγ+ cells (cyan, n=4) pupae. Shaded areas, SD.

C. Cycle duration (left) and cycles/hour (right) binned by hour and normalized to control activity between 55 and 65 hAPF. Shaded areas, SD. Genotypes color-matched to B.

D. Representative traces of activity in control (black, n=19), *trpγ*/$Trp\gamma^{G4}$ (orange, n=5), *trpγ*/$Trp\gamma^{DropIn\text{-}TG4}$ (gray, n=5), *trpγ*/Df(2L)1102 (magenta, n=7), and *trpγ*/Df(2L)1109 pupae (green, n=7).

E. Average amplitude (left) and sweeps/cycle (right) binned by hour and normalized to control activity between 55 and 65 hAPF. Shaded areas, SD. Genotypes color-matched to D.

Supplementary Figure 3.2.

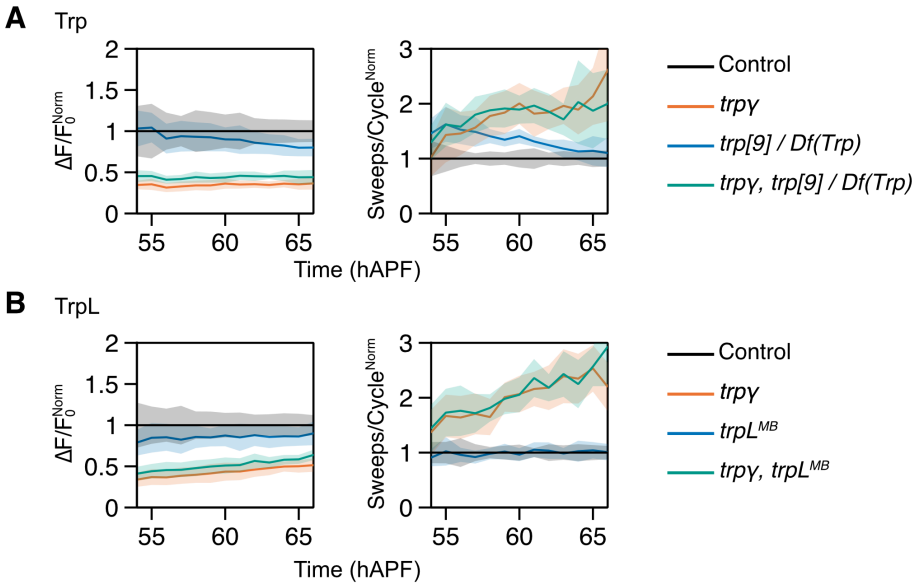

Supplementary Figure 3.2. No genetic requirement for Trp or TrpL in PSINA.

A. Active phase average amplitude (left) and sweeps/cycle (right) binned by hour and normalized to control activity during the periodic stage, between 55 and 65 hAPF, for control (black, n=10), *trpγ* null (orange, n=9), *trp* null (blue, n=10), and *trp* null + *trpγ* null (green, n=10). Shaded areas, SD.

B. Active phase average amplitude (left) and sweeps/cycle (right) binned by hour and normalized to control activity during the periodic stage, between 55 and 65 hAPF, for control (black, n=10), *trpγ* null (orange, n=10), *trpL* null (blue, n=10), and *trpL* null+ *trpγ* null (green, n=10). Shaded areas, SD.

Supplementary Figure 3.3.

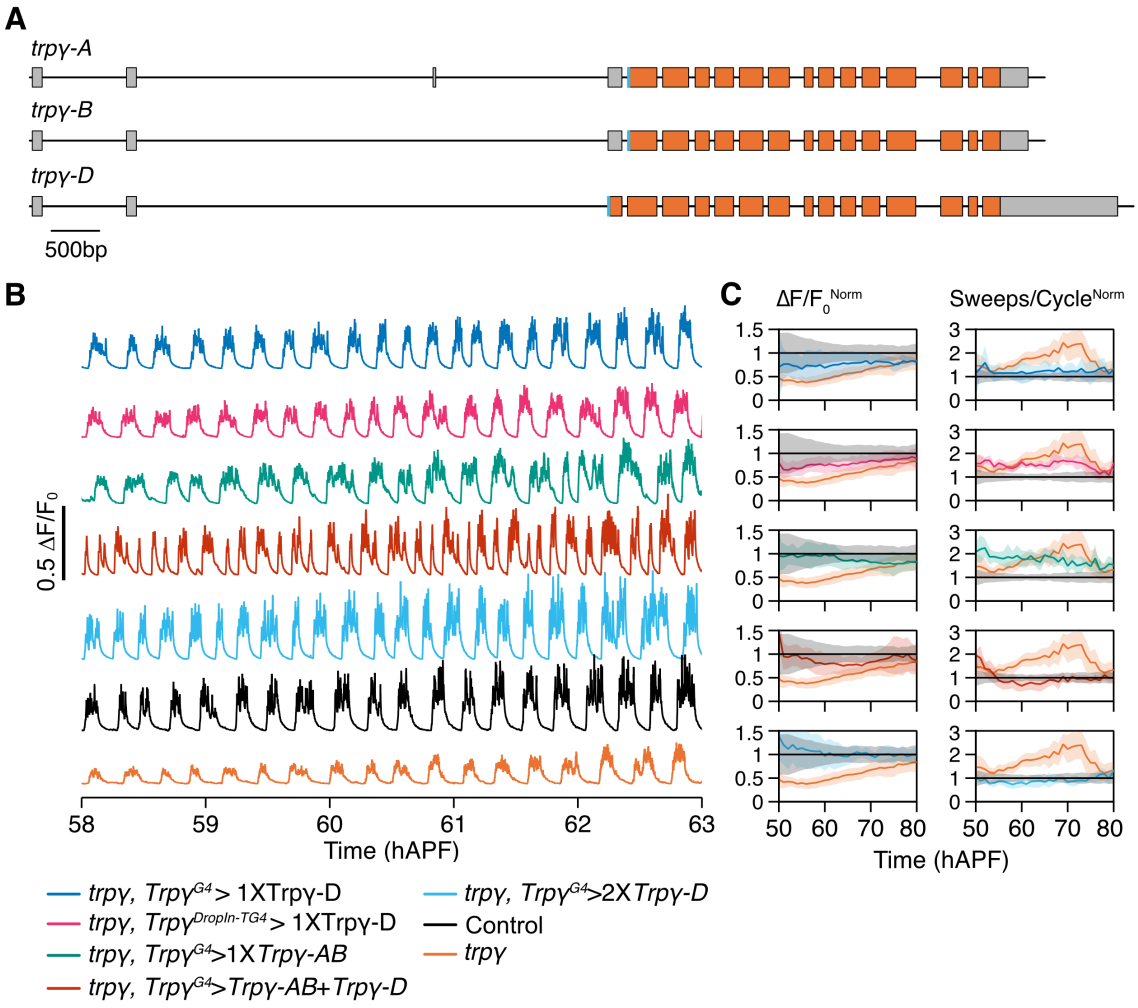

Supplementary Figure 3.3. Trpγ-D is sufficient to rescue wildtype PSINA.

A. Schematic of *Trpγ* locus indicating locations of exons (orange rectangles), untranslated regions (gray rectangles), and introns (black lines between exons or untranslated regions) for each isoform. Scale bar, 500 bp.

B. Representative traces of activity in: Trpγ-D expression with $Trp\gamma^{G4}$ (blue, n=8), Trpγ-D expression with $Trp\gamma^{DropIn\text{-}TG4}$ (magenta, n=7), Trpγ-AB expression with $Trp\gamma^{G4}$ (green, n=9), Trpγ-AB and Trpγ-D expression with $Trp\gamma^{G4}$ (red, n=10), double Trpγ-D expression with $Trp\gamma^{G4}$ (cyan, n=4), control (black, n=19), and *trpγ* mutant (orange, n=31) pupae.

C. Active phase average amplitude (left) and sweeps/cycle (right) binned by hour and normalized to control activity between 55 and 65 hAPF. Shaded areas, SD. Genotypes color-matched to B.

Supplementary Figure 3.4.

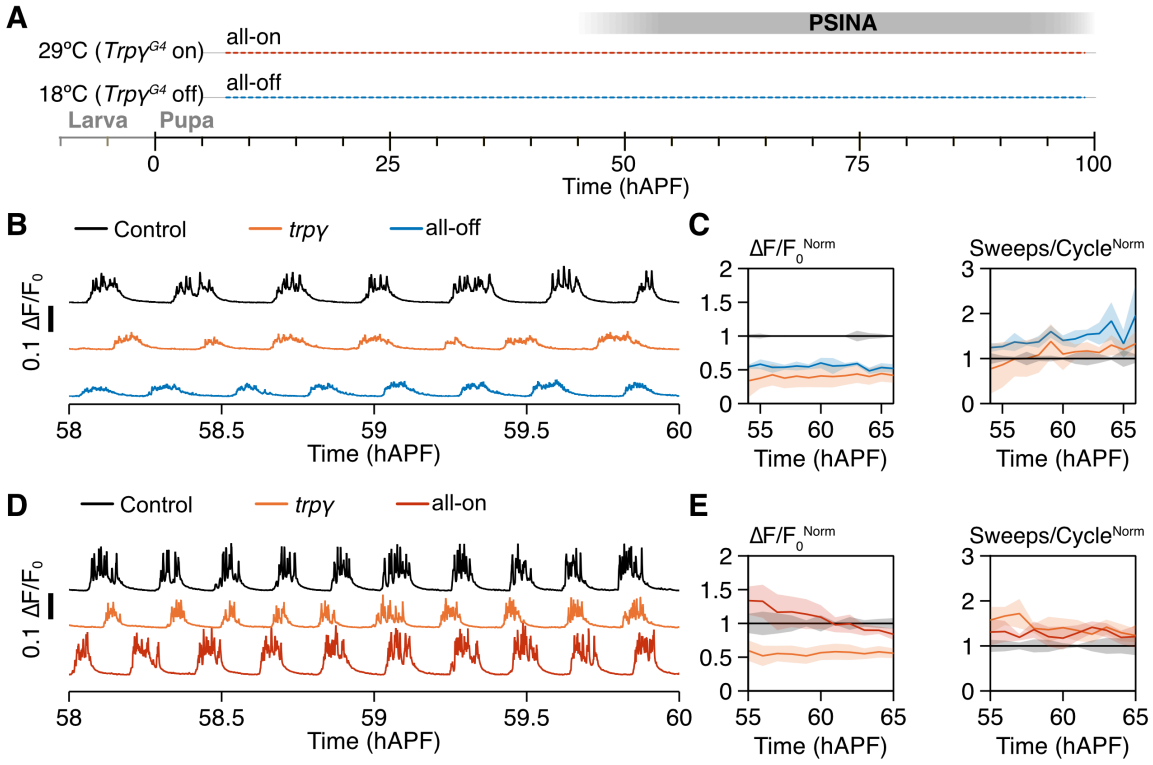

Supplementary Figure 3.4. Temperature-dependent rescue controls.

A. Expression control of UAS-Trpγ-D with TARGET (i.e. GAL80ts). In the 'all-on' condition, flies are reared at 29ºC. In the 'all-off' condition, flies are reared at 18ºC.

B,D. Representative traces of activity in control pupae (black, n=3), *trpγ* null pupae (orange, n=3), and (B) all-off pupae (blue, n=3) or (D) all-on pupae (red, n=3).

C,E. Active phase average amplitude (left) and sweeps/cycle (right) binned by hour and normalized to control activity between 55 and 65 hAPF. Shaded areas, SD. Genotypes color-matched to B and D.

Supplementary Figure 3.5.

A Wildtype medulla synapse counts

Cell Type	Takemura et al., 2008	Takemura et al., 2013	Chen et al., 2014	This work
R8	35 ± 1 (n = 3)	50 (n = 1)	46 ± 5 (n = 30)	50 ± 6 (n = 46)
L4	22 ± 2 (n = 3)	26 (n = 1)	26 ± 4 (n = 30)	22 ± 3 (n = 44)

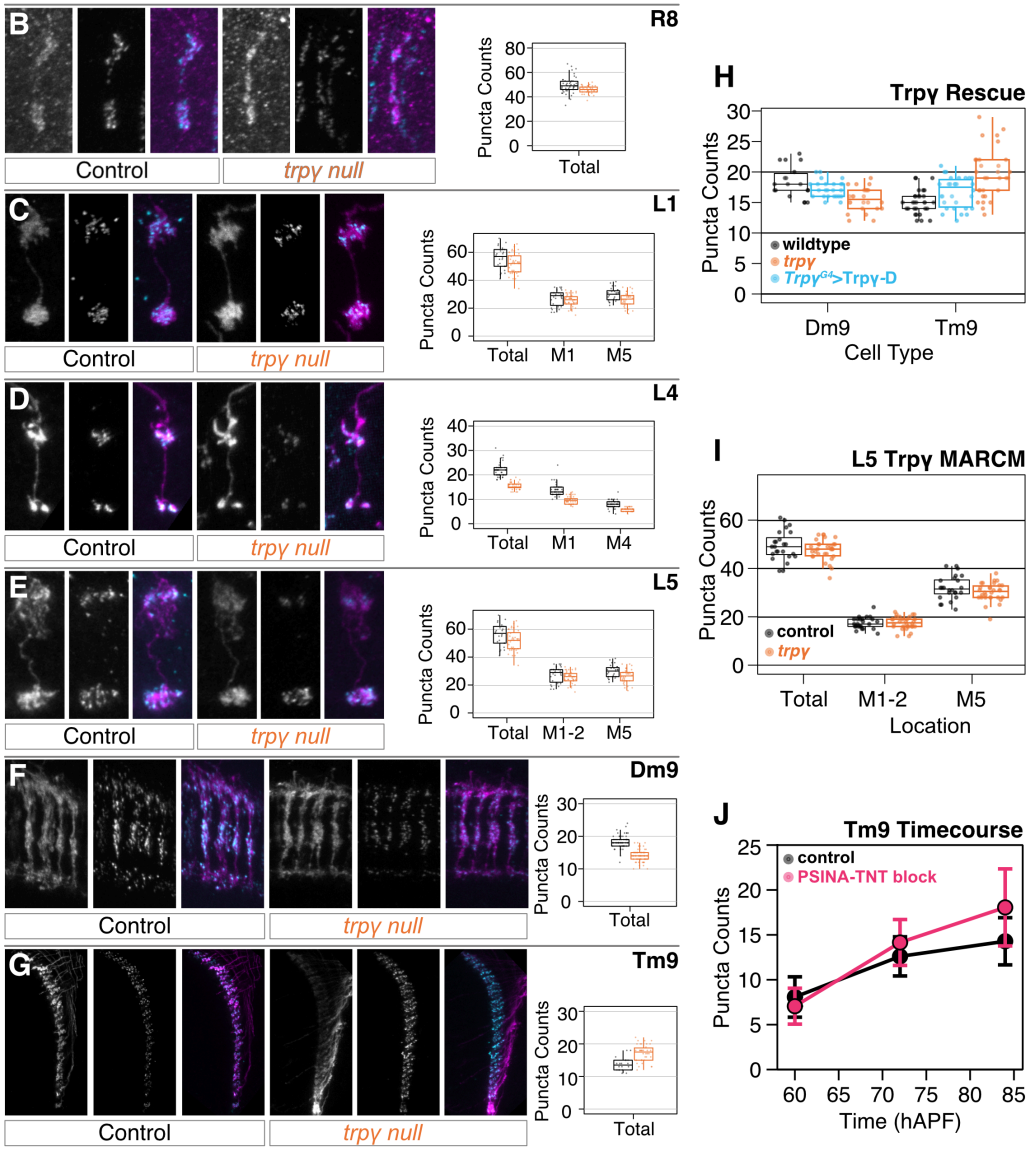

Supplementary Figure 3.5. Synapse formation in the visual system depends on PSINA.

A. Table comparing control synapse counts in cells with sparse synaptic density across EM and light microscopy studies. Values are mean synapse count ± SD, with sample size in parentheses.

B-G. *Left*: representative micrographs of R8 (B), L1 (C), L4 (D), L5 (E), Dm9 (F), and Tm9 (G) neurons in control (left set) and *trpγ* (right set) animals with cell membranes (myr::tdTOM, magenta in merged) and presynaptic sites (BRP-V5, cyan in merged) labeled. *Right*: Brp puncta counts by layer in heterozygous control (black, n=18-61 per cell type) and *trpγ* (orange, n=26-65 per cell type) animals. Points indicate individual cells. Box-and-whiskers mark 5^{th}, 25^{th}, 50^{th}, 75^{th}, and 95^{th} percentiles.

H. Brp puncta counts in *Trpγ* heterozygotes (black, n=18 for Dm9, n=30 for Tm9), *trpγ* nulls (orange, n=24 for Dm9, n=30 for Tm9), or *trpγ* null with Trpγ-D expressed in Trpγ+ cells (cyan, n=24 for Dm9, n=30 for Tm9). Boxplots as in B-G.

I. Brp puncta counts in control (black, n = 24) or *trpγ* null (orange, n = 30) L5 clones generated by MARCM. Boxplots as in B-G.

J. Average Brp puncta through development in control (black, n=64-88 per timepoint) or animals with PSINA blocked with pan-neuronally expressed TNT (magenta, n=35-68 per timepoint). Presynaptic sites assessed at 60, 72, and 84 hAPF. Error bars, SD.

Supplementary Figure 3.6.

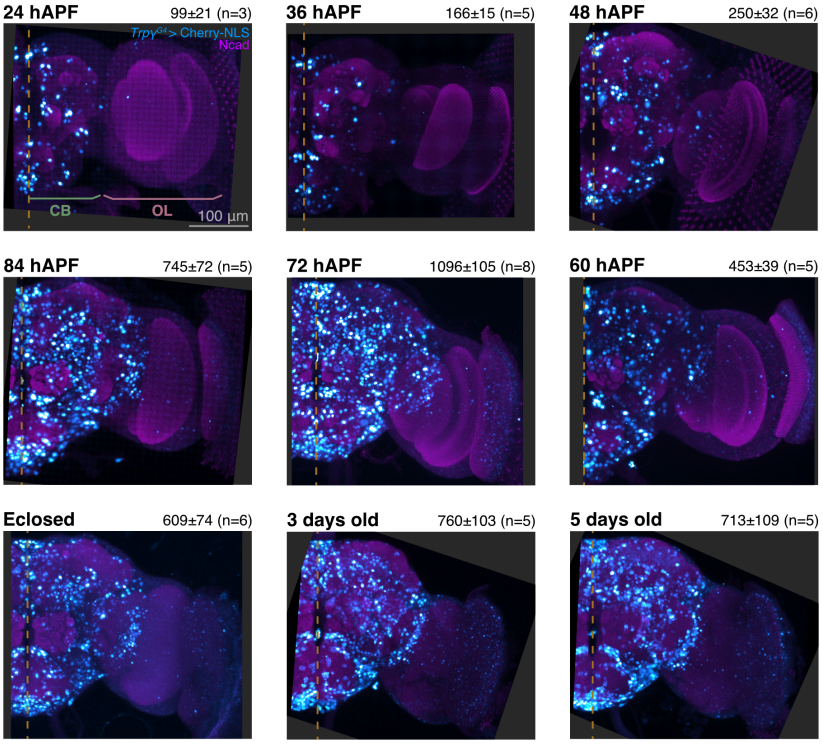

Supplementary Figure 3.6. *Trpγ* expression domain transiently expands during pupal development.

MIPs of half-brain confocal stacks from different times during pupal development and early adult life. Nuclei of mCherry-NLS expressing Trpγ+ neurons shown (cyan); reference marker is Ncad (magenta). Average, SD, and number of samples for each time point are printed top-right of panels; these values are plotted in Figure 3.4A. Dashed yellow lines mark the median plane. CB, central brain. OL, optic lobe. Scale bar, 100μm.

Supplementary Figure 3.7.

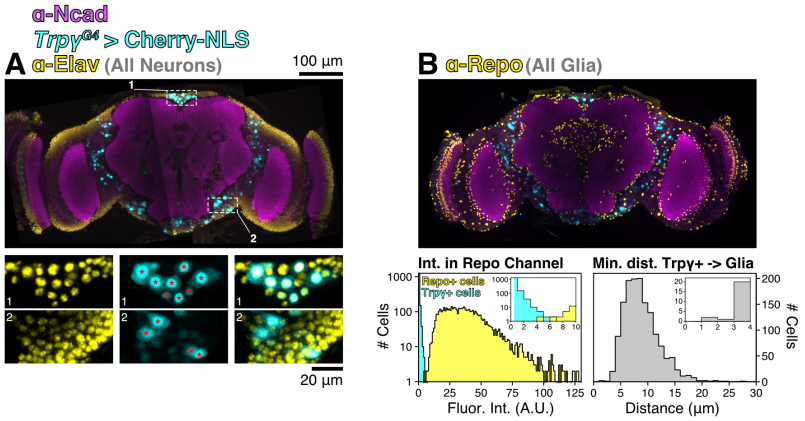

Supplementary Figure 3.7. Trpγ+ cells in the developing brain are neurons.

A. *Top:* 13μm-thick MIP of a 72 hAPF brain stained for neuronal nuclei (anti-Elav, yellow), Trpγ+ nuclei (mCherry-NLS, cyan), and a reference marker (Ncad, magenta). Image derived from three stitched confocal stacks. Scale bar, 100μm. *Bottom:* Expanded views of two regions-of-interest (ROIs) boxed in top panel. Columns are neuronal, Trpγ+, and merged channels, left to right. All Trpγ+ nuclei fully captured in the MIP (red asterisks) co-localize with the neuronal stain. Scale bar, 20μm. **B.** *Top:* 13μm-thick MIP of a 72 hAPF brain stained for glial nuclei (anti-Repo, yellow), Trpγ+ nuclei (mCherry-NLS, cyan), and a reference marker (Ncad, magenta). Image derived from three stitched confocal stacks. Scale bar, 100μm. *Bottom-left:* Histogram of average voxel intensities of segmented Repo+ and Trpγ+ nuclei measured in the anti-Repo channel of the top image. n=5055 (Repo+), 1464 (Trpγ+); half-brain complements analyzed. Inset shows where 9/1464 Trpγ+ cell intensities overlap with the dimmest Repo+ glia. *Bottom-right:* Histogram of minimum pairwise distance between centroids of 1464 segmented Trpγ+ and Repo+ nuclei. Inset shows all pairs of Trpγ+ and Repo+ nuclei are at least 1μm apart.

Supplementary Figure 3.8.

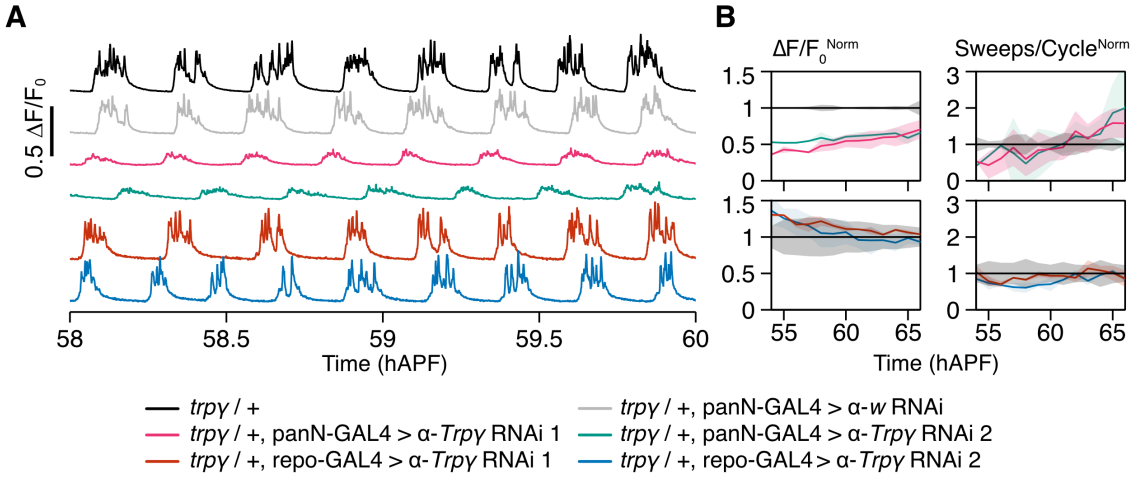

Supplementary Figure 3.8. *Trpγ* knockdown reveals requirement in neurons.

A. Representative traces of activity in control pupae (black), pan-neuronal control knockdown pupae (gray, n=2), pan-neuronal *Trpγ* knockdown (magenta, n=3; green, n =3), pan-glial *Trpγ* knockdown (red, n=2; blue, n=2) in heterozygous *Trpγ* background.

B. Active phase average amplitude (left) and sweeps/cycle (right) binned by hour and normalized to control activity between 55 and 65 hAPF. Shaded areas, SD. Genotypes color-matched to A.

Supplementary Figure 3.9.

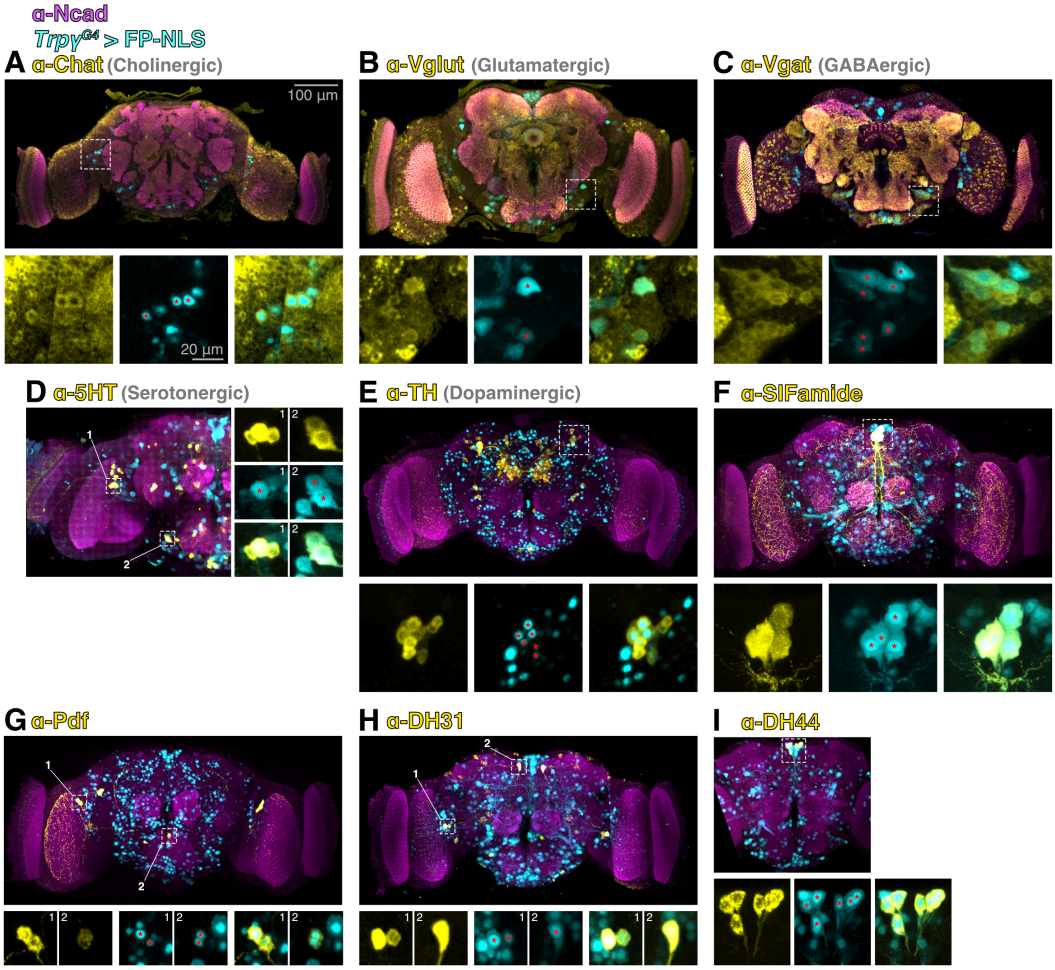

Supplementary Figure 3.9. Trpγ+ neurons are a diverse population.

A-I. *Top:* 13µm-thick (A-C) or full (D-I) MIPs of 72 hAPF brains stained for neuronal class marker (yellow), Trpγ+ nuclei (mCherry-NLS or GFP-NLS, cyan), and a reference marker (Ncad, magenta). Images (A-C, E-H) derived from three stitched confocal stacks. Scale bar, 100µm. *Bottom:* Expanded view(s) of ROI(s) boxed in top panel. Columns (D, rows) are class marker, Trpγ+, and merged channels, left to right (D, top to bottom). Marked Trpγ+ nuclei (red asterisks) co-localize with the neuronal class marker. Scale bar, 20µm.

Supplementary Figure 3.10.

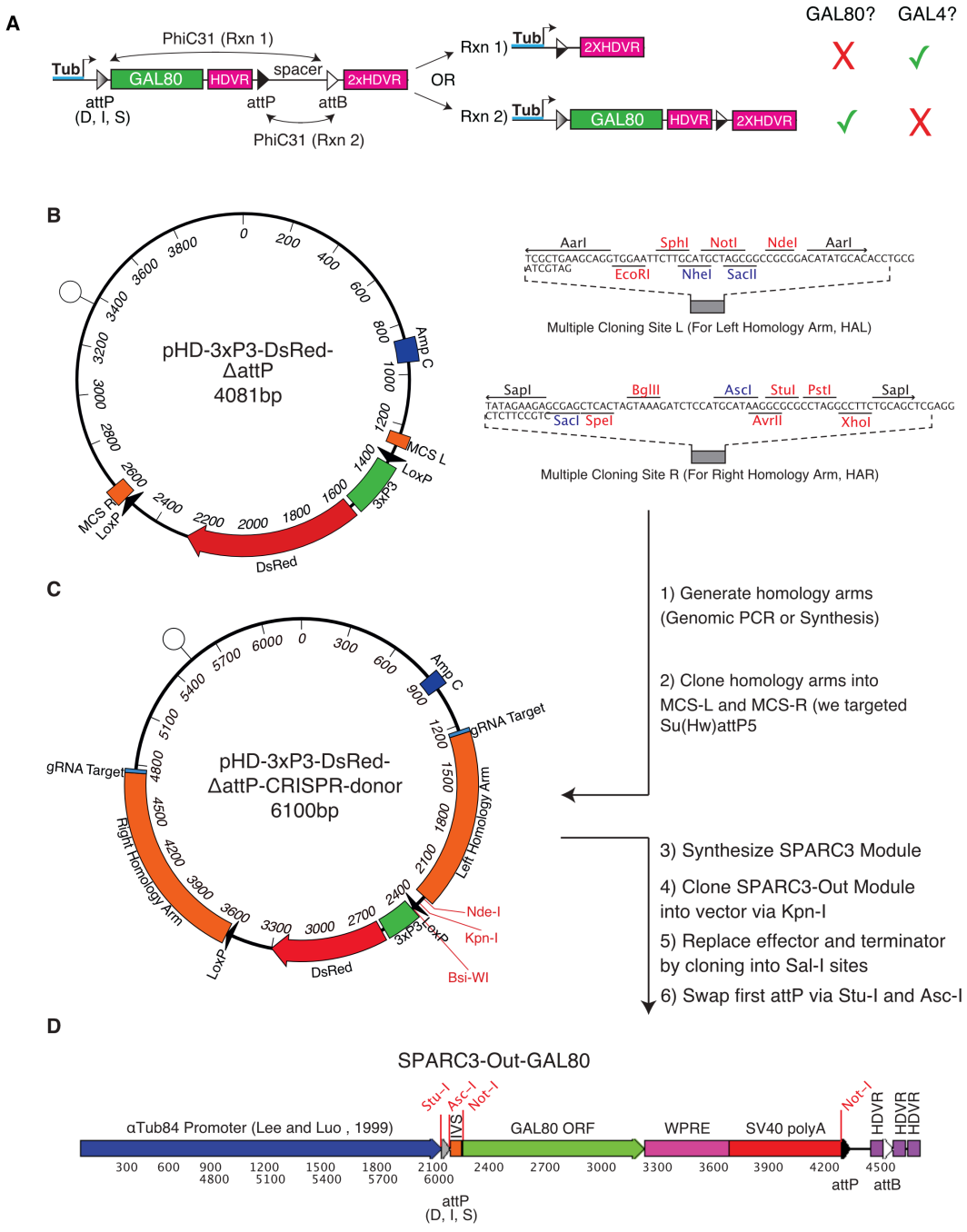

Supplementary Figure 3.10. SPARC3-Out-GAL80

A. Schematic of the SPARC3-Out-GAL80 cassette. PhiC31 recombines one of two competing *attP* target sequences with one *attB* target sequence. Rxn 1 leads to loss of the GAL80 ORF, disinhibiting GAL4-driven effector expression. Rxn 2 preserves Tubulin promoter driven GAL80 expression, maintaining GAL4 inhibition. Three progressively truncated variants for the first *attP* sequence were designed {Isaacman-Beck et al. 2020} to bias the recombination in favor of Rxn 2, resulting in frequent (Dense), sporadic (Intermediate), or rare (Sparse) loss of GAL80 and disinhibition of GAL4>UAS expression.

B. Map of pHD-3xP3-DsRed-Δ*attP* (a CRISPR-HDR-donor precursor) showing multiple cloning sites for homology arm insertion (right).

C. Map of pHD-3xP3-DsRed-Δ*attP*-CRISPR-donor (example includes homology arms targeting the *Su(Hw)AttP5* region of the *Drosophila* genome). **D.** Assembled SPARC3-Out-GAL80 cassette; see Materials and Methods for details. MCS, multiple cloning site. gRNA, guide RNA. HDVR, hepatitis delta virus ribozyme sequence.

Supplementary Figure 3.11.

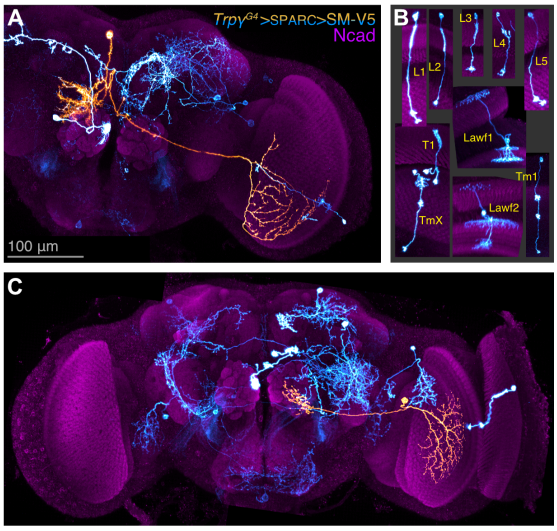

Supplementary Figure 3.11. SPARC reveals morphologies of individual Trpγ+ neurons.

A,C. Single *Trpγ*+ neuron (orange, manually segmented) in the context of others (cyan) labeled using SPARC. Neurons expressing myr::SM-V5. Reference marker (magenta), Ncad. Image MIP of stitched confocal stacks of 72 hAPF brain. Scale bar, 100µm.

B. *Trpγ*+ visual processing neurons identified in 72 hAPF brains using SPARC. We observed a given neuron up to three times in 30 sparsely labeled brains.

Supplementary Figure 3.12.

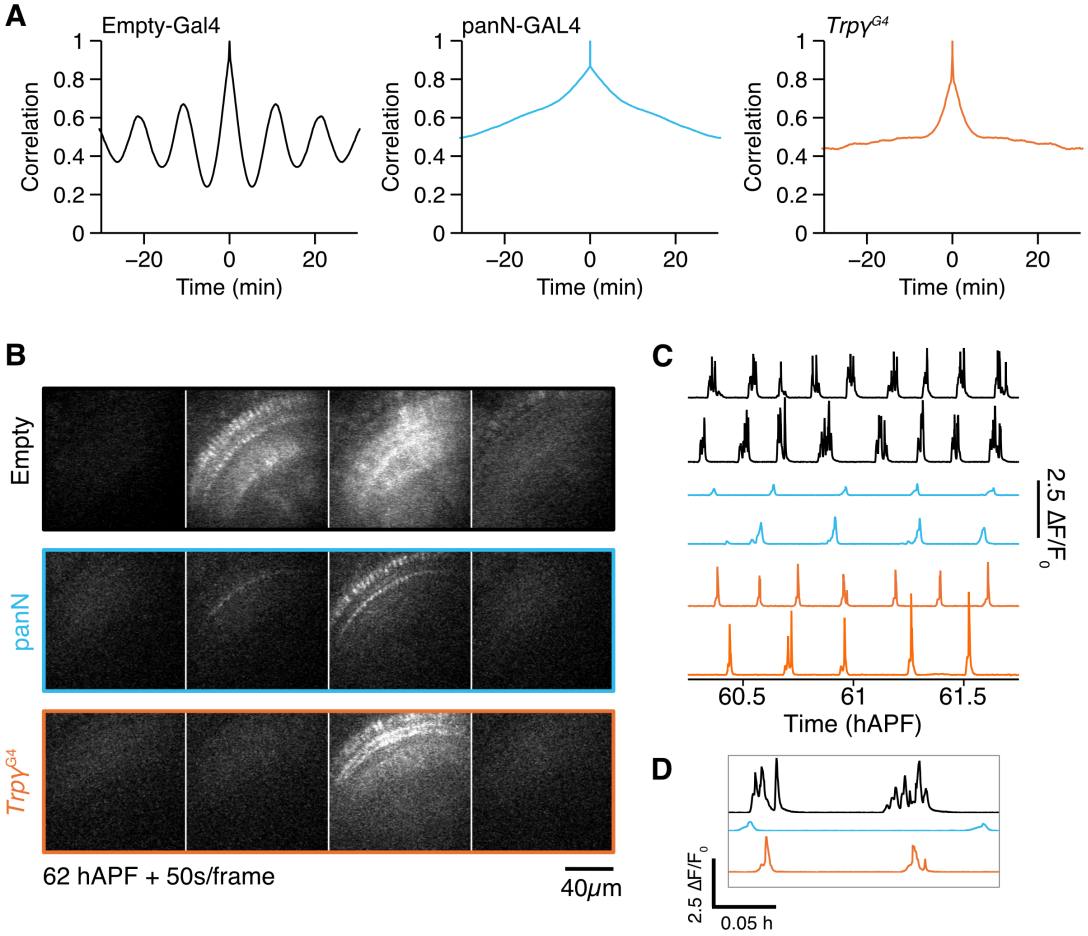

Supplementary Figure 3.12. PSINA requires Trpγ+ neuron activity.

A. Representative autocorrelograms from pan-neuronal GCaMP6s in control (empty-GAL4, black), panN-GAL4>Kir2.1 (blue), and $Trp\gamma^{G4}$>Kir2.1 (orange) pupae.

B,C. Representative micrographs (B) and traces (C) from 2PM imaging of pan-neuronal GCaMP6s in control (empty-GAL4, black), panN-GAL4>Kir2.1 (blue), and $Trp\gamma^{G4}$>Kir2.1 (orange) pupae. Scale bar, 40μm. D. *Inset*: expanded view showing fewer sweeps in panN-GAL4 and $Trp\gamma^{G4}$ conditions.

Supplementary Figure 3.13.

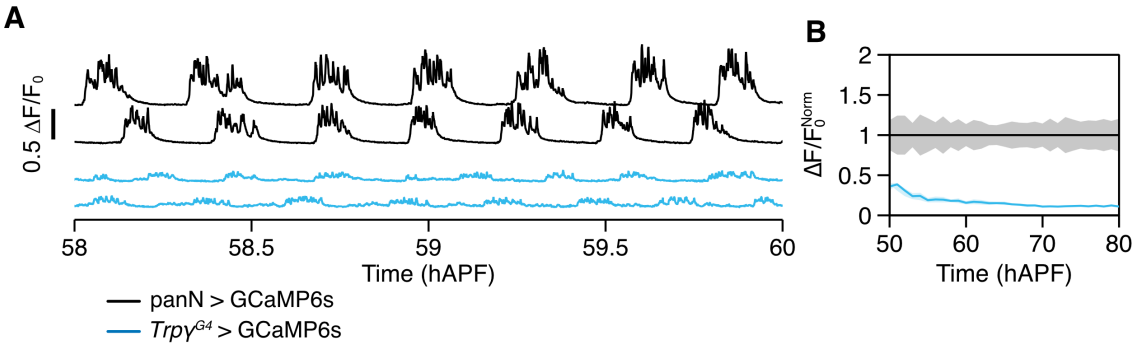

Supplementary Figure 3.13. Trpγ+ neurons account for ~15% of total PSINA amplitude.

A. Representative traces for Trpγ+ neurons expressing GCaMP6s (cyan, n=10) and pan-neuronal expression of GCaMP6s (black, n=10) by wide-field imaging with a ROI encompassing the head. B. Active phase average amplitude for Trpγ+ neurons expressing GCaMP6s (cyan) binned by hour and normalized to pan-neuronal expression of GCaMP6s (black). Shaded areas, SD.

Supplementary Figure 3.14.

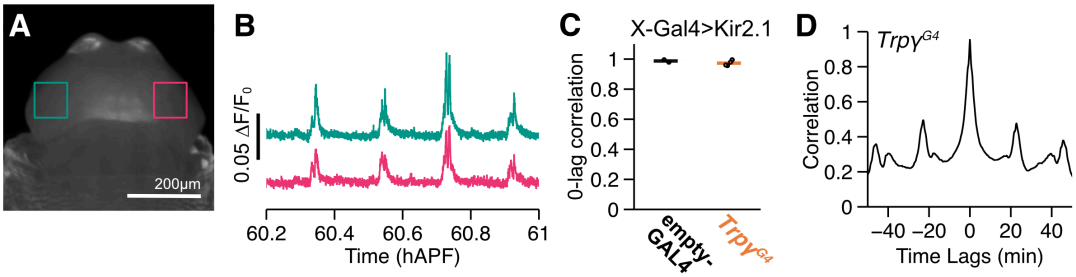

Supplementary Figure 3.14. Residual activity is correlated across the brain.

A,B. AIP of pupae expressing pan-neuronal GCaMP6s (A). ROIs indicate regions used to calculate traces (B) from optic lobes. Scale bar, 200μm.

C. 0-lag correlation between traces in each optic lobe in control (empty-GAL4, black, n=4), and $Trp\gamma^{G4}$>Kir2.1 (orange, n=4) pupae. Round markers are values from individual time series, bars are averages for each genotype.

D. Correlogram between traces in each optic lobe in $Trp\gamma^{G4}$>Kir2.1 pupa

Supplementary Figure 3.15.

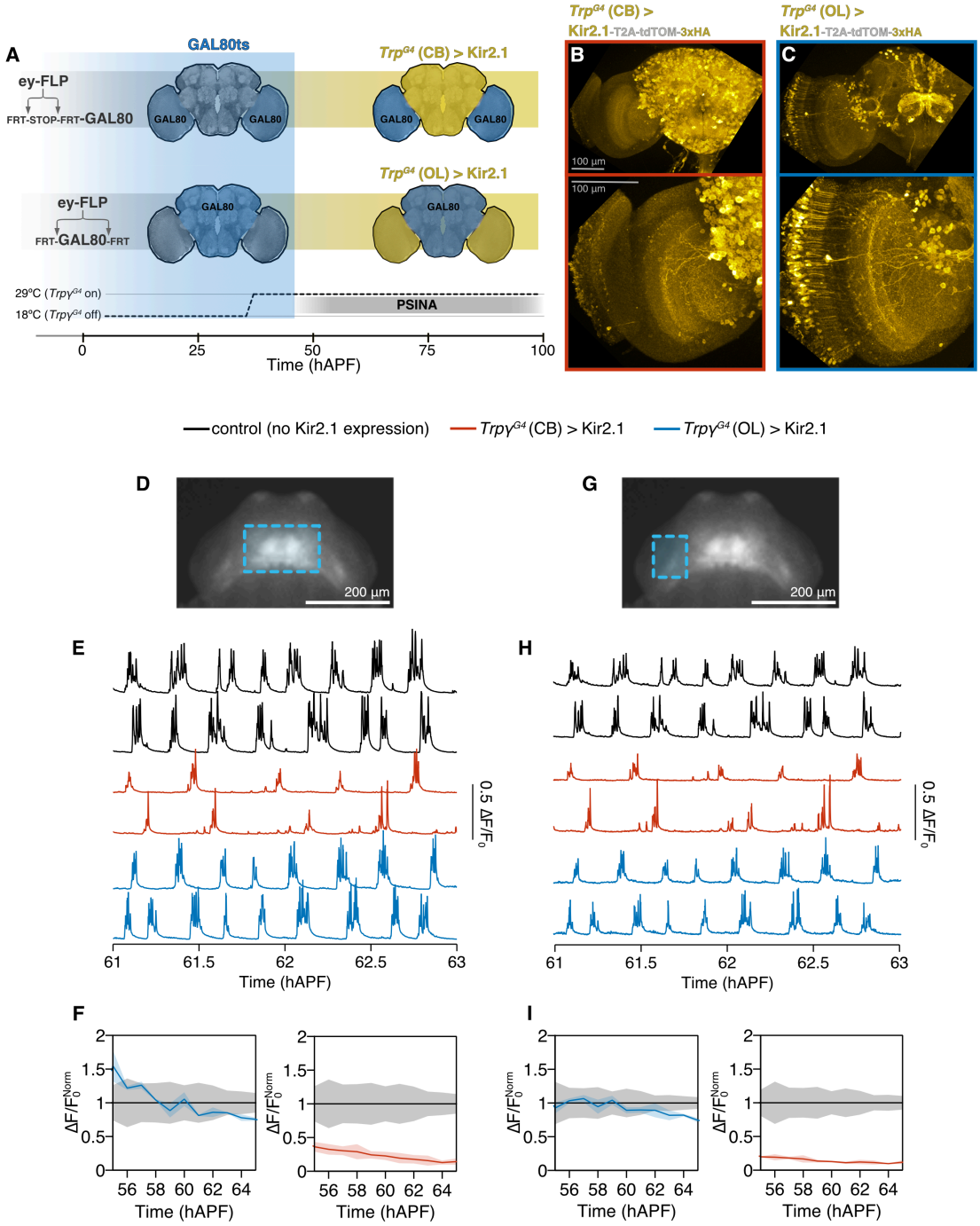

Supplementary Figure 3.15. Silencing Trpγ+ neurons in the central brain, but not the optic lobes, attenuates PSINA.

A. Schematic of spatially-targeted Kir2.1 expression. Both experimental genotypes carry two variants of tubP-GAL80: GAL80ts and one of two FLP-responsive conditional alleles. In the optic lobes, ey-FLP either turns on GAL80 expression by removing the interruption cassette ('-STOP-', top) or turns it off by locally excising the FRT-flanked ORF (bottom). Animals are reared at 18ºC and shifted 29ºC at 40 hAPF to unmask these differential GAL80 expression domains (blue) just prior to PSINA onset; GAL4-driven Kir2.1 expression is disinhibited in the complementary domains (yellow). CB, central brain. OL, optic lobe.

B,C. MIPs of half-brains (top) or optic lobes (bottom) at 60 hAPF in which $Trp\gamma^{G4}$ is driving Kir2.1 expression in the CB (B) or the OL (C). The OL condition also includes expression in the antennal lobes and a small number of CB neurons. Kir2.1 expression domain detected by staining against 3xHA tagged co-cistronic tdTOM. Scale bar, 100μm.

D,G. AIP of ~60 hAPF pupa expressing GCaMP6s pan-neuronally. CB (D) and OL (G) ROIs used for measuring PSINA outlined (cyan). Scale bar, 200μm.

E,H. PSINA traces from CB (E) and OL (H) for control (no Kir2.1, black, n=5), $Trp\gamma^{G4}$(CB)>Kir2.1 (red, n=3), and $Trp\gamma^{G4}$(OL)>Kir2.1 (blue, n=3) genotypes.

F,I. Average amplitude measured in CB (F) and OL (G) normalized to corresponding control activity. Shaded areas, SD. Genotypes color-matched to E.

Supplementary Figure 3.16.

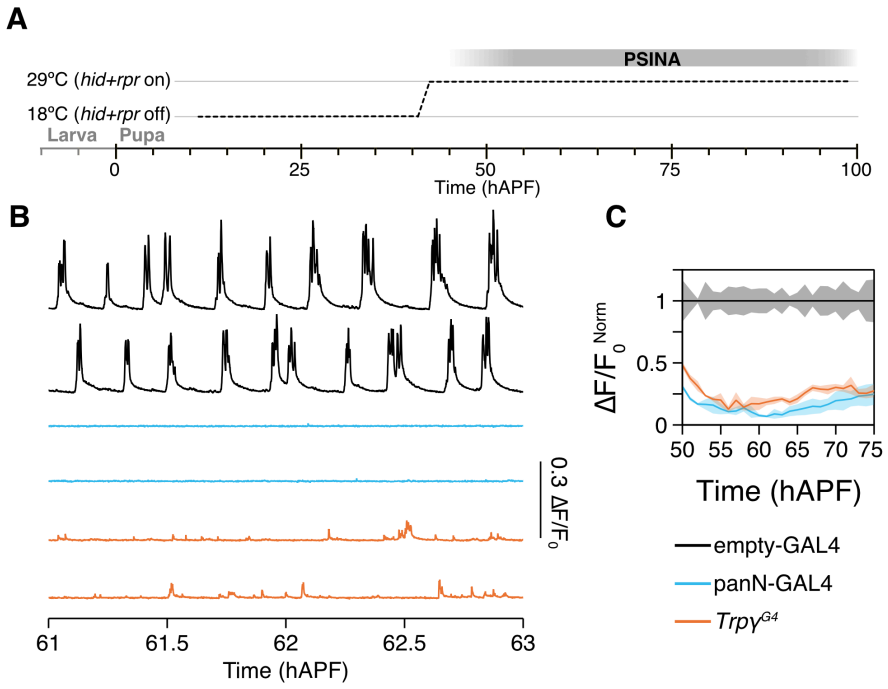

Supplementary Figure 3.16. Trpγ+ neurons are necessary for PSINA.

A. Expression control of UAS-hid, rpr with TARGET; animals shifted from 18ºC to 29ºC at 40 hAPF.

B. PSINA traces from pan-neuronal GCaMP6s in control (empty-GAL4, black, n=3), panN-GAL4>hid, rpr (blue, n=3), and $Trp\gamma^{G4}$>hid, rpr (orange, n=3) pupae.

C. Average amplitude normalized to control activity between 55 and 75 hAPF. Shaded areas, SD. Genotypes color-matched to B.

Supplementary Figure 3.17.

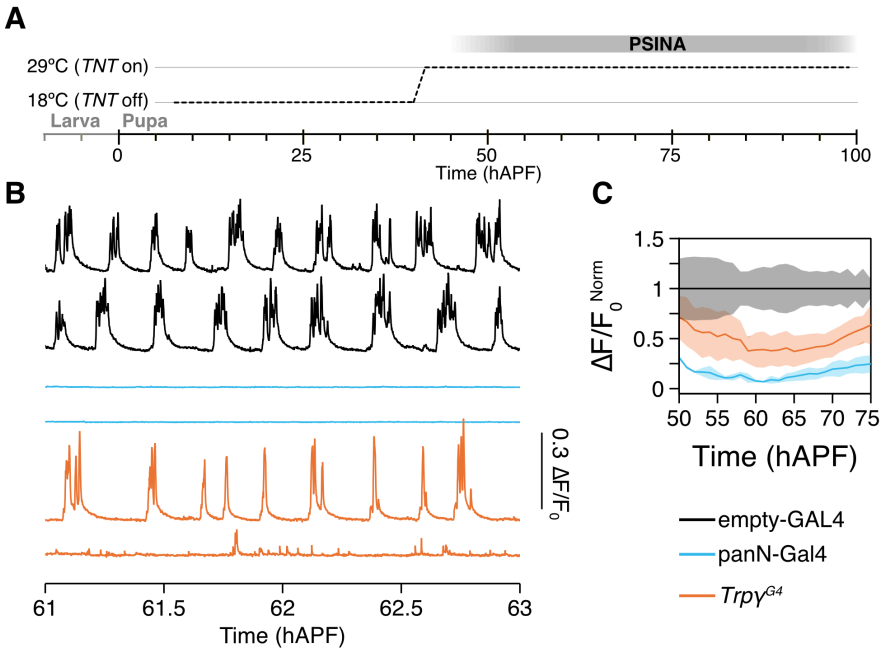

Supplementary Figure 3.17. Neurochemical transmission by Trpγ+ neurons is necessary for PSINA.

A. Expression control of UAS-TNT with TARGET; animals shifted from 18ºC to 29ºC at 40 hAPF.

B. PSINA traces from pan-neuronal GCaMP6s in control (empty-GAL4, black, n=7), panN-GAL4>TNT (blue, n=7), and $Trp\gamma^{G4}$>TNT (orange, n=8) pupae.

C. Average amplitude normalized to control activity between 55 and 75 hAPF. Shaded areas, SD. Genotypes color-matched to B.

Supplementary Figure 3.18.

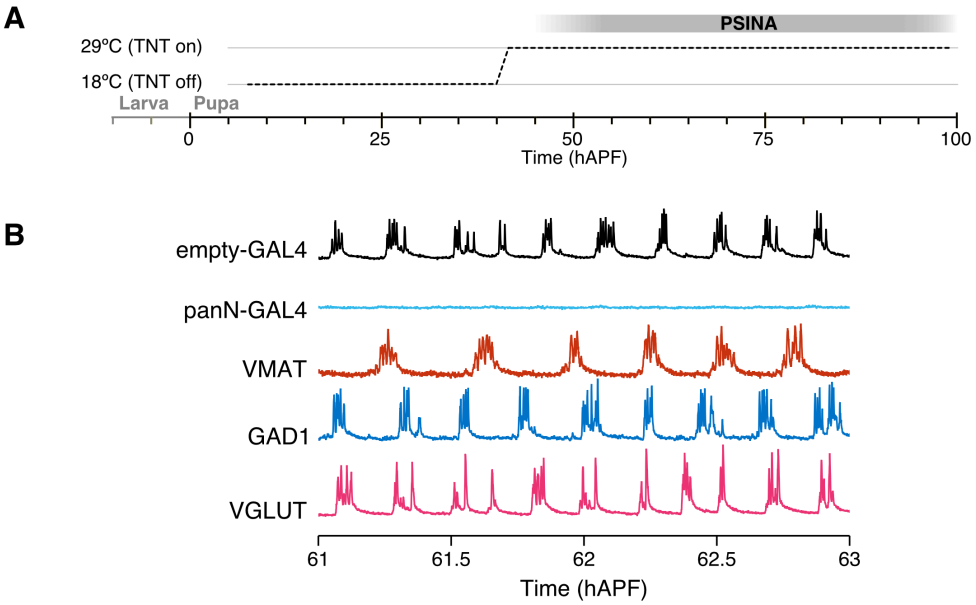

Supplementary Figure 3.18. Generic neuronal silencing does not attenuate PSINA.

A. Expression control of UAS-TNT with TARGET; animals shifted from 18ºC to 29ºC at 40 hAPF.

B. Representative traces of pupae expressing pan-neuronal GCaMP6s, with TNT expressed in expression domains of the indicated neuronal class. n=4 tested for each genotype.

Supplementary Figure 3.19.

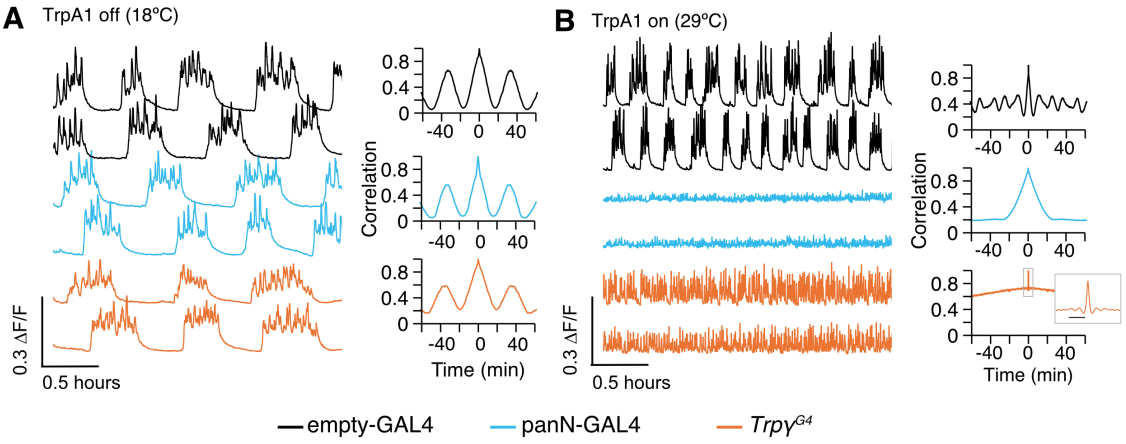

Supplementary Figure 3.19. Activation of Trpγ+ neurons increases brain-wide activity frequency.

A-B. *Left*: PSINA traces from pan-neuronal GCaMP6s in control (empty-GAL4, black, n=3), panN-GAL4>TrpA1 (blue, n=3), and $Trp\gamma^{G4}$>TrpA1 (orange, n=3) pupae at 18ºC (A) or 29ºC (B). *Right*: representative auto-correlograms calculated from the first trace shown for each genotype. *Inset (B)*: expanded view of boxed region. Scale bar, 2min

Table 3. List of genotypes used in this work.

Figure	Cells Imaged / Label	Description in Figure	Fly Genotype	Notes
Fig3.1A-C	PanN / GCaMP	Control	*w;* *R57C10-lexA (attP40), TI-Trpγ[1], 13XLexAop2-opGCaMP6s (su(Hw)attP5) / +;* *+*	
Fig3.1C-D	PanN / GCaMP	*trpγ*	*w;* *R57C10-lexA (attP40), TI-Trpγ[1], 13XLexAop2-opGCaMP6s (su(Hw)attP5) / TI-Trpγ[1];* *+*	
Fig3.1D, FigS3.3B-C	PanN / GCaMP	*trpγ*, 2X UAS-Trpγ-D rescue in Trpγ+ neurons	*w;* *R57C10-lexA (attP40), TI-Trpγ[1], 13XLexAop2-opGCaMP6s (su(Hw)attP5) / TI-Trpγ^{G4};* *UAS-Trpγ-D (su(Hw)attP1)*	
Fig3.1G-I, FigS3.4	PanN / GCaMP	Control	*w;* *R57C10-lexA (attP40), TI-Trpγ[1], 13XLexAop2-opGCaMP6s (su(Hw)attP5) / +;* *UAS-Trpγ-D (su(Hw)attP1) / tubP-GAL80ts(2)*	
Fig3.1G-I, FigS3.4	PanN / GCaMP	*trpγ*, 1X UAS-Trpγ-D rescue in Trpγ+ neurons	*w;* *R57C10-lexA (attP40), TI-Trpγ[1], 13XLexAop2-opGCaMP6s (su(Hw)attP5) / TI-Trpγ^{G4};* *UAS-Trpγ-D (su(Hw)attP1) / tubP-GAL80ts(2)*	
Fig3.1G-I, FigS3.4	PanN / GCaMP	*trpγ*	*w;* *R57C10-lexA (attP40), TI-Trpγ[1], 13XLexAop2-opGCaMP6s (su(Hw)attP5) / TI-Trpγ[1]*; UAS-*Trpγ-D (su(Hw)attP1) / tubP-GAL80ts(2)*	
Fig3.2	L1 / GCaMP	Control	*20XUAS-IVS-Syn21-opGCaMP6s-p10 (su(Hw)attP8) / w;* *R57C10-LexA (attP40), 13XLexAop2-IVS-NES-jRCaMP1b-p10 (su(Hw)attP5) / TI-Trpγ[1];* *20XUAS-IVS-Syn21-opGCaMP6s-p10 (su(Hw)attP1) / svp-GAL4 (87B5)*	jRCaMP1b not used in analysis
Fig3.2	L3 / GCaMP	Control	*20XUAS-IVS-Syn21-opGCaMP6s-p10 (su(Hw)attP8) / w;* *R57C10-LexA (attP40), 13XLexAop2-IVS-NES-jRCaMP1b-p10 (su(Hw)attP5) / TI-Trpγ[1];* *20XUAS-IVS-Syn21-opGCaMP6s-p10 (su(Hw)attP1) / R29F12-GAL4 (attP2)*	jRCaMP1b not used in analysis
Fig3.2	L5 / GCaMP	Control	*20XUAS-IVS-Syn21-opGCaMP6s-p10 (su(Hw)attP8) / w;* *R57C10-LexA (attP40), 13XLexAop2-IVS-NES-jRCaMP1b-p10 (su(Hw)attP5) / TI-Trpγ[1];* *20XUAS-IVS-Syn21-opGCaMP6s-p10 (su(Hw)attP1) / R64B07-GAL4 (attP2)*	jRCaMP1b not used in analysis
Fig3.2	Mi1 / GCaMP	Control	*20XUAS-IVS-Syn21-opGCaMP6s-p10 (su(Hw)attP8) / w;* *R57C10-LexA (attP40), 13XLexAop2-IVS-NES-jRCaMP1b-p10 (su(Hw)attP5) / TI-Trpγ[1];* *20XUAS-IVS-Syn21-opGCaMP6s-p10 (su(Hw)attP1) / R89C04-GAL4 (attP2)*	jRCaMP1b not used in analysis
Fig3.2	Mi4 / GCaMP	Control	*20XUAS-IVS-Syn21-opGCaMP6s-p10 (su(Hw)attP8) / w;* *R57C10-LexA (attP40), 13XLexAop2-IVS-NES-jRCaMP1b-p10 (su(Hw)attP5) / TI-Trpγ[1];* *20XUAS-IVS-Syn21-opGCaMP6s-p10 (su(Hw)attP1) / R49B06-GAL4 (attP2)*	jRCaMP1b not used in analysis
Fig3.2	Tm3 / GCaMP	Control	*20XUAS-IVS-Syn21-opGCaMP6s-p10 (su(Hw)attP8) / w;* *R57C10-LexA (attP40), 13XLexAop2-IVS-NES-jRCaMP1b-p10 (su(Hw)attP5) / TI-Trpγ[1];* *20XUAS-IVS-Syn21-opGCaMP6s-p10 (su(Hw)attP1) / R13E12-GAL4 (attP2)*	jRCaMP1b not used in analysis
Fig3.2	Tm4 / GCaMP	Control	*20XUAS-IVS-Syn21-opGCaMP6s-p10 (su(Hw)attP8) / w;* *R57C10-LexA (attP40), 13XLexAop2-IVS-NES-jRCaMP1b-p10 (su(Hw)attP5) / TI-Trpγ[1];* *20XUAS-IVS-Syn21-opGCaMP6s-p10 (su(Hw)attP1) / R35H01-GAL4 (attP2)*	jRCaMP1b not used in analysis

Figure	Cells Imaged / Label	Description in Figure	Fly Genotype	Notes
Fig3.2	Tm9 / GCaMP	Control	*20XUAS-IVS-Syn21-opGCaMP6s-p10 (su(Hw)attP8) / w;* *R57C10-LexA (attP40), 13XLexAop2-IVS-NES-jRCaMP1b-p10 (su(Hw)attP5) / TI-Trpγ[1];* *20XUAS-IVS-Syn21-opGCaMP6s-p10 (su(Hw)attP1) / R24C08-GAL4 (attP2)*	jRCaMP1b not used in analysis
Fig3.2	T4, T5 / GCaMP	Control	*20XUAS-IVS-Syn21-opGCaMP6s-p10 (su(Hw)attP8) / w;* *R57C10-LexA (attP40), 13XLexAop2-IVS-NES-jRCaMP1b-p10 (su(Hw)attP5) / TI-Trpγ[1];* *20XUAS-IVS-Syn21-opGCaMP6s-p10 (su(Hw)attP1) / R23G12-GAL4 (attP2)*	jRCaMP1b not used in analysis
Fig3.2	Dm9 / GCaMP	Control	*20XUAS-IVS-Syn21-opGCaMP6s-p10 (su(Hw)attP8) / w;* *R57C10-LexA (attP40), 13XLexAop2-IVS-NES-jRCaMP1b-p10 (su(Hw)attP5) / TI-Trpγ[1];* *20XUAS-IVS-Syn21-opGCaMP6s-p10 (su(Hw)attP1) / R67E07-GAL4 (attP2)*	jRCaMP1b not used in analysis
Fig3.2	L1 / GCaMP	*trpγ*	*20XUAS-IVS-Syn21-opGCaMP6s-p10 (su(Hw)attP8) / w;* *R57C10-LexA (attP40), TI-Trpγ[1], 13XLexAop2-IVS-NES-jRCaMP1b-p10 (su(Hw)attP5) / TI-Trpγ[1];* *20XUAS-IVS-Syn21-opGCaMP6s-p10 (su(Hw)attP1) / svp-GAL4 (87B5)*	jRCaMP1b not used in analysis
Fig3.2	L3 / GCaMP	*trpγ*	*20XUAS-IVS-Syn21-opGCaMP6s-p10 (su(Hw)attP8) / w;* *R57C10-LexA (attP40), TI-Trpγ[1], 13XLexAop2-IVS-NES-jRCaMP1b-p10 (su(Hw)attP5) / TI-Trpγ[1];* *20XUAS-IVS-Syn21-opGCaMP6s-p10 (su(Hw)attP1) / R29F12-GAL4 (attP2)*	jRCaMP1b not used in analysis
Fig3.2	L5 / GCaMP	*trpγ*	*20XUAS-IVS-Syn21-opGCaMP6s-p10 (su(Hw)attP8) / w;* *R57C10-LexA (attP40), TI-Trpγ[1], 13XLexAop2-IVS-NES-jRCaMP1b-p10 (su(Hw)attP5) / trpγ;* *20XUAS-IVS-Syn21-opGCaMP6s-p10 (su(Hw)attP1) / R64B07-GAL4 (attP2)*	jRCaMP1b not used in analysis
Fig3.2	Mi1 / GCaMP	*trpγ*	*20XUAS-IVS-Syn21-opGCaMP6s-p10 (su(Hw)attP8) / w;* *R57C10-LexA (attP40), TI-Trpγ[1], 13XLexAop2-IVS-NES-jRCaMP1b-p10 (su(Hw)attP5) / TI-Trpγ[1];* *20XUAS-IVS-Syn21-opGCaMP6s-p10 (su(Hw)attP1) / R89C04-GAL4 (attP2)*	jRCaMP1b not used in analysis
Fig3.2	Mi4 / GCaMP	*trpγ*	*20XUAS-IVS-Syn21-opGCaMP6s-p10 (su(Hw)attP8) / w;* *R57C10-LexA (attP40), TI-Trpγ[1], 13XLexAop2-IVS-NES-jRCaMP1b-p10 (su(Hw)attP5) / TI-Trpγ[1];* *20XUAS-IVS-Syn21-opGCaMP6s-p10 (su(Hw)attP) / R49B06-GAL4 (attP2)*	jRCaMP1b not used in analysis
Fig3.2	Tm3 / GCaMP	*trpγ*	*20XUAS-IVS-Syn21-opGCaMP6s-p10 (su(Hw)attP8) / w;* *R57C10-LexA (attP40), TI-Trpγ[1], 13XLexAop2-IVS-NES-jRCaMP1b-p10 (su(Hw)attP5) / TI-Trpγ[1];* *20XUAS-IVS-Syn21-opGCaMP6s-p10 (su(Hw)attP1) / R13E12-GAL4 (attP2)*	jRCaMP1b not used in analysis
Fig3.2	Tm4 / GCaMP	*trpγ*	*20XUAS-IVS-Syn21-opGCaMP6s-p10 (su(Hw)attP8) / w;* *R57C10-LexA (attP40), TI-Trpγ[1], 13XLexAop2-IVS-NES-jRCaMP1b-p10 (su(Hw)attP5) / TI-Trpγ[1];* *20XUAS-IVS-Syn21-opGCaMP6s-p10 (su(Hw)attP1) / R35H01-GAL4 (attP2)*	jRCaMP1b not used in analysis
Fig3.2	Tm9 / GCaMP	*trpγ*	*20XUAS-IVS-Syn21-opGCaMP6s-p10 (su(Hw)attP8) / w;* *R57C10-LexA (attP40), TI-Trpγ[1], 13XLexAop2-IVS-NES-jRCaMP1b-p10 (su(Hw)attP5) / TI-Trpγ[1];* *20XUAS-IVS-Syn21-opGCaMP6s-p10 (su(Hw)attP1) / R24C08-GAL4 (attP2)*	jRCaMP1b not used in analysis

Figure	Cells Imaged / Label	Description in Figure	Fly Genotype	Notes
Fig3.2	T4, T5 / GCaMP	*trpγ*	*20XUAS-IVS-Syn21-opGCaMP6s-p10 (su(Hw)attP8) / w; R57C10-LexA (attP40), TI-Trpγ[1], 13XLexAop2-IVS-NES-jRCaMP1b-p10 (su(Hw)attP5) / TI-Trpγ[1]; 20XUAS-IVS-Syn21-opGCaMP6s-p10 (su(Hw)attP1) / R23G12-GAL4 (attP2)*	jRCaMP1b not used in analysis
Fig3.2	Dm9 / GCaMP	*trpγ*	*20XUAS-IVS-Syn21-opGCaMP6s-p10 (su(Hw)attP8) / w; R57C10-LexA (attP40), TI-Trpγ[1], 13XLexAop2-IVS-NES-jRCaMP1b-p10 (su(Hw)attP5) / TI-Trpγ[1]; 20XUAS-IVS-Syn21-opGCaMP6s-p10 (su(Hw)attP1) / R67E07-GAL4 (attP2)*	jRCaMP1b not used in analysis
Fig3.3, FigS3.5	Tm3 / STaR	Control	*hsFLPG5-fco (attP3) / Tub84B(FRT.GAL80)(1); 20XUAS-R::PEST / TI-Trpγ[1]; 13XLexAop2-IVS-myr::tdTOM(attP18), 79c23s-RSR-smGdP-V5-2A-LexA (VK31) / R13E12-GAL4 (attP2)*	
Fig3.3, FigS3.5	Tm3 / STaR	*trpγ*	*hsFLPG5-fco (attP3) / Tub84B(FRT.GAL80)(1); 20XUAS-R::PEST, TI-Trpγ[1] / TI-Trpγ[1]; 13XLexAop2-IVS-myr::tdTOM(attP18), 79c23s-RSR-smGdP-V5-2A-LexA (VK31) / R13E12-GAL4 (attP2)*	
Fig3.3, FigS3.5	Mi1 / STaR	Control	*hsFLPG5-fco (attP3) / Tub84B(FRT.GAL80)(1); 20XUAS-R::PEST / TI-Trpγ[1]; 13XLexAop2-IVS-myr::tdTOM (attP18), 79c23s-RSR-smGdP-V5-2A-LexA (VK31) / R89C04-GAL4 (attP2)*	
Fig3.3, FigS3.5	Mi1 / STaR	*trpγ*	*hsFLPG5-fco (attP3) / Tub84B(FRT.GAL80)(1); 20XUAS-R::PEST, TI-Trpγ[1] / TI-Trpγ[1] 13XLexAop2-IVS-myr::tdTOM (attP18), 79c23s-RSR-smGdP-V5-2A-LexA (VK31) / R89C04-GAL4 (attP2)*	
Fig3.3, FigS3.5	Tm9 / STaR	Control	*hsFLPG5-fco (attP3) / Tub84B(FRT.GAL80)(1); 20XUAS-R::PEST / TI-Trpγ[1], 13XLexAop2-IVS-myr::tdTOM (attP18), 79c23s-RSR-smGdP-V5-2A-LexA (VK31) / R24C08-GAL4 (attP2)*	
Fig3.3, FigS3.5	Tm9 / STaR	*trpγ*	*hsFLPG5-fco (attP3) / Tub84B(FRT.GAL80)(1); 20XUAS-R::PEST, TI-Trpγ[1] / TI-Trpγ[1]; 13XLexAop2-IVS-myr::tdTOM (attP18), 79c23s-RSR-smGdP-V5-2A-LexA (VK31) / R24C08-GAL4(attP2)*	
Fig3.3, FigS3.5	T4/5 / STaR	Control	*hsFLPG5-fco (attP3) / Tub84B(FRT.GAL80)(1); 20XUAS-R::PEST / +; 13XLexAop2-IVS-myr::tdTOM (attP18), 79c23s-RSR-smGdP-V5-2A-LexA (VK31) / TI-Trpγ[1], R42F06-GAL4 (attP2)*	
Fig3.3, FigS3.5	T4/5 / STaR	*trpγ*	*hsFLPG5-fco (attP3) / Tub84B(FRT.GAL80)(1); 20XUAS-R::PEST, TI-Trpγ[1] / TI-Trpγ[1]; 13XLexAop2-IVS-myr::tdTOM (attP18), 79c23s-RSR-smGdP-V5-2A-LexA (VK31) /R42F06-GAL4 (attP2)*	

Figure	Cells Imaged / Label	Description in Figure	Fly Genotype	Notes
Fig3.3, FigS3.5	L4 / STaR	Control	*hsFLPG5-fco (attP3) / Tub84B(FRT.GAL80)(1); 20XUAS-R::PEST / TI-Trpγ[1]; 13XLexAop2-IVS-myr::tdTOM (attP18), 79c23s-RSR-smGdP-V5-2A-LexA (VK31) / R29F12-GAL4 (attP2)*	
Fig3.3, FigS3.5	L4 / STaR	*trpγ*	*hsFLPG5-fco (attP3) / Tub84B(FRT.GAL80)(1); 20XUAS-R::PEST, TI-Trpγ[1] / TI-Trpγ[1]; 13XLexAop2-IVS-myr::tdTOM (attP18), 79c23s-RSR-smGdP-V5-2A-LexA (VK31) /TI-Trpγ[1], R29F12-GAL4 (attP2)*	
Fig3.3, FigS3.5	L1 / STaR	Control	*hsFLPG5-fco (attP3) / Tub84B(FRT.GAL80)(1); 20XUAS-R::PEST / TI-Trpγ[1]; 13XLexAop2-IVS-myr::tdTOM (attP18), 79c23s-RSR-smGdP-V5-2A-LexA (VK31) / R48A08-GAL4 (attP2)*	
Fig3.3, FigS3.5	L1 / STaR	*trpγ*	*hsFLPG5-fco (attP3) / Tub84B(FRT.GAL80)(1); 20XUAS-R::PEST, TI-Trpγ[1]; TI-Trpγ[1], 13XLexAop2-IVS-myr::tdTOM (attP18), 79c23s-RSR-smGdP-V5-2A-LexA (VK31) /TI-Trpγ[1], R48A08-GAL4 (attP2)*	
Fig3.3, FigS3.5	L5 / STaR	Control	*hsFLPG5-fco (attP3) / Tub84B(FRT.GAL80)(1); 20XUAS-R::PEST / TI-Trpγ[1]; 13XLexAop2-IVS-myr::tdTOM (attP18), 79c23s-RSR-smGdP-V5-2A-LexA (VK31) / TI-Trpγ[1], R64B07-GAL4 (attP2)*	
Fig3.3, FigS3.5	L5 / STaR	*trpγ*	*hsFLPG5fco(attP3)/Tub84B(FRT.GAL80)(1); 20XUAS-R::PEST, TI-Trpγ[1] / TI-Trpγ[1]; 13XLexAop2-IVS-myr::tdTOM (attP18), 79c23s-RSR-smGdP-V5-2A-LexA (VK31) / R64B07-GAL4 (attP2)*	
Fig3.3, FigS3.5	R8 / STaR	Control	*hsFLPG5-fco (attP3) / Tub84B(FRT.GAL80)(1); 20XUAS-R::PEST / TI-Trpγ[1]; 13XLexAop2-IVS-myr::tdTOM (attP18), 79c23s-RSR-smGdP-V5-2A-LexA (VK31) / TI-Trpγ[1], Rh6-GAL4*	
Fig3.3, FigS3.5	R8 / STaR	*trpγ*	*hsFLPG5fco(attP3) / Tub84B(FRT.GAL80)(1); 20XUAS-R::PEST, TI-Trpγ[1] / TI-Trpγ[1]; 13XLexAop2-IVS-myr::tdTOM (attP18), 79c23s-RSR-smGdP-V5-2A-LexA (VK31) / TI-Trpγ[1], Rh6-GAL4*	
Fig3.3, FigS3.5	Dm9 / STaR	Control	*hsFLPG5-fco (attP3) / w; 20XUAS-R::PEST / TI-Trpγ[1]; 13XLexAop2-IVS-myr::tdTOM (attP18), 79c23s-RSR-smGdP-V5-2A-LexA (VK31) / R67E07-GAL4 (attP2)*	
Fig3.3, FigS3.5	Dm9 / STaR	*trpγ*	*hsFLPG5-fco (attP3) / w; 20XUAS-R::PEST, TI-Trpγ[1] / TI-Trpγ[1]; 13XLexAop2-IVS-myr::tdTOM (attP18), 79c23s-RSR-smGdP-V5-2A-LexA (VK31) / TI-Trpγ[1], R67E07-GAL4 (attP2)*	

Figure	Cells Imaged / Label	Description in Figure	Fly Genotype	Notes
Fig3.3D, FigS3.5	Dm9 / STaR	*trpγ*, 1X UAS-Trpγ-D rescue in Trpγ+ neurons	*w, 13XLexAop2-FSF-myr::smGdP-FLAG (su(Hw)attp8) / w;* *TI-Trpγ[1], R42H01-LexA (attP40) / TI-Trpγ^{G4};* *UAS-Trpγ-D (su(Hw)attP1) / 8XLexAop2-FlpL (attP2), 79c23s-FSF-smGdP-V5-2A-LexA (VK31)*	
Fig3.3, FigS3.5	Dm9 / STaR	*PSINA>TNT block*	*w / w, UAS-TeTxLC.tnt(C1);* *tubP-GAL80ts(10) / R67E07-LexA (attP40);* *R57C10-GAL4 (attP2) / 8XLexAop2-FlpL (attP2), 79c23s-FSF-smGdP-V5-2A-LexA (VK31)*	
Fig3.3D, FigS3.5	Tm9 / STaR	*trpγ*, 1X UAS-Trpγ-D rescue in Trpγ+ neurons	*w, 13XLexAop2-FSF-myr::smGdP-FLAG (su(Hw)attp8) / yw, 8XLexAop2-IVS-GAL80-WPRE (su(Hw)attP8);* *TI-Trpγ[1], R24C08-LexA (attP40) / TI-Trpγ^{G4};* *UAS-Trpγ-D (su(Hw)attP1) / 8XLexAop2-FlpL (attP2), 79c23s-FSF-smGdP-V5-2A-LexA (VK31)*	
Fig3.3, FigS3.5	Tm9 / STaR	*PSINA>TNT block*	*w / w, UAS-TeTxLC.tnt(C1);* *tubP-GAL80ts(10) / R24C08-LexA (attP40);* *R57C10-GAL4 (attP2) / 8XLexAop2-FlpL (attP2), 79c23s-FSF-smGdP-V5-2A-LexA (VK31)*	
Fig3.4A, FigS3.6, FigS3.7, FigS3.9	Trpγ+ neurons / mCherry	N/A	*w;* *TI-Trpγ^{G4} / +;* *UAS-mCherry.NLS (3) / +*	
Fig3.4B	Trpγ+ neurons / SM-FLAG	Trpγ^{G4} > SM-FLAG	*hsFLPG5:PEST (attP3) / w;* *10XUAS-IVS-myr::tdTOM (attp40) / TI-Trpγ^{G4};* *10XUAS(FRT.stop)myr::smGdP-HA (VK5), 10XUAS(FRT.stop)myr::smGdP-V5-THS-10XUAS(FRT.stop)myr::smGdP-FLAG (su(Hw)attP1) / +*	
Fig3.4C	Trpγ+ neurons / SM-V5	N/A	*nSyb-IVS-ϕC31 (attP18) / 10XUAS-IVS-myr::smGdP-HA (attP18), 13XLexAop2-IVS-myr::smGdP-V5 (su(Hw)attP8);* *TI-Trpγ^{G4}, SPARC3-OUT-S-GAL80 (50F1) / 20XUAS-SPARC2-S-LexA::p65 (24C06);* *+*	
Fig3.4D-H	Trpγ+ neurons / GCaMP	Control	*20XUAS-IVS-Syn21-opGCaMP6s-p10 (su(Hw)attP8) / w;* *R57C10-LexA (attP40), 13XLexAop2-IVS-NES-jRCaMP1b-p10 (su(Hw)attP5) / TI-Trpγ^{G4};* *20XUAS-IVS-Syn21-opGCaMP6s-p10 (su(Hw)attP1) / +*	
Fig3.4D-H	Trpγ+ neurons / GCaMP	*trpγ*	*20XUAS-IVS-Syn21-opGCaMP6s-p10 (su(Hw)attP8) / w;* *R57C10-LexA (attP40), TI-Trpγ[1], 13XLexAop2-IVS-NES-jRCaMP1b-p10 (su(Hw)attP5) / TI-Trpγ^{G4};* *20XUAS-IVS-Syn21-opGCaMP6s-p10 (su(Hw)attP1) / +*	
Fig3.5, FigS3.12	PanN / GCaMP	PanN-GAL4, Kir2.1	*yw, UAS-Kir2.1-T2A-myr::tdTOM-3xHA (attP3) / w;* *tubP-GAL80ts(10) / +;* *13XLexAop2-opGCaMP6s (su(Hw)attP1), R57C10-lexAp65 (VK20), UAS-his-RFP(3) / R57C10-GAL4 (attP2)*	
Fig3.5, FigS3.12, FigS3.14	PanN / GCaMP	empty-GAL4, Kir2.1	*yw, UAS-Kir2.1-T2A-myr::tdTOM-3xHA (attP3) / w;* *tubP-GAL80ts(10) / +;* *13XLexAop2-opGCaMP6s (su(Hw)attP1), R57C10-lexAp65 (VK20), UAS-his-RFP(3) / empty-GAL4 (attP2)*	

Figure	Cells Imaged / Label	Description in Figure	Fly Genotype	Notes
Fig3.5, FigS3.12, FigS3.14	PanN / GCaMP	*Trpγ^{G4}*, Kir2.1	*yw, UAS-Kir2.1-T2A-myr::tdTOM-3xHA (attP3) / w;* *tubP-GAL80ts(10) / TI-Trpγ^{G4};* *13XLexAop2-opGCaMP6s (su(Hw)attP1), R57C10-lexAp65 (VK20), UAS-his-RFP(3) / +*	
Fig3.5, FigS3.19	PanN / GCaMP	empty-GAL4, TrpA1	*w;* *R57C10-lexA (attP40), 13XLexAop2-opGCaMP6s (su(Hw)attP5) / +;* *UAS-TrpA1 (attP2) / empty-GAL4 (attP2)*	
Fig3.5, FigS3.19	PanN / GCaMP	PanN-GAL4, TrpA1	*w;* *R57C10-lexA (attP40), 13XLexAop2-opGCaMP6s (su(Hw)attP5) / +;* *UAS-TrpA1 (attP2) / R57C10-GAL4 (attP2)*	
Fig3.5, FigS3.19	PanN / GCaMP	*Trpγ^{G4}*, TrpA1	*w;* *R57C10-lexA (attP40), 13XLexAop2-opGCaMP6s (su(Hw)attP5) / TI-Trpγ^{G4};* *UAS-TrpA1 (attP2) / +*	
FigS3.1D, E	PanN / GCaMP	Control	*w;* *R57C10-lexA (attP40), TI-Trpγ[1], 13XLexAop2-opGCaMP6s (su(Hw)attP5) / +;* *+*	
FigS3.1D, E	PanN / GCaMP	*trpγ / Trpγ^{G4}*	*w;* *R57C10-lexA (attP40), TI-Trpγ[1], 13XLexAop2-opGCaMP6s (su(Hw)attP5) / TI-Trpγ^{G4};* *+*	
FigS3.1D, E	PanN / GCaMP	*trpγ / Trpγ$^{DropIn-TG4}$*	*w;* *R57C10-lexA (attP40), TI-Trpγ[1], 13XLexAop2-opGCaMP6s (su(Hw)attP5) / TI-Trpγ$^{DropIn-TG4}$;* *+*	
FigS3.1D, E	PanN / GCaMP	*trpγ / Df(2L)ED1102*	*w;* *R57C10-lexA (attP40), TI-Trpγ[1], 13XLexAop2-opGCaMP6s (su(Hw)attP5) / Df(2L)ED1102;* *+*	
FigS3.1D, E	PanN / GCaMP	*trpγ / Df(2L)ED1109*	*w;* *R57C10-lexA (attP40), TI-Trpγ[1], 13XLexAop2-opGCaMP6s (su(Hw)attP5) / Df(2L)ED1109;* *+*	
FigS3.2A	PanN / GCaMP	Control	*w;* *R57C10-lexA (attP40), TI-Trpγ[1], 13XLexAop2-opGCaMP6s (su(Hw)attP5) / +;* *Trp[9] / +*	
FigS3.2A	PanN / GCaMP	*trpγ*	*w;* *R57C10-lexA (attP40), TI-Trpγ[1], 13XLexAop2-opGCaMP6s (su(Hw)attP5) / TI-Trpγ[1];* *Trp[9] / +*	
FigS3.2A	PanN / GCaMP	*trp[9] / Df(3R)BSC861*	*w;* *R57C10-lexA (attP40), TI-Trpγ[1], 13XLexAop2-opGCaMP6s (su(Hw)attP5) / +;* *trp[9] / Df(3R)BSC861*	
FigS3.2A	PanN / GCaMP	*trpγ; trp[9] / Df(3R)BSC861*	*w;* *R57C10-lexA (attP40), TI-Trpγ[1], 13XLexAop2-opGCaMP6s (su(Hw)attP5) / TI-Trpγ[1];* *Trp[9] / Df(3R)BSC861*	
FigS3.2B	PanN / GCaMP	Control	*w;* *TI-Trpγ[1], trpl[MB10553] / +;* *13XLexAop2-opGCaMP6s (su(Hw)attP1), R57C10-lexAp65 (VK20), UAS-his-RFP(3) / +*	

Figure	Cells Imaged / Label	Description in Figure	Fly Genotype	Notes
FigS3.2B	PanN / GCaMP	*trpγ*	*w;* *TI-Trpγ[1], trpl[MB10553] / TI-Trpγ[1];* *13XLexAop2-opGCaMP6s (su(Hw)attP1), R57C10-lexAp65 (VK20), UAS-his-RFP(3) / +*	
FigS3.2B	PanN / GCaMP	*trpL[MB]*	*W;* *TI-Trpγ[1], trpl[MB10553] / trpl[MB10553];* *13XLexAop2-opGCaMP6s (su(Hw)attP1), R57C10-lexAp65 (VK20), UAS-his-RFP(3) / +*	
FigS3.2B	PanN / GCaMP	*trpγ, trpL[MB]* / *trpL[MB]*	*w;* *TI-Trpγ[1], / trpl[MB10553] / TI-Trpγ[1], / trpl[MB10553];* *13XLexAop2-opGCaMP6s (su(Hw)attP1), R57C10-lexAp65 (VK20), UAS-his-RFP(3) / +*	
FigS3.3B-C	PanN / GCaMP	*trpγ / Trpγ^{G4}* ; 1X UAS-Trpγ-D	*w;* *R57C10-lexA (attP40), TI-Trpγ[1], 13XLexAop2-opGCaMP6s (su(Hw)attP5) / TI-Trpγ^{G4};* *UAS-Trpγ-D (su(Hw)attP1) / +*	
FigS3.3B-C	PanN / GCaMP	*trpγ / Trpγ$^{DropIn-TG4}$* ; 1X UAS-Trpγ-D	*w;* *R57C10-lexA (attP40), TI-Trpγ[1], 13XLexAop2-opGCaMP6s (su(Hw)attP5) / TI-Trpγ$^{DropIn-TG4}$;* *UAS-TI-Trpγ-D (su(Hw)attP1)*	
FigS3.3B-C	PanN / GCaMP	*trpγ / Trpγ^{G4}* ; 1X UAS-Trpγ-A/B	*w;* *R57C10-lexA (attP40), TI-Trpγ[1], 13XLexAop2-opGCaMP6s (su(Hw)attP5) / TI-Trpγ^{G4};* *UAS-Trpγ-A/B (su(Hw)attP1) / +*	
FigS3.3B-C	PanN / GCaMP	*trpγ / Trpγ^{G4}* ; UAS-Trpγ-A/B+Trpγ-D	*w;* *R57C10-lexA (attP40), TI-Trpγ[1], 13XLexAop2-opGCaMP6s (su(Hw)attP5) / TI-Trpγ^{G4};* *UAS-Trpγ-A/B (su(Hw)attP1) / UAS-Trpγ-D (su(Hw)attP1)*	
FigS3.3B-C	PanN / GCaMP	*trpγ / Trpγ^{G4}* ; 2X UAS-Trpγ-D	*w;* *R57C10-lexA (attP40), TI-Trpγ[1], 13XLexAop2-opGCaMP6s (su(Hw)attP5) / TI-Trpγ^{G4};* *UAS-Trpγ-D (su(Hw)attP1)*	
FigS3.3B-C	PanN / GCaMP	Control	*w;* *R57C10-lexA (attP40), TI-Trpγ[1], 13XLexAop2-opGCaMP6s (su(Hw)attP5) / +;* *UAS-TI-Trpγ-D (su(Hw)attP1) / empty-GAL4 (attP2)*	
FigS3.3B-C	PanN / GCaMP	*trpγ*	*w;* *R57C10-lexA (attP40), TI-Trpγ[1], 13XLexAop2-opGCaMP6s (su(Hw)attP5) / TI-Trpγ[1];* *UAS-Trpγ-D (su(Hw)attP1) / +*	
FigS3.5H	Dm9 / STaR	Control	*w, 13XLexAop2-FSF-myr::smGdP-FLAG (su(Hw)attp8) / yw, 8XLexAop2-IVS-GAL80-WPRE (su(Hw)attP8);* *TI-Trpγ[1], R42H01-LexA (attP40) / +;* *UAS-Trpγ-D (su(Hw)attP1) / 8XLexAop2-FlpL (attP2), 79c23s-FSF-smGdP-V5-2A-LexA (VK31)*	
FigS3.5H	Dm9 / STaR	*trpγ*	*w, 13XLexAop2-FSF-myr::smGdP-FLAG (su(Hw)attp8) / yw, 8XLexAop2-IVS-GAL80-WPRE (su(Hw)attP8);* *TI-Trpγ[1], R42H01-LexA (attP40) / TI-Trpγ[1];* *UAS-Trpγ-D (su(Hw)attP1) / 8XLexAop2-FlpL (attP2), 79c23s-FSF-smGdP-V5-2A-LexA (VK31)*	
FigS3.5H	Dm9 / STaR	*trpγ*, 1X UAS-Trpγ-D rescue in Trpγ+ neurons	*w, 13XLexAop2-FSF-myr::smGdP-FLAG (su(Hw)attp8) / yw, 8XLexAop2-IVS-GAL80-WPRE (su(Hw)attP8);* *TI-Trpγ[1], R42H01-LexA (attP40) / TI-Trpγ^{G4};* *UAS-Trpγ-D (su(Hw)attP1) / 8XLexAop2-FlpL (attP2), 79c23s-FSF-smGdP-V5-2A-LexA (VK31)*	

Figure	Cells Imaged / Label	Description in Figure	Fly Genotype	Notes
FigS3.5H	Tm9 / STaR	Control	*w, 13XLexAop2-FSF-myr::smGdP-FLAG (su(Hw)attp8) / yw, 8XLexAop2-IVS-GAL80-WPRE (su(Hw)attP8);* *TI-Trpγ[1], R24C08-LexA (attP40) / +;* *UAS-Trpγ-D (su(Hw)attP1) / 8XLexAop2-FlpL (attP2), 79c23s-FSF-smGdP-V5-2A-LexA (VK31)*	
FigS3.5H	Tm9 / STaR	*trpγ*	*w, 13XLexAop2-FSF-myr::smGdP-FLAG (su(Hw)attp8) / yw, 8XLexAop2-IVS-GAL80-WPRE (su(Hw)attP8);* *TI-Trpγ[1], R24C08-LexA (attP40) / TI-Trpγ[1];* *UAS-Trpγ-D (su(Hw)attP1) / 8XLexAop2-FlpL (attP2), 79c23s-FSF-smGdP-V5-2A-LexA (VK31)*	
FigS3.5H	Tm9 / STaR	*trpγ*, 1X UAS-Trpγ-D rescue in Trpγ+ neurons	*w, 13XLexAop2-FSF-myr::smGdP-FLAG (su(Hw)attp8) / yw, 8XLexAop2-IVS-GAL80-WPRE (su(Hw)attP8);* *TI-Trpγ[1], R24C08-LexA (attP40) / TI-Trpγ^{G4};* *UAS-Trpγ-D (su(Hw)attP1) / 8XLexAop2-FlpL (attP2), 79c23s-FSF-smGdP-V5-2A-LexA (VK31)*	
FigS3.5I	L5 / STaR	Control MARCM	*w, 29C07-FLP1-4 (su(Hw)attP8) / yw, UAS-FSF-R::PEST (attP18);* *tubP-GAL80(LL10), FRT40A / FRT40A;* *13XLexAop2-IVS-myr::tdTOM (attP18), 79c23s-RSR-smGdP-V5-2A-LexA (VK31) / R64B07-GAL4 (attP2)*	
FigS3.5I	L5 / STaR	*trpγ* MARCM	*w, 29C07-FLP1-4 (su(Hw)attP8) / yw, UAS-FSF-R::PEST (attP18);* *tubP-GAL80(LL10), FRT40A / TI-Trpγ[1], FRT40A;* *13XLexAop2-IVS-myr::tdTOM (attP18), 79c23s-RSR-smGdP-V5-2A-LexA (VK31) / R64B07-GAL4 (attP2)*	
FigS3.5J	Tm9 / STaR	Control (PSINA>TNT block)	*w / Y;* *tubP-GAL80ts(10) / R24C08-LexA (attP40);* *R57C10-GAL4 (attP2) / 8XLexAop2-FlpL (attP2), 79c23s-FSF-smGdP-V5-2A-LexA (VK31)*	
FigS3.5J	Tm9 / STaR	PSINA>TNT block	*w / w, UAS-TeTxLC.tnt(C1);* *tubP-GAL80ts(10) / R24C08-LexA (attP40);* *R57C10-GAL4 (attP2) / 8XLexAop2-FlpL (attP2), 79c23s-FSF-smGdP-V5-2A-LexA (VK31)*	
FigS3.8	PanN / GCaMP	PanN-GAL4 > α-w RNAi	*UAS-Dcr-2.D(1) / +;* *R57C10-lexA (attP40), 13XlexAop2-opGCaMP6s (su(Hw)attP5) / +;* *R57C10-GAL4 (attP2) / TRiP.JF01786 (attP2)*	
FigS3.8	PanN / GCaMP	PanN-GAL4 > α-Trpγ RNAi 1	*UAS-Dcr-2.D(1) / +;* *R57C10-lexA (attP40), 13XlexAop2-opGCaMP6s (su(Hw)attP5) / +;* *R57C10-GAL4 (attP2) / TRiP.HMC03542 (attP2)*	
FigS3.8	PanN / GCaMP	PanN-GAL4 > α-Trpγ RNAi 2	*UAS-Dcr-2.D(1) / +;* *R57C10-lexA (attP40), 13XlexAop2-opGCaMP6s (su(Hw)attP5) / +;* *R57C10-GAL4 (attP2) / TRiP.JF01243 (attP2)*	
FigS3.8	PanN / GCaMP	repo-GAL4 > α-w RNAi	*UAS-Dcr-2.D(1) / +;* *R57C10-lexA (attP40), 13XlexAop2-opGCaMP6s (su(Hw)attP5) / +;* *repo-GAL4 / TRiP.JF01786 (attP2)*	
FigS3.8	PanN / GCaMP	repo-GAL4 > α-*Trpγ* RNAi 1	*UAS-Dcr-2.D(1) / +;* *R57C10-lexA (attP40), 13XlexAop2-opGCaMP6s (su(Hw)attP5) / +;* *repo-GAL4 / TRiP.HMC03542 (attP2)*	

Figure	Cells Imaged / Label	Description in Figure	Fly Genotype	Notes
FigS3.8	PanN / GcaMP	repo-GAL4 > α-*Trpγ* RNAi 2	*UAS-Dcr-2.D(1) / +;* *R57C10-lexA (attP40), 13XlexAop2-opGCaMP6s (su(Hw)attP5) / +;* *repo-GAL4 / TRiP.JF01243 (attP2)*	
FigS3.9	Trpγ+ neurons / GFP	N/A	*w;* *TI-Trpγ^{G4} / +;* *UAS-GFP.nls(8) / +*	
FigS3.13	Trpγ+ neurons / GCaMP	*Trpγ^{G4}* > GCaMP6s	*w;* *TI-Trpγ^{G4} / +* *UAS-opGCaMP6s (su(Hw)attP1) / +*	
FigS3.13	PanN / GCaMP	PanN > GCaMP6s	*w;* *+* *UAS-opGCaMP6s (su(Hw)attP1) / R57C10-GAL4 (attP2)*	
FigS3.15	PanN / GCaMP	Control	*yw, ey-FLP.N(1) / Y;* *TrpγG4, tubP-GAL80ts (10) / Tub84B(FRT.GAL80)(2);* *13XLexAop2-opGCaMP6s (su(Hw)attP1), R57C10-lexAp65 (VK20), UAS-his-RFP(3) / +*	
FigS3.15	PanN / GCaMP	*Trpγ^{G4}* (OL), Kir2.1	*yw, ey-FLP.N(1) / yw, UAS-Kir2.1-T2A-myr::tdTOM-3xHA (attP3);* *TI-Trpγ^{G4}, tubP-GAL80ts (10) / Tub84B(FRT.GAL80)(2);* *13XLexAop2-opGCaMP6s (su(Hw)attP1), R57C10-lexAp65 (VK20), UAS-his-RFP(3) / +*	
FigS3.15	PanN / GCaMP	Control	*yw, ey-FLP.N(1) / Y;* *TI-Trpγ^{G4}, tubP-GAL80ts (10) / tubP(FRT.stop)GAL80(2);* *13XLexAop2-opGCaMP6s (su(Hw)attP1), R57C10-lexAp65 (VK20), UAS-his-RFP(3) / +*	
FigS3.15	PanN / GCaMP	*Trpγ^{G4}* (CB), Kir2.1	*yw, ey-FLP.N(1) / yw, UAS-Kir2.1-T2A-myr::tdTOM-3xHA (attP3);* *TI-Trpγ^{G4}, tubP-GAL80ts (10) / tubP(FRT.stop)GAL80(2);* *13XLexAop2-opGCaMP6s (su(Hw)attP1), R57C10-lexAp65 (VK20), UAS-his-RFP(3) / +*	
FigS3.16	PanN / GCaMP	empty-GAL4, TNT	*w, UAS-TeTxLC.tnt(C1) / w;* *tubP-GAL80ts(10) / +;* *13XLexAop2-opGCaMP6s (su(Hw)attP1), R57C10-lexAp65 (VK20), UAS-his-RFP(3) / empty-GAL4 (attp2)*	
FigS3.16	PanN / GCaMP	PanN-GAL4, TNT	*w, UAS-TeTxLC.tnt(C1) / w;* *tubP-GAL80ts(10) / +;* *13XLexAop2-opGCaMP6s (su(Hw)attP1), R57C10-lexAp65 (VK20), UAS-his-RFP(3) / R57C10-GAL4 (attP2)*	
FigS3.16	PanN / GCaMP	*Trpγ^{G4}*, TNT	*w, UAS-TeTxLC.tnt(C1) / w;* *tubP-GAL80ts(10) / TrpγG4;* *13XLexAop2-opGCaMP6s (su(Hw)attP1), R57C10-lexAp65 (VK20), UAS-his-RFP(3) / +*	
FigS3.17	PanN / GCaMP	Control	*w, P[UAS-rpr], P[UAS-hid] / w;* *tubP-GAL80ts(10) / +;* *13XLexAop2-opGCaMP6s (su(Hw)attP1), R57C10-lexAp65 (VK20), UAS-his-RFP(3) / empty-GAL4 (attP2)*	

Figure	Cells Imaged / Label	Description in Figure	Fly Genotype	Notes
FigS3.17	PanN / GCaMP	PanN-GAL4, hid, rpr	*w, P[UAS-rpr], P[UAS-hid] / w;* *tubP-GAL80ts(10) / +;* *13XLexAop2-opGCaMP6s (su(Hw)attP1), R57C10-lexAp65 (VK20), UAS-his-RFP(3) / R57C10-GAL4 (attP2)*	
FigS3.17	PanN / GCaMP	*Trpγ*^{G4}, rpr, hid	*w, P[UAS-rpr], P[UAS-hid] / w;* *tubP-GAL80ts(10) / TrpγG4;* *13XLexAop2-opGCaMP6s (su(Hw)attP1), R57C10-lexAp65 (VK20), UAS-his-RFP(3) / +*	
FigS3.18	PanN / GCaMP	Control	*w;* *R57C10-lexA (attP40), 13XLexAop2-opGCaMP6s (su(Hw)attP5) / tubP-GAL80ts(10);* *10XUAS-IVS-myr::tdTOM (attP2), 13XLexAop-opGCaMP6s (su(Hw)attP1) / R57C10-GAL4 (attP2)*	
FigS3.18	PanN / GCaMP	PanN-GAL4, TNT	*w, UAS-TeTxLC.tnt(C1) / +;* *R57C10-lexA (attP40), 13XLexAop2-opGCaMP6s (su(Hw)attP5) / tubP-GAL80ts(10);* *10XUAS-IVS-myr::tdTOM (attP2), 13XLexAop-opGCaMP6s (su(Hw)attP1) / R57C10-GAL4 (attP2)*	
FigS3.18	PanN / GCaMP	VMAT-GAL4, TNT	*w, UAS-TeTxLC.tnt(C1) / w;* *R57C10-lexA (attP40), 13XLexAop2-opGCaMP6s (su(Hw)attP5) / Vmat*$^{MI07680\text{-}TG4}$*;* *10XUAS-IVS-myr::tdTOM (attP2), 13XLexAop-opGCaMP6s (su(Hw)attP1) / tubP-GAL80ts(2)*	
FigS3.18	PanN / GCaMP	GAD1-GAL4, TNT	*w, UAS-TeTxLC.tnt(C1) / w;* *R57C10-lexA (attP40), 13XLexAop2-opGCaMP6s (su(Hw)attP5) / Gad1-GAL4.3.098(2);* *10XUAS-IVS-myr::tdTOM (attP2), 13XLexAop-opGCaMP6s (su(Hw)attP1) / tubP-GAL80ts(2)*	
FigS3.18	PanN / GCaMP	VGLUT-GAL4, TNT	*w, UAS-TeTxLC.tnt(C1) / w;* *R57C10-lexA (attP40), 13XLexAop2-opGCaMP6s (su(Hw)attP5) / Vglut*$^{MI04979\text{-}TG4}$*;* *10XUAS-IVS-myr::tdTOM (attP2), 13XLexAop-opGCaMP6s (su(Hw)attP1) / tubP-GAL80ts(2)*	

3.11. REFERENCES

Ackman, J. B., Burbridge, T. J., and Crair, M. C. (2012). Retinal waves coordinate patterned activity throughout the developing visual system. Nature *490*, 219-225.

Ackman, J. B., and Crair, M. C. (2014). Role of emergent neural activity in visual map development. Curr Opin Neurobiol *24*, 166-175.

Akin, O., Bajar, B. T., Keles, M. F., Frye, M. A., and Zipursky, S. L. (2019). Cell-type-Specific Patterned Stimulus-Independent Neuronal Activity in the Drosophila Visual System during Synapse Formation. Neuron *101*, 894-904.e5.

Akin, O., and Zipursky, S. L. (2016). Frazzled promotes growth cone attachment at the source of a Netrin gradient in the. Elife *5*,

Akitake, B., Ren, Q., Boiko, N., Ni, J., Sokabe, T., Stockand, J. D., Eaton, B. A., and Montell, C. (2015). Coordination and fine motor control depend on Drosophila TRPγ. Nat Commun *6*, 7288.

Akrouh, A., and Kerschensteiner, D. (2013). Intersecting circuits generate precisely patterned retinal waves. Neuron *79*, 322-334.

Bainbridge, S. P., and Bownes, M. (1981). Staging the metamorphosis of Drosophila melanogaster. J Embryol Exp Morphol *66*, 57-80.

Bansal, A., Singer, J. H., Hwang, B. J., Xu, W., Beaudet, A., and Feller, M. B. (2000). Mice lacking specific nicotinic acetylcholine receptor subunits exhibit dramatically altered spontaneous activity patterns and reveal a limited role for retinal waves in forming ON and OFF circuits in the inner retina. J Neurosci *20*, 7672-7681.

Batut, P., and Gingeras, T. R. (2013). RAMPAGE: promoter activity profiling by paired-end sequencing of 5'-complete cDNAs. Curr Protoc Mol Biol *104*, Unit 25B.11.

Berdnik, D., Chihara, T., Couto, A., and Luo, L. (2006). Wiring stability of the adult Drosophila olfactory circuit after lesion. J Neurosci *26*, 3367-3376.

Blankenship, A. G., and Feller, M. B. (2010). Mechanisms underlying spontaneous patterned activity in developing neural circuits. Nat Rev Neurosci *11*, 18-29.

Blum, T., Moreno-Pérez, A., Pyrski, M., Bufe, B., Arifovic, A., Weissgerber, P., Freichel, M., Zufall, F., and Leinders-Zufall, T. (2019). Trpc5 deficiency causes hypoprolactinemia and altered function of oscillatory dopamine neurons in the arcuate nucleus. Proc Natl Acad Sci U S A *116*, 15236-15243.

Brand, A. H., and Perrimon, N. (1993). Targeted gene expression as a means of altering cell fates and generating dominant phenotypes. Development *118*, 401-415.

Burbridge, T. J., Xu, H. P., Ackman, J. B., Ge, X., Zhang, Y., Ye, M. J., Zhou, Z. J., Xu, J., Contractor, A., and Crair, M. C. (2014). Visual circuit development requires patterned activity mediated by retinal acetylcholine receptors. Neuron *84*, 1049-1064.

Cabrero, P., Radford, J. C., Broderick, K. E., Costes, L., Veenstra, J. A., Spana, E. P., Davies, S. A., and Dow, J. A. (2002). The Dh gene of Drosophila melanogaster encodes a diuretic peptide that acts through cyclic AMP. J Exp Biol *205*, 3799-3807.

Daniels, R. W., Collins, C. A., Gelfand, M. V., Dant, J., Brooks, E. S., Krantz, D. E., and DiAntonio, A. (2004). Increased expression of the Drosophila vesicular glutamate transporter leads to excess glutamate release and a compensatory decrease in quantal content. J Neurosci *24*, 10466-10474.

Fei, H., Chow, D. M., Chen, A., Romero-Calderón, R., Ong, W. S., Ackerson, L. C., Maidment, N. T., Simpson, J. H., Frye, M. A., and Krantz, D. E. (2010). Mutation of the Drosophila vesicular GABA transporter disrupts visual figure detection. J Exp Biol *213*, 1717-1730.

Chen, T. W., Wardill, T. J., Sun, Y., Pulver, S. R., Renninger, S. L., Baohan, A., Schreiter, E. R., Kerr, R. A., Orger, M. B., Jayaraman, V., Looger, L. L., Svoboda, K., and Kim, D. S. (2013). Ultrasensitive fluorescent proteins for imaging neuronal activity. Nature *499*, 295-300.

Chen, Y., Akin, O., Nern, A., Tsui, C. Y., Pecot, M. Y., and Zipursky, S. L. (2014). Cell-type-specific labeling of synapses in vivo through synaptic tagging with recombination. Neuron *81*, 280-293.

Chiang, A. S., Lin, C. Y., Chuang, C. C., Chang, H. M., Hsieh, C. H., Yeh, C. W., Shih, C. T., Wu, J. J., Wang, G. T., Chen, Y. C., Wu, C. C., Chen, G. Y., Ching, Y. T., Lee, P. C., Lin, C. Y., Lin, H. H., Wu, C. C., Hsu, H. W., Huang, Y. A., Chen, J. Y., Chiang, H. J., Lu, C. F., Ni, R. F., Yeh, C. Y., and Hwang, J. K. (2011). Three-dimensional reconstruction of brain-wide wiring networks in Drosophila at single-cell resolution. Curr Biol *21*, 1-11.

Dana, H., Mohar, B., Sun, Y., Narayan, S., Gordus, A., Hasseman, J. P., Tsegaye, G., Holt, G. T., Hu, A., Walpita, D., Patel, R., Macklin, J. J., Bargmann, C. I., Ahrens, M. B., Schreiter, E. R., Jayaraman, V., Looger, L. L., Svoboda, K., and Kim, D. S. (2016). Sensitive red protein calcium indicators for imaging neural activity. Elife *5*,

Galli, L., and Maffei, L. (1988). Spontaneous impulse activity of rat retinal ganglion cells in prenatal life. Science *242*, 90-91.

Helfrich-Förster, C. (1997). Development of pigment-dispersing hormone-immunoreactive neurons in the nervous system of Drosophila melanogaster. J Comp Neurol *380*, 335-354.

Hiesinger, P. R., Zhai, R. G., Zhou, Y., Koh, T. W., Mehta, S. Q., Schulze, K. L., Cao, Y., Verstreken, P., Clandinin, T. R., Fischbach, K. F., Meinertzhagen, I. A., and Bellen, H. J. (2006). Activity-independent prespecification of synaptic partners in the visual map of Drosophila. Curr Biol *16*, 1835-1843.

Isaacman-Beck, J., Paik, K. C., Wienecke, C. F. R., Yang, H. H., Fisher, Y. E., Wang, I. E., Ishida, I. G., Maimon, G., Wilson, R. I., and Clandinin, T. R. (2020). SPARC enables genetic manipulation of precise proportions of cells. Nat Neurosci *23*, 1168-1175.

Kanca, O., Zirin, J., Garcia-Marques, J., Knight, S. M., Yang-Zhou, D., Amador, G., Chung, H., Zuo, Z., Ma, L., He, Y., Lin, W. W., Fang, Y., Ge, M., Yamamoto, S., Schulze, K. L., Hu, Y., Spradling, A. C., Mohr, S. E., Perrimon, N., and Bellen, H. J. (2019). An efficient CRISPR-based strategy to insert small and large fragments of DNA using short homology arms. Elife *8*,

Kurmangaliyev, Y. Z., Yoo, J., Valdes-Aleman, J., Sanfilippo, P., and Zipursky, S. L. (2020). Transcriptional Programs of Circuit Assembly in the Drosophila Visual System. Neuron *108*, 1045-1057.e6.

Lai, S. L., and Lee, T. (2006). Genetic mosaic with dual binary transcriptional systems in Drosophila. Nat Neurosci *9*, 703-709.

Lee, T., and Luo, L. (1999). Mosaic analysis with a repressible cell marker for studies of gene function in neuronal morphogenesis. Neuron *22*, 451-461.

Leong, A. T., Chan, R. W., Gao, P. P., Chan, Y. S., Tsia, K. K., Yung, W. H., and Wu, E. X. (2016). Long-range projections coordinate distributed brain-wide neural activity with a specific spatiotemporal profile. Proc Natl Acad Sci U S A *113*, E8306-E8315.

Luhmann, H. J., Sinning, A., Yang, J. W., Reyes-Puerta, V., Stüttgen, M. C., Kirischuk, S., and Kilb, W. (2016). Spontaneous Neuronal Activity in Developing Neocortical Networks: From Single Cells to Large-Scale Interactions. Front Neural Circuits *10*, 40.

McGuire, S. E., Le, P. T., Osborn, A. J., Matsumoto, K., and Davis, R. L. (2003). Spatiotemporal rescue of memory dysfunction in Drosophila. Science *302*, 1765-1768.

McLaughlin, T., Hindges, R., and O'Leary, D. D. (2003). Regulation of axial patterning of the retina and its topographic mapping in the brain. Curr Opin Neurobiol *13*, 57-69.

Meister, M., Wong, R. O., Baylor, D. A., and Shatz, C. J. (1991). Synchronous bursts of action potentials in ganglion cells of the developing mammalian retina. Science *252*, 939-943.

Mulloney, B., and Smarandache, C. (2010). Fifty Years of CPGs: Two Neuroethological Papers that Shaped the Course of Neuroscience. Front Behav Neurosci *4*,

Munsch, T., Freichel, M., Flockerzi, V., and Pape, H. C. (2003). Contribution of transient receptor potential channels to the control of GABA release from dendrites. Proc Natl Acad Sci U S A *100*, 16065-16070.

Muthukumar, A. K., Stork, T., and Freeman, M. R. (2014). Activity-dependent regulation of astrocyte GAT levels during synaptogenesis. Nat Neurosci *17*, 1340-1350.

Özel, M. N., Simon, F., Jafari, S., Holguera, I., Chen, Y. C., Benhra, N., El-Danaf, R. N., Kapuralin, K., Malin, J. A., Konstantinides, N., and Desplan, C. (2021). Neuronal diversity and convergence in a visual system developmental atlas. Nature *589*, 88-95.

Nern, A., Pfeiffer, B. D., and Rubin, G. M. (2015). Optimized tools for multicolor stochastic labeling reveal diverse stereotyped cell arrangements in the fly visual system. Proc Natl Acad Sci U S A *112*, E2967-76.

Park, D., Veenstra, J. A., Park, J. H., and Taghert, P. H. (2008). Mapping peptidergic cells in Drosophila: where DIMM fits in. PLoS One *3*, e1896.

Peng, H., Ruan, Z., Long, F., Simpson, J. H., and Myers, E. W. (2010). V3D enables real-time 3D visualization and quantitative analysis of large-scale biological image data sets. Nat Biotechnol *28*, 348-353.

Preibisch, S., Saalfeld, S., and Tomancak, P. (2009). Globally optimal stitching of tiled 3D microscopic image acquisitions. Bioinformatics *25*, 1463-1465.

Pulver, S. R., Pashkovski, S. L., Hornstein, N. J., Garrity, P. A., and Griffith, L. C. (2009). Temporal dynamics of neuronal activation by Channelrhodopsin-2 and TRPA1 determine behavioral output in Drosophila larvae. J Neurophysiol *101*, 3075-3088.

Sanes, J. R., and Masland, R. H. (2015). The types of retinal ganglion cells: current status and implications for neuronal classification. Annu Rev Neurosci *38*, 221-246.

Schindelin, J., Arganda-Carreras, I., Frise, E., Kaynig, V., Longair, M., Pietzsch, T., Preibisch, S., Rueden, C., Saalfeld, S., Schmid, B., Tinevez, J. Y., White, D. J., Hartenstein, V., Eliceiri, K., Tomancak, P., and Cardona, A. (2012). Fiji: an open-source platform for biological-image analysis. Nat Methods *9*, 676-682.

Scott, E. K., Reuter, J. E., and Luo, L. (2003). Dendritic development of Drosophila high order visual system neurons is independent of sensory experience. BMC Neurosci *4*, 14.

Soto, F., Ma, X., Cecil, J. L., Vo, B. Q., Culican, S. M., and Kerschensteiner, D. (2012). Spontaneous activity promotes synapse formation in a cell-type-dependent manner in the developing retina. J Neurosci *32*, 5426-5439.

Sugie, A., Marchetti, G., and Tavosanis, G. (2018). Structural aspects of plasticity in the nervous system of Drosophila. Neural Dev *13*, 14.

Takemura, S. Y., Bharioke, A., Lu, Z., Nern, A., Vitaladevuni, S., Rivlin, P. K., Katz, W. T., Olbris, D. J., Plaza, S. M., Winston, P., Zhao, T., Horne, J. A., Fetter, R. D., Takemura, S., Blazek, K., Chang, L. A., Ogundeyi, O., Saunders, M. A., Shapiro, V., Sigmund, C., Rubin, G. M., Scheffer, L. K., Meinertzhagen, I. A., and Chklovskii, D. B. (2013). A visual motion detection circuit suggested by Drosophila connectomics. Nature *500*, 175-181.

Takemura, S. Y., Lu, Z., and Meinertzhagen, I. A. (2008). Synaptic circuits of the Drosophila optic lobe: the input terminals to the medulla. J Comp Neurol *509*, 493-513.

Terhzaz, S., Rosay, P., Goodwin, S. F., and Veenstra, J. A. (2007). The neuropeptide SIFamide modulates sexual behavior in Drosophila. Biochem Biophys Res Commun *352*, 305-310.

Tritsch, N. X., Yi, E., Gale, J. E., Glowatzki, E., and Bergles, D. E. (2007). The origin of spontaneous activity in the developing auditory system. Nature *450*, 50-55.

Valdes-Aleman, J., Fetter, R. D., Sales, E. C., Heckman, E. L., Venkatasubramanian, L., Doe, C. Q., Landgraf, M., Cardona, A., and Zlatic, M. (2021). Comparative Connectomics Reveals How Partner Identity, Location, and Activity Specify Synaptic Connectivity in Drosophila. Neuron *109*, 105-122.e7.

Wang, H. C., Lin, C. C., Cheung, R., Zhang-Hooks, Y., Agarwal, A., Ellis-Davies, G., Rock, J., and Bergles, D. E. (2015). Spontaneous Activity of Cochlear Hair Cells Triggered by Fluid Secretion Mechanism in Adjacent Support Cells. Cell *163*, 1348-1359.

Xu, X. Z., Chien, F., Butler, A., Salkoff, L., and Montell, C. (2000). TRPgamma, a drosophila TRP-related subunit, forms a regulated cation channel with TRPL. Neuron *26*, 647-657.

Chapter 4

Developmental neural activity requires neuron-astrocyte interactions

ABSTRACT

Developmental neural activity is a common feature of neural circuit assembly. Although glia have established roles in synapse development, the contribution of neuron-glia interactions to developmental activity remains largely unexplored. Here we show that astrocytes are necessary for developmental activity during synaptogenesis in *Drosophila*. Using wide-field epifluorescence and two-photon imaging, we show that the glia of the central nervous system participate in developmental activity with type-specific patterns of intracellular calcium dynamics. Genetic ablation of astrocytes, but not of cortex or ensheathing glia, leads to severe attenuation of neuronal activity. Likewise, inhibition of neuronal activity results in the loss of astrocyte calcium dynamics. By altering these dynamics, we show that astrocytic calcium cycles can influence neuronal activity but are not necessary *per se*. Taken together, our results indicate that, in addition to their recognized role in the structural maturation of synapses, astrocytes are also necessary for the function of synapses during development.

4.1. INTRODUCTION

Stimulus-independent activity during development contributes to synapse formation in both vertebrate and invertebrate systems. In vertebrates, such developmental activity has been observed in various regions of the brain, where they are generally initiated by local circuitry and, in some systems, have been shown to have broad roles in circuit maturation (Blankenship and Feller, 2010). In *Drosophila*, patterned, stimulus-independent neural activity (PSINA, '*see-na*') accompanies synaptogenesis in the adult brain (Akin et al., 2019). PSINA engages the whole brain and manifests as cycles of coordinated active and silent phases which begin ~50 hours after pupal formation (hAPF) and continue until the last hour prior to eclosion. Perturbation of PSINA results in cell-type-specific alterations to synaptic structure in the visual system (Bajar B.T. et al., *Nature* In Revision).

Neuron-glia interactions are critical to neural activity in the mature nervous system, but the contribution of glia to developmental activity is less well understood. Glia play key roles in development, ranging from controlling neural proliferation and apoptosis (Corty and Freeman, 2013) to influencing axon guidance and synapse formation (Barres, 2008; Perez-Catalan et al., 2021). In *Drosophila*, astrocytes participate in PSINA with waves of activity complementary to neuronal activity (Akin et al., 2019). However, whether astrocytes or other glial cell types have specific roles in the regulation of developmental activity remains an open question.

There are seven subtypes of glia in the *Drosophila* central nervous system (CNS): astrocytes (or astrocyte-like glia, ALG), which penetrate the neuropil, ensheathing glia (EG) wrap neuropils and axonal tracts, cortex glia (CG) wrap the cortices, and the subperinuerial and perineurial glia cover the whole CNS (Kremer et al., 2017; Yildirim et al., 2019) (**Figure 4.1a**). Astrocytes, in particular, are critical for synaptic development. These specialized glia elaborate

peri-synaptic processes during synaptogenesis, and genetic ablation of astrocytes results in a 25-50% loss of synapses in different brain regions (Muthukumar et al., 2014). The co-dependence of synaptogenesis on glia and on PSINA (Bajar B.T. et al., *Nature* In Revision) suggests that neuron-glia interactions may regulate PSINA.

Here we show that astrocytes are necessary for developmental neuronal activity in *Drosophila*. In turn, calcium cycles in astrocytes are dependent on neuronal activity. These results indicate that neuron-glia interactions influence neural circuit formation through developmental activity.

4.2. RESULTS

Glial cell types participate in PSINA

Drivers specific to glial cell types have been described for the adult fly (Kremer et al., 2017). We tested this set for developmental expression and identified drivers for astrocytes (R25H07-GAL4), EG (R56F03-GAL4), and CG (R54H02-GAL4) (**Figure 4.1b-d**) that are largely specific from mid-pupa onwards. This expands the existing toolkit (Richier et al., 2017; Muthukumar et al., 2014) of type-specific glial drivers for developmental studies.

PSINA comprises coordinated cycles of active and silent phases; between 55-70 hAPF these cycles arrive with a regular period of 12-15 minutes (**Figure 4.1e**). Each active phase consists of multiple bouts of activity termed 'sweeps'. We have previously shown that astrocytes participate in PSINA with a pattern complementary to neuronal activity ((Akin et al., 2019) and see below): To ask whether other glial cell types also participate in PSINA, we expressed the green genetically-encoded calcium indicator (GECI) GCaMP6s (Chen et al., 2013) in glia and the red GECI jRCaMP1b (Dana et al., 2016) with orthogonal expression systems, and assessed activity *in vivo* using two-photon (2P) imaging of live pupae (**Figure 4.1f**) (Akin and Zipursky, 2016). We found that additional glial subtypes also participate in PSINA and do so in type-specific fashion (**Figure 4.1g-i**). As noted, astrocyte calcium cycles are complementary or anti-phase to neuronal activity: broadly, intracellular calcium levels rise during neuronal silent phases and fall during active phases. The reversal points, the peak before the fall and the trough before the rise, come after the beginning and end of neuronal active phases, respectively. CG follow a similar pattern but with a distinctive bi-phasic rise which transitions from gradual to abrupt with the onset of neuronal activity. By contrast to astrocytes and CG, EG have cycles that are in phase with neuronal activity and display calcium transients that appear to be delayed and broadened

versions of the neuronal traces. Astrocytes, CG, and EG have cycle frequencies that match that of neuronal PSINA (**Figure 4.1j-l**). In sum, the three glial subtypes most closely associated with the neurons and neuronal processes of the CNS have type-specific calcium cycles during PSINA.

Figure 4.1

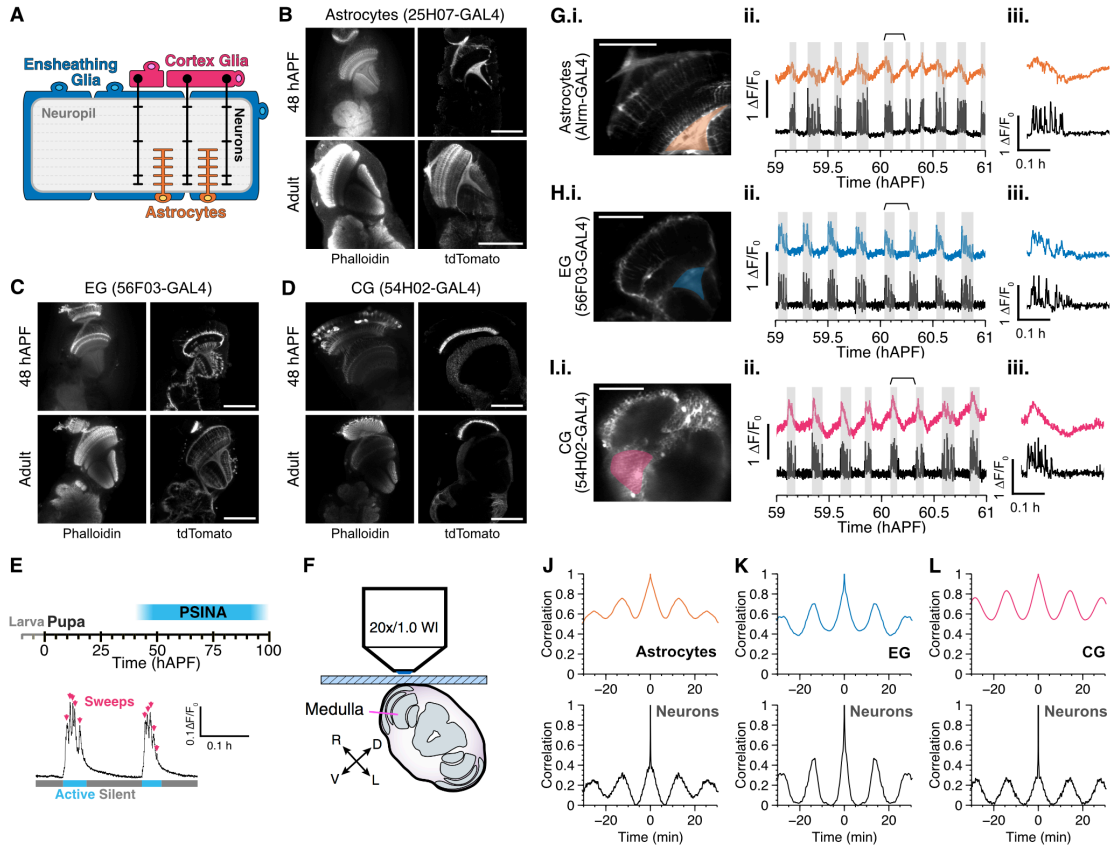

Figure 4.1. Multiple glial cell types participate in PSINA.

A. Schematic showing location and morphology of glial cell types in the Drosophila central nervous system. Astrocytes infiltrate the neuropil and interact with neuronal processes (orange), ensheathing glia envelop the neuropil (blue), and cortex glia envelop the soma (magenta).

B-D. Developmental characterization of drivers for astrocytes (B), ensheathing glia (C), and cortex glia (D). Representative micrographs from 48 hours after pupal formation (hAPF, top row) or newly eclosed adult (bottom row). *Left*, neuropil counterstain. *Right*, cell membrane

labeled with tdTomato and stained with anti-dsRed antibody. Note that R56F03-GAL4 shows sparse neuronal labeling. Scale bars, 100μm.

E. Above, timeline of PSINA during pupal development. Below, two representative cycles. Arrows indicate individual sweeps, while cyan and gray bars mark active and silent phases, respectively.

F. Schematic showing live 2P imaging preparation. Adapted from Akin et al. 2016.

G-H. Representative micrographs (i), traces (ii), and a single highlighted cycle (iii) showing calcium transients in astrocytes (G), cortex glia (H), and ensheathing glia (I) compared to neuronal activity. Highlighted region of interest on left used to generate glial traces on right. Shaded gray areas indicate neuronal active phases. Time-period indicated by the braces used to generate the single cycle in iii. Scale bars, 40μm.

J-L. Representative autocorrelograms from astrocytes (J), ensheathing glia (K), and cortex glia (L), with corresponding autocorrelograms from neurons measured in the same animal below.

For a complete list of genotypes used in this figure, see Table 3.

Astrocytes are necessary for PSINA

To ask whether any of these glial cell types are necessary for neuronal PSINA, we used the TARGET system (McGuire et al., 2003) to dis-inhibit expression of the proapoptotic gene *hid* during the second half of pupal development (**Figure 4.2a**). In the background of this type-specific ablation, we followed whole-brain neuronal activity from pan-neuronal jRCaMP1b using wide-field epifluorescence imaging. We confirmed ablation efficiency after imaging by quantifying surviving nuclei labeled with Stinger (Barolo et al., 2000).

Ablation of CG or EG did not affect PSINA (**Figure 4.2b-c**). Although expression of *hid* results in a significant loss of glia (57±20% ablation for CG and 84±4% ablation for EG, assessed at 84 hAPF), there was no significant alteration to PSINA. By contrast, ablation of astrocytes resulted in strong attenuation of PSINA. With the alrm-GAL4 astrocyte driver, 68±3% of astrocytes were ablated by 84 hAPF, and ~50% of PSINA amplitude was lost (**Figure 4.2d**). We observed a similar but stronger effect with the R25H07-GAL4 astrocyte driver: 71±7% of astrocytes were ablated by 84 hAPF, and >80% of PSINA amplitude was lost (**Figure 4.2e**). Differences between the astrocyte drivers could be due to non-astrocyte expression in alrm-GAL4 (Kremer et al., 2017) or to driver-strength-dependent timing of ablation. Additionally, we found that ablation of astrocytes with R25H07-GAL4 led to a >80% decrease in sweeps per cycle and ~50% fewer cycles relative to controls (**Figure 4.2f**).

Taken together, these results indicate that astrocytes are required for wildtype PSINA.

Figure 4.2

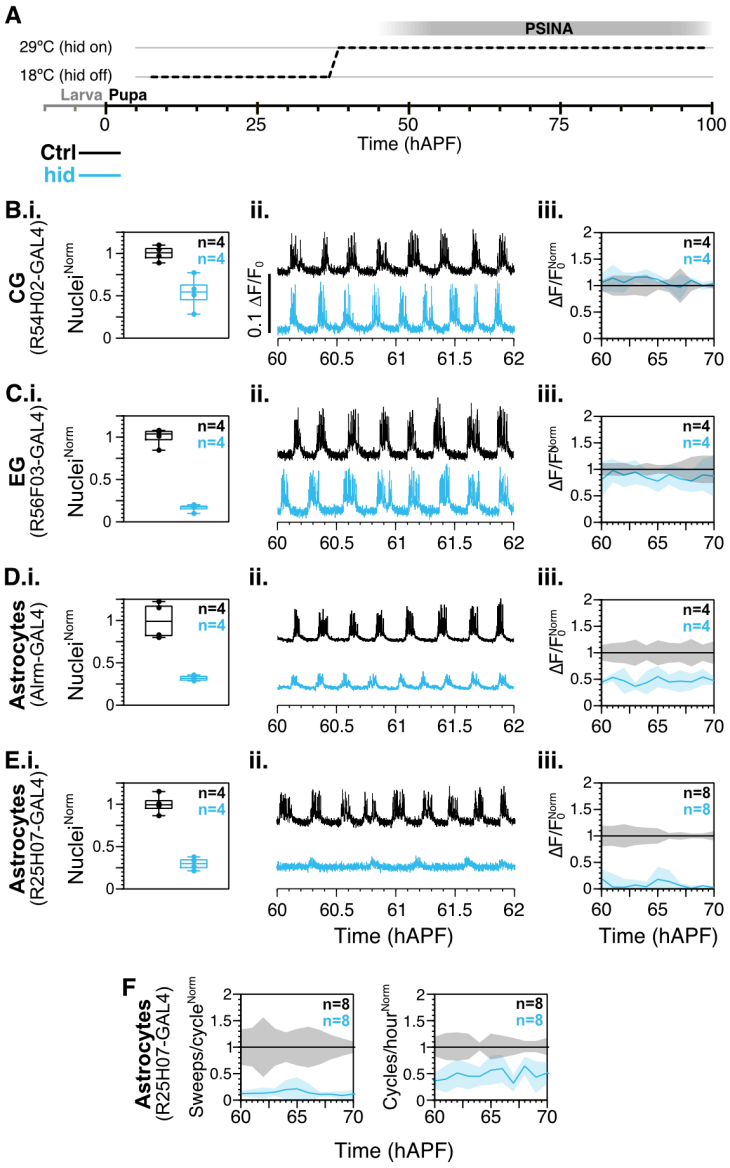

Figure 4.2. Astrocytes are required for PSINA.

A. Expression control of UAS-hid with TARGET; animals shifted from 18ºC to 29ºC at 38 hAPF.

B-E. i. Quantification of glial subtype ablation in control (black) and hid-expressing (teal) animals. Sample counts indicated in top right corner. ii. Representative traces from neurons expressing jRCaMP1b in control (black) and in genetic background of glial subtype ablation (teal). iii. Active phase average amplitude binned by hour and normalized to wildtype activity between 60 and 70 hAPF. Shaded areas, standard deviation. Colors match genotypes in i. Sample sizes in top right corner.

F. Sweeps/cycle (left) and cycles/hour (right) when astrocytes are ablated with 25H07-GAL4 driven hid. Data binned by hour and normalized to control. Shaded areas, standard deviation. Genotypes color-matched to B-E. Sample sizes in top right corner.

For a complete list of genotypes used in this figure, see Table 3.

Reciprocal influence of neuron-glia PSINA dynamics

Next, we asked whether PSINA in neurons and calcium cycles in astrocytes influence each other. To test for neuronal effects on glia, we expressed either the inward rectifying potassium channel, Kir2.1, or the inhibitor of synaptic release, tetanus toxin (TNT), in all neurons. As with the ablation experiments, we used the TARGET system to limit these severe perturbations to the second half of pupal development (**Figure 4.3a**). Pan-neuronal Kir2.1 or TNT expression results in near-complete loss of developmental activity (**Figure 4.3b**), consistent with previous observations (Bajar B.T. et al., *Nature* In Revision). Remarkably, targeted silencing of neuronal activity results in the loss of astrocytic calcium cycles (**Figure 4.3c-d**).

Astrocytes express the GABA transporter GAT in a manner dependent on neuronal GABA release (Muthukumar et al., 2014). To ask whether GAT expression requires PSINA, we silenced PSINA either with pan-neuronal Kir2.1 expression or with Kir2.1 expression in Trpγ expressing neurons (Bajar B.T. et al., *Nature* In Revision) and assessed GAT expression in the antennal lobes. We found that both approaches to inhibiting neuronal PSINA result in a ~20% decrease in astrocytic GAT expression (**Figure 4.3e-f**). The pan-neuronal expression domain also includes GABAergic neurons; therefore, loss of GAT expression with this global silencing approach is consistent with the established feedback between GABAergic activity and astrocytic GAT expression (Muthukumar et al., 2014). By contrast, Trpγ is expressed in ~2,000 neurons during PSINA and is thought to be a marker for relay neurons that set up the brain-wide coordination of developmental activity: silencing this small population of Trpγ+ neurons leads to near-complete loss of PSINA (Bajar B.T. et al., *Nature* In Revision). As such, the comparable loss of astrocytic GAT expression under these two conditions indicate that the mechanisms that

initiate and coordinate PSINA are upstream of the immediate neuron-astroglia interactions that regulate GAT expression levels.

Together, these data indicate that developmental neuronal activity is required for astrocytic calcium cycles and wild-type GAT expression levels.

Finally, to ask if astrocyte calcium cycles affect neuronal activity, we expressed the thermosensitive calcium channel TrpA1 in astrocytes. While TrpA1 is vital for calcium homeostasis in mammalian astrocytes (Shigetomi et al., 2013), it is not natively expressed in *Drosophila* astrocytes (Kurmangaliyev et al., 2020). As such, heterologous TrpA1 expression can be used to induce calcium influx in these cells (Pulver et al., 2009; Zhang et al., 2017). We activated 25H07-driven TrpA1 at the onset of PSINA (**Figure 4.4a**) and observed two phases of altered astrocyte calcium dynamics (**Figure 4.4b,c**). In the first ~20 hours after the activating temperature shift, astrocytes exhibit a gradual increase in baseline intracellular calcium while maintaining the periodic cycles. During this first phase, neuronal PSINA amplitude increases alongside the astrocyte baseline, with modest increases to active phase length and sweeps per cycle (**Figure 4.4b**). After about 20 hours, calcium baseline returns to pre-activation levels, and, notably, the astrocytic calcium cycles are lost (**Figure 4.4c**). In this second phase, neuronal PSINA amplitude also returns to pre-activation values and activity persists despite the loss of astrocytic calcium cycles (**Figure 4.4c**). These changes to GECI-reported calcium dynamics do not affect GAT expression (**Figure 4.4d-e**), suggesting that this aspect of astrocyte physiology is not sensitive to the perturbation of PSINA-associated calcium cycles. We conclude that astrocyte calcium cycles can modulate PSINA but are dispensable for ongoing neuronal activity.

Figure 4.3

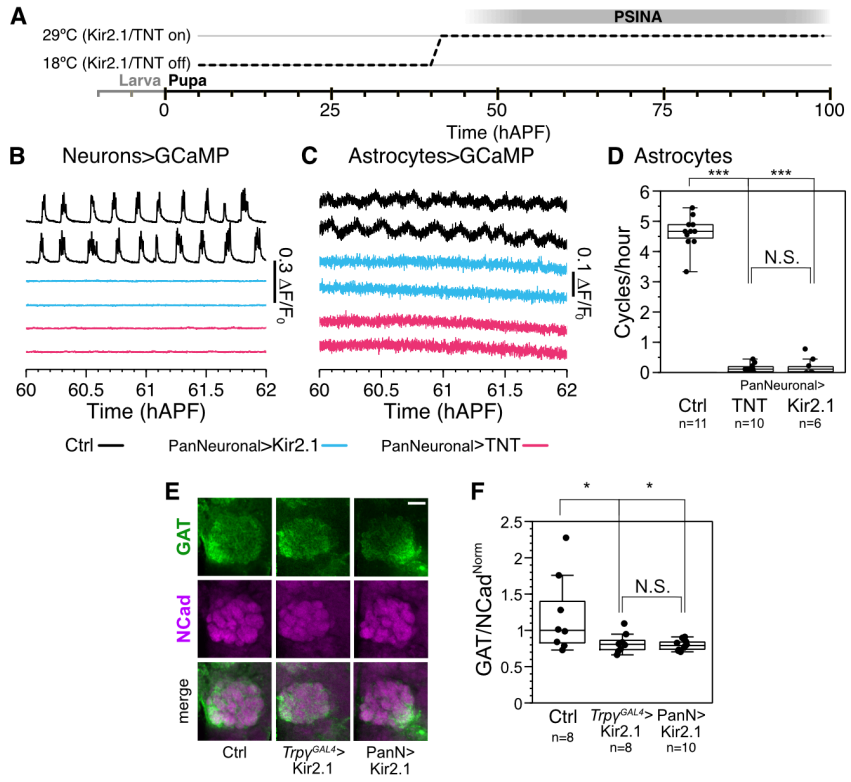

Figure 4.3. Astrocyte calcium cycles depend on neuronal activity

A. Expression control of UAS-Kir2.1 or TNT with TARGET; animals shifted from 18ºC to 29ºC at 38 hAPF.

B-C. Representative traces of pupae expressing GCaMP6s in neurons (B) or astrocytes (C). Wildtype activity in the empty-GAL4>Kir2.1 condition (black, top), and reduced activity in the pan-neuronal-GAL4>Kir2.1 (blue, middle) and pan-neuronal-Gal4>TNT condition (magenta, bottom).

D. Astrocyte calcium cycles per hour from 60 hAPF to 70 hAPF. Box-and-whiskers mark 5th, 25th, 50th, 75th, and 95th percentiles. ***, $p < 0.0001$ by Tukey's post-hoc test following ANOVA.

E. Representative micrographs of GAT expression in the antennal lobe in flies expressing Kir2.1 under the control of empty-GAL4, $Trp\gamma^{GAL4}$, or pan-neuronal -GAL4. Scale bar, 20μm.

F. GAT to NCad expression ratio, normalized to median control value, in flies expressing Kir2.1 under the control of empty-GAL4, $Trp\gamma^{GAL4}$, or pan-neuronal-GAL4. Boxplots as in D. *, $p < 0.05$ by Tukey's post-hoc test following ANOVA.

For a complete list of genotypes used in this figure, see Table 3.

Figure 4.4

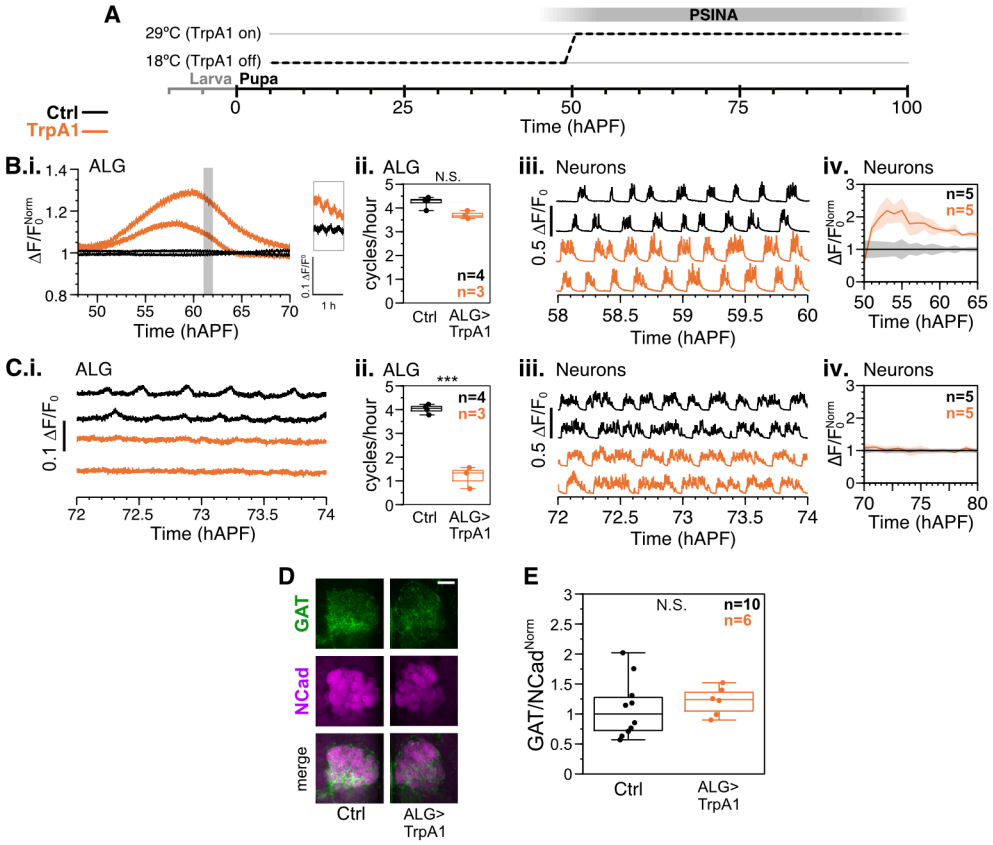

Figure 4.4. Neuronal activity does not require astrocyte calcium cycles.

A. TrpA1 activation in astrocytes by temperature shift; animals shifted from 18ºC to 29ºC at 50 hAPF.

B-C.i. Representative traces of pupae expressing GCaMP6s in: (B) astrocytes in the 20 hours after temperature shift. Control (black) and TrpA1 (orange) traces normalized to average control trace. Inset shows time period highlighted in gray; or (C) astrocytes after 70 hAPF. Control (black) and TrpA1 (orange) traces plotted as $\Delta F/F_0$. ii. Astrocyte calcium cycles per hour from 60 to 70 hAPF. Box-and-whiskers mark 5th, 25th, 50th, 75th, and 95th percentiles. ***, $p < 0.0001$ by Welch's unpaired t-test following Shapiro-Wilk test. Sample sizes indicated in top right

corner. iii. Representative traces of pupae expressing GCaMP6s in neurons with control (black) or TrpA1 expression in astrocytes (orange). iv. Active phase average amplitude binned by hour and normalized to wildtype activity. Shaded error bar represents standard deviation. Colors match genotypes in i. Sample sizes indicated in top right corner.

D. Representative micrographs of GAT expression in the antennal lobe in control flies vs flies expressing TrpA1 under the control of R25H07-GAL4 (astrocytes). Scale bar, 20μm.

E. GAT to NCad expression ratio, normalized to median control value, in control flies vs flies expressing TrpA1 under the control of R25H07-GAL4 (astrocytes). Boxplots as in B-C. *, $p < 0.05$ by Tukey's post-hoc test following ANOVA.

For a complete list of genotypes used in this figure, see Table 3.

4.3. Discussion

Here we show that astrocytes specifically are necessary for PSINA. Ablation of other glial cell types did not have a significant effect on developmental activity, indicating either that they are dispensable for PSINA, or that the survivors are able to compensate for the lost cells. Glial cell types show type-specific calcium dynamics. In astrocytes, these dynamics depend on neuronal PSINA, but a reciprocal dependence does not hold: while manipulating astrocytic calcium dynamics does modestly alter PSINA, robust neuronal activity persists even when astrocyte calcium cycles are nearly eliminated. These data suggest that astrocyte calcium dynamics are unlikely to be driving PSINA; instead, the glial calcium cycles are likely a response to neuronal activity.

Astrocytes have established roles in synapse formation, pruning, and maintenance (Perez-Catalan et al., 2021). During synaptogenesis in *Drosophila*, astrocytes extend numerous branches into the neuropil that closely interact with neuronal processes (Muthukumar et al., 2014; Richier et al., 2017). The developmental time-course of astrocytic morphological maturation closely tracks the accumulation of synapses in the fly brain (Muthukumar et al., 2014). Indeed, ablation of astrocytes during the second half of pupal development results in a ~25-50% reduction of synapses in different regions of the brain (Muthukumar et al., 2014). Here we show that PSINA, which takes place over the same time period, requires astrocytes, indicating that astrocytes are also necessary for synapse function during development. These data are consistent with *in vitro* results showing that spontaneous activity in retinal ganglion cells depend on the presence of glia (Pfrieger and Barres, 1997). And, as in the fly, loss of astrocytes in mammalian models results in fewer and functionally immature synapses (Ullian et al., 2001). In adult neuronal activity, astrocytes have multiple roles in influencing synaptic transmission and synaptic strength, ranging

from modulation of the peri-synaptic extracellular matrix to neuron-glia communication via gap junctions (Perez-Catalan et al., 2021; Allen and Eroglu, 2017). How or whether these mechanisms are responsible for astrocytic control of PSINA remain open questions.

Little is known about the role of glia in developmental activity. A transient population of astrocyte-like supporting cells initiates developmental activity in the sensory neurons of the cochlea via release of ATP (Tritsch et al., 2007). In the retina, Müller glia display calcium transients alongside retinal waves that depend on neurotransmitter spillover (Zhang et al., 2019; Rosa et al., 2015). These observations suggest that astrocytes may play varied roles in initiating or maintaining developmental activity. Our results support two possible mechanisms by which developmental activity depends on astrocytes in *Drosophila*. First, given that astrocytes promote synaptic function in the adult (Perez-Catalan et al., 2021), developmental synaptic function may also rely on astrocytes. In the absence of astrocytes, synapses appear to experience either arrested or delayed development (Muthukumar et al., 2014). The attenuation of PSINA in this background could thus be due to a global loss or reduction in synaptic function. Secondly, astrocytes may be directly involved in the rhythmogenesis of PSINA, perhaps through release of neuromodulators that stimulate a central pattern generator that initiates activity. Our data suggest that such a mechanism should be independent of glial calcium cycles (**Figure 4.4**). Identifying the molecular mechanisms that link astrocyte function to developmental activity will be key to understanding the relationship between glia, neuronal activity, and synaptic development.

4.4. Materials and Methods

Experimental Model and Subject Details

Flies were reared at 18º, 25º, or 29ºC on standard cornmeal/molasses medium; developmental time was matched to the 25°C standard (1x) using relative rates of 0.5x and 1.25x for 18°C and 29°C, respectively. Pupal development was staged with respect to white pre-pupa formation (0 hAPF) or head eversion (12 hAPF). GAL4/UAS (Brand and Perrimon, 1993) and LexA/LexAop (Lai and Lee, 2006) expression systems were used to drive cell-type-specific transgene expression.

2P imaging

2P imaging was performed as described previously (Akin et al., 2019).

Wide-field imaging

Wide-field imaging was performed as described previously (Bajar B.T. et al., *Nature* In Revision).

Immunohistochemistry

Brains were dissected in cold Schneider Medium (SM, Gibco #21720–024) and fixed with 3% v/v glyoxal solution (Electron Microscopy Sciences #16525) for 30 minutes at room temperature (RT) or with 4% v/v PFA (Electron Microscopy Sciences #15710) in SM for 20 minutes at RT. Brains were then washed out of fixative into PBS (Quality Biological), solubilized in PBST (0.5% Tween-20 (Sigma #P9416) in PBS) for 1 h, and blocked in PBTN (5% Normal Donkey

Serum (Jackson ImmunoResearch #017-000-121) in PBST) for 1-2 h, all at RT. Brains were sequentially incubated in primary and secondary antibodies diluted in PBTN for 24-48h at 4^{o}C, with at least 3 washes through PBST over 2 h at RT in between and afterwards. Brains were post-fixed with 3% v/v glyoxal for 30 minutes at RT or with 4% v/v PFA in SM for 20 minutes at RT, followed by multiple washes into PBST over 10 minutes. Brains were finally transferred to Everbrite mounting medium (Biotium #23001) and mounted on to slides for imaging.

Primary antibodies and dilutions used in this study were as follows: Mouse monoclonal anti-V5 (Novus Biologicals #NBP2-52703-0.2mg, 1:150), rat monoclonal anti-FLAG (DYKDDDDK) (Novus Biologicals #NBP1-06712, 1:100), mouse monoclonal anti-c-MYC (Developmental Studies Hybridoma Bank (DSHB) #9E10-concentrate, 1:100), rabbit polyclonal anti-dsRed (Clontech #632496, 1:125), chicken anti-GFP (Abcam #ab13970, 1:1000), rabbit monoclonal anti-HA (Cell Signaling Technology #3724, 1:300), rat monoclonal anti-Ncad (DSHB #DN-Ex #8-c, 1:100), rabbit anti-GAT ((Muthukumar et al., 2014), 1:5000).

Secondary antibodies and dilutions used in this study were as follows: Alexa 488 donkey polyclonal anti-chicken (Jackson ImmunoResearch # 703-545-155, 1:400), Alexa 488 donkey polyclonal anti-mouse (Jackson ImmunoResearch #715-545-151, 1:400), Alexa 568 donkey polyclonal anti-rabbit (Invitrogen #A10042, 1:400), Alexa 647 donkey polyclonal anti-rat (Jackson ImmunoResearch #712-605-153, 1:400), Alexa 647 goat polyclonal anti-rabbit (ThermoFisher # A-21244, 1:200).

Immunofluorescence images were acquired using Zeiss LSM 780 confocal microscope with 20x/0.8 air or 40x/1.2 glycerol immersion objectives (Zeiss).

Quantification and Statistical Analysis.

Analysis of 2P imaging data was carried out as previously described (Akin et al., 2019).

Analysis of pupal wide-field imaging data was carried out as previously described (Bajar B.T. et al., *Nature* In Revision).

Processing and quantification of confocal images.

Counting nuclei: Three-dimensional binary masks of the half-brain were manually generated for each confocal stack using Fiji (ImageJ). Labeled nuclei within these masks were segmented from confocal stacks using custom scripts written in MATLAB; a function critical to this task was sourced from the MathWorks File Exchange repository (Tim Jerman (2021). Jerman Enhancement Filter (https://github.com/timjerman/JermanEnhancementFilter), GitHub.).

Quantifying GAT immunofluorescence: Antennal lobes were analyzed for GAT signal. Z-stacks were analyzed in Fiji (ImageJ). The z-slice with the largest antennal lobe diameter was selected, and an ROI encircling the antennal lobe was used to measure average signal in the antennal lobe at the selected slice. GAT signal was normalized to N-Cadherin signal in each antennal lobe.

Statistical analysis.

Statistical analysis was performed on RStudio. We used either Welch's t-test following the Shapiro-Wilk test for normality for comparisons between two groups, or Tukey's post-hoc test following ANOVA to assess statistical significance of differences between groups. Population averages are given as mean ± standard deviation (SD).

Table 3. List of genotypes used in this work.

Figure	Cells Imaged / Label	Fly Genotype	Notes
Fig4.1B	Astrocytes / myr::tdTomato	*pBPhsFLP2::PEST (attP3);* *10X-UAS-myr::tdTOM (attP40) / +;* *UAS-FSF-myr::smGdP-HA/V5/FLAG (VK5) / R25H07-GAL4 (attP2)*	HA/V5/FLAG not used in analysis
Fig4.1C	Ensheathing glia / myr::tdTomato	*pBPhsFLP2::PEST (attP3);* *10X-UAS-myr::tdTOM (attP40) / +;* *UAS-FSF-myr::smGdP-HA/V5/FLAG (VK5) / R56F03-GAL4 (attP2)*	HA/V5/FLAG not used in analysis
Fig4.1D	Cortex glia / myr::tdTomato	*pBPhsFLP2::PEST (attP3);* *10X-UAS-myr::tdTOM (attP40) / +;* *UAS-FSF-myr::smGdP-HA/V5/FLAG (VK5) / R54H02-GAL4 (attP2)*	HA/V5/FLAG not used in analysis
Fig4.1G,J	Astrocytes / GCaMP, Neurons / RCaMP	*20XUAS-IVS-Syn21-OpGCaMP6s-p10 (su(Hw)attP8)/w;* *R57C10-lexA (attP40), 13XLexAop2-IVS-NES-jRCaMP1b (VK00005) / alrm-Gal4.D.3;* *20XUAS-IVS-Syn21-OpGCaMP6s-p10 (su(Hw)attP1) / alrm-Gal4.D.2*	
Fig4.1H,K	Ensheathing glia / GCaMP, Neurons / RCaMP	*20XUAS-IVS-Syn21-OpGCaMP6s-p10 (su(Hw)attP8)/w;* *R57C10-lexA (attP40), 13XLexAop2-IVS-NES-jRCaMP1b (VK00005) / +;* *20XUAS-IVS-Syn21-OpGCaMP6s-p10 (su(Hw)attP1) / R56F03-GAL4 (attP2)*	
Fig4.1I,L	Cortex glia / GCaMP, Neurons / RCaMP	*20XUAS-IVS-Syn21-OpGCaMP6s-p10 (su(Hw)attP8)/w;* *R57C10-lexA (attP40), 13XLexAop2-IVS-NES-jRCaMP1b (VK00005) / +;* *20XUAS-IVS-Syn21-OpGCaMP6s-p10 (su(Hw)attP1) / R54H02-GAL4 (attP2)*	
Fig4.2B	Cortex glia / hid, Neurons /RCaMP	*w;* *R57C10-LexA (attP40), 13X-LexAop2-IVS-NES-jRCaMP1b-p10 (su(Hw)attP5) / UAS-Stinger, UAS-hidZ;* *tubP-GAL80ts(2) / R54H02-GAL4 (attP2)*	
Fig4.2C	Ensheathing glia / hid, Neurons /RCaMP	*w;* *R57C10-LexA (attP40), 13X-LexAop2-IVS-NES-jRCaMP1b-p10 (su(Hw)attP5) / UAS-Stinger, UAS-hidZ;* *tubP-GAL80ts(2) / R56F03-GAL4 (attP2)*	
Fig4.2D	Astrocytes / hid, Neurons /RCaMP	*w;* *R57C10-LexA (attP40), 13X-LexAop2-IVS-NES-jRCaMP1b-p10 (su(Hw)attP5) / UAS-Stinger, UAS-hidZ;* *tubP-GAL80ts(2) / alrm-GAL4*	
Fig4.2E,F	Astrocytes / hid, Neurons /RCaMP	*w;* *R57C10-LexA (attP40), 13X-LexAop2-IVS-NES-jRCaMP1b-p10 (su(Hw)attP5) / UAS-Stinger, UAS-hidZ;* *tubP-GAL80ts(2) / R25H07-GAL4 (attP2)*	
Fig4.3B,E,F	Neurons / GCaMP	*yw, UAS-Kir2.1-2A-myr::tdTOM-3xHA (attP3) / w;* *tubP-GAL80ts(10) / +;* *R57C10-lexAp65 (VK20), lexAop2-opGCaMP6s (su(Hw)attP1), UAS-his::RFP (attP2) / R57C10-GAL4 (attP2)*	
Fig4.3B,E,F	Neurons / Kir2.1, Neurons / GCaMP	*yw, UAS-Kir2.1-2A-myr::tdTOM-3xHA (attP3) / w;* *tubP-GAL80ts(10) / +;* *R57C10-lexAp65 (VK20), lexAop2-opGCaMP6s (su(Hw)attP1), UAS-his::RFP (attP2) / empty-GAL4 (attP2)*	
Fig4.3B,E,F	Trpγ Neurons / Kir2.1, Neurons / GCaMP	*yw, UAS-Kir2.1-2A-myr::tdTOM-3xHA (attP3) / w;* *tubP-GAL80ts(10) / TI-Trpγ-GAL4 ;* *R57C10-lexAp65 (VK20), lexAop2-opGCaMP6s (su(Hw)attP1), UAS-his::RFP (attP2) / +*	

Figure	Cells Imaged / Label	Fly Genotype	Notes
Fig4.3B	Neurons / GCaMP	*w, UAS-TeTxLC (C1) / w;* *tubP-GAL80ts(10) / +;* *R57C10-lexAp65 (VK20), lexAop2-opGCaMP6s (su(Hw)attP1), UAS-his::RFP (attP2) / empty-GAL4 (attp2)*	
Fig4.3B	Neurons / TNT, Neurons / GCaMP	*w, UAS-TeTxLC (C1) / w;* *tubP-GAL80ts(10) / +;* *R57C10-lexAp65 (VK20), lexAop2-opGCaMP6s (su(Hw)attP1), UAS-his::RFP (attP2) / R57C10-GAL4 (attP2)*	
Fig4.3C,D	Astrocytes / GCaMP	*w, UAS-TeTxLC (C1) / w;* *tubP-GAL80ts(10) / R25H07-lexAp65 (attP40), lexAop2-opGCaMP6s (su(Hw)attP5);* *lexAop2-opGCaMP6s (su(Hw)attP1) / empty-GAL4 (attP2)*	
Fig4.3C,D	Neurons / Kir2.1, Astrocytes / GCaMP	*w, UAS-Kir2.1-2A-myr::tdTOM-3xHA (attP3) / w;* *tubP-GAL80ts(10) / R25H07-lexAp65 (attP40), lexAop2-opGCaMP6s (su(Hw)attP5);* *lexAop2-opGCaMP6s (su(Hw)attP1) / R57C10-GAL4 (attP2)*	
Fig4.3C,D	Neurons / TNT, Astrocytes / GCaMP	*w, UAS-TeTxLC (C1) / w;* *tubP-GAL80ts(10) / R25H07-lexAp65 (attP40), lexAop2-opGCaMP6s (su(Hw)attP5);* *lexAop2-opGCaMP6s (su(Hw)attP1) / R57C10-GAL4 (attP2)*	
Fig4.4B,C	Astrocytes / GCaMP	*w;* *R25H07-lexAp65 (attP40), lexAop2-opGCaMP6s (su(Hw)attP5);* *R25H07-GAL4 (attP2) / +*	
Fig4.4B,C,D,E	Astrocytes / TrpA1, Astrocytes / GCaMP	*w;* *R25H07-lexAp65 (attP40), lexAop2-opGCaMP6s (su(Hw)attP5);* *R25H07-GAL4 (attP2) / UAS-TrpA1 (attP2)*	
Fig4.4B,C	Neurons / GCaMP	*w;* *R57C10-lexAp65 (attP40), lexAop2-opGCaMP6s (su(Hw)attP5);* *R25H07-GAL4 (attP2) / +*	
Fig4.4B,C	Astrocytes / TrpA1, Neurons / GCaMP	*w;* *R57C10-lexAp65 (attP40), lexAop2-opGCaMP6s (su(Hw)attP5);* *UAS-TrpA1 (attP2) / R25H07-GAL4 (attP2)*	

4.5. References

Akin, O., Bajar, B. T., Keles, M. F., Frye, M. A., and Zipursky, S. L. (2019). Cell-type-Specific Patterned Stimulus-Independent Neuronal Activity in the Drosophila Visual System during Synapse Formation. Neuron *101*, 894-904.e5.

Akin, O., and Zipursky, S. L. (2016). Frazzled promotes growth cone attachment at the source of a Netrin gradient in the. Elife *5*, e20762.

Allen, N. J., and Eroglu, C. (2017). Cell Biology of Astrocyte-Synapse Interactions. Neuron *96*, 697-708.

Barolo, S., Carver, L. A., and Posakony, J. W. (2000). GFP and beta-galactosidase transformation vectors for promoter/enhancer analysis in Drosophila. Biotechniques *29*, 726, 728, 730, 732.

Barres, B. A. (2008). The mystery and magic of glia: a perspective on their roles in health and disease. Neuron *60*, 430-440.

Blankenship, A. G., and Feller, M. B. (2010). Mechanisms underlying spontaneous patterned activity in developing neural circuits. Nat Rev Neurosci *11*, 18-29.

Brand, A. H., and Perrimon, N. (1993). Targeted gene expression as a means of altering cell fates and generating dominant phenotypes. Development *118*, 401-415.

Chen, T. W., Wardill, T. J., Sun, Y., Pulver, S. R., Renninger, S. L., Baohan, A., Schreiter, E. R., Kerr, R. A., Orger, M. B., Jayaraman, V., Looger, L. L., Svoboda, K., and Kim, D. S. (2013). Ultrasensitive fluorescent proteins for imaging neuronal activity. Nature *499*, 295-300.

Corty, M. M., and Freeman, M. R. (2013). Cell biology in neuroscience: Architects in neural circuit design: glia control neuron numbers and connectivity. J Cell Biol *203*, 395-405.

Dana, H., Mohar, B., Sun, Y., Narayan, S., Gordus, A., Hasseman, J. P., Tsegaye, G., Holt, G. T., Hu, A., Walpita, D., Patel, R., Macklin, J. J., Bargmann, C. I., Ahrens, M. B., Schreiter, E. R., Jayaraman, V., Looger, L. L., Svoboda, K., and Kim, D. S. (2016). Sensitive red protein calcium indicators for imaging neural activity. Elife *5*, e12727.

Kremer, M. C., Jung, C., Batelli, S., Rubin, G. M., and Gaul, U. (2017). The glia of the adult Drosophila nervous system. Glia *65*, 606-638.

Kurmangaliyev, Y. Z., Yoo, J., Valdes-Aleman, J., Sanfilippo, P., and Zipursky, S. L. (2020). Transcriptional Programs of Circuit Assembly in the Drosophila Visual System. Neuron *108*, 1045-1057.e6.

Lai, S. L., and Lee, T. (2006). Genetic mosaic with dual binary transcriptional systems in Drosophila. Nat Neurosci *9*, 703-709.

McGuire, S. E., Le, P. T., Osborn, A. J., Matsumoto, K., and Davis, R. L. (2003). Spatiotemporal rescue of memory dysfunction in Drosophila. Science *302*, 1765-1768.

Muthukumar, A. K., Stork, T., and Freeman, M. R. (2014). Activity-dependent regulation of astrocyte GAT levels during synaptogenesis. Nat Neurosci *17*, 1340-1350.

Perez-Catalan, N. A., Doe, C. Q., and Ackerman, S. D. (2021). The role of astrocyte-mediated plasticity in neural circuit development and function. Neural Dev *16*, 1.

Pfrieger, F. W., and Barres, B. A. (1997). Synaptic efficacy enhanced by glial cells in vitro. Science *277*, 1684-1687.

Pulver, S. R., Pashkovski, S. L., Hornstein, N. J., Garrity, P. A., and Griffith, L. C. (2009). Temporal dynamics of neuronal activation by Channelrhodopsin-2 and TRPA1 determine behavioral output in Drosophila larvae. J Neurophysiol *101*, 3075-3088.

Richier, B., Vijandi, C. M., Mackensen, S., and Salecker, I. (2017). Lapsyn controls branch extension and positioning of astrocyte-like glia in the Drosophila optic lobe. Nat Commun *8*, 317.

Rosa, J. M., Bos, R., Sack, G. S., Fortuny, C., Agarwal, A., Bergles, D. E., Flannery, J. G., and Feller, M. B. (2015). Neuron-glia signaling in developing retina mediated by neurotransmitter spillover. Elife *4*, e09590.

Shigetomi, E., Jackson-Weaver, O., Huckstepp, R. T., O'Dell, T. J., and Khakh, B. S. (2013). TRPA1 channels are regulators of astrocyte basal calcium levels and long-term potentiation via constitutive D-serine release. J Neurosci *33*, 10143-10153.

Tritsch, N. X., Yi, E., Gale, J. E., Glowatzki, E., and Bergles, D. E. (2007). The origin of spontaneous activity in the developing auditory system. Nature *450*, 50-55.

Ullian, E. M., Sapperstein, S. K., Christopherson, K. S., and Barres, B. A. (2001). Control of synapse number by glia. Science *291*, 657-661.

Yildirim, K., Petri, J., Kottmeier, R., and Klämbt, C. (2019). Drosophila glia: Few cell types and many conserved functions. Glia *67*, 5-26.

Zhang, R. W., Du, W. J., Prober, D. A., and Du, J. L. (2019). Müller Glial Cells Participate in Retinal Waves via Glutamate Transporters and AMPA Receptors. Cell Rep *27*, 2871-2880.e2.

Zhang, Y. V., Ormerod, K. G., and Littleton, J. T. (2017). Astrocyte Ca2+ influx negatively regulates neuronal activity. eNeuro *4*, ENEURO.0340-16.2017.

Chapter 5

Discussion

5.1. SUMMARY OF RESULTS

Developmental activity independent of environmental stimulus has been observed during neural circuit formation in a variety of species and regions within the central nervous system (CNS). Decades of work have shown a broad role for this activity in the maturation of nascent circuitry (Blankenship and Feller, 2010; Ackman and Crair, 2014). Prior to the work described here, developmental activity had not been observed in the development of the adult nervous system in invertebrates. Additionally, the role of such activity at the resolution of individual synapses and cell types remained largely unknown.

The experiments described here establish the presence of patterned, stimulus-independent neural activity (PSINA) in the developing *Drosophila* brain. PSINA temporally coincides with synaptogenesis, beginning around halfway through metamorphosis, and continuing until the hour before eclosion. This time spans approximately two days, during which PSINA evolves from an earlier periodic stage, characterized by regular cycles of active and silent phases, to a later turbulent stage, where this regularity is lost. PSINA is not restricted to electrical activity in neurons: glia participate in PSINA with oscillations in intracellular calcium that are complementary to neuronal oscillations. In the visual system, cell types participate in PSINA with unique activity signatures, in which cell types that are connected in the adult display correlated activity patterns.

PSINA depends on activity from neurons that express the cation channel Trpγ. In *trpγ* mutants, the signal amplitude of PSINA active phases is reduced by over 50%, and the cell-type-specific activity dynamics among visual processing neurons is altered in a stereotyped fashion. Silencing Trpγ+ neurons leads to a near-complete loss of PSINA, and exogenously activating these neurons leads to continuous activity. Finally, Trpγ is expressed in wide-field neurons that

extend space-filling processes in multiple neuropils. Taken together, these data indicate that Trpγ neurons represent a relay system that propagates activity throughout the brain.

Using the Trpγ mutant as a handle on PSINA, we observed that synapse formation depends on neural activity. In trpγ null animals, visual processing cells display altered synapse counts. These changes are cell-type-specific in both the sign and magnitude of change. This synaptic phenotype is cell-non-autonomous and can be phenocopied with brain-wide silencing of PSINA, indicating that PSINA influences synaptogenesis in a cell-type-specific manner.

5.2. ORGANIZATION OF DEVELOPMENTAL ACTIVITY IN *DROSOPHILA*

Our data suggest that a designated circuit initiates PSINA and propagates activity throughout the brain. This circuit minimally consists of: 1) a central pattern generator (CPG) that initiates PSINA, 2) Trpγ+ neurons that propagate PSINA brain-wide, and 3) downstream neurons that comprise all other neurons of the brain. Intermediate components may act in between any of these features. Below, I discuss the rationale for each of these indicated components.

A CPG initiates PSINA

CPGs are circuits that govern rhythmic activity without a requirement for external stimulus. Such circuits have been well-characterized for locomotive activity, particularly in invertebrate systems for flying, walking, or digestion (Mulloney and Smarandache, 2010; Mantziaris et al., 2020; Marder and Calabrese, 1996). In particular, the crustacean stomatogastric ganglion has been vital for uncovering the circuit principles, ion channels, and logic underlying CPGs (Marder and Calabrese, 1996). In vertebrate systems, CPGs are thought to govern repetitive locomotive activity, contrasting with the previous notion that peripheral circuitry independent of CNS control governed such behaviors (Mulloney and Smarandache, 2010).

Outside of repetitive behaviors, the role for CPGs is less defined. Although rhythmic activity has been observed in a variety of contexts in both invertebrate and vertebrate neural circuits, it is often unknown whether this activity originates from discrete circuits or whether they are an emergent property of the network (Blankenship and Feller, 2010). Of particular interest are infraslow oscillations, defined as rhythmic activities oscillating at <1 Hz. In some contexts, discrete populations of neurons have been identified as the generators of infraslow activity (Blum et al., 2019; Zylbertal et al., 2017).

Several lines of evidence support the presence of a CPG as the origin of PSINA. First, invertebrate CPGs are characteristically temperature-dependent (Tang et al., 2010; Zornik et al., 2010). We find that PSINA frequency directly correlates with temperature, similar to recently described CPGs for *Drosophila* repetitive behaviors (Ravbar P, 2020). Second, some residual activity persists even with pan-neuronal silencing of PSINA with Kir2.1 or TNT, suggesting either that the pan-neuronal drivers we use do not sufficiently express in all neurons, and that those neurons are intrinsically active, or that there is a set of intrinsically active neurons during PSINA that govern cycle frequency. In either case, these data indicate the presence of cells that are active when the full brain is nearly completely silenced. Third, the characterization of Trpγ and Trpγ+ neurons indicates that this cell population is less likely to instruct cycle frequency or initiate cycles independent of other input (Chapter 3). Finally, the regularity of the cycle frequency of PSINA suggests a population of cells dedicated to the control of rhythmicity, similar to oscillations functioning at much slower time-scales such as circadian rhythms (King and Sehgal, 2020), or at faster timescales including breathing (Ashhad and Feldman, 2020), locomotion, or flight (Mulloney and Smarandache, 2010).

We propose that the PSINA CPG is driven almost entirely by excitation, with little to no role for inhibition in the generation of active phases. Silencing the output of the main inhibitory neurotransmitters in the fly, GABA and glutamate, does not affect cycle frequency (Chapter 3). This model of an excitation-based CPG contrasts in logic with well-described CPG circuits that depend on reciprocal inhibition between ensembles of neurons, such as the crustacean stomatogastric ganglion or the locust flight circuit (Marder and Bucher, 2001; Mulloney and Smarandache, 2010). In vertebrate systems, CPGs that act primarily through excitation have been described, including in the mouse olfactory bulb (Zylbertal et al., 2017).

Identifying the circuits, cells, and molecules that comprise the PSINA CPG will be critical to understanding the organization of developmental activity.

Trpγ neurons relay activity

Downstream of the presumptive CPG, Trpγ+ neurons relay activity throughout the brain. Inhibition or ablation of Trpγ+ neurons attenuates PSINA to the same extent as pan-neuronal inhibition, indicating that activity flows from Trpγ+ neurons to the rest of the brain. Conversely, activation of Trpγ+ neurons induces brain-wide activity during the timeframe of PSINA. These data are supported by the morphology of a population of Trpγ+ neurons that are characterized by axons projecting from the central brain to the various neuropils of the brain, in which they elaborate wide-field processes.

Notably, the Trpγ+ population is partially transient: the complement of Trpγ+ neurons peak during PSINA and then decreases and stabilizes in number by eclosion. There is some precedence in the literature for transient populations of cells driving neuronal activity. The best-characterized case is in the vertebrate cochlea, where astrocyte-like supporting cells comprise a transient structure called Kölliker's organ during development. The supporting cells of Kölliker's organ release ATP, which drives developmental activity in hair cells, the first-order sensory neurons of the auditory system (Tritsch et al., 2007). Upon maturation of the circuit and onset of hearing, the Kölliker's organ undergoes apoptosis (Wang et al., 2015). Additionally, transient populations of Cajal-Retzius and sub-plate neurons are thought to drive activity in the developing neocortex, although some fraction of these cells persist into adulthood (Luhmann et al., 2016). Similar to these cases, we hypothesize that there are a subset of Trpγ+ neurons that are dedicated to the propagation of PSINA, and after eclosion, either undergo apoptosis or stop expressing Trpγ.

The notion that neurons may require Trpγ to appropriately relay PSINA hints at the intracellular role the channel may play. One of the mammalian orthologs of Trpγ, TRPC4, has been shown to amplify electrical activity (Munsch et al., 2003). Indeed, in *trpγ* mutants, the activity of Trpγ+ neurons is muted, suggesting that Trpγ amplifies electrical activity within Trpγ+ neurons to wildtype levels, which is then transmitted to the rest of the brain. An additional ortholog of Trpγ is TRPC5, which plays a role in the hypothalamo-pituitary axis, where it is expressed in dopaminergic neurons and sets their rhythmic patterns of activity (Blum et al., 2019). However, Trpγ is less likely to control rhythmogenesis, as *trpγ* mutants do not have altered cycle dynamics, and cycles of characteristic periodicity persist with inhibition of Trpγ+ neurons. Thus, how Trpγ acts in relay neurons to appropriately amplify and pattern PSINA remains an open question.

The Trpγ+ population is diverse both in morphology and use of neurotransmitters and neuromodulators. Notably, various neuropeptidergic cells developmentally express Trpγ+ that have roles in rhythmogenesis in adult physiology. For example, cells that express pigment dispersing factor (Pdf) or DH44 are crucial for maintaining circadian rhythms in adult behavior and physiology (Cavanaugh et al., 2014; Renn et al., 1999), and express Trpγ+ at 72 hAPF (Chapter 3). These neurons are responsible for frequencies much slower than that of PSINA. However, we entertain the possibility that these cells could utilize intracellular circadian mechanisms (e.g. the oscillations of clock genes) to control the periodicity of PSINA.

Another prominent neuropeptidergic population among Trpγ+ neurons is SIFamide, comprising a population of <10 neurons in the pars intercerebralis (PI). In adult physiology, SIFamide contributes to circadian feeding rhythms (Dreyer et al., 2019). In crustaceans, SIFamide regulates rhythms in the cardiac and stomatogastric ganglia (Blitz et al., 2019).

Interestingly, during midpupal development, the SIFamide receptor is expressed pan-neuronally as part of what is considered a "pan-neuronal code" (Kurmangaliyev et al., 2020). It would be possible to assess the role of SIFamide+/Trpγ+ neurons on PSINA with existing handles on these neurons and neuronal silencing tools. The transcriptomic data combined with its role in rhythmogenesis across invertebrate systems suggest that it may be crucial for PSINA.

The neuromodulators described above act chiefly through metabotropic receptors, by contrast to neurotransmitters that utilize ionotropic receptors. Neuropeptidergic signaling is unlikely to confer cell-type-specific activity patterns, which require spatial resolution at the level of seconds to milliseconds. Given that Trpγ+ neurons form the template for activity throughout the brain, there must be a crucial role for ionotropic neurotransmission between Trpγ+ neurons and their downstream partners. Understanding how Trpγ+ neurons utilize neuromodulation and neurotransmission will be crucial for determining how PSINA dynamics are generated, and how specific patterns of activity instruct circuit assembly.

All other neurons receive input from the relay system

All neurons that we have assessed thus far participate in PSINA. Throughout the CNS, neurons are active in globally shared active phases. In the visual system, cells participate with cell-type-specific dynamics, although we hypothesize that neurons throughout the brain will show a similar diversity in activity patterns. The sweep dynamics captured by coordination and coherence metrics (Chapter 2) indicate a variation in activity patterns ranging from highly synchronous to wave-like structure.

How other neurons outside of the visual system participate in PSINA has not been assessed at the level of two-photon imaging, due to the absence of an amenable imaging preparation. Anecdotally, there appears to be a fat-free zone on the dorsal aspect of the pupal

head that may enable two-photon imaging of the olfactory system. If such a preparation were developed and optimized, it could be possible to assess the cell-type-specific dynamics of mushroom body neurons. We anticipate that these central brain neurons will display a similar diversity in activity patterns to those in the optic lobes.

How is this diversity in activity patterns generated? We hypothesize that Trpγ+ neurons form the 'activity scaffold' for pan-neuronal activity, such that the activity pattern of a given cell type can be predicted from its connectivity to Trpγ+ neurons. This hypothesis is supported by the high correlation of Trpγ+ neuron activity to pan-neuronal activity (Chapter 3), observed both at the level of epifluorescence and two-photon imaging. An alternative explanation to this observation is that Trpγ+ neurons exist at a parallel hierarchical level to all other neurons and receive identical input from the central pattern generator. However, this alternative model is not supported by the observation that silencing Trpγ+ neurons results in pan-neuronal silencing.

Future studies of the relay system should focus on identifying genetic handles and/or existing drivers of individual Trpγ+ neurons. Once such tools are found, it will be possible to assess the postsynaptic partners of these Trpγ+ neurons with genetic approaches such as trans-Tango (Talay et al., 2017), and assess how the activity patterns of individual neurons correlate with their upstream Trpγ+ partners. Such characterization of PSINA dynamics will make it possible to determine how patterns of activity originate and influence circuit assembly.

A role for astrocytes

In addition to the Trpγ relay system, astrocyte-like glia have been shown to have a critical role in the propagation of activity. Astrocytes participate in PSINA in a complementary pattern (Chapter 2). Loss of astrocytes by ablation immediately prior to PSINA results in a loss of neuronal PSINA (Chapter 4). We show that glial and neuronal activity transients can influence

each other, but that neuronal activity is required for glial calcium transients (Chapter 4). These data indicate that astrocytes are a crucial component of PSINA.

Astrocytes do not express Trpγ, indicating that they are unlikely to play a role similar to that of the Trpγ+ relay system. Instead, I hypothesize that astrocytes are required to support neurotransmission at synapses throughout the brain in a calcium-independent manner. The importance of neuron-glia interactions to neurotransmission has been shown to be crucial in a variety of both vertebrate and invertebrate systems, where astrocytes in particular have been shown to mediate glutamate transport (Rothstein et al., 1996), directly interact with neuromodulators to influence neural activity (Ma et al., 2016), or modify synapses through cytokine secretion (Allen and Eroglu, 2017), and provide structural and functional support to synapses (Allen and Eroglu, 2017). During PSINA, astrocytes could contribute to any of these mechanisms that would be critical to neuronal function.

To further elucidate the role of astrocytes in PSINA, it would be ideal to identify molecules that regulate the reciprocal signaling between neurons and astrocytes. Such molecules could be identified through a genetic screen of candidates identified by developmental transcriptomic profiling (Kurmangaliyev et al., 2020). In a future experiment, it would be possible to knock down gene candidates with RNA interference driven by R25H07-GAL4, which expresses strongly and specifically in astrocytes (Chapter 4), and monitor pan-neuronal calcium imaging during development via widefield epifluorescence imaging to assess changes to neuronal PSINA. Such an approach could be multiplexed to observe many samples simultaneously to quickly screen through candidates. I hypothesize that such a screen would reveal secreted factors that are specifically expressed in astrocytes and mediate neuron-glia signaling during development.

5.3. ROLE OF DEVELOPMENTAL ACTIVITY IN SYNAPSE FORMATION

We have shown that alterations to PSINA, either in the *trpγ* mutant or with pan-neuronal tetanus toxin expression, leads to cell-type-specific alterations in synapse structure. While examples abound of activity-dependent changes to synapse structure in vertebrate development and in adult physiology, our results challenge the previous notion that the invertebrate brain develops independent of activity.

How does developmental activity influence synapse formation? A long-held debate in vertebrate developmental activity has been whether activity is instructive or permissive for the observed changes in circuit maturation (Sun et al., 2008; Xu et al., 2011; Burbridge et al., 2014). If developmental activity is permissive, then the broad presence of activity alone is sufficient for physiological circuit assembly to proceed. If developmental activity is instructive, the activity itself provides information that affects the mature state of the circuit. Our data suggest that PSINA is instructive to neural circuit assembly. The *trpγ* mutant, which has attenuated activity amplitude and altered patterns of activity, phenocopies a total loss of PSINA with respect to changes in synaptic structure (Chapter 3). The simplest explanation for the correspondence of these results is that the presence of some activity alone is insufficient to produce wild-type complements of synapses; instead, the activity patterns of wild-type PSINA, lost in the *trpγ* mutant, must have a critical role.

If PSINA were permissive, then we would expect to see a synaptic phenotype that tracked with the level of attenuation (i.e. a more extreme phenotype with total PSINA silencing compared to the milder attenuation with *trpγ*). An alternative explanation in favor of a permissive role is that there is some "activity threshold" required for physiological synapse development that neither *trpγ* nor pan-neuronal PSINA silencing reach. Since *trpγ* mutants have

a ~50% decrease in PSINA, this activity threshold would need to lie somewhere above that level, and would constitute a significant level of activity. This high activity threshold that would be required of a permissive model, combined with the aforementioned synaptic phenotypes and the complexity held within the spatiotemporal patterns of PSINA, strongly support an instructive role for developmental activity.

PSINA could instruct synapse development through Hebbian mechanisms, whereby synaptic strength is determined by integration of activity. Cell types that are synaptic partners in the adult brain have highly correlated PSINA (Chapter 2). This correlation occurs at the level of individual sweeps within shared active phases, where synaptic partners are more likely to have temporally coordinated sweeps of similar duration and amplitude. Due to these characteristics, Hebbian principles could explain how PSINA influences circuit assembly.

In particular, spike-timing dependent plasticity (STDP) could be a useful model to understand the role of PSINA. STDP states that the weight of a given synapse depends on the relative timing between the arrival of presynaptic and postsynaptic spikes at the synapse (Caporale and Dan, 2008). Cases in which presynaptic spikes very closely precede postsynaptic spikes are thought to produce strong increases in synaptic weight. This model of synaptic plasticity has been validated in various adult circuitry, in vitro and in vivo, across both invertebrate and vertebrate models (Tazerart et al., 2020; Flavell and Greenberg, 2008; Cassenaer and Laurent, 2007), and is thought to contribute to neural circuit formation (Kimura and Itami, 2019). Additionally, the regular oscillations of PSINA with active and silent phases could contribute to STDP-based development via “temporal encoding” of activity patterns within active phases (Masquelier, 2014). Biochemical mechanisms underlying such plasticity are thought to primarily depend on calcium-dependent intracellular signaling (Lisman et al., 2012).

Applying STDP to PSINA, the correspondence of individual sweeps between future synaptic pairs could strengthen connections between nascent synapses. Structurally, at least some synapses appear to be present prior to PSINA (Chen et al., 2014), and the channels required for electrical activity begin to be expressed at a similar time (Kurmangaliyev et al., 2020). These observations would be consistent with a model in which synaptic specificity is configured prior to the start of PSINA, and the strength of new synapses are tuned by PSINA throughout development. By the end of PSINA, the animal ecloses and circuits are sufficiently tuned for adult sensory processing and behavior.

Whether STDP explains the effect of PSINA on synapse formation depends on higher temporal resolution for imaging, perhaps with newer voltage indicators (Villette et al., 2019), to determine whether presynaptic activity precedes postsynaptic activity. Additionally, whether PSINA affects synaptic weights could be assessed via optogenetics paired with calcium imaging.

However, this model cannot completely explain the results shown here. First, we observe changes to synaptic count and structure, manifested as a change in the number of presynaptic sites as assessed by STaR (Chapter 3). This observation could manifest functionally as a change in synaptic weights, but could also represent a change in synaptic specificity, which we have not yet tested. Additionally, we observe cell-type-specific changes to synaptic structure, in which at least one cell type displays increased presynaptic sites in the *trpγ* mutant. If we assume that presynaptic activity precedes postsynaptic activity across synaptic partners, then we would expect the sign of synaptic changes to remain the same. Again, higher temporal resolution would be required to further investigate the correspondence of activity.

Additional mechanisms can be invoked to account for these experimental observations. First, PSINA is almost certain to induce transcriptional programs vital to development. Activity

is known to induce the expression of hundreds of activity-regulated genes, many of which are transcription factors that could in turn control different expression programs (Flavell and Greenberg, 2008). Recent data in both the visual (Tyssowski et al., 2018) and olfactory system (Nakashima et al., 2013) has shown that patterns of activity influence the induction of transcriptional programs. Given that each cell type, at least in the visual system, displays a unique PSINA signature, developmental activity could be driving cell-type-specific wiring programs that underlie synaptic specificity. RNA sequencing can be performed to determine the role of transcription in activity-dependent synaptogenesis, and in particular the role it might have in cell-type-specific wiring. Performing whole optic lobe sequencing through development using conditions with altered activity, including *trpγ* and Kir2.1 driven by $Trp\gamma^{G4}$, may elucidate how PSINA controls expression of wiring genes. I hypothesize that cell-surface molecules that regulate synaptic connectivity (e.g. DIPs and Dprs (Tan et al., 2015)) and ion channels that regulate synaptic strength (e.g. neurotransmitter receptors) are dynamically regulated by PSINA in a cell-type-specific fashion.

Cell-type-specific transcriptional programs induced by PSINA dynamics could explain the cell-type-specific changes to synaptic structure that we observed (Chapter 3). For example, Tm9 shows an increase in synapse count in the absence of PSINA, which would be inconsistent with potentiation related to STDP. Through the latter half of pupal development, Tm9 synapses increase monotonically (Chapter 3). This timecourse of Tm9 synapse development would be inconsistent with a role for PSINA in the pruning of overproliferated synapses, as is seen in the neuromuscular junction, for example (Vonhoff and Keshishian, 2017).

It is possible that activity-regulated transcription does not play a role in PSINA-dependent synaptogenesis. Instead, effects on translation and post-translational modifications

could drive alterations to synaptic structure, as seen in long-term potentiation (Lisman et al., 2012). Here, alternative approaches to assessing biochemical changes at the synapse may be required, perhaps at the level of proteomics, metabolomics, or phosphorylation dynamics. Any of these efforts would constitute a significant undertaking, so it will be necessary to first identify a specific cell, circuit, or set of molecules that are likely to be sensitive to activity regulation and demonstrate a robust phenotype. Ongoing work in electron microscopy, activity-dependent transcriptomics, and characterization of *Trpγ+* neurons may help identify a well-defined system.

5.4. DEVELOPMENTAL ACTIVITY IS A FUNDAMENTAL FEATURE OF BRAIN DEVELOPMENT

Oscillatory activity during development has been observed in a variety of vertebrate model organisms, including rats (Galli and Maffei, 1988), ferrets (Meister et al., 1991), mice (Ackman et al., 2012), chick (O'Donovan et al., 1998), and zebrafish (Avitan et al., 2017). Our work, along with other work in *Drosophila*, has now shown that developmental activity accompanies circuit assembly in both the adult nervous system (Chapter 2) and the larval nervous system (Baines and Bate, 1998). Additionally, comparable patterns of activity have been recorded via electrocephalogram or magnetic resonance imaging in human premature neonates, suggesting that developmental activity occurs in humans as well (Tolonen et al., 2007).

Developmental activity in *Drosophila* occurs in a brain-wide fashion (Chapter 2). In vertebrate systems, regimes of activity have been characterized individually throughout the central nervous system, including the auditory system, hippocampus, brainstem, spinal cord, and neocortex (Blankenship and Feller, 2010). Activity in the visual system has been shown to propagate broadly from the retina to the lateral geniculate nucleus and superior colliculus to the visual cortex (Ackman et al., 2012). Whether there exists broadly coordinated activity in vertebrate brains similar to the organization of PSINA in *Drosophila* remains an open question, but appears unlikely due to the temporal distance of regional events (Blankenship and Feller, 2010).

An additional difference in organization between vertebrate and *Drosophila* developmental activity is the frequency of active phases. During the periodic stage in PSINA, cycles occur regularly every 12-15 minutes (Chapter 2). By contrast, in the mouse visual system, retinal waves occur every 1-3 minutes, and in the hippocampus and cerebellum, oscillations

occur at faster frequencies (Blankenship and Feller, 2010). The differences in dynamics suggest different mechanisms underlying developmental activity between species. Faster imaging in *Drosophila* and hours-long time-lapse intravital imaging in the mouse will more clearly delineate how dynamics compare across phyla.

These broad observations of developmental activity during synaptogenesis across disparate circuits and species suggest that developmental activity is an evolutionarily conserved component of neurodevelopment. Intriguingly, if the mechanisms underlying developmental activity are indeed different between vertebrates and invertebrates, then patterned activity may be an evolutionarily convergent mechanism of circuit assembly. The observed effects of developmental activity on circuit structure have been modest (Chapter 3, as well as (Valdes-Aleman et al., 2021; Xu et al., 2011; Vonhoff and Keshishian, 2017; Burbridge et al., 2014)). Nevertheless, these modest alterations can result in behavioral phenotypes (Valdes-Aleman et al., 2021), supporting the notion that developmental activity is a critical step in the refinement of a mature and functional nervous system. I propose that developmental activity plays a role in circuit maturation throughout the entire central nervous system, in which activity is responsible for fine-tuning the structures set in place by neurogenesis, proliferation, and the elaboration of neural processes.

5.5. FUTURE DIRECTIONS AND CONCLUSIONS

In this discussion I have laid out several future experiments to further elucidate the mechanisms that drive PSINA and the mechanisms by which PSINA regulates synaptogenesis. By dissecting the *Trpγ*^{G4} expression domain and the cells upstream of it, it may be possible to identify both the circuit that drives PSINA and the cells that imbue downstream neurons with cell-type-specific dynamics. By screening astrocyte-specific molecules expressed during development, it may be possible to determine how PSINA depends on neuron-glia interactions. Single-cell RNA sequencing will elucidate whether PSINA regulates synaptogenesis via dynamic control of transcriptional wiring programs. Finally, advances in genetically-encoded indicators of neural activity will enable better characterization of PSINA dynamics, offering insight into both the regulation of activity and how its cell-type-specific patterns affect development. These results will help discern how specific patterns of developmental activity influence neural circuit assembly at the level of synaptic structure, cellular physiology, and synaptic specificity.

In conclusion, developmental activity is a fundamental feature of brain development. In this work in *Drosophila*, I have described the presence of developmental activity during synaptogenesis, identified a role for activity in synapse formation, and found a genetically specified population of neurons that controls activity. The genetic tractability of the fruit fly will facilitate understanding how developmental activity contributes to circuit assembly at the level of cells, synapses, and molecules. I anticipate that these insights will establish a fundamental understanding of how activity sculpts neurodevelopment in both physiology and disease.

5.6. REFERENCES

Ackman, J. B., Burbridge, T. J., and Crair, M. C. (2012). Retinal waves coordinate patterned activity throughout the developing visual system. Nature *490*, 219-225.

Ackman, J. B., and Crair, M. C. (2014). Role of emergent neural activity in visual map development. Curr Opin Neurobiol *24*, 166-175.

Allen, N. J., and Eroglu, C. (2017). Cell Biology of Astrocyte-Synapse Interactions. Neuron *96*, 697-708.

Ashhad, S., and Feldman, J. L. (2020). Emergent Elements of Inspiratory Rhythmogenesis: Network Synchronization and Synchrony Propagation. Neuron *106*, 482-497.e4.

Avitan, L., Pujic, Z., Mölter, J., Van De Poll, M., Sun, B., Teng, H., Amor, R., Scott, E. K., and Goodhill, G. J. (2017). Spontaneous Activity in the Zebrafish Tectum Reorganizes over Development and Is Influenced by Visual Experience. Curr Biol *27*, 2407-2419.e4.

Baines, R. A., and Bate, M. (1998). Electrophysiological development of central neurons in the Drosophila embryo. J Neurosci *18*, 4673-4683.

Blankenship, A. G., and Feller, M. B. (2010). Mechanisms underlying spontaneous patterned activity in developing neural circuits. Nat Rev Neurosci *11*, 18-29.

Blitz, D. M., Christie, A. E., Cook, A. P., Dickinson, P. S., and Nusbaum, M. P. (2019). Similarities and differences in circuit responses to applied Gly. J Neurophysiol *121*, 950-972.

Blum, T., Moreno-Pérez, A., Pyrski, M., Bufe, B., Arifovic, A., Weissgerber, P., Freichel, M., Zufall, F., and Leinders-Zufall, T. (2019). Trpc5 deficiency causes hypoprolactinemia and altered function of oscillatory dopamine neurons in the arcuate nucleus. Proc Natl Acad Sci U S A *116*, 15236-15243.

Burbridge, T. J., Xu, H. P., Ackman, J. B., Ge, X., Zhang, Y., Ye, M. J., Zhou, Z. J., Xu, J., Contractor, A., and Crair, M. C. (2014). Visual circuit development requires patterned activity mediated by retinal acetylcholine receptors. Neuron *84*, 1049-1064.

Caporale, N., and Dan, Y. (2008). Spike timing-dependent plasticity: a Hebbian learning rule. Annu Rev Neurosci *31*, 25-46.

Cassenaer, S., and Laurent, G. (2007). Hebbian STDP in mushroom bodies facilitates the synchronous flow of olfactory information in locusts. Nature *448*, 709-713.

Cavanaugh, D. J., Geratowski, J. D., Wooltorton, J. R., Spaethling, J. M., Hector, C. E., Zheng, X., Johnson, E. C., Eberwine, J. H., and Sehgal, A. (2014). Identification of a circadian output circuit for rest:activity rhythms in Drosophila. Cell *157*, 689-701.

Chen, Y., Akin, O., Nern, A., Tsui, C. Y., Pecot, M. Y., and Zipursky, S. L. (2014). Cell-type-specific labeling of synapses in vivo through synaptic tagging with recombination. Neuron *81*, 280-293.

Dreyer, A. P., Martin, M. M., Fulgham, C. V., Jabr, D. A., Bai, L., Beshel, J., and Cavanaugh, D. J. (2019). A circadian output center controlling feeding:fasting rhythms in Drosophila. PLoS Genet *15*, e1008478.

Flavell, S. W., and Greenberg, M. E. (2008). Signaling mechanisms linking neuronal activity to gene expression and plasticity of the nervous system. Annu Rev Neurosci *31*, 563-590.

Galli, L., and Maffei, L. (1988). Spontaneous impulse activity of rat retinal ganglion cells in prenatal life. Science *242*, 90-91.

Kimura, F., and Itami, C. (2019). A Hypothetical Model Concerning How Spike-Timing-Dependent Plasticity Contributes to Neural Circuit Formation and Initiation of the Critical Period in Barrel Cortex. J Neurosci *39*, 3784-3791.

King, A. N., and Sehgal, A. (2020). Molecular and circuit mechanisms mediating circadian clock output in the Drosophila brain. Eur J Neurosci *51*, 268-281.

Kurmangaliyev, Y. Z., Yoo, J., Valdes-Aleman, J., Sanfilippo, P., and Zipursky, S. L. (2020). Transcriptional Programs of Circuit Assembly in the Drosophila Visual System. Neuron *108*, 1045-1057.e6.

Lisman, J., Yasuda, R., and Raghavachari, S. (2012). Mechanisms of CaMKII action in long-term potentiation. Nat Rev Neurosci *13*, 169-182.

Luhmann, H. J., Sinning, A., Yang, J. W., Reyes-Puerta, V., Stüttgen, M. C., Kirischuk, S., and Kilb, W. (2016). Spontaneous Neuronal Activity in Developing Neocortical Networks: From Single Cells to Large-Scale Interactions. Front Neural Circuits *10*, 40.

Ma, Z., Stork, T., Bergles, D. E., and Freeman, M. R. (2016). Neuromodulators signal through astrocytes to alter neural circuit activity and behaviour. Nature *539*, 428-432.

Mantziaris, C., Bockemühl, T., and Büschges, A. (2020). Central pattern generating networks in insect locomotion. Dev Neurobiol *80*, 16-30.

Marder, E., and Bucher, D. (2001). Central pattern generators and the control of rhythmic movements. Curr Biol *11*, R986-96.

Marder, E., and Calabrese, R. L. (1996). Principles of rhythmic motor pattern generation. Physiol Rev *76*, 687-717.

Masquelier, T. (2014). Oscillations can reconcile slowly changing stimuli with short neuronal integration and STDP timescales. Network *25*, 85-96.

Meister, M., Wong, R. O., Baylor, D. A., and Shatz, C. J. (1991). Synchronous bursts of action potentials in ganglion cells of the developing mammalian retina. Science *252*, 939-943.

Mulloney, B., and Smarandache, C. (2010). Fifty Years of CPGs: Two Neuroethological Papers that Shaped the Course of Neuroscience. Front Behav Neurosci *4*,

Munsch, T., Freichel, M., Flockerzi, V., and Pape, H. C. (2003). Contribution of transient receptor potential channels to the control of GABA release from dendrites. Proc Natl Acad Sci U S A *100*, 16065-16070.

Nakashima, A., Takeuchi, H., Imai, T., Saito, H., Kiyonari, H., Abe, T., Chen, M., Weinstein, L. S., Yu, C. R., Storm, D. R., Nishizumi, H., and Sakano, H. (2013). Agonist-independent GPCR activity regulates anterior-posterior targeting of olfactory sensory neurons. Cell *154*, 1314-1325.

O'Donovan, M. J., Chub, N., and Wenner, P. (1998). Mechanisms of spontaneous activity in developing spinal networks. J Neurobiol *37*, 131-145.

Ravbar P, Z. N., Simpson JH (2020). Behavioral evidence for nested central pattern generator control of *Drosophila* grooming. bioRxiv

Renn, S. C., Park, J. H., Rosbash, M., Hall, J. C., and Taghert, P. H. (1999). A pdf neuropeptide gene mutation and ablation of PDF neurons each cause severe abnormalities of behavioral circadian rhythms in Drosophila. Cell *99*, 791-802.

Rothstein, J. D., Dykes-Hoberg, M., Pardo, C. A., Bristol, L. A., Jin, L., Kuncl, R. W., Kanai, Y., Hediger, M. A., Wang, Y., Schielke, J. P., and Welty, D. F. (1996). Knockout of glutamate transporters reveals a major role for astroglial transport in excitotoxicity and clearance of glutamate. Neuron *16*, 675-686.

Sun, C., Warland, D. K., Ballesteros, J. M., van der List, D., and Chalupa, L. M. (2008). Retinal waves in mice lacking the beta2 subunit of the nicotinic acetylcholine receptor. Proc Natl Acad Sci U S A *105*, 13638-13643.

Talay, M., Richman, E. B., Snell, N. J., Hartmann, G. G., Fisher, J. D., Sorkaç, A., Santoyo, J. F., Chou-Freed, C., Nair, N., Johnson, M., Szymanski, J. R., and Barnea, G. (2017). Transsynaptic Mapping of Second-Order Taste Neurons in Flies by trans-Tango. Neuron *96*, 783-795.e4.

Tan, L., Zhang, K. X., Pecot, M. Y., Nagarkar-Jaiswal, S., Lee, P. T., Takemura, S. Y., McEwen, J. M., Nern, A., Xu, S., Tadros, W., Chen, Z., Zinn, K., Bellen, H. J., Morey, M., and Zipursky, S. L. (2015). Ig Superfamily Ligand and Receptor Pairs Expressed in Synaptic Partners in Drosophila. Cell *163*, 1756-1769.

Tang, L. S., Goeritz, M. L., Caplan, J. S., Taylor, A. L., Fisek, M., and Marder, E. (2010). Precise temperature compensation of phase in a rhythmic motor pattern. PLoS Biol *8*,

Tazerart, S., Mitchell, D. E., Miranda-Rottmann, S., and Araya, R. (2020). A spike-timing-dependent plasticity rule for dendritic spines. Nat Commun *11*, 4276.

Tolonen, M., Palva, J. M., Andersson, S., and Vanhatalo, S. (2007). Development of the spontaneous activity transients and ongoing cortical activity in human preterm babies. Neuroscience *145*, 997-1006.

Tritsch, N. X., Yi, E., Gale, J. E., Glowatzki, E., and Bergles, D. E. (2007). The origin of spontaneous activity in the developing auditory system. Nature *450*, 50-55.

Tyssowski, K. M., DeStefino, N. R., Cho, J. H., Dunn, C. J., Poston, R. G., Carty, C. E., Jones, R. D., Chang, S. M., Romeo, P., Wurzelmann, M. K., Ward, J. M., Andermann, M. L., Saha, R. N., Dudek, S. M., and Gray, J. M. (2018). Different Neuronal Activity Patterns Induce Different Gene Expression Programs. Neuron *98*, 530-546.e11.

Valdes-Aleman, J., Fetter, R. D., Sales, E. C., Heckman, E. L., Venkatasubramanian, L., Doe, C. Q., Landgraf, M., Cardona, A., and Zlatic, M. (2021). Comparative Connectomics Reveals How Partner Identity, Location, and Activity Specify Synaptic Connectivity in Drosophila. Neuron *109*, 105-122.e7.

Villette, V., Chavarha, M., Dimov, I. K., Bradley, J., Pradhan, L., Mathieu, B., Evans, S. W., Chamberland, S., Shi, D., Yang, R., Kim, B. B., Ayon, A., Jalil, A., St-Pierre, F., Schnitzer, M. J., Bi, G., Toth, K., Ding, J., Dieudonné, S., and Lin, M. Z. (2019). Ultrafast Two-Photon Imaging of a High-Gain Voltage Indicator in Awake Behaving Mice. Cell *179*, 1590-1608.e23.

Vonhoff, F., and Keshishian, H. (2017). Cyclic nucleotide signaling is required during synaptic refinement at the Drosophila neuromuscular junction. Dev Neurobiol *77*, 39-60.

Wang, H. C., Lin, C. C., Cheung, R., Zhang-Hooks, Y., Agarwal, A., Ellis-Davies, G., Rock, J., and Bergles, D. E. (2015). Spontaneous Activity of Cochlear Hair Cells Triggered by Fluid Secretion Mechanism in Adjacent Support Cells. Cell *163*, 1348-1359.

Xu, H. P., Furman, M., Mineur, Y. S., Chen, H., King, S. L., Zenisek, D., Zhou, Z. J., Butts, D. A., Tian, N., Picciotto, M. R., and Crair, M. C. (2011). An instructive role for patterned spontaneous retinal activity in mouse visual map development. Neuron *70*, 1115-1127.

Zornik, E., Katzen, A. W., Rhodes, H. J., and Yamaguchi, A. (2010). NMDAR-dependent control of call duration in Xenopus laevis. J Neurophysiol *103*, 3501-3515.

Zylbertal, A., Yarom, Y., and Wagner, S. (2017). Synchronous Infra-Slow Bursting in the Mouse Accessory Olfactory Bulb Emerge from Interplay between Intrinsic Neuronal Dynamics and Network Connectivity. J Neurosci *37*, 2656-2672.